Study on overall thermal performance of metal curtain walls

Hua Ge

A thesis

In

The Department

of

Building, Civil and Environmental Engineering

Presented in Partial Fulfillment of the Requirements

for the Degree of Doctor of Philosophy at

Concordia University

Montreal, Quebec, Canada

October 2002

0-612-78623-4

Canadä

ABSTRACT

Study on overall thermal performance of metal curtain walls

Hua Ge, Ph.D.
Concordia University, 2002

Metal curtain walls are widely used in commercial buildings and offer many advantages including space saving, high quality in manufacturing, light weight, significant aesthetic freedom, and rapid construction. However, their thermal performance is still low due to the fact that metal curtain walls consist of a large portion of glazing, and glass and metal are high heat conductors. In practice, metal curtain walls are referred to as "heat sink" in heating-dominant climate. The relatively low thermal resistance results in low surface temperature in cold winter, and thus may cause condensation and thermal discomfort problems in addition to high energy consumption.

Initially, metal curtain walls grew within metal window industry and the current methodology and standards developed for evaluating window performance are also used for curtain walls. However, metal curtain walls differ from windows in that they have a much larger continuous glazing portion, more complex configuration and heat flow at the joints. Their overall performance depends on the interaction and integration of individual constituents as well as the performance of each component. However, the assessment of curtain wall performance by existing standards is segmented and no study has addressed the overall thermal performance of curtain walls by treating them as integrated systems.

The objective of this study is to evaluate the overall thermal performance of metal curtain walls using a developed holistic approach for the purpose of providing technical information on the improvement of curtain wall design. A comprehensive research program has been designed and implemented to establish the overall performance of curtain walls by experimental testing, analytical and simulation studies.

For the first time, extensive experimental testing has been conducted on full-scale specimen under field conditions reproduced in a large-scale environmental chamber. The two-story full-size specimen (3.8m by 6.7m) includes two commercially available curtain wall systems with different design details. The experimental program includes: 1) full-scale air leakage test, 2) thermal performance test, 3) measurement of local convection film coefficient, and, 4) measurement of local draft induced by curtain wall cold surface. The analytical and simulation studies include: 1) effect of design details on thermal transmittance using the simulation program FRAME, 2) effect of local film coefficients on the condensation resistance prediction using the simulation program FRAME, 3) effect of thermal performance of curtain walls on occupant thermal comfort and on energy consumption.

Results from extensive testing and simulations have revealed the intricate links among the components, the overall wall assembly performance and the impact on the energy use and indoor comfort; and, therefore, provided solid technical information for manufacturers on the productive direction of future R&D and for designers on the selection of curtain wall systems to achieve energy-efficient buildings with healthy and

comfort indoor environment. The extensive testing provided a valuable set of experimental data to validate the current and future computer simulation programs.

Acknowledgements

I would like to thank my parents who have been supportive and patient during all the years of my studies. Finally, I would like to thank my husband, Ye Zhang, for everything he has done in helping me to pursue my Ph.D., for all the time he spent with me discussing my research, for all the nights he accompanied me with carrying out the tests, and for all the effort he made in helping me to edit the thesis.

Table of contents

xiii

List of figures

List of tables

Nomenclature

Symbol	Parameter	Unit
α	thermal diffusivity, $k/\rho c_p$	$[\text{m}^2/\text{s}]$
β	thermal coefficient of volume expansion	$[1/\text{K}]$
υ	kinematic viscosity of fluid	$[\text{m}^2/\text{s}]$
μ	dynamic viscosity	$[\text{g/m·s}]$
ρ	density	$[\text{kg/m}^3]$
ρ	reflectance	$[-]$
δ	Stefan-Boltzmann constant	$[\text{W/m}^2\text{·K}^4]$
ε	hemispherical emittance	$[-]$
φ	weighting factor	$[-]$
A	area	$[\text{m}^2]$
A	aspect ratio	$[-]$
c_p	specific heat at constant pressure	$[\text{kJ/(kg·K)}]$
C	flow coefficient	$[\text{L/s·Pa}^n]$
C	cooling load	$[\text{MJ/m}^2\text{·yr}]$
E	radiative energy	$[\text{W/m}^2]$
F	view factor	$[-]$
g	gravitational acceleration	$[\text{N/kg}]$
G	irradiation; total radiation incident on surface per unit time and per unit area	$[\text{W/m}^2]$
Gr	Grashof number	$[-]$
h	heat transfer coefficient	$[\text{W/(m}^2\text{·K)}]$

h	height	[m]
H	energy	[W]
H	heating load	[MJ/m^2·yr]
h$_{fg}$	latent heat of evaporation of water	[kJ/kg]
I	Internal heat gain	[W/m^2]
J	radiosity; total radiation that leaves surface per unit time and per unit area	[W/m^2]
k	thermal conductivity	[W/(m· K)]
L	length	[m]
Nu	Nusselt number	
P, ΔP	pressure, pressure differential	[Pa]
Pr	Prandtl number	
Q	volumetric rate of air flow	[L/s]
q	heat flow	[W/m^2]
R	thermal resistance	[(m^2·K)/W]
Ra	Rayleigh number	
T	temperature	[K] or [^{o}C]
Tu	turbulent intensity	[%]
U	overall coefficient of heat transfer	[W/(m^2·K)]
v	air velocity	[m/s]
VS	Vertical incident solar energy on façade under consideration	[W/m^2·day]
W	humidity ratio	[kg/kg of dry air]
W	internal gain parameter	[W/m^2]

Subscripts

a	air	l	latent heat
b	Baffle/black body	m	mean
c	convection	meas	measurements
cg	center-of-glass	o	outdoor
d	divider	p	parallel path method
e	extraneous air leakage	pr	plane radiant
eg	edge-of-glass	r	radiation
es	edge-of-spandrel	ref	reference
f	frame	s	sensible heat
g	glazing	smpl	sample
i	indoor	surf	surface
IR	infrared	t	total
iso	isothermal plane method	w	window
j	directions	∞	mainstream flow

Abbreviations

AAMA	American Architectural Manufacturer Association
CDD	Cooling Degree Days
CRF	Condensation Resistance Factor
CSA	Canadian Standard Association
CTS	Calibration Transfer Standard
ELA	Equivalent Leakage Area

HDD	Heating Degree Days
IGU	Insulated Glazing Unit
IR	Infrared Thermography
LPM	Liter Per Minute
LTP	Linear Temperature Profile
mil	Microinch
MRT	Mean Radiant Temperature
NBCC	National Building Code of Canada
NFCR	National Fenestration Council Rating
PD	Percentage of Dissatisfied
PER	Pressure Equalization Rainscreen
PPD	Percentage of People Dissatisfied
RH	Relative Humidity
SC	Shading Coefficient
SHGC	Solar Heat Gain Coefficient
TI	Temperature Index
ZHF	Zero Heat Flux

Chapter 1

Introduction

1.1 Problem statement

Curtain walls are non-load bearing exterior walls, which are suspended in front of the structural frame by point anchorages fastened to the structural frame (Schaal, 1961). Typically, a curtain wall assembly is composed of vision glazing units, insulated spandrel units, and connecting metal joints. One typical curtain wall assembly is shown in Figure 1.1 and the joint cross section is shown in Figure 1.2. The design of the joints between curtain wall elements and the fasteners permit the erection of continuous wall surfaces of any size. Curtain walls could be constructed of many materials, such as wood, stone, stainless steel, aluminum, PVC, concrete, glass, etc. A metal curtain wall system may consist entirely or principally of metal or it may be a combination of metal, glass and other surfacing materials supported by or within metal framework (AAMA, 1979). Although the use of metal and glass to produce building facades dates back to the 19th century, the first true use of metal curtain walls was the Hallidie Building in San Francisco designed by Willis Polk in 1917 (Ledbetter, 1991). Most of today's metal curtain wall systems are constructed of lightweight aluminum. The ready availability of aluminum as a building material in the 1950's led to the development of modern curtain wall systems. The wide use of these curtain wall systems since then is attributed to their

1

advantages such as space saving, lightweight, high quality in manufacturing, fast construction, and significant aesthetic freedom.
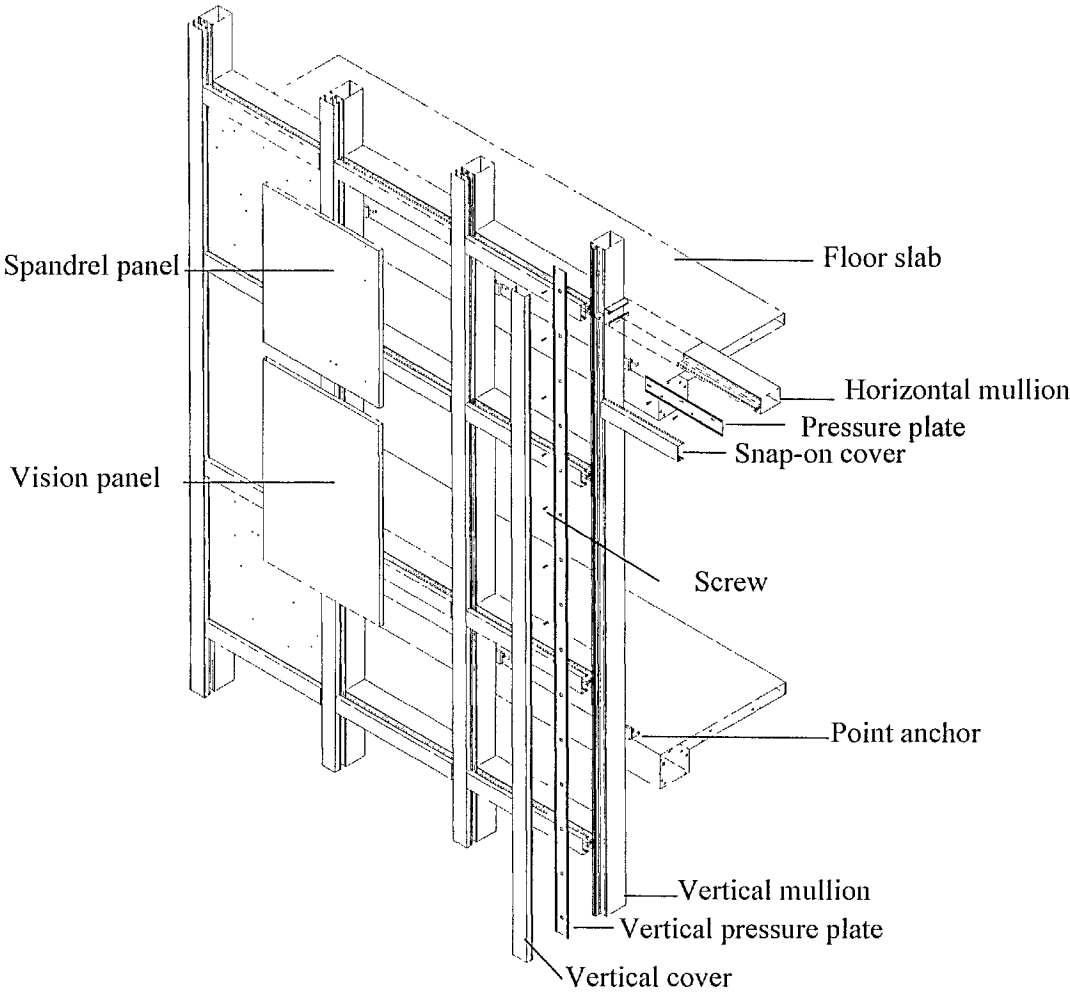
Figure 1.1   A typical curtain wall system
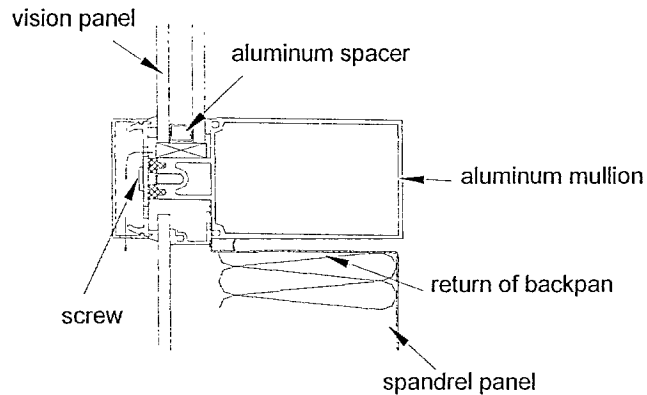
Figure 1.2 Joint section of a standard metal curtain wall

The building envelope has been the center of research efforts recently in the construction industry due to the concerns over the need to reduce greenhouse gas emission, to alleviate energy shortage situation, and to improve the indoor environment. According to World Watch Institute, building construction consumes 40% of the raw stone, gravel, and sand used globally each year, and 25% of the virgin wood. Buildings also account for 40% of the energy and 16% of the water used annually worldwide (Roodman, et al., 1995). In Canada alone, about 40% of the national annual resource expenditure is consumed by the construction industry. People spend up to 90% of their time inside the built environment (Hawken, et al., 1999). The quality of indoor environment directly imposes on ones' health and welfare. The performance of the building envelope is one of the important factors in achieving energy-efficient buildings with comfort and healthy indoor environment.

Metal curtain walls are the dominant envelope types for commercial buildings. Earlier curtain wall systems frequently experienced problems such as rain penetration due to

3

inadequate design concepts, large icicles formed on the outside horizontal mullions due to air exfiltration, and condensation on the inside mullion surfaces. With improvements in design and materials over the past decades, most of these problems have been overcome (Quirouette, 1982). However, their thermal performance is still low due to the high conductivity of metal and glass. Metal curtain walls are typically referred to as "heat sinks" in practice.

The typically large continuous span of glazing in curtain walls can provide occupants with pleasant view, contact with outdoors and natural lighting. However, the high thermal transmittance of the glazing may also lead to a number of potential problems, such as high-energy consumption, thermal discomfort to occupant in the perimeter zones, and condensation risk. A standard clear insulated double glazing unit has a U-factor of 2.76 $W/m^2 \cdot K$ at center-of-glass. When the edge-of-glass and frame are taken into account, the overall U-factor will become even higher. The thermal performance of glazing units can be enhanced by: 1) the use of low-emissivity coating to reduce the radiation heat transfer within the glazing cavity; 2) filling low conduction gas such as Argon or Krypton into the glazing cavity or vacuuming the glazing cavity to reduce the convection heat transfer; 3) increasing the number of glazing panes to take advantage of the insulating value of the extra air or gas layer; 4) by substituting warm spacers for the conventional metal spacers to reduce the heat conduction at the edge-of-glass.

The benefits provided by these Insulated Glazing Units (IGUs) are greatly influenced by the overall design of a curtain wall system in addition to the enhancement in glazing.

4

Although the high performance IGUs can reduce the overall U-factor of metal curtain walls, the amount of reduction can be greatly lowered by the performance of mullions and spandrel panels. A simple calculation using FRAME/VISION (Enermodal Engineering Ltd., 1995) programs on an aluminum curtain wall with 56% glazing area has indicated that by replacing the standard double IGU with high performance glazing unit, the overall thermal conductance is reduced by 19% although the high performance glazing unit provides 45% lower thermal conductance. This difference indicates that the overall thermal performance of metal curtain walls depends as much on the design details as on the properties of materials. As shown in Figure 1.2, the joint is a key component for curtain wall system and it fulfills the following functions:

1) it carries the wall assembly's dead load and transfers wind and other live loads to the structure;

2) it accommodates movements caused by wind loads, temperature changes, structural deflection, and frame creep etc.;

3) it provides airtightness and prevents rainwater penetration into the wall assembly.

These requirements complicate the joint configuration and compromise the thermal performance of the joint. Although a thin strip of nylon as a thermal break is used in the joint section, the screws used to fasten the wall assembly produce thermal bridges and have a significant effect on the thermal performance of curtain walls (Enermodal Engineering Ltd., 1994). The magnitude of this thermal bridging depends on the materials and spacing of screws (Griffith et al., 1998c). The spandrel panel usually consists of a metal back-pan filled with insulation and covered with a sheet of glass or

5

other facing materials on the exterior. Although the thermal resistance in the center of the spandrel panel can be sufficiently high, the thermal bridge created by the return of the metal back-pan significantly reduces the thermal resistance of the assembly (Carpenter, 1994). In addition, the application of the Pressure Equalization Rainscreen (PER) design makes the spandrel adapters and mullion noses exposed to the cold air. The washing effect of the cold air at the mullion nose may lower the function of thermal breaks. The free air movement within the air cavities in the mullion can further lower the thermal resistance. All of these factors affect the overall performance of metal curtain walls and their relative importance is critical for achieving good overall thermal performance. Therefore, to evaluate the thermal performance of metal curtain walls accurately it is necessary to treat them as integrated systems.

The metal curtain wall industry initially grew within the metal window industry, and standards developed for windows are also used to evaluate the performance of metal curtain walls. For decades, metal curtain walls have been treated as windows plus walls. The U-factor of metal curtain walls has been represented only by the U-factor of the vision panel. For energy consumption calculation, only the U-factors for center-of-glass and for center-of-spandrel are considered in practice. The new edition of standard CSA-A440.2 (CSA 1998) —"Energy Performance of Windows and Other Fenestration Systems" incorporates curtain walls and recommends that the thermal performance of both spandrel panels and vision panels should be evaluated, but separately. Metal curtain walls differ from windows in that they have a much larger continuous glazing portion, more complex configuration at the joints, and more complex connection between frame

6

and the spandrel panels. The separation of the glazing panel from the spandrel panel may be an oversimplification and the U-factor evaluated in accordance with CSA A440.2 procedure or the U-factor calculated conventionally may cause discrepancy when estimating energy consumption for metal curtain wall buildings. Meanwhile, the temperature distribution may be different when evaluating the curtain wall as an integrated system instead of as separate panels. The temperature measurements are used to predict condensation risk. How much discrepancy this oversimplification can cause in term of U-factor and condensation resistance has not been studied.

Through literature survey it has been found that a substantial amount of effort has been expended on improving performance of windows (Bernier, et al., 1997; Carpenter, et al., 1993; Elmahdy, et al., 1993; Wright, et al., 1994; McGowan, 1995, 1998a; Griffith, et al., 1996, etc), but few on metal curtain walls. Due to the difference between windows and curtain walls, the established knowledge in windows may not be 100% applicable to curtain walls. The successful transfer of advancements in windows to metal curtain walls in bringing about better curtain wall systems requires research efforts targeted specifically for the curtain wall systems. Currently, these few existing studies on metal curtain walls are limited to address the U-factor only and treat curtain walls as individual isolated components. No study, to our best knowledge, has been reported to address the impact of design details on the overall performance of metal curtain walls including energy consumption, thermal comfort, and condensation resistance.

High performance curtain walls are available on the market, but they have difficulty in competing with the "main-stream" products because they cost more. If the benefits of high-performance curtain walls, such as energy savings and improved thermal comfort in heating-dominant cold climates, can be quantitatively demonstrated, the higher initial cost of high-performance curtain walls would be better justified and market resistance would be reduced.

1.2 Research objectives and approaches

As discussed in the previous section, curtain walls are widely used as building envelope systems in commercial buildings, and their performance is vital for achieving an energy efficient building with healthy, and comfort indoor environment. However, few research efforts have been made exclusively on metal curtain walls, and none of the few existing studies has ever addressed the performance of metal curtain walls from the overall perspective.

For the first time, a comprehensive research program has been designed and carried out to evaluate the overall thermal performance of large-scale metal curtain walls using a holistic approach. The scope of this research is to evaluate the thermal performance of metal curtain walls in a more realistic way, and to provide technical information on improving curtain wall designs and on selecting curtain wall systems at design stage in term of energy consumption, thermal comfort and condensation risk.

The specific objectives of this thesis are:

- to synthesize the technical information concerning metal curtain walls including fabrication, standard tests, and performance evaluations, and to identify gaps in the current research;

- to evaluate the effects of design details on the overall thermal performance of metal curtain walls to provide information on improvement in designing curtain wall products with better performance;

- to quantify the benefits provided by high performance curtain walls such as energy savings and thermal comfort improvement to provide information on optimal design and selection of curtain wall system to achieve energy efficient buildings with comfort and healthy indoor environment;

- to obtain well-documented experimental data on full-scale metal curtain walls that can be used to validate computer simulation programs;

- to compare the overall U-factor of curtain walls determined by the integrated method to that obtained using current standard and practical methods and to compare the resulting difference in energy consumption calculation; and

- to investigate the applicability of computer simulations in predicting condensation potential for curtain wall systems.

To achieve these objectives, experimental investigations, analytical calculations, and simulation studies have been carried out. Extensive experimental testing has been performed to study the performance of two commercially-available curtain wall systems under various testing conditions.

1.3 Outline of the thesis

A comprehensive literature review on metal curtain walls is presented in chapter 2. This review provides background knowledge over a number of areas and research fields concerning metal curtain walls, heat transfer mechanisms, testing and standards, and simulation tools. The current status of research on thermal performance of fenestration systems is reviewed in depth, and the research gaps are identified.

Due to the wide range of aspects addressed in this thesis, an overview on the research program is presented in Chapter 3. To resolve the issues and questions raised following the comprehensive literature review in Chapter 2, a series of experiments and simulations are designed and carried out. There are three main tests conducted including full-scale air leakage tests, thermal performance tests and air movement tests. The simulations conducted include U-factor calculation, temperature prediction, thermal comfort analysis and energy consumption estimation. In addition to the overview on the research program, a general description of the test facility and the test specimen is also presented in Chapter 3.

The extensive experiments conducted in an Environmental Chamber are presented in four chapters from Chapter 4 to Chapter 7. Each chapter is devoted to one specific aspect and follows the similar format: experimental setup, test procedure, result analysis and conclusion. The air leakage tests conducted on large-scale curtain walls are presented in Chapter 4. A different test approach than the standard pressurization method has been

developed in order to measure the air leakage for the curtain wall systems while mounted in the test frame.

The thermal performance tests are discussed in Chapter 5. The curtain wall specimen was tested under different conditions including a set of steady outdoor temperatures, a periodic outdoor temperature, and with introduced air infiltration. Performance comparison is made between the two wall systems with different design details by the temperature measurements. The effect of air leakage is also addressed. The extensive temperature measurements obtained in this test will be used to validate computer simulations, and serve as basis for other performance analysis such as thermal comfort, and determination of surface film coefficients.

Chapter 6 describes the procedure to determine surface film coefficients. An experiment setup has been designed and built to measure the local convection film coefficients on the room side. The results obtained will be used as more realistic boundary conditions in computer simulations to validate the applicability of the program in predicting condensation potential for curtain walls. The radiation film coefficients are obtained by detailed analysis using the measured data. A thermal network analysis is carried out for the center-of-glass as well to estimate the surface film coefficients based on the measured temperatures on glass surfaces.

Chapter 7 reports the measurement on the cold draft induced by the cold glass surfaces. The local thermal sensation PD (percentage dissatisfied) is calculated following ASHRAE 55 procedure using the measured data.

The effect of design details on U-factors is studied by simulation using FRAME/VISION programs and the results are presented in Chapter 8. The measured temperatures at joint section are compared to those predicted by FRAME simulations. The sensitivity of the prediction accuracy to the local film coefficients is studied.

The effect of curtain wall configurations on occupant thermal comfort and energy consumption are studied in Chapter 9. The thermal sensation analysis resulting from cold glass surface is carried out using measured data. A simplified energy simulation model is employed to calculate energy consumption for a prototype office building. The climate sensitivity is studied as well.

Finally, the conclusion and possible future works are presented in the last Chapter.

Chapter 2

Literature review

2.1 Curtain wall as a building envelope system

The building envelope system functions as a barrier for a building to separate the indoor environment from the outdoor climate. To fulfill this basic function, it must (Hutcheon, 1963): 1) control heat flow; 2) control air flow; 3) control water vapor flow; 4) control rain penetration; 5) control light, solar and other radiation; 6) control noise; 7) control fire; 8) provide strength and rigidity; 9) be durable; 10) be aesthetically pleasing; and 11) be economical. As a building envelope system, the curtain wall assembly must meet these principal requirements. Figure 2.1 shows the cross-section of a typical curtain wall system.
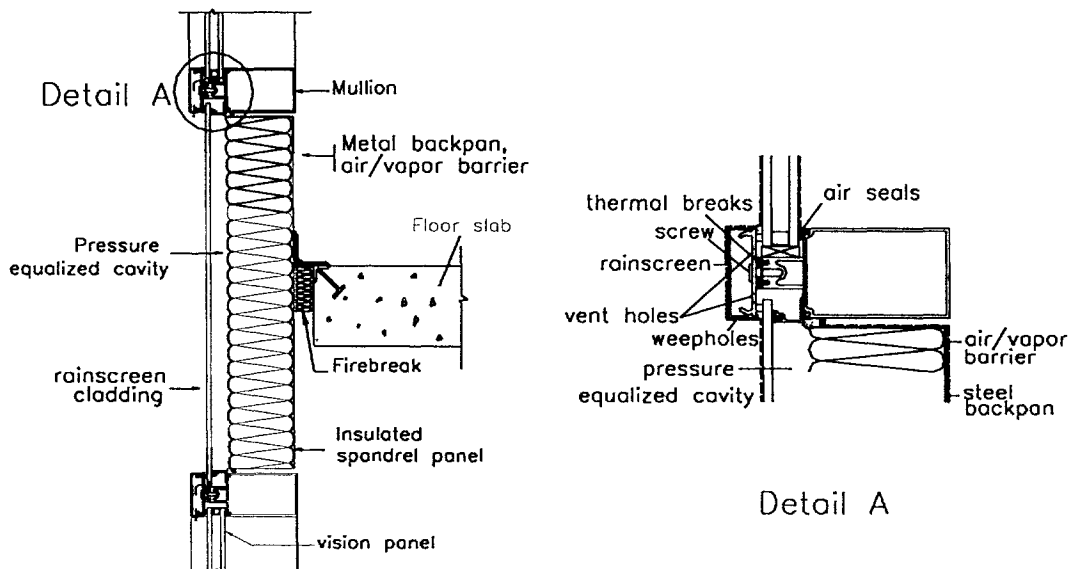
Figure 2.1   The cross-section of a typical curtain wall system

The capability of a building envelope system to control heat flow is characterized by its overall thermal resistance, R-value, which affects the heating and cooling loads of the building directly. The thermal resistance of metal curtain walls is provided by the insulated spandrel panels, the insulated double glazed units, and the thermally broken mullions. The overall R-value of the wall assembly is determined by the thermal properties of each of these components, and the design detail as well. Metal curtain walls have relatively low overall thermal resistances due to the high conductivity of metal and glass. A physical test done by Carpenter and Elmahdy (1994) showed that for a standard curtain wall system shown in Figure 2.1, the measured overall thermal transmittance (U-factor) was even slightly higher than the U-factor of the double insulated glazing unit although the insulated spandrel panel offered sufficiently high thermal resistance at the center. The reason for such a high overall thermal transmittance was believed to be due to the high heat loss through the aluminum mullion and the edge-of-spandrel panel. At the earlier stage of the metal curtain wall history, the mullions were typically not thermally broken, which frequently caused condensation on the interior frame surfaces.

The control of airflow through the building envelope is important. Air infiltration/exfiltration not only increases the energy consumption but also causes problems such as interstitial condensation, deterioration of building materials, degradation of insulation, and growth of mold. Moreover, air tightness is critical for the control of rain penetration through the building envelope. The control of air and vapor flow through a building envelope is achieved by a layer of air barrier made of airtight materials, whose air leakage rate must be lower than 0.02 L/(s·m^2), and by a layer of

vapor barrier whose permeance must be less than 15 ng/(Pa·s·m^2) (NBCC, 1995). To function properly, the air barrier must be continuous. In curtain wall assemblies, glass, aluminum and steel back-pan perform as efficient air and vapor barriers. The continuity of the air/vapor barrier is achieved by the air seals at the flanges of the tubular mullions and the air tightness of curtain walls depends mainly on the air seals at the joints. Imperfect air seal can result from poor workmanship, such as missing seals at some place, or from joint movement caused by temperature variation, wind loads, and structural deflection, or from air seals deterioration due to the weathering. Additionally, the air barrier system must be strong enough to resist the pressure difference induced from stack effect, wind load, and the ventilation systems. Typically, the steel back pans in the spandrel area of curtain walls are reinforced by intermediate stiffeners securely fastened to withstand peak wind load pressures (Quirouette, 1985). With improvement in materials such as the use of high performance sealant, and improvement in construction quality control, the air tightness of curtain walls has been greatly improved and the occurrence of large icicle hanging out curtain wall envelope due to air infiltration has been eliminated.

Water penetration into the building enclosure may cause many problems, such as metal corrosion, cladding fracture, material disintegration and coating deterioration. Damage to interior finishes and furnishings may disturb occupants; wetted insulation materials lose insulation value; and uncontrolled moisture infiltration eventually results in bad indoor air quality and possible health risks. The remedy for such problems is often very costly and time-consuming, and requires the knowledge of the causes that in some cases are not

easy to identify. Therefore, successful water penetration control is very important for good overall performance of the building envelope. The conventional approach to control rain penetration is to attempt to eliminate openings on the envelope, which is referred to as the "face-seal" approach. This approach relies on the perfect sealing of the façade and requires continuous attention and maintenance. The more reliable and effective approach is to eliminate the driving forces. Most of the driving forces can be countered by proper design details, for example, the joints should slope downward towards the outside to eliminate the gravity, a discontinuity or air gap should be introduced in the joint to break the capillary path, and drips should be used to avoid surface tension, etc.. The most difficult force to combat is the wind induced pressure differentials. An effective approach to eliminate this force is the Pressure Equalization Rainscreen (PER) principle.

The main feature of the PER wall design is to use two layers of defense and to neutralize the pressure difference across the outer layer by the purpose-provided openings on the outer layer. Figure 2.2 shows the generic configuration of a PER wall. It consists of five essential elements: one outer layer, which is called rainscreen, to protect the inner layer from direct sun and rain; one airtight inner layer that acts as an air barrier; the air cavity enclosed by the two layers, which has to be compartmentalized; vent holes and weepholes on the outer layer. The openings on the outer layer allow the pressure in the air cavity to be equal or close to the exterior pressure so that the driving force of pressure differential to move rainwater across the outer layer can be eliminated or reduced. The rainwater, which can penetrate the outer layer in some circumstances, can be drained out

through weepholes. The air barrier system of the inner layer must sustain the total pressure difference exerted across the building envelope. The pressure equalization performance depends mainly on vent area, airtightness of the air barrier, cavity volume, and stiffness of the rainscreen and air barrier (Ganguli and Quirouette, 1987; Sakhnovsky, 1991). The PER principle has been applied in metal curtain wall designs. The grid structure of metal curtain walls provides compartmentalized air cavities. For the vision panel, an air cavity is enclosed between the mullion nose and the ends of double glazing unit. For the spandrel panel, the air cavity is enclosed between spandrel glass and the steel back-pan. As shown in Figure 2.1, those compartmentalized air cavities are vented by the vent holes predrilled on the horizontal pressure plates for pressure equalization. Water that penetrates into the cavity can be drained by weepholes on the mullion cap.

Although the rainscreen concept was introduced in Canada in the early 1960's (Garden, 1963) and continuous efforts have been made since then on the understanding of the basic theory (Killip & Cheetham, 1984; Ganguli & Dalgliesh, 1988; Brown, et al., 1991; and Ganguli et al., 1987), the application of this principle is not well developed yet in practice. Most of the designs still follow the rule-of-thumb, for example, the number and the size of vent holes. The failure of the PER design in metal curtain walls is most likely due to the improper design such as weepholes or vent holes not big enough, or due to the improper installation such as weepholes being installed upside down, or sealant being missed on top of the fasteners, which provides paths for the rainwater to penetrate into the inner wall (Endean, 1995).
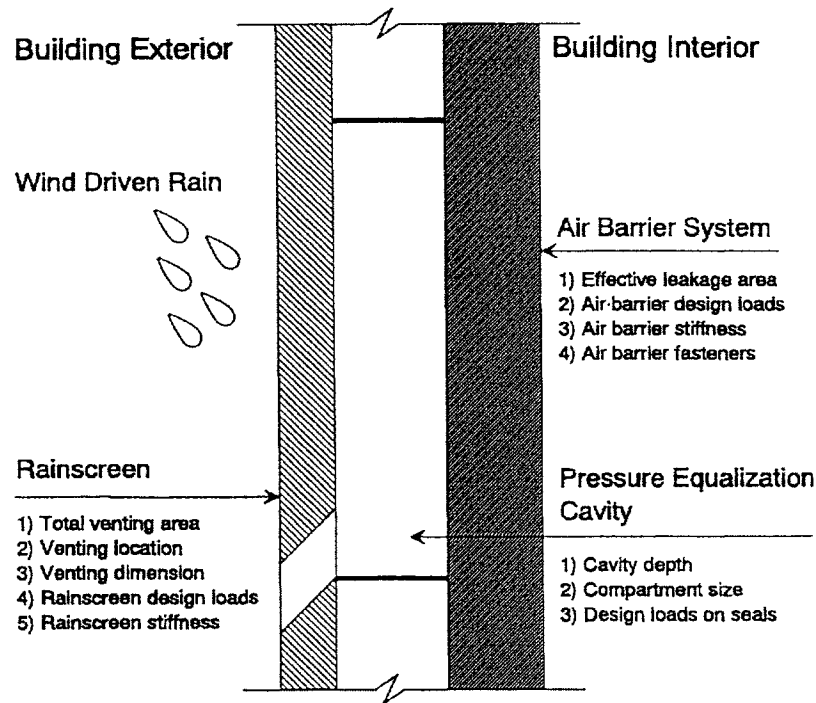
Figure 2.2 Components of a pressure equalization rainscreen wall (Baskaran and Brown, 1992)

Another important function of the building envelope is to control fire. The goal of fire safety in high-rise buildings is to confine the fire at the start point long enough to remove occupants from danger and to prevent structural collapse (AAMA, 1979). In a curtain wall system, a space ranging between one inch and six inches in width exists between the floor slab and the wall assembly, as marked by "firebreak" in Figure 2.1. This space must be filled with fire retardant materials. The lack of fire retardant in the void space was a major factor in the vertical spread of fire in the 62-story First interstate Bank Building in Los Angeles in May 1988 (Drennen, 1994). The achievement of fire control depends on the cooperation among building parties including architect, contractor,

18

fabricator, and owner in the design, fabrication, installation and management of the building.

Generally, the building envelope is an integrated system, and each component of this system has to work together so that its principal functions can be fulfilled.

2.2 Standards to evaluate curtain wall performance

Factory-built and quality control is one of the reasons accounting for the rapid development and popularity of curtain walls (Brooks, 1998). Since curtain walls are prefabricated in the factory, pre-testing can be carried out to ensure that they meet the performance requirements. Extensive tests are needed before curtain wall products are placed on the market. The main tests to evaluate curtain wall performance include: 1) Thermal transmittance test, 2) Air leakage test; 3) Water penetration test; 4) Structural performance. The relevant standards used in North America are listed in Appendix A.

These test standards were originally designed for the evaluation of metal windows. Metal curtain walls and their manufacturers have evolved from window technology and window fabricators. In practice, curtain wall products are specified by these standards. However, curtain walls perform differently from windows and some requirements for windows may not be applicable to curtain walls. There are no national codes of practice or standards specifically for curtain walls. Curtain walls are treated as components such as vision panels in standard CSA-A440.2.

19

The following discussion focuses on individual standards related to energy performance, (thermal transmittance and solar heat gain coefficient), air leakage, condensation resistance and water penetration.

2.2.1   Energy performance

In Canada, the CSA-A440.2 standard is used for energy performance comparison and evaluation of windows. The 1998 version includes provisions for curtain walls as well. The assessment of energy performance of fenestration systems includes overall coefficient of heat transfer (U-factor), solar heat gain coefficient (SHGC), and air leakage rate. The standard recommends that the properties for curtain walls shall be determined separately for the vision panel and the spandrel panel. The procedure to evaluate vision panel is also applied to the spandrel panel. The standard recommends both physical tests and computer simulations to obtain the overall heat transfer coefficient (U-factor) and SHGC for fenestration products.

2.2.1.1   Overall heat transfer coefficient (U-factor)

The overall heat transfer coefficient (U-factor) is defined as the time rate of heat flow per unit area under steady-state conditions from the air on the warm side of a body to the air on the cold side, per unit temperature difference between warm and cold air (AAMA 1998). It can be measured in accordance with ASTM standard C1199 (ASTM, 2000) which is designed exclusively for fenestration systems using "guarded hot box" measurement. The basic principle of the test method described is to determine the heat flux transfer through the test specimen. By measuring the air temperatures on the cold

side and warm side, the overall heat transfer coefficient can be calculated by dividing the heat flux by the temperature difference between warm side air and cold side air. The test specimen should be a complete window with glazing, frame and sash. In the case of curtain walls, the vision panel and spandrel panel shall include full-size frame. The U-factor obtained from the measurement is an average value for the whole window assembly. When measuring the U-values of windows in accordance with standard C1199, air leakage is eliminated by sealing the cracks and maintaining zero pressure differential across the assembly. The reason for eliminating air leakage is to reduce the complexity of the test procedure and data processing. The contribution of air leakage to the energy consumption can be estimated, to a certain extent, by calculating the sensible heat and latent heat carried by the expected amount of air leakage. The measurement of air leakage rate is discussed in section 2.2.2.

The overall U-factor of window can also be obtained by computer simulation. A window assembly can be divided into three parts: center-of-glass area, edge-of-glass area, and frame area. If dividers exist, more area such as divider area, edge-of-divider area may be defined. The edge-of-glass area is defined to encompass all glazed vision areas within 63.5 mm of any part of the frame or sash. The center-of-glass area is the remaining vision area of the glazing. The frame area refers to the projected area from the plane of the glazing (CSA A440.2, 1998 and ASHRAE Standard 142P, 1996). For the center of the insulated glazing unit, one-dimensional analysis is normally assumed for the purpose of U-value calculation. For the edge-of-glass and frame, two-dimensional analysis is

necessary. In some cases three-dimensional analysis is preferred, e.g. to model the corner effect.

The overall U-factor for the window assembly is an area-weighted average of U-factor for each component as expressed in the following formula:

$$U_w = \frac{(U_{cg}A_{cg} + U_{eg}A_{eg} + U_f A_f)}{A_w} \tag{2.1}$$

where,

U_w = U-factor of the total window product, $W/(m^2 \cdot K)$;

U_{cg} = U-factor of the center-of-glass, $W/(m^2 \cdot K)$;

U_{eg} = U-factor of the edge-of-glass, $W/(m^2 \cdot K)$;

U_f = U-factor of frame, $W/(m^2 \cdot K)$;

A_{cg} = area of the center-of-glass, m^2;

A_{eg} = area of the edge-of-glass, m^2;

A_f = projected area of frame, m^2; and

A_w = area of the total window product, m^2.

The standard CSA A440.2 recommends running VISION/FRAME programs to obtain the U-factor for each part. VISION is a one-dimensional program to analyze the thermal performance for the center-glazing portion. The simulation results include U-factor, solar heat gain coefficient, temperature profile and visible transmittance values. It can also perform a two-dimensional computational fluid dynamics (CFD) analysis to generate a fill gas flow field in the glazing cavity. The 2D CFD data can be imported into program FRAME to predict the condensation risk in the edge-of-glass region. FRAME is a two-

22

dimensional finite volume program to simulate the heat transfer through edge-of-glass and frame sections. It uses the concept of effective conductivity to account for convective and radiative heat transfer within frame cavities. It outputs U-factor for edge-of-glass and frame, and also temperature distribution.

The testing and modeling procedures to obtain the U-factor for the spandrel panel are to follow the same guidelines set out for the vision panel. To adequately model the heat transfer mechanisms at edge-of-spandrel and frame areas in a computer simulation analysis, two-dimensional techniques and tools are required.

For decades, the U-value of metal curtain walls has been represented by the U-value of the vision panel only. The energy performance of the spandrel panel has been only quoted by the R-value of the center-of-spandrel without accounting for the frame and thermal bridging. The incorporation of evaluating the thermal performance of spandrel panels in the new edition of CSA-A440.2 (CSA, 1998) is an improvement in more accurately assessing the thermal performance of metal curtain walls. However, due to the complexity of the connection between spandrel panel and the frame, to separate the glazing section from the spandrel section may be an oversimplification. This simplification can introduce discrepancy in determining the overall U-factor, thus the energy consumption, and in predicting the condensation potential for edge-of-glass. How much discrepancy the conventional procedure and the CSA procedure can cause in evaluating the energy performance has not yet been reported.

2.2.1.2   Solar Heat Gain Coefficient (SHGC) and Shading Coefficient (SC)

The Solar Heat Gain Coefficient is the ratio of solar heat gain through a window component to the solar radiation incident on it, for a given angle of incidence and for given environmental conditions such as indoor temperature, outdoor temperature, wind speed, and solar radiation (CSA, 1998). The window component applies to both the transparent part and the opaque parts such as frame and divider. The solar heat gain includes both the directly transmitted portion and the absorbed and re-emitted portion. The solar energy absorbed by the transparent part can be redirected to the indoor space by radiation and convection. The solar energy absorbed by the outdoor surface of the opaque parts can be redirected to the indoor side by conduction, convection and radiation. The SHGC can be either measured following the procedure in "Determining of Fenestration Thermal Performance Using Simulated Solar Irradiance" (CANMET, 1993) or calculated by area-weighting the solar heat gain coefficients of the glazing, frame, and divider elements when present.

$$SHGC_w = \left(\frac{SHGC_g A_g + SHGC_f A_f + SHGC_d A_d}{A_w} \right) \qquad (2.2)$$

where, SHGC is solar heat gain coefficient, dimensionless, and A_d is the projected divider area, m^2.

The SHGC for the glass area can be obtained from VISION program, in which a spectral analysis is carried out for the specific glazing unit. The SHGC of glass depends on the solar irradiance, which is determined by the air mass, altitude, seasonal change, characteristics of surroundings, and the spectral properties of glass (ASHRAE Fundamental, 1997). By changing the characteristics of the glazing, the solar energy can

24

be selectively transmitted or reflected, thus the heating or cooling load can be positively

managed. The SHGC for the opaque part, frame or divider, can be estimated using

equation 2.3 (ASHRAE, 1997):

$$SHGC_f = \alpha_f^s (\frac{U_f}{h_f})(\frac{A_f}{A_{surf}}) \tag{2.3}$$

where, α_f^s is the solar absorptivity of the outdoor surface of the frame, h_f is the heat

transfer coefficient between the frame and the outdoor environment. The projected-to-

surface area ratio (A_f/A_{surf}) corrects for the fact that U_f is based on projected area A_f, and h_f

is based on the total exposed outdoor frame surface area A_{surf}.

The Shading Coefficient (SC) is the ratio of solar heat gain through a window, under a

specific set of conditions, to the solar heat gain through a 3 mm single pane of clear

double-strength glass under the same conditions. Here the solar heat gain includes the

fraction directly transmitted as well as the part absorbed and re-emitted. The SHGC for

the reference single pane glass is 0.87 at normal incidence and for the standard ASTM

solar spectrum. The shading coefficient is commonly used in simplified energy analysis

programs. For accurate peak cooling load calculation, detailed SHGC analysis is

preferred (ASHRAE, 1997).

2.2.2 Air leakage test

Air infiltration can increase the heating load of the building, lower the local indoor

surface temperature, or cause local cold draft in winter, which may result in surface

condensation and thermal discomfort. Air exfiltration can cause interstitial condensation

within the building assembly that may lead to moisture sensitive material to deteriorate, foster fungi growth, and lower insulation R-value. It can cause icicle formation at the building envelope exterior that may damage the façade or exert danger to the pedestrians. To reduce energy consumption, to ensure durability of building envelopes, and to achieve comfortable indoor environment, air leakage through building envelope has to be controlled. Building components and the entire building envelope, as an integrated system, must meet the air tightness requirement.

The air tightness of fenestration systems can be measured in laboratory following two ASTM test standards: E283 and E1424. The ASTM E283 (ASTM, 1999) standard requires the test specimen to be subjected to a specified pressure difference while both sides of the window are maintained at the same ambient temperature. Normally, 75 Pa pressure difference, which represents 25mph wind induced pressure, is used to evaluate the air tightness of windows. The acceptable leakage rate differs according to window type. The main reason for using the window air leakage at 75 Pa to calculate the heat loss due to air leakage was to reduce the financial burden on window manufacturers and to avoid any additional testing (Elmahdy, 1995). The ASTM E1424 (ASTM, 2000) standard requires the specimen to be subjected to both pressure difference and temperature difference to represent a more realistic test condition. Under thermal load, the components may distort, and the air leakage paths and cracks may change shape, thus alter the air leakage rate. Studies on window assemblies (Elmahdy, 1995 and Henry, et al., 1998) showed that air leakage rate changes with the temperature differential across windows. For some types of windows, air leakage rates increase as the temperature

difference increases, while/for some other types of windows, air leakage rates decrease. The magnitude of the thermal load effect depends on window materials, window types and design details, but no correlation was found between the change in air leakage and the type or materials of windows. Although standard E1424 test can represent more realistic conditions, the complex experiment setup and the much higher testing cost limit its application. ASTM E283 is still the commonly used standard test.

Metal curtain walls have much more joints than the discrete windows. The air leakage more likely concentrates in a relatively small area. The American Architectural Manufacturer Association (AAMA) recommends $0.3L/m^2$ ·s as the maximum allowable air leakage rate for the building envelope under 75 Pa. However, this air leakage rate is inappropriate for the severe climate of Canada, and the National Building Code of Canada (NBCC, 1995, art. 5.4.2.1) recommends different airtightness requirement depending on the indoor relative humidity for opaque or fixed panels of the building envelope (Table 2.1).

Table 2.1 Maximum air leakage rate for opaque or fixed panels for ΔP= 75 Pa

Relative humidity on the warm side at 21 °C (%)	Maximum recommended leakage rate (L/ m^2 ·s)
<27	0.15
between 27 and 55	0.10
>55	0.05

The pressure differential across the building envelope is induced by the mechanical system, stack effect, and/or wind. The curtain wall system is frequently used in high-rise buildings, where stack effect and wind-induced pressure differentials can reach very high values. The field measurement conducted by Ganguli (1988) showed that the pressure

difference induced by the HVAC system and stack effect could reach a value as high as 150 Pa at the 24th floor under a 40°C temperature differential. The wind-induced pressure could reach as high as 450 Pa for a considerable length of time. The sealant and gasket in curtain wall assemblies must sustain these pressures induced by HVAC and stack effect for days as compared to wind-induced pressures that usually endured for a few hours. Thus, a much higher pressure differential value of 300 Pa is normally used in the curtain wall industry instead of 75 Pa for windows in the air leakage tests. The air leakage tests require a complete full-scale curtain wall including both vision panel, spandrel panel and joints to be tested.

The contribution of air leakage to the energy consumption is normally considered by calculating the sensible and latent heat carried by the amount of air leakage expected under representative pressure difference.

2.2.3 Condensation resistance

Condensation resistance is an important factor for evaluating thermal performance of fenestration systems. In cold weather, condensation frequently occurs on single glazing and on non-thermally broken aluminum frames. For the insulated double glazed windows, normally the edge-of-glass areas, especially at the bottom of the glazing, have the lowest indoor surface temperature and are most vulnerable to condensation. There are three contributing factors to this vulnerability. The first factor is the thermal bridges created by metal spacers and edge-seals at the perimeter of IGUs. The second is the convection effect of fill gas within the glazing cavity. During the heating seasons, the fill

gas is warmed up and flows upward near the indoor glass, while cooled down and flows downward near the outdoor glazing. The descending gas becomes progressively colder when it reaches the bottom of the cavity and then turns to the indoor glazing. As a result, the surface temperature is the lowest at the bottom of the glazing. The third factor is the reduced surface film coefficient at these areas. There are reductions in convection due to the stagnation flow approaching the frame steps and reductions in radiative heat exchange due to the lower surface temperature on the frame, which is in view to the edge-of-glass areas.

Two test standards, CAN/CSA A440 (CSA, 1990) and AAMA 1503 (AAMA, 1998), are normally used to define the condensation resistance. The CSA A440 test procedure determines the Temperature Index, TI, of a product by the following ratio:

$$TI = (\frac{T_{surf} - T_o}{T_i - T_o}) \times 100 \qquad (2.4)$$

where,

T_{surf} = specimen surface temperature (^{o}C);

T_o = temperature of cold side air, and,

T_i = temperature of warm side air (^{o}C).

The specimen surface temperature T_{surf} is an average value of temperature measurements at the coldest location on the frame plus three other locations on the glass, each 50 mm above the bottom sight line.

The AAMA procedure for condensation resistance specifies two separate factors: one for the frame (CRF_f) and the other for the glazing unit (CRF_g). The lower number of the CRF_g or CRF_f is reported as the product CRF. These two factors are determined by:

$$CRF_g = \frac{GT - T_o}{T_i - T_o} \times 100 \qquad (2.5)$$

$$CRF_f = \frac{FT - T_o}{T_i - T_o} \times 100 \qquad (2.6)$$

The term GT is the average temperature of 6 predetermined locations on the glazing, three located ½″ from the sight-line at the edge-of-glass area and three located at the center-of-glass. The term FT is the weighted frame temperature and is calculated by:

$$FT = FT_{pd}(1 - W) + WFT_{rc} \qquad (2.7)$$

The term FT_{pd} in the above equation is the average temperature of 14 predetermined locations on frame and sash members. The term FT_{rc} is the average of temperatures on four coldest locations of frame or sash members. The term W is a weighting factor that represents the ratio between FT_{pd} and FT_{rc}. It is calculated as:

$$W = \frac{FT_{pd} - FT_{rc}}{FT_{pd} - (T_o + 10)} \times 0.40 \qquad (2.8)$$

where the numerical values 10 and 0.40 account for the arbitrary temperature adjustment and the arbitrary weighting factor, respectively. CRF numbers shall be rounded to whole numbers.

Th condensation resistance performance determined by both standards is based on the assumption that a relatively small amount of condensation in comparison to the overall area is acceptable. The interpretation of the results obtained requires careful analysis

30

since the location for coldest frame temperature needs judgment, the temperature used for CRF calculation is an average value, and the locations of temperature measurement on glazing are away from the sight-line where the lowest temperature exists. When using the condensation resistance performance to determine the selection of fenestration products for high-humidity buildings such as hospital, museum and art galleries, care must be taken in specifying the locations of thermocouples.

Both test standards exclude the air leakage effect when measuring the condensation resistance by balancing the pressure across the specimen and by sealing the operable panel perimeters. However, in most of their service life, fenestration systems experience not only thermal loads but also pressure differentials. The resulting air infiltration and exfiltration can change the temperature distribution of the fenestration system and, thus, the condensation resistance. However, there is no available algorithm or procedure to adjust the condensation resistance factor measured in the test with air leakage omitted. In fact, there has been little research reported on the effect of air leakage on the condensation resistance factor (CRF). Elmahdy (2001) studied the effect of not sealing the specimen and he concluded that the air leakage due to the open cracks has considerable impact on the condensation resistance of windows. However, in his study the pressure difference across the test specimen was maintained at less than 10 Pa as required by the standards. Although the cracks were kept open, the balanced pressure prevented air flowing through the cracks, hence the effect of air leakage on the condensation resistance performance was not fully recognized. Metal curtain walls are commonly used in high-rise buildings, where high-pressure differentials due to wind,

stack effect and mechanical systems occur. Normally, a little condensation along the edge-of-glass is acceptable in many cases. However, in other cases, such as hospitals, and museums, condensation is not allowed under any conditions. In these strict situations, the CRF measured in the test with a zero pressure differential may not be reliable for predicting the condensation risk, especially in situations where high-pressure differences prevail.

Besides measurement, the condensation resistance performance of windows may also be evaluated by simulation. Programs such as FRAME (EEL, 1995) and THERM (LBL, 1998) have been validated by physical tests and recommended by standards to calculate U-factors for edge-of-glass and frame. However, the reliability of these programs and the procedure to predict the condensation resistance performance is still under development. Both FRAME and THERM are two-dimensional programs. The three-dimensional effect of thermal bridges such as screws cannot be accurately simulated but approximated two-dimensionally. Some existing studies (Curcija, 1998; McGowan, 1995 and 1998; and Wright, 1998) found that a big discrepancy in temperature between measurement and simulation exists for edge-of-glass and frame sections. The details regarding the causes for the discrepancy and the research status on this subject will be discussed in section 2.3.4.

2.2.4   Water penetration test

Rainwater penetration is a main source of building envelope failures and moisture related problems within the building envelope. The water penetration tests can be carried out

either on site or in a controlled laboratory. The pressure driven rainwater penetration through envelope sections is simulated by spraying a controlled amount of water on the test specimen under specified patterns of pressure difference across the specimen. Currently, there are three main standard test methods used in North America: ASTM E331, ASTM E547 and AAMA 501.1. Standard E331 (ASTM, 2000) applies a static pressure difference across the wall and a uniform water spray. The pressures used are defined according to both window type and building height and they range from 137 Pa to 360 Pa. Standard E547 (ASTM, 2000) applies a cyclic static pressure difference and the procedure is similar to ASTM E331. AAMA 501.1 (AAMA, 1994) uses a wind generator such as an aircraft engine and propeller to simulate the action of water driven on the wall surface by a gust of wind. The most frequently used test pressure employs 20% of the positive design wind but not less than 300 Pa and not more than 575 Pa.

There are different opinions as to the merits of these test methods. The static method, which holds a sustained, relatively low pressure over a period of minutes, is inappropriate to simulate the wind gust that typically lasts a few seconds but reaches high pressures. This method is often considered to be a more severe test on rigid walls with wet glazing seals (Brook, 1992). The cycling pressure test may be more or less severe than a static pressure test at a similar pressure depending on the characteristic of joints. A cycling pressure may alternately open and close seals and create a pumping action, while a static pressure may drive water through a longer leakage path.

For metal curtain walls using pressure equalization rainscreen design with dry glazing sealant, the dynamic test is more suitable due to the consideration of the lateral or upward flow induced by wind. Glass and metal are non-absorbent materials so that none of the rainwater striking such materials can be absorbed. A substantial film of water flows down the wall surface. When wind is present, water flows laterally, and on parts of the building facade it may flow upward as well. Under wind pressure much of the lateral flow becomes concentrated at vertical irregularities in the wall surface, either projections or depressions or joints. The smoother the wall surface and the greater the distance between such joints, the greater will be the water concentration at the joints (AAMA, 1979). Under static conditions, the water may not be driven into the pressure equalization holes as readily as when under dynamic conditions. The use of aircraft engine provides a dynamic wind loading, but it is not calibrated to the gusting behavior of wind on a real building and does not represent the real situation.

In addition, ASTM E331 and AAMA 501.1 specify a minimum water spray rate of 3.4 $L/m^2 \cdot min$. This rate is not correlated to climatic conditions, —no place in Canada receives such a high rate of rainfall. The rate may be excessive for low-rise buildings and inadequate for high-rises, where cumulative water rundown has a significant impact. Increased surface water flows would likely have little effect on face-sealed walls, but it can affect rainscreen wall performance by overflowing or blocking drainage paths (Brook, 1992). Therefore, the water flow rate should be determined according to building height and geometry as well as the wall type.

A lot of research work has been done on simulating wind driven rain, and the effect of rain penetration on building envelope. However, it is still a challenge to theoretically and experimentally simulate the climatic load from rainwater more realistically.

2.3 Review of studies on thermal performance of windows

A review of the thermal performance of windows is presented in this section because of the generic connection between metal curtain walls and windows. The heat transfer mechanisms in windows carry over to the glazing units in the curtain walls. Understanding these mechanisms will help understanding the performance of the curtain wall systems.

As an indispensable component of the building envelope, window provides daylight, pleasant visual contact with the outdoors, potential for natural ventilation, and, if designed and used properly, reduction of heating and cooling load (de Abreu, 1996). However, windows have traditionally been a weak component in terms of heat transmission compared to other components of the building envelope. The low thermal performance of windows not only increases energy consumption but also causes thermal discomfort. In cold weather, the low surface temperature of windows may cause surface condensation or frost that would block the view; also cold radiation and cold draft from the cold window surface may make the occupants close to the window uncomfortable. A substantial amount of efforts has been expended on the improvement of window performance over the years.

All the three main heat transfer mechanisms of conduction, convection and radiation take place in the window assembly. Each of the heat transfer mechanisms in the center-of-glass area, edge-of-glass area and the frame area is discussed below.

2.3.1 Heat transfer through center-of-glass

In winter conditions, the interior glass pane is warmed up by convection from room air and radiation from indoor surroundings. Heat transfers from the warm pane to the cold pane by radiation, convection and conduction through the glazing cavities. The heat is released to the outdoor by exterior convection and radiation. In summer conditions, the same heat transfer processes happens in the reverse direction. Without considering solar heat gain and air infiltration, the overall thermal resistance (R-value) of the center-of-glass can be expressed as:

$$R_w = R_i + \sum_{i=1}^{n} R_g + R_o = \frac{1}{h_i} + \sum_{i=1}^{n} \frac{L}{k} + \sum_{j=1}^{n-1} R_{jcavity} + \frac{1}{h_o} \qquad (2.9)$$

where,

n = the number of glass pane;

h_i = interior surface coefficient including convection h_{ic} and radiation h_{ir}, W/m^2·K;

h_o = exterior surface coefficient including convection h_{oc} and radiation h_{or}, W/m^2·K;

L = thickness of the glass pane, m;

k = the conductivity of glass, W/m· K;

i = the number of glazing panes;

j = the number of glazing cavity; and

36

R_{cavity} = the thermal resistance of glazing cavity, which includes convection heat transfer coefficient and radiation heat transfer coefficient, $m^2 \cdot K/W$.

The values of h_i and h_o depend on the conditions of air temperature, air velocity, and surrounding surface properties. These coefficients are discussed in detail later in section 2.3.3. The conductivity of glass panes is approximately 1 $W/m \cdot K$, which does not provide much insulating value for windows. Therefore, the improvement of thermal performance of windows depends on reducing the heat transfer within the glazing cavity.

2.3.1.1   Convective heat transfer within a glazing cavity

The natural convective heat transfer within the glazing unit is driven by the temperature difference between the interior glass pane and the exterior glass pane. The flow behavior in the cavity is governed by the aspect ratio A, Prandtl number Pr, and Rayleigh number, Ra (Figure 2.3).

$$A = \frac{h}{L}$$

$$Pr = \frac{\upsilon}{\alpha}$$

$$Ra = \frac{g\beta\Delta T L^3}{\alpha\upsilon}$$
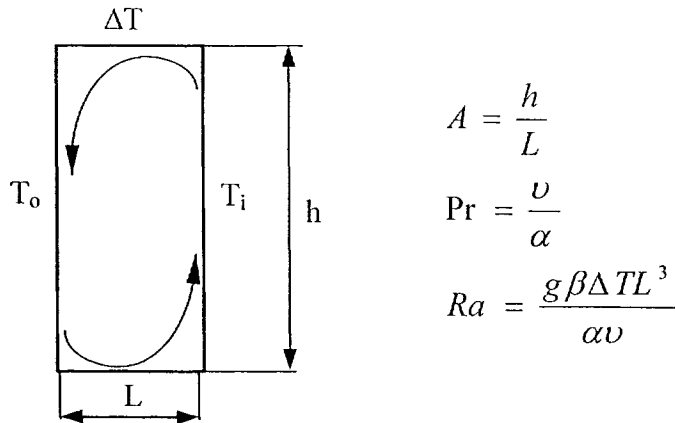
Figure 2.3 Schematic geometry of a glazing cavity

Where, h is the height of the glazing unit, L is the width of the glazing cavity, ΔT is the temperature difference between indoor and outdoor surface and g, β, α and v are thermal properties of fill gas, which are a function of temperature.

Significant effort has been made on the understanding of natural convective heat transfer within vertical slots. Wright et al. (1989) and Zhao et al. (1999) conducted comprehensive reviews on this subject. When the Rayleigh number Ra is small, which may be due to small temperature difference or a narrow cavity, the warmed up flow near the indoor surface is influenced by the cooled down flow near the outdoor surface so that the circulation movement is limited. Under this condition, heat transfer across the cavity is primarily dominated by conduction, which is referred to as the "conduction regime" (Batchelor, 1954). The temperature profile across the cavity is linear and little vertical temperature gradient exists. When Ra increases to be large enough because of greater temperature difference or larger cavity width, two separate boundary layers develop along the cold and warm cavity walls, and leave a core region in between with uniform temperature. The higher the Ra, the more distinct the boundary separation is. Under this condition, convective heat transfer takes place, which is recognized as "boundary layer regime" (Batchelor, 1954). Eckert and Carlson (1961) and Elder (1965) observed the existence of a vertical temperature gradient in the core region for flow beyond the conduction regime, which suggested the existence of a transition regime. In this transition regime, both conduction and convection heat transfer are present in the fluid core region and the horizontal temperature gradients are higher close to the walls and lower across the fluid core. There is another distinct flow regime called "secondary

flow" besides the three main regimes mentioned above. This secondary flow has a regular "cat-eye" pattern within the core of the base flow, which is caused by a hydrodynamic instability. This phenomenon occurs under certain Ra range (Wright, et al. 1989).

The correlations for predicting convective heat transfer within glazing cavities have been developed over the years experimentally, analytically and numerically (El-Sherbiny et al, 1982; Lee and Korpela 1983; Wright, 1996; Zhao et al, 1998). All of these studies assumed isothermal glass surfaces with linear temperature profile (LTP) or zero heat flux (ZHF) boundary conditions. The most widely used correlations, especially in North America, have been the correlations developed by El-Sherbiny et al. (1982), which were based on his well-designed experimental work. These were some of the first correlations which include the dependency of Nusselt number on the aspect ratio. However, the dependency applies only for aspect ratios below 20. These correlations have been adopted in WINDOW/THERM (LBL, 1998), the programs recommended by the National Fenestration Rating Council (NFRC) to evaluate thermal performance of windows in the United States. The dependence of the Nusselt number on the aspect ratio extends to a much higher value, although not as strongly as for aspect ratios less than 20 according to Wright (1996). Wright improved El-Sherbiny's correlations and increased the aspect ratio to 25 and his correlations have been adopted by ASHRAE SPC-142P (ASHRAE, 1996). Zhao et al. (1998) carried out a numerical analysis to cover a much wider range of aspect ratio from 5 to 110. Two sets of correlations were formulated, one for the range of A from 5 to 30 and the other one for the range of A from 30 to 110.

Typically, the laminar flow dominates within the glazing cavity. However, for cavities with a high aspect ratio, turbulent flows can develop directly from the conduction regime without passing through the laminar transition or laminar boundary layer regimes (Wright, 1989). Power et al. (1998) conducted a two-dimensional numerical study on the turbulent flow in tall glazing cavities with an aspect ratio of 76. The turbulent numerical results agreed well with the laminar numerical results and experimental measurements, which indicated that the flow was in the initial stages of turbulent flow in the glazing cavity.

These studies led to improvements in glazing unit design. For the glazing cavity filled with air, the convective heat transfer coefficient reaches its minimum value for a 13mm cavity width and stays constant beyond 13 mm (El-Sherbiny et al, 1982). Therefore, the optimum width for the glazing cavity filled with air is 13mm. The theoretical studies indicate that both conduction and convection contribute to the heat transfer within the glazing cavity, thus, the fill gas, if used, should have a low thermal conductivity to reduce the conduction heat transfer, and a high viscosity and density to minimize the convection heat transfer. Argon or Krypton are the possible options. The optimum cavity width for Argon is the same as for air, but for Krypton the optimum width is around 6mm. It is difficult to fill 100% Argon or Krypton into the glazing cavity as it mixes with the air when it is pumped in. Normally, 90 to 95 percent concentration can be achieved. Slightly more than 5 percent improvement in the thermal resistance of the center-of-glass can be achieved by filling 90 percent of Argon for the standard double insulating glazing unit (John Carmody, et al.1996). Krypton can provide higher performance, but it is more

expensive than Argon. Increasing the number of glazing panes to take advantage of the insulating value of air is another option to improve thermal performance of windows. During the service life of IGU, its U-factor can be changed by the glass plate curvature caused by barometric pressure or gas space temperature variation. Bernier's (1997) study showed that the U-factor of a particular IG unit (triple glazing, low emissivity with air) may vary up to 5% above and 10% below the yearly average.

2.3.1.2   Radiative heat transfer

The radiative heat transfer from the warmer pane of glazing to the cooler pane contributes a large percentage to the overall heat transfer through an insulated glazing unit. For example, for a standard double glazing unit in the winter condition, the convective heat transfer coefficient within the cavity is around 2 $W/m^2 \cdot K$, while the radiation heat transfer coefficient is around 4 $W/m^2 \cdot K$. If one coating with low-emittance, e.g. $\varepsilon=0.1$, is applied on one of the cavity surface, the radiation heat transfer can be reduced by around 90% (Athienitis, 1998). The improvement in insulating value due to the low-E coating approximately equals to the effect of adding another pane of glass. The placement of low-E coating does not affect the overall U-factor, but it does affect the solar heat gain coefficient (SHGC). Normally, in cold climates where the heating load dominates, the low-E coating is added on the outer surface of the inner glazing pane to maximize the passive solar gain. In hot climates where the cooling load dominates, the low-E coating is added on the inner surface of the outer pane to minimize the solar heat gain. The type of low-E coating may also be chosen based on the climate. In heating-dominated climates, high-transmission low-E coating, which allows the visible and near-infrared

41

solar radiation to enter, is suitable. Selective-transmission low-E coatings are suited for buildings having both heating and cooling requirements since they allow the daylight through but block most of the infrared energy from entering in the summer. Low-transmission low-E coatings can be used to control solar heat gain and glare as it increases the reflection of solar beam. When low-E coatings have significantly reduced the heat loss through insulated glazing units, the impact of the fill gas becomes greater and 15 to 20 percent improvement can be achieved by the filling Argon or Krypton (John Carmody, et al.1996).

2.3.2 Heat transfer through edge-of-glass and frame

In a window assembly, the edge-of-glass area is usually the coldest part where condensation may occur and glass may break due to the thermal stress caused by the temperature difference between edge-of-glass and center-of-glass. As explained in section 2.2.3, both the edge-seal conduction and the convection effect of the fill gas contribute to the lowest surface temperature at the bottom of the glazing. Traditionally, the spacer is made of a hollow aluminum extrusion partially filled with desiccant which absorbs moisture to prevent condensation in the glazing cavity. The aluminum and glass provide little thermal resistance. With the emergence of high performance windows with low-emittance coatings and/or low-conductivity gas fill, the weakness of the edge-of-glass in thermal performance is more significant. Studies indicated that the thermal performance of the edge of IGU depends on the material and on the physical configuration of the spacer bar, and the type and size of the edge seals (Wright et al. 1994).

The configurations of different edge-seals are shown in Figure 2.4. Figure 2.4a shows a conventional single-seal aluminum spacer unit and Figure 2.4e, f, g show three types of so-called warm spacers. The sealant between the spacer bar and glass is called the primary seal, which is usually a low permeance material. The construction with both the primary and edge sealants is called dual-seal. If only edge sealant is used, it is called single-seal. For a high conductive spacer bar, the thermal performance of the edge-seal unit is influenced by the conductivity and thickness of the metal, and the thickness of the primary sealant if dual-seal construction is used. The property of edge sealant does not have much effect. For a low conductive spacer bar, such as a fiberglass spacer, the conductivity of the edge sealant is more significant (Wright's, 1994).

(a)   (b)
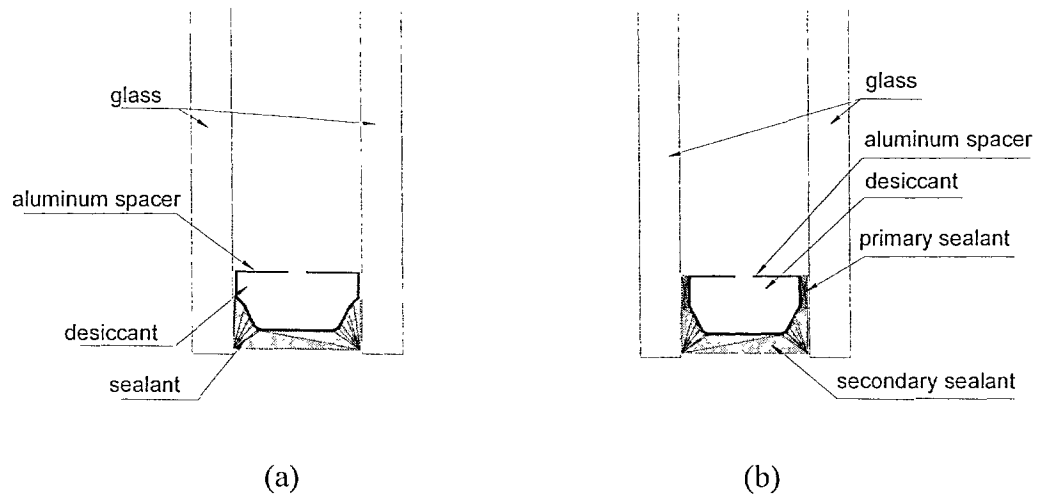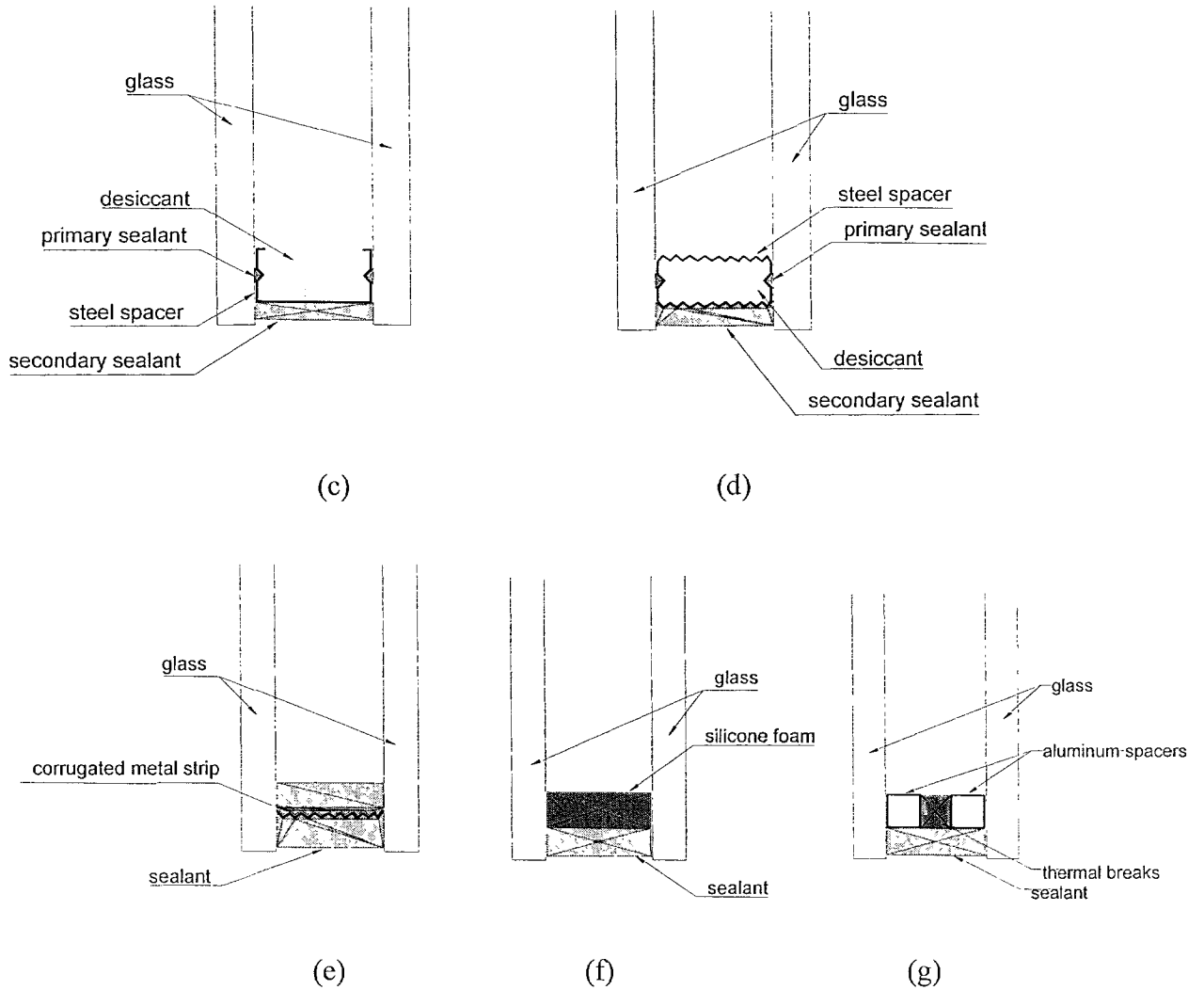
Figure 2.4 Configuration of spacer units: (a) single-seal aluminum spacer; (b) dual-seal aluminum spacer; (c) and (d) stainless steel spacer; (e) corrugated metal strip spacer (f) silicone foam spacer (g) aluminum spacer with thermal breaks. (Carmody, et al.1996).

Based on detailed two-dimensional modeling, Arasteh (1989) developed the following correlation to calculate the edge-of-glass U-factor as a function of spacer type and center-of-glass U-factor:

$$U_{eg} = A + BU_{cg} + CU_{cg}^{2} \qquad (2.10)$$

Where, *A*, *B*, and *C* are correlation coefficients, which correspond to the spacer types: metal spacer, insulating spacer, fused-glass and a combination of insulating and metal spacers.

The effect of spacer type on the edge-of-glass U-factor increases with the decrease of the U-factor at the center-of-glass. With the presence of a frame, the effect of spacers varies with the frame type as well. For a high-conductive frame, such as aluminum, the spacer conductivity and the sealant properties have little impact on the U-factor of edge-of-glass due to the high heat loss through the frame itself. However, the impact on a low-conductive frame such as wood or PVC is more significant (Reilly, 1994). Certainly, the influence on the entire fenestration assembly depends on the area proportions of center-of-glass, edge-of-glass, and frame.

The U-factor of the frame depends not only on its material and design configuration, but also on the spacer unit and the thickness of the insulated glazing unit since a small segment of glazing panes is concealed within the frame. However, the frame U-factor is independent of the U-factor of center-of-glass (Carpenter, 1992). Computer simulations have indicated that heat transfers through the frame in most fenestration systems are controlled by a single controlling resistance, and changes in this component can significantly affect the U-factor of the frame (EEL 1990). For relatively low conductivity frames such as wood and vinyl, the shortest heat flow path is at the edge-seals, thus the type of spacers and the thickness of IG units have a significant impact. For high heat transmission frames such as aluminum frames, most of the heat flows through the metal

frame itself, and the impact of the spacers and thickness of the sealed glazing unit is small. The critical resistance for a thermally broken aluminum frame is the depth of the thermal break and for a non-thermally broken aluminum frame the critical factor is the interior surface film coefficient.

2.3.3 Surface heat transfer coefficients

The surface heat transfer coefficient plays a significant role in the heat transmission through windows. For example, for a double IGU with a U-factor of 2.78 $W/m^2 \cdot K$ at the center-of-glass, the indoor surface coefficient provides one third of the overall thermal resistance while outdoor film coefficient provides 10% under CSA winter conditions (-18°C outdoor and 21°C indoor). Obviously, the accurate estimation of the film coefficients is important for accurate assessments of the thermal performance of windows. The surface film coefficient depends on two heat transfer mechanisms: convection and radiation. Normally, a free natural convection develops between the indoor window surface and the room air, and a forced convection due to the wind effect exists along the outdoor surfaces. The thermal radiation heat transfer coefficient can be determined based on the assumptions of gray body material and the surrounding surface temperature equivalent to the ambient air temperature.

2.3.3.1 Indoor convection coefficient

In most of the models calculating building energy consumption and heat transfer through fenestration systems, for example, DOE2.0, FRAME/VISION, and WINDOW/THERM, an average constant surface film coefficient is typically assigned for the boundary

condition. This average surface coefficient is normally calculated using a ASHRAE correlation (ASHRAE, 1997) which is an integration of local coefficients of the laminar natural convection developed along an isothermal flat plate. Although this simplification may be sufficient for the U-factor and energy consumption calculation, it is inadequate for predicting the window surface temperatures, especially at edge of glass and frame areas. The reasons are three-fold. First, the local convective coefficient decreases with the development of the free convection flow along the isothermal plate. Secondly, the assumption of isothermal plate is not valid for the window assembly because of the gas convection within the glazing cavity and the thermal bridge effect of the edge-of-seal. Thirdly, the real window assembly is not a simple flat plate but with the frame and sash. These components deflect the flow and cause flow stagnation at the window head and sill.

The effect of applying one constant film coefficient in simulations on the prediction of glazing surface temperature was demonstrated by a collaborative research project (Sullivan, et al., 1996). This research compared the IGU surface temperatures between experimental measurements and computer simulations. The study concluded that the two-dimensional simulation results based on one constant film coefficient and the infrared thermographic measurements agreed well at the center-of-glass (within 1°C), but showed large discrepancies as high as 3°C at the edge-of-glass (Elmahdy, 1996; Griffith, 1996; de Abreu et al, 1996; and Zhao et al, 1996) even though only the insulated glazing unit was chosen and installed flush with the surrounding walls to avoid the complex local airflow variations at sill or head, if present. The fact that the simulations did not consider

47

variations of the local film coefficients along the IGU surface was believed to be one of the possible causes for the discrepancy.

Efforts have been made to develop analytical formulae and correlations for the local convective heat transfer coefficient based on the non-isothermal plate assumption. Yeoh (1989) modified the correlations developed by Raithby and Hollands (1975) and yielded the following formula:

$$h_{ci}(y) = k\, C(\text{Pr}) \left(\frac{g\beta}{\upsilon\alpha}\right)^{0.25} \frac{\left(T(y)-T_i\right)^{2/3}}{\left(\int_0^{y'} \left(T(y')-T_i\right)^{5/3} dy'\right)^{0.25}} \tag{2.11}$$

where,

$h_{ci}(y)$ = local convective heat transfer coefficient at a distance y from the start of the boundary layer, W/m$^2\cdot$K;

k = thermal conductivity of the fluid, W/m$\cdot$K;

$T(y)$ = local surface temperature, $^\circ$C; and

T_i = ambient indoor temperature, $^\circ$C.

The constant $C(Pr)$ in the above equation is given by Churchill and Ozoe (1973) as:

$$C(\text{Pr}) = \frac{0.53}{(1+(\frac{0.47}{\text{Pr}})^{\frac{9}{16}})^{\frac{4}{9}}} \tag{2.12}$$

This non-isothermal model was used in the work of Schrey et al. (1998) who attempted to extract local convective heat transfer coefficients over the interior surface of IGUs from the measured temperatures obtained by Elmahdy (1996) and Griffith (1996) using infrared cameras. Iterations were carried out using a two-dimensional simulation

48

program to find the local film coefficients with the assumption that local surface temperature varies linearly with the local heat transfer coefficients within a small range of heat transfer coefficients. Equation 2.12 was modified to account for the discrete distance (Δy_i) between temperature observations and the unknown starting point of the free convection boundary as:

$$h_{c,y_i} = kC(\text{Pr})(\frac{g\beta}{\upsilon\alpha})^{0.25} \frac{(T_{meas}(y_i)-T_i)^{2/3}}{C_0 + (\sum_{i=1}^{N_{y_i}}(T_{meas}(y_i)-T_i)^{5/3}\Delta y_i)^{0.25}} \tag{2.13}$$

The unknown constant C_0 accounts for the missing part of the integral function starting from y=0 mm to the top edge of the IGUs, which is deduced from the thermography data. Good agreement in temperature profiles was obtained between simulation results and experimental measurements for most portions of the IGUs except for the bottom and top regions. The reasons for that may be due to the two-dimensional heat transfer effect, the inaccuracy of constant heat flux assumption, and the error from the unknown value C_0.

Curcija and Goss (1993) conducted 2-dimensional numerical simulations to correlate the local film coefficients for a complete window assembly with frame. This study concluded that the correlation developed for the natural convection over an isothermal flat plate, in the form of equation 2.14, can be used for the center-of-glass region.

$$h_y = C_1 \frac{k}{y} Ra_y^{0.25} \tag{2.14}$$

where C_1 is a constant. Its benchmarking values are listed in Table 2.2. In the regions where the flow stagnates, such as the edge-of-glass area or re-circulates right after the frame step, there is a large depression in the value of the local convective heat transfer coefficient. A linear correlation over an average length of two inches from zero to the

49

value at the center-of-glass or the value after the re-circulation can be used to represent a close approximation for these local vertical surfaces. The correlations for the horizontal surfaces of the frames were also reported.

Table 2.2 Values of coefficient C_1

Source	C_1
Ostrach (1952)	0.3856
McAdams (1954)	0.4425
Le Fevre (1956)	0.3845

Besides the numerical analysis by Curcija and Goss (1993), some researchers (Griffith, et al., 1998b) have also tried to measure the local convection heat transfer coefficients along a complete window assembly. According to the classic free convection theory (Raithby and Hollands, 1975), the boundary layer formed along a vertical plate can be divided into inner and outer two regions. In the inner region, conduction heat transfer dominates and the temperature profile can be approximated linearly. By mapping the air velocity and air temperature in the vicinity of window surface, the local convection film coefficients were estimated. The test results showed that the local convection heat transfer coefficient remains almost flat through the center-of-glass with maximum value on the top of 3 $W/m^2 \cdot K$, and reduces at window head and sill areas close to 1.0 $W/m^2 \cdot K$.

2.3.3.2   Outdoor convection film coefficient

Due to the wind effect, the outdoor air movement over the building envelope surface is normally assumed as forced convection. The survey conducted by Fürler et al. (1988) found that as many as 14 sets of correlations have been derived to calculate the outdoor convection coefficient from laboratory measurements, computer simulations or field measurements under various conditions. Most of these correlations present the outdoor

convection coefficient as a function of wind speed. However, there is a large disagreement between these correlations (Klems, 1989).

For many years, ASHRAE had been using a constant value of 34 W/m$^2 \cdot$ K as the standard outdoor film coefficient in winter condition with an assumed wind speed of 6.7 m/s. After removing the radiation portion, the convection coefficient was approximately 31 W/m$^2 \cdot$ K. This value was derived from the wind-tunnel measurements using a tangential wind by Rowley and Eckley (1932). The standard value currently recommended by ASHRAE is from a revised set of correlations developed by Lokmanhekim (1975). These correlations are based in part on measurements from the sixth floor of a medium-rise building by Ito and Kimura (1972). The Kimura model predicted a lower value of 25 W/m$^2 \cdot$K for the convection coefficient at the wind speed of 6.7 m/s. The combined outdoor film coefficient of 30 W/m$^2 \cdot$K is used as standard value in both CSA and ASHRAE conditions.

The detailed field measurements for windows in low-rise buildings by Yazdanian and Klems (1994) indicated that the correlation based on local wind speed of 6.7 m/s was incorrect for low-rise buildings since this wind speed is unlikely to occur. In their model, the exterior coefficient included two parts, one is for the natural convection for situations with no wind and the other part is for forced convection, which is function of realistic wind speed.

Similar to the room side, the exterior convection film coefficient varies along window surface, especially at places with the presence of frame. Curcija and Goss (1995) conducted a two-dimensional simulation for a wood frame window with assumptions of a laminar forced convection flow perpendicular to an isothermal surface. The results showed that the correlation derived for the vertical plate can be applied to the center-of-glass area, but for the edge-of-glass and frame areas, the local coefficient decreases from the constant value at center-of-glass to the lower conduction limit value in the stagnation and separation regions.

The exterior film coefficient had been a strong determinant of the window nighttime U-factor until the emergence of high performance products. The exterior film coefficient does not become entirely unimportant until the thermal resistance of window reaches the range of 1.4-1.8 $m^2 \cdot$ K/W (Yazdanian and Klems, 1994).

2.3.3.3   Radiation heat transfer coefficient

The radiative heat exchange between the interior glass surface and the room surfaces accounts for more than 50% of the indoor surface film coefficient. The radiation coefficient is usually calculated based on the assumption that the radiant temperature of the indoor surfaces is equivalent to the indoor air temperature. This assumption is correct for small fenestration products exposed to a large room whose surface temperature equals air temperature, but is not valid for fenestration product exposed to other large glazing areas, such as greenhouse, and skylights etc.

A constant radiation coefficient is normally used in energy simulation programs. This simplification is accurate enough for calculating the overall U-factor, but is not sufficient for accurate predictions of surface temperatures at local regions where the glazing surface can view the frame or itself. Results from a detailed view-factor radiation model developed by Griffith et al. (1998a) were compared to infrared thermography measurements for a foam garden window. The results indicated that the use of radiation view-factor model in simulation improved the accuracy of the simulation.

The radiation makes up only a very small part of the outdoor surface film coefficient. The radiative temperature of the outdoor environment is frequently assumed to be equal to the outdoor air temperature for a fully cloudy sky. During nights with clear skies, additional radiative heat loss occurs between the fenestration and the sky and must be accounted for.

2.3.4 Effect of local film coefficients on temperature prediction

The prediction of the interior surface temperatures is influenced by the local film coefficients on both indoor and outdoor sides, but it is more sensitive to the interior surface heat transfer coefficient. The sensitivity study by de Abreu et al. (1996) showed that doubling the value of h_o from 20 to 40 W/m² K decreased the warm-side surface temperature by only about 1°C, while a small change of h_i from 7 to 8 W/m²·K increased the warm-side surface temperature by 1.1°C.

The variations of local film coefficients especially at edge-of-glass and frame areas have been recognized as the main cause for the discrepancy in temperature distributions over the fenestration surfaces obtained from testing and modeling. McGowan (1998) studied the effect of variations in local film coefficients on the numerical prediction of surface temperature for edge-of-glass and frame areas using FRAME program. The edge-of-glass (63.5mm) area was divided equally into five segments. A convection coefficient proportional to the distance away from the sightline was assigned to each segment in the range from zero to the value at center-of-glass. The radiation heat transfer coefficient for each segment was also modified to account for the radiative heat exchange between glass surface and the frame. The comparison to some limited measured data indicated that by varying the room-side local film coefficient the difference between test and simulation was reduced to a typical order of 1°C to 2°C with a worst of 3.3°C for the edge-of-glass area. However, for the frame area, simulation was typically 3°C higher than the test, with a worst case of 5°C for the aluminum frame. The possible reasons for the large disagreement on frame surface were believed by McGowan are: 1) wind-washing effect and air leakage effect were not addressed by the simulations; 2) test data were limited due to the omission of reporting test conditions or the inaccurately reported measurement locations; and 3) errors in the measurements can be as much as 5°C between test agencies (Elmahdy, 1990).

In a similar study by Curcija et al. (1998), the element-to-element radiative heat transfer and view factor were calculated over the indoor surface in addition to varying the local convection film coefficients. The outdoor convection coefficients were also localized

based on the recommendation from Branchaud (1997). The simulations from the program THERM indicated that better agreements with the measured results were achieved by varying local film coefficients. The best results were from the simulations with localized film coefficients for both indoor and outdoor surfaces.

Well-designed and accurately measured surface temperatures for fenestration systems under more realistic conditions are needed to validate the capability of the simulation models. Adjusting the local film coefficients for frame surface may reduce the discrepancy for metal frames.

2.3.5 Studies on thermal comfort related to window performance

While windows are generally not the primary element affecting the comfort of the occupants, they can become quite influential on the occupants close to the windows during very hot or cold weathers. In the cold winter, discomfort may be experienced by the occupant close to the window due to 1) the radiative heat exchange between a human body and the window surface, 2) cold draft induced by air flowing off the cold window surface, and 3) thermal stress experienced by human body due to the radiant asymmetry between the window and room. In a hot summer day, solar heat gains from the direct transmission through the window and the re-radiated heat from windows and surroundings may subject the occupant in the perimeter zone to radiant temperatures above $60^{\circ}C$ (Lyons, et al., 2000).

Heiselberg (1994) studied the cold draft effect by measuring the air velocities and air temperatures at different distances from a cooled flat surface and at different heights from floor under laboratory conditions. A set of empirical equations was formulated to calculate the maximum velocity and minimum air temperature in regions near to the floor. These equations are:

$$v_{max}(x) = \begin{cases} 0.05\sqrt{h\Delta T} & x < 0.4 \\ 0.095\dfrac{\sqrt{h\Delta T}}{x + 1.32} & 0.4 \le x \le 2.0 \\ 0.028\sqrt{h\Delta T} & x > 2.0 \end{cases} \qquad (2.15)$$

$$T_{floor}(x) = T_{ref} - (0.3 - 0.034x)\Delta T \qquad (2.16)$$

where,

v_{max} = maximum air velocity resulted from the cold draft in the near floor region, m/s;

T_{floor} = minimum air temperature in the near floor region, °C;

T_{ref} = room air temperature at the reference point, °C;

ΔT = temperature difference between the window surface and the room air, °C;

h = height of the window, m; and,

x = distance from window surface, m.

As shown in the above equations, velocity profile is divided into three regions. In the first region, which is within 0.4m from the cooled surface, the velocity is constant and is a function of temperature difference between the cooled surface and the room air (ΔT), and the surface height (h). The velocity gradually decreases with distance from the cooled surface in the second region, which is from 0.4m to 2m. In the third region, which is after 2 m, the velocity becomes a constant again and is also a function of ΔT and

surface height but with smaller values. The temperature increases continuously with distance from the cooled surface and is a function of ΔT, surface height, and distance. This correlation was developed based on the measurements for a flat surface without frame. The cold draft effect may be overestimated based on this correlation under certain circumstances. For example, when the window frames are present, the cold air is re-directed to mix with the room air first before it hits the floor. In this process, the air velocity will be reduced and the air temperature will be elevated. The effect of frame width on breaking the boundary layer and reducing cold draft along large glazed façade was also studied by Heiselberg (1995). He concluded that the use of structural system as obstacles in the boundary layer flow is an energy efficient way to improve the comfort conditions in occupied zone in cases with large glazed surface. The width of the frame has to be large enough to allow the boundary flow to separate from the surface. Care should be taken when using this method since the presence of window frames may introduce condensation risks at the edge-of-glass region due to flow stagnation. As a matter of fact, the effect of frame width on condensation potential has never been studied.

Lyons et al. (2000) did a complete study on the impact of window thermal performance on the occupant's thermal comfort. Three factors including long-wave radiation, solar radiation, and cold draft were analyzed by using a two-node model, ASHRAE comfort Tool (ASHRAE, 1995). It was found that long-wave exchange between the human body and the window was the most significant factor except for the case where the body was directly in the sunlight in summer condition. For most residential-sized windows, draft effects are typically small.

In practice, warm air is normally delivered underneath windows to counter the downward cold draft and to warm up the glass surface so that the radiant asymmetry experienced by occupants and the condensation risk can be reduced. If the cold draft and the radiant asymmetry induced by the window surface can be reduced to an acceptable thermal comfort level by using high performance windows, it is not necessary to deliver the supply air to the perimeter of buildings. In this way, the direct heat loss through windows and the heat loss through duct can be reduced, and the ductwork length can be shorten. The impact of this method on energy consumption and thermal comfort was examined by Hawthorne et al. (2000) and it was concluded that in many cases the initial cost savings in the ductwork can offset the cost of high performance windows while meeting the thermal comfort requirements.

Metal curtain walls have large and continuous glazing area, which increases the chances for occupants in the perimeter zone to be exposed to the cold glazing surfaces. Meanwhile, the mullion surface temperature is normally low as well and the area portion of mullion is much higher than for regular windows. The conclusions drawn for residential windows may not applicable to curtain walls.

2.4 Studies on thermal performance of metal curtain walls

The overall thermal performance of curtain wall systems depends on the interactions and integration of individual constituents as well as the performance of each component. Although the application of high performance IGUs in curtain walls can increase the

overall thermal resistance of the wall, the performance of spandrel panel and frame are critical for achieving good overall thermal performance for the entire assembly. Even though thermal breaks are used on the mullions, the screws used to fasten the wall assembly can produce thermal bridges and reduce the benefit of the performance improvement. The return of the steel back-pan is connected with the spandrel adapters and creates another thermal bridge. The pressure equalization rainscreen (PER) design of the spandrel panel allows the cold air to ventilate through the air cavity behind the spandrel glass, which exposes the spandrel adapters and mullion nose to the cold air. The washing effect of cold air at the mullion nose may lower the effect of the thermal breaks. Therefore, the evaluation of the thermal performance of curtain walls is not complete without taking spandrel panels and mullions into account, and the complex configurations of mullions and spandrel panels make the analysis of curtain wall thermal performance much more complicated than windows.

Currently, only a few studies have been conducted on the thermal performance of curtain wall assemblies and most of them focused only on the analysis of U-factors. From the experimental measurements and computer simulations on a curtain wall sample sized 2.11m by 1.97m, Han (1992) concluded that although the frame area was only 12.7%, the frame took up 51.6% of the total heat loss. A study by Enermodal Engineering Ltd. (1994) drew similar conclusions and stated that "despite having half its area in spandrel panel, the curtain wall total U-factor is slightly higher than a standard double-glazed window. The high U-factor is due to high heat transfer through the mullions and steel bolts". In this study both physical tests and computer simulations were carried out on a

curtain wall specimen with a dimension of 2.07m by 1.82m. Griffith et al. (1998c) studied the thermal bridge effect of bolts by experimental tests and two-dimensional simulations. The test specimen was composed of curtain wall frame sections with a small portion of glazing filled with extruded polystyrene boards to represent the edge-of-glass. The specimen was constructed this way to eliminate all influencing factors other than the configuration of bolts. Various screw materials and screw spacing settings were examined. He concluded that stainless steel bolts with a thermal conductivity of 14.3 W/m·K affected minimally the curtain wall thermal performance (approximately 18%) when spaced at least 230mm apart. When the screw spacing was less than 230 mm or when steel bolts, having a higher thermal conductivity of 48 W/m·K, were used, the thermal performance was increasingly compromised. The impact of screws may be exaggerated in this study since the real IGUs were substituted by sandwiched insulation boards and the complicated two-dimensional heat transfer was thus simplified.

The spandrel panel and its integration into the entire curtain wall system are as complex, if not more, as the vision panels. Complex heat transfer mechanisms and paths are present through the spandrel area. Metal curtain walls have been treated as regular windows plus walls. In curtain wall practice, the energy performance is evaluated based on the U-factor of center-of-spandrel only without considering the frame and edge-of-spandrel effect. Two-dimensional simulations on an aluminum frame curtain wall showed that with a U-factor of 0.34 W/ m^2· K for the center-of-spandrel, the U-factor for the edge-of-spandrel was 2.56 W/ m^2· K (Carpenter and Elmahdy, 1994), which indicated that the two-dimensional effect at the edge-of-spandrel was significant.

As discussed in section 2.2.1, the new edition of CSA-A440.2 (CSA, 1998) recommends to include the performance of spandrel panel in the assessment of thermal performance of metal curtain walls for the first time. The new CSA procedure will give more accurate evaluation, however, the separation between spandrel panel and vision panel maybe oversimplified because of the complex connection between spandrel panel and frame. The ASHRAE Fundamental handbook (ASHRAE, 1997) suggested to take the same frame U-factor for spandrel panel as for vision panel and to assume the U-factor of edge-of-spandrel to be 40% of the value for the frame U-factor. This treatment is too simplistic and does not consider different spandrel configurations. The discrepancy due to this simplification in term of U-factor and corresponding energy consumption has yet to be studied.

In recognizing the significance of the thermal effect of mullions and screws, a few manufacturers have improved the design of the frame. Figure 2.5 shows two new designs from two different manufacturers. In Figure 2.5a, the integrated aluminum nose with a thin strip of thermal break is replaced by the reinforced nylon nose to form a much larger thermal break. Figure 2.5b shows the non-metal connection between interior and exterior frame sections and added insulation inside the cavity. The effect of these improvements on the overall thermal performance of metal curtain walls has not been reported.

Reinforced Nylon nose
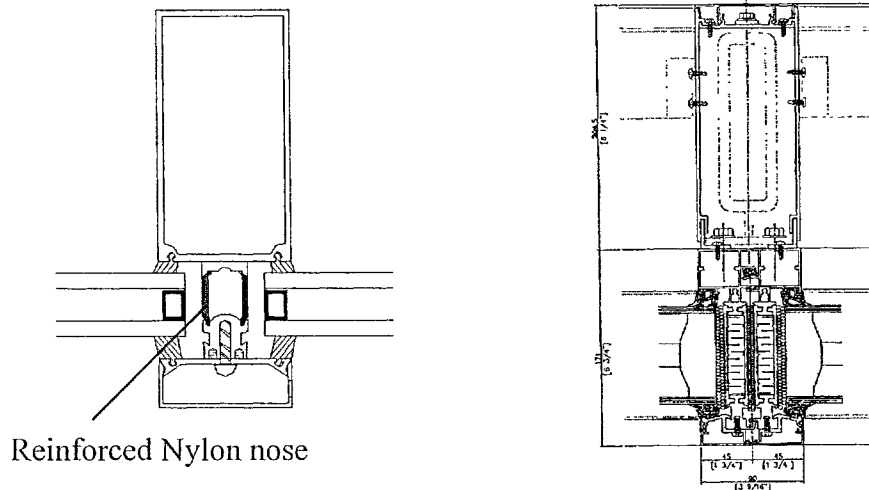
Figure 2.5 Typical configuration of mullions in advanced design from two different manufacturers

2.5 Conclusion

Metal curtain walls have been widely used in the construction industry due to their inherent advantages in providing high quality building envelope systems in term of quality control and construction. However, they have low thermal performance and are referred to as "heat sink" for heating-dominant climate in practice due to its high thermal conductance. This chapter summarized the background information and research status on metal curtain walls. Through the literature review, it was found that studies on thermal performance of curtain walls had been rarely reported.

Although some of the few existing studies have recognized the significant effect of the thermal bridges at the joint section, no comprehensive study has emerged in the survey to treat metal curtain walls as integrated systems and to study the effect of design details on the energy consumption, occupant thermal comfort, and condensation resistance.

62

Although the new CSA standard has made an improvement over the conventional evaluation procedure and recommended to evaluate the performance of spandrel panel, its prescribed testing procedure to separate spandrels panel from vision panels may introduce errors in the U-factor calculation and condensation prediction. The exact extend of errors of this simplified treatment has yet to be addressed.

Computer simulation programs FRAME/VISION have been validated by physical tests and recommended by the standards to calculate U-factors for fenestration systems. However, the reliability of these programs to predict the condensation resistance performance is still under study. Well-designed and accurately measured surface temperatures under more realistic conditions are needed to validate the capability of the simulation models.

The benefits provided by high-performance curtain walls need to be quantified so that their higher initial cost would be better justified and more consumers would see the benefits of making the additional initial investment during the construction of the building.

In summary, the literature review has identified the research gaps on metal curtain walls. To address all the issues identified, a comprehensive research program has been designed and implemented. The work plan of this research program is outlined in Chapter 3.

Chapter 3

Overview of the research program

3.1 Introduction

The literature review in Chapter 2 found that the assessment of curtain wall performance by existing standards is segmented, and the few existing studies have addressed curtain wall performance by the U-factor alone. No comprehensive study has been reported to treat curtain walls as integrated systems and address their overall thermal performance. For example, the literature review in Chapter 2 raised many questions and issues which remained unresolved. Among these are the following:

1. What is the relative importance of each design detail in achieving better-performing curtain walls? How does each design detail affect the thermal performance of curtain walls when assessed under a more realistic condition?

2. How do different curtain wall systems affect the energy consumption of a building and its indoor thermal environment?

3. How much discrepancy would the current practice cause in calculating the U-factor for curtain walls and the corresponding energy consumption?

4. Would program FRAME be reliable to predict condensation risks if more realistic boundary conditions are applied in simulations and more accurate measurements are available for validation?

5. Metal curtain walls are usually claimed having relatively high airtightness. Would air leakage affect the condensation resistance performance of curtain walls?

The research program in this thesis has been designed to evaluate the overall performance of metal curtain wall systems using a holistic approach and resolve many of the issues identified in Chapter 2. This chapter presents an overview on the research program, test facility, and test specimen.

3.2 Research program

In order to carry out an overall evaluation, extensive experimental testing, analytical and simulation studies are planned. Because of its length and complexity the research work is broken down into the following aspects:

1. Air leakage test

   Airtightness is an important aspect of building performance and it has a significant influence on the thermal performance, indoor air quality, energy consumption, condensation resistance, occupant comfort, and envelope component life span. The air-tightness and leakage characteristic of each curtain wall section are measured separately right after the specimen installation. A different approach than the standard pressurization method is developed.

2. Thermal performance tests

   Design details have a significant impact on the thermal performance of curtain walls. This effect is demonstrated by thermal performance tests. The approach employed is to measure detailed temperature distributions across the wall rather than to obtain an

average U-value by guarded hot box measurements. Two temperature monitoring techniques are used. One is the thermocouple measurement, which is thoroughly distributed across the wall assembly. The other one is the infrared thermography measurement. The test specimen are subjected to different test conditions including a series of steady winter conditions, a cyclic winter condition, and one CSA winter condition with air infiltration introduced. The test results will be reported by temperature comparison for these two curtain wall systems, condensation resistance factors, and the temperature responses to the air infiltration.

3. Measurement of local convection film coefficient

The air velocity and air temperature in the boundary layer of curtain wall surface are measured to determine the local convection film coefficients in order to provide realistic boundary conditions for computer simulations. A customized 3-dimensional computer controlled traverse system is built to measure the air velocity and air temperature close to the curtain wall surface with high spatial resolution.

4. Measurement of cold draft

The air velocity and air temperature in the cold draft induced by the cold glazing surfaces is measured to evaluate the cold draft effect on the local percentage of dissatisfied (PD) for occupants seated in the perimeter zone. Two winter conditions are simulated. One is the CSA winter condition, the other one is the worst Montreal winter condition.

5. Evaluation of the impact of design details on U-factors

66

In order to establish the effect of design details on curtain wall U-factors, simulations using FRAME/VISION are conducted. The overall U-factors calculated for curtain walls by different methods are compared.

6. Effect of local film coefficients on temperature prediction

   The accuracy in predicting temperature distribution by program FRAME is studied by applying more realistic boundary conditions in simulations. The simulation results are compared to the well-documented and accurately measured experimental data.

7. Effect of thermal performance on the occupants and on energy consumption

   The impact of curtain wall thermal characteristic on occupants thermal comfort and energy consumption are evaluated using measured data by a simplified energy calculation model.

3.3 Test facility

The Environmental Chamber (Figure 3.1) has been designed as a multiple purpose research and testing facility to evaluate the performance of large-scale building envelope systems under simulated outdoor climatic and indoor environmental conditions. This facility can accommodate wall specimens of up to 4.1 m wide by 7.2 m high, the equivalent of approximately two commercial stories or three residential stories. The Environmental Chamber consists of a cold box, a hot box, and a structural frame to accommodate the wall specimen between the cold and hot boxes. A second frame is available to interchange specimens. This facility can be used in different testing modes: guarded hot box (ASTM C236), calibrated hot box (ASTM C976), or a single large environmental chamber. In the last mode, two boxes are joined together without the

specimen to form a large chamber for hosting a test hut inside. Several research projects have been carried out using this configuration (Desmarais et al., 1998 and Fazio, et al., 1998).

Temperature and relative humidity can be controlled to follow the design profiles in both the cold box and the hot box. The data acquisition system used for this test has 400 input and 22 output channels and can measure temperature, moisture content, relative humidity, heat fluxes, pressure and other parameters. Data are recorded and stored automatically by a computer. A second data acquisition system with 384 channels has been added to the system recently, which increases the capacity to about 800 channels. More information regarding this facility can be found in Fazio et al. (1997). The layout of the chamber used for this experiment is shown in Figure 3.2.
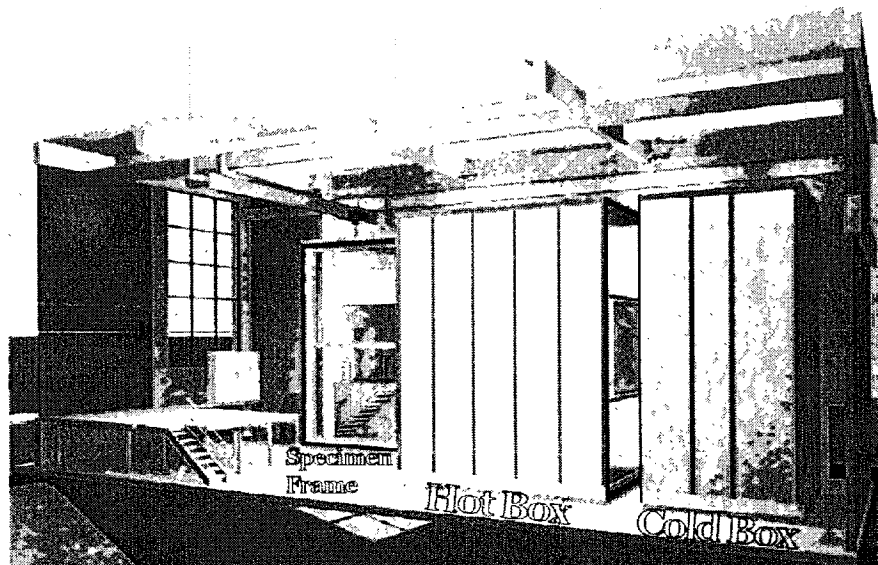
Figure 3.1 Environmental chamber facility
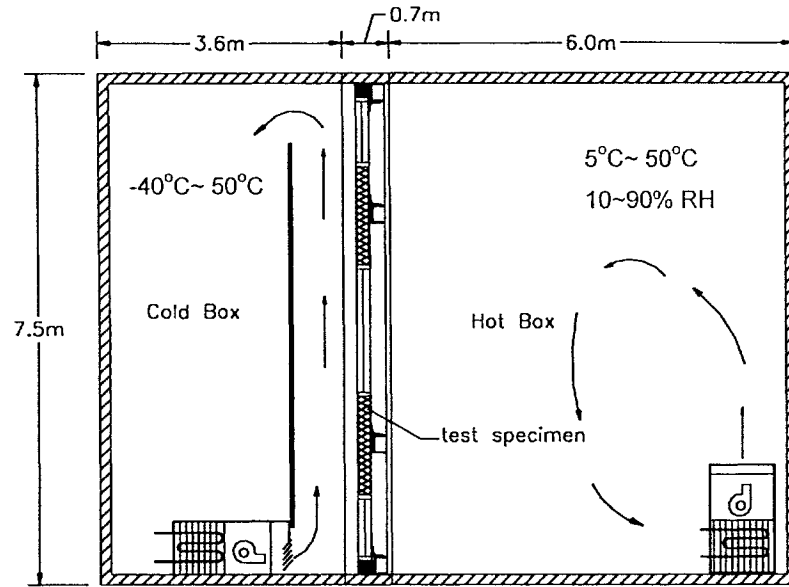
Figure 3.2 Experimental setup in the environmental chamber

3.4 Test specimen

The test specimen (Figure 3.3) is designed to incorporate as many different elements as possible to study the impact of design details on the overall thermal performance of metal curtain walls. The overall dimensions of the specimen are 3.81m wide by 6.71m high. It consists of two different types of curtain walls. The first is a standard system, referred to as system A, and the second is an improved system, referred to as system B in this thesis.

The difference between these two systems includes three aspects. First, with respect to the frame configuration, a much larger thermal break is achieved by using the reinforced nylon in the frame section of system B, while in system A, a thin strip of nylon works as the thermal break, as shown in Figure 3.4. Secondly, with respect to the glazing panels, all glazing units in system A are clear double-glazed IGUs with a conventional aluminum

spacer. System B incorporates clear double-glazed units with low-e coating (ε=0.1), 95%/5% argon/air gas filling, and thermally broken aluminum spacers in the middle section. Thirdly, in respect to the back-pan design in the insulated spandrel panel, System A uses the regular design, and system B uses the revised back-pan design, which connects the steel backpan to the interior flange of the mullion tube to eliminate the thermal bridge effect created by the return of the backpan as shown in Figure 3.4. The detailed configurations of these two systems are listed in Table 3.1.

The test specimen was designed and fabricated by Kawneer Canada Inc., a curtain wall manufacturer. The on-site installation at the laboratory was carried out by a construction team of the company to represent actual workmanship used on-site. The construction procedure was divided into two stages to allow the sensor installation. To facilitate the installation and to avoid damage to the glazing panels, the main grids and spandrel panels of the test specimen were built up first, outside the environmental chamber (Figure 3.5a). After this step was completed, the structural frame accommodating the curtain wall assembly was lifted by a crane and moved into the space between the cold box and the hot box. In the second stage, the installation of insulating glazing units, spandrel glasses, and pressure plates was carried out in the space between the cold box and the structural frame (Figure 3.5b). After the construction of the test specimen and the installation of sensors were completed, the structural frame containing the test specimen was lifted and attached to the cold box. Then the movable hot box was closed and sealed onto the structural frame.

Table 3.1 Components of the test specimen

	System A	System B
Glazing panels	all glazing panels: double insulated glazing units with ¼" (6.4mm) clear annealed glass pane, ½" (12.7mm) air space and conventional aluminum spacer	top and bottom glazing panels: double insulated glazing units with ¼" (6.4mm) clear annealed glass pane, ½" (12.7mm) air space and conventional aluminum spacer
		middle glazing panels: double insulated glazing units with ¼" clear annealed glass, 95% Argon space, low-E coating (ε=0.1) on the exterior surface of the inner glass pane, thermal broken aluminum spacer
Spandrel panels	¼" (6.4mm) clear annealed spandrel glass, ¾" (19.2mm) air gap, 4" rigid fiberglass insulation with standard steel back-pan design	¼" (6.4mm) clear annealed spandrel glass, ¾" (19.2mm) air gap, 4" rigid fiberglass insulation with revised steel back-pan design
Mullions	2½" (63.5mm) high by 4"(101.6mm) deep integrated aluminum mullion with a continuous strip of nylon as thermal break	2½" high by 4" deep aluminum mullion with reinforced nylon as a thermal break

The curtain wall specimen was attached to the horizontal beams of the structural frame by angle anchors. The horizontal beams represent floor slabs in a real building. The section between these two middle beams represents a standard floor and is the main study region in this experiment. The test specimen was insulated at the perimeter by polystyrene foam and all the joints are sealed by latex sealant to separate the indoor environment from the outdoor climate. The construction details are shown in Figure 3.4

71
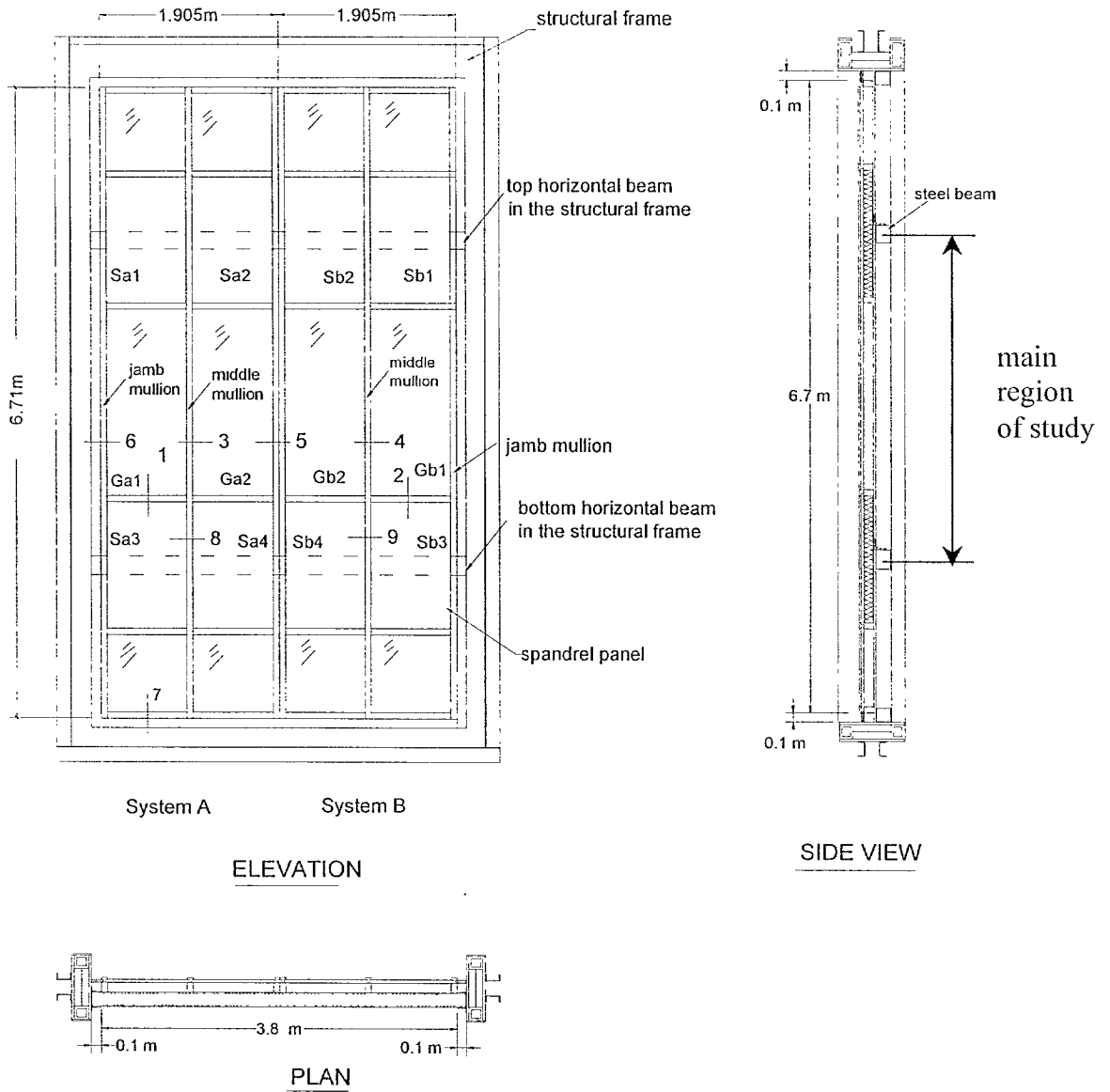
Figure 3.3 Configuration of the test specimen (interior view)
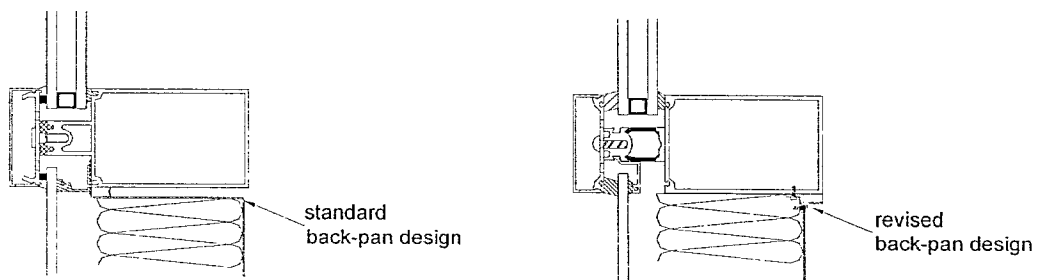
(a) Section 1: vision sill of system A

(b) Section 2: vision sill of system B

nylon
thermal breaks

reinforced Nylon nose
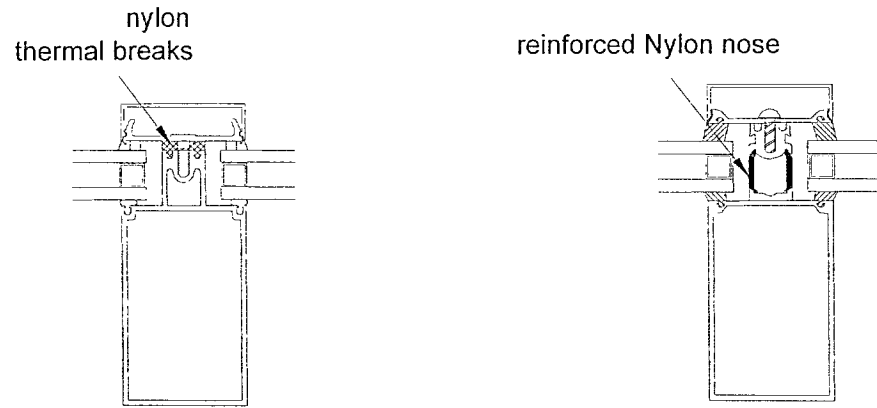
(c) Section 3&4: glazing meeting rails

System A

System B

continuous
sponge tape

styrofoam
insulation
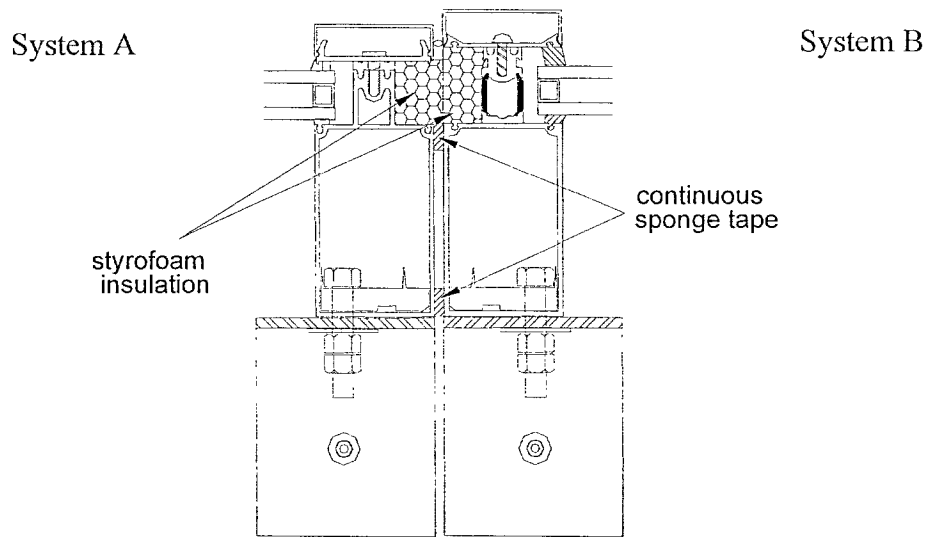
(d) Section5: vertical junction of systems A and B in the test setup

1/4" plywood continuous
sealant styrofoam insulation

continuous
styrofoam insulation

insulated
structural frame

steel channel
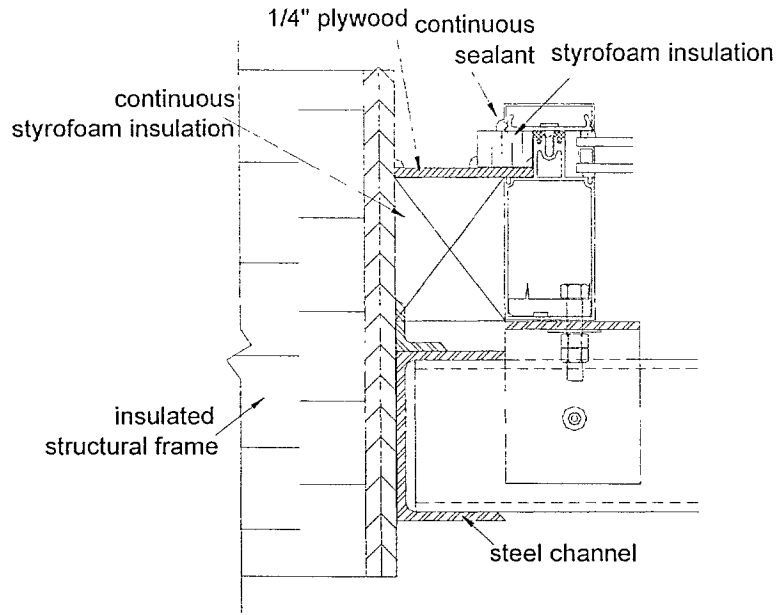
(e) Section 6: vertical jamb detail

slip anchor
assembly

styrofoam insulation

steel beam

sealant
1/4"plywood

continuous
styrofoam insulation

insulated
structural frame
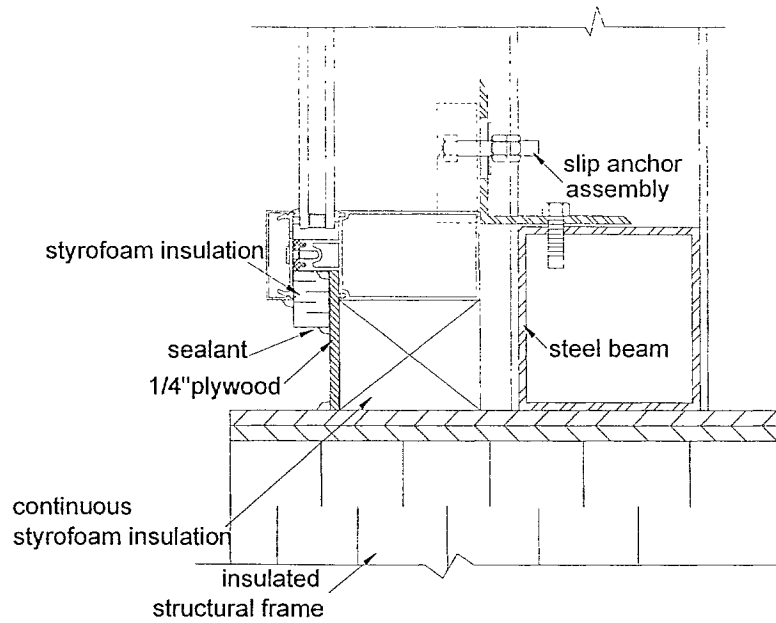
(f) Section 7: bottom jamb detail

Figure 3.4 Construction and installation details

74
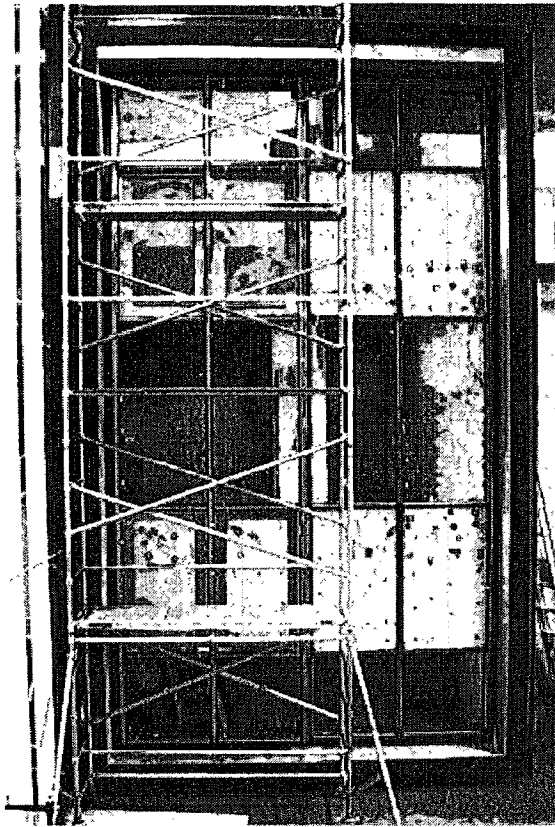
Figure 3.5a Photo taken when main frame and spandrel panel completed.

cold box

glazing   panel
being installed

structural
frame
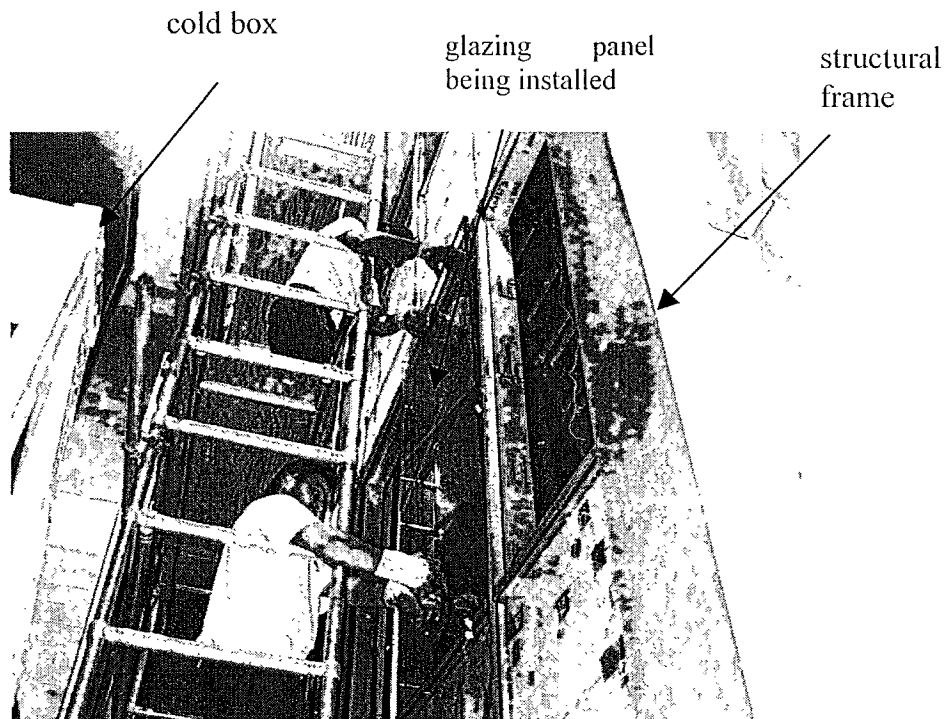
Figure 3.5b Photo taken when a glazing panel was being installed

75

Chapter 4

Air leakage test

4.1 Introduction

Airtightness is an important aspect of building performance and it has a significant influence on the thermal performance, indoor air quality, energy consumption, condensation resistance, occupant comfort, and envelope component life span. Additionally, it adversely affects the rain penetration control performance of the pressure equalization rainscreen in cases where this system is used. As stated in Chapter 2, the continuity of the air barrier in a curtain wall assembly is achieved by the air seals at the shoulder flanges of the tubular mullions. The airtightness of curtain walls relies mainly on the performance of the air seals at the joints, which is affected by wind loads, structural deflections, weathering deterioration, and workmanship.

To carry out the airtightness measurement, a new testing method, "flexible double-chamber method", was developed and it was used to test one of the two curtain wall systems installed in the environmental chamber. The new approach overcomes the difficulty in applying the standard fan pressurization method to this test due to the relatively low air leakage rate of metal curtain walls and the relatively large amount of extraneous air leakage. The experimental setup, special features in the new approach, and the data processing procedure are described in detail in the following sections.

4.2 Experimental setup

4.2.1 Standard pressurization test

Both Canadian standard CSA-A440.2 "Energy performance of windows and other fenestration systems" and AAMA publication "Methods of test for metal curtain walls" specify that the air leakage performance of metal curtain walls should be determined in accordance with ASTM standard E283 on "Standard test method for determining rate of air leakage through exterior windows, curtain walls, and doors under specified pressure difference across the specimen". The specimen should include spandrel panels, glazing panels, and other details as installed in the buildings.

The ASTM E283 approach requires a well-sealed chamber into or against which the specimen is mounted and secured for testing (Figure 4.1a). The test chamber shall be capable of withstanding the differential pressure applied in the test. A blower fan can be used to maintain a positive or negative pressure inside the chamber by pressurization or depressurization. When the equilibrium is reached and maintained under a specified pressure, the measured airflow rate is used to obtain the air leakage characteristics of the test specimen. This basic method assumes that all the air pushed inside or extracted out of the chamber by the fan passes through the specimen area being tested, that is, there is no extraneous air leakage through paths other than those through the specimen being tested. However, extraneous air leakage does occur through the chamber itself and the incomplete seal between the chamber and the specimen, and through the air paths within the wall that lead from the tested section to the untested area. In such situation, the ASTM E283 requires either to eliminate the extraneous air leakage or measure the

77

extraneous air leakage rate under the same specified pressure by sealing the test specimen. The test specimen can be sealed either by a loosely fit sheet of thin polyethylene film over the higher-pressure side of the test specimen or by a tightly fit sheet of polyethylene film over the lower pressure side of the test specimen (ASTM E783, 1993), as shown in Figure 4.1b.

a) standard pressurization   b) extraneous air leakage calibration
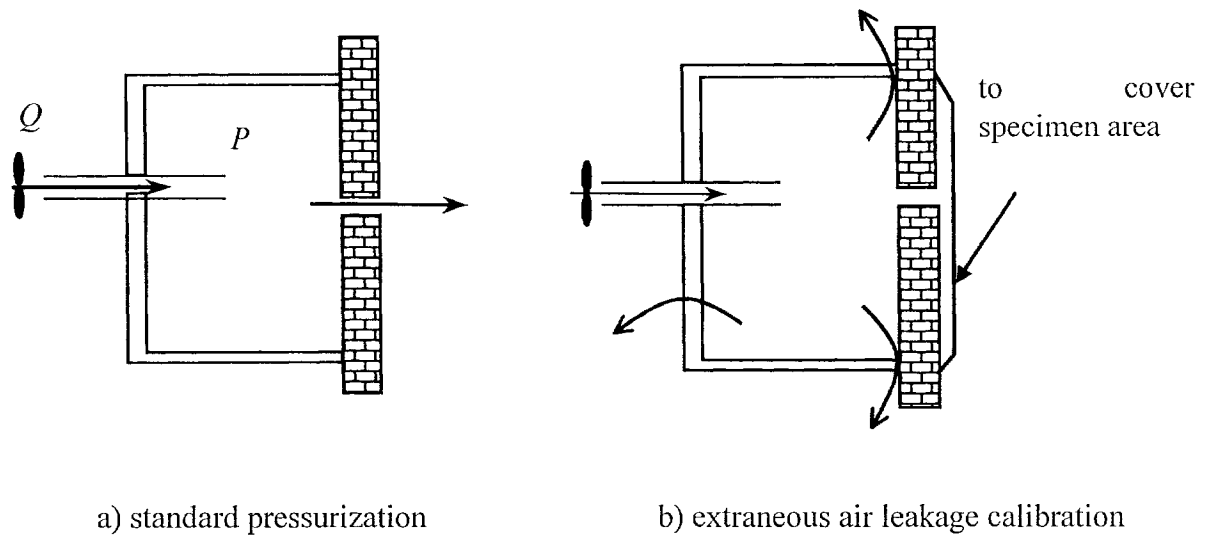
Figure 4.1 Standard pressurization air leakage test

4.2.2 Air leakage test with a flexible single-chamber

In this specific air leakage test, it is difficult to implement the ASTM E283 test procedure. The large-scale test specimen requires the pressurization chamber to be large enough. The hot box or cold box in the environmental chamber may be used as the pressurization chamber. However, to get accurate results, the extraneous air leakage through the chamber itself should be reasonably small compared to the air leakage rate through the test specimen. The pressure differential of 300 Pa is normally used to specify the air leakage performance for metal curtain walls. A simple estimation shows that the

air flows through the test specimen would be around 7.67 L/s over an area of $13m^2$ under 300 Pa, while either the hot box or the cold box is hundreds times leakier than this. Therefore, the test using hot box or cold box as rigid pressurization chamber would not give reasonably accurate results.

In this situation, a different pressurization/depressurization setup was developed, shown in Figure 4.2. A flexible air chamber was formed by attaching a layer of polyethylene film using duct tape to the surface of the aluminum mullion caps from the exterior side. The reason to build a flexible chamber instead of a rigid box is because of the large effort and expenses involved with the rigid box and its very small possibility to be reused. Therefore, a more economical alternative was chosen. The flexible chamber was formed on the exterior of the specimen because of the difficulty in installing such a chamber on the inside over the curtain wall anchors at bottom, middle and top three levels attached to the structural beams.

The use of flexible sheets in place of rigid panels entails certain considerations to the experimental setup. The pressure forces on the flexible chamber concentrate on all the contact areas and may be strong enough to loose or pull off the tape connecting the plastic to the perimeter of the specimen. Plastic sheets stretch and expand under tension forces created by the chamber pressure. As a consequence of the volume increase, the equilibrium takes much longer time to reach. A larger time constant requires a longer time to collect data with a greater chance of introducing more errors in the measurements. Based on these considerations, depressurization of the flexible chamber was chosen for

the air leakage test for two distinct advantages: 1) smaller volume between the flexible sheet and the specimen surface is created, and therefore, will significantly reduce the time required to reach pressure equilibrium and increase the speed of the data collection; 2) the arrangement reduces the tension required to retain the plastic sheet on the mullion cap surface without tearing or introducing air leakage, and thus, allows higher pressure differentials to be achieved.

To avoid the plastic sheet to make contact with the wall surface and to provide unhindered air paths to all potential air leakage locations on the surface, metal mesh (¼" by ¼") pans were placed in the recess formed by the exterior mullions. Small blocks of extruded polystyrene were spaced on the covered mullion caps as shown in Figure 4.2. To eliminate the air penetration through the polyethylene sheet, the thickness of polyethylene should be between 0.1 mm to 0.25 mm and of a virgin stock (Elmahdy, 1995). In this test, 10 mil (0.25 mm) polyethylene sheets were used.

As shown in Figure 4.2, the flexible chamber was depressurized by a blower fan. The flow rate was adjusted manually by a needle valve. The airflow rate was measured by a high-precision laminar flow element, which has a measuring range of 0~100 CFM (0~47.2 L/s), and an accuracy of ±0.0133 L/s. The pressure difference across the test specimen was monitored by two pressure taps installed on both sides of the specimen at the same elevation. The air temperatures at the same locations were recorded as well. The temperature sensors and pressure taps were installed at the bottom and top two levels to monitor the uniformity of temperature and pressure distribution.

duct tape

specimen frame

polythylene film

structural beam

metal-mesh pans

insulation block

depressurization
chamber

anchors

sealant

4 3 2 1

5
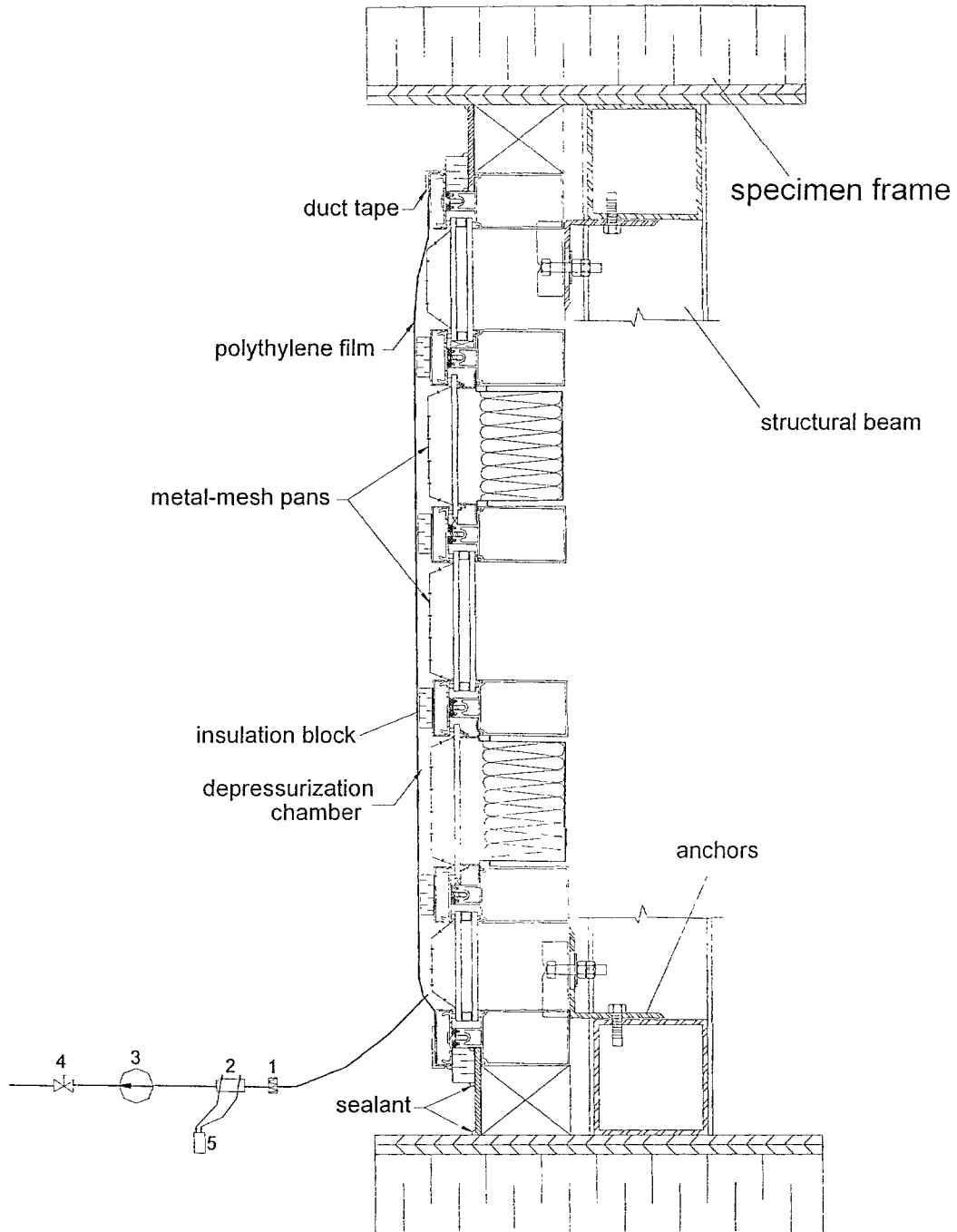
Note: 1-inline filter 2-laminar air flow meter 3-fan 4-needle valve 5-pressure meter

Figure 4.2 Test setup of single depressurization air-chamber (vertical section)

81

The pressure taps were connected to a 12-channel scanning valve unit. The pressure was read by a digital pressure meter with accuracy of ±1 Pa, which was calibrated to a precise pressure calibration setup with a precision of ±0.06 Pa. The barometric pressure, ambient temperature and relative humidity were recorded as well. These parameters were used to convert the directly measured airflow rate to the flow rate under standard conditions (21.1°C and 101.3 K Pa barometric pressure). A photo of the single flexible chamber test is shown in Figure 4.3.

Figure 4.3 Photo taken during a single chamber depressurization test

In accordance with the standard pressurization method, all of the air pushed into the chamber goes through the specimen if there is no extraneous air leakage through paths other than the test specimen; otherwise, the extraneous air leakage rate has to be

calibrated. There are two possible paths in the test setup, those due to the flexible chamber and those that exist on the specimen. The possible extraneous air leakage for the flexible chamber was through the seals between plastic sheet and the mullion surface. To eliminate the perimeter air paths, meticulous attention was taken to seal the polyethylene sheet to the mullion surface. The mullion surface was cleaned with alcohol for good adherence for the tape. Latex sealant was used at places where the bond between the tape and the plastic was thought not tight enough. For the specimen, the joints between the specimen and the structure of the chamber were carefully sealed by latex sealant as well (Figure 4.4). The only potential air leakage path was the joint section of these two wall systems, as shown in Figure 4.4. The pressure plates were fastened to the frame by screws, and the caps were snapped to the pressure plates. For system A, there is a layer of nylon as thermal breaks underneath the pressure plate, which works as gasket. Therefore, as long as the cap can be tightly snapped to the pressure plate, this side should be very airtight. For system B, the situation can be different because of the direct connection between pressure plate and the mullion nose without any gasket. To monitor the perimeter leakage at this joint section, a layer of tape was applied to enclose this small chamber. The pressure inside the small chamber was monitored during the depressurization tests. If the pressure differential is negligible, it can be confidently assumed that no air leaks through the caps. Otherwise, the leakage through the caps has to be considered. A flexible double-chamber setup has been developed to account for the possible perimeter leakage.
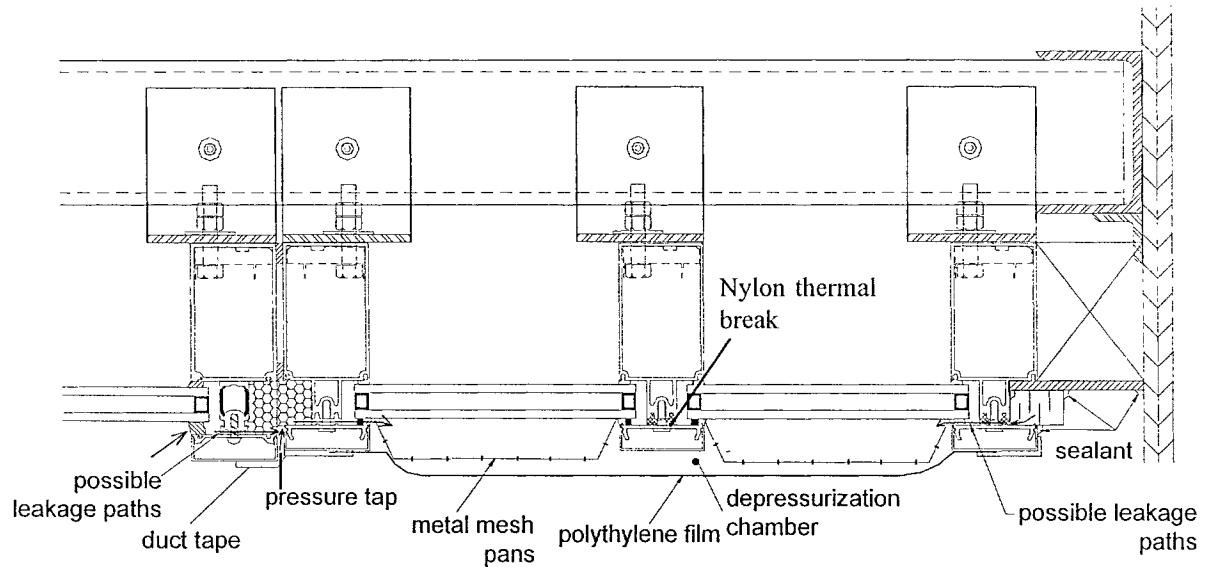
Figure 4.4 Details of the depressurization chamber (horizontal section, not to scale)

4.2.3 Air leakage test with a flexible double-chamber

Besides the calibration procedure prescribed by ASTM E283, another approach to eliminate the extraneous air leakage is to use additional chambers to enclose all the possible "outlet" of the unintended air leakage paths. This approach can be considered as a "guarded chambers method" (Figure 4.5a). During an air leakage test, the pressures in the "guarded" chambers are adjusted to the same level as in the main chamber, thus the pressure difference across all the unintended air leakage paths are neutralized. Therefore, no extraneous air leakage occurs. This method has been used in field measurements (Shaw, 1980; Reardon et al., 1987; and Shaw et al., 2000). The target section of walls was covered with a rigid chamber, and the adjacent rooms or air spaces were pressurized to the same pressure through additional blower fans to balance the pressure across the extraneous air leakage paths.

84

a) guarded chambers   b) flexible double chambers
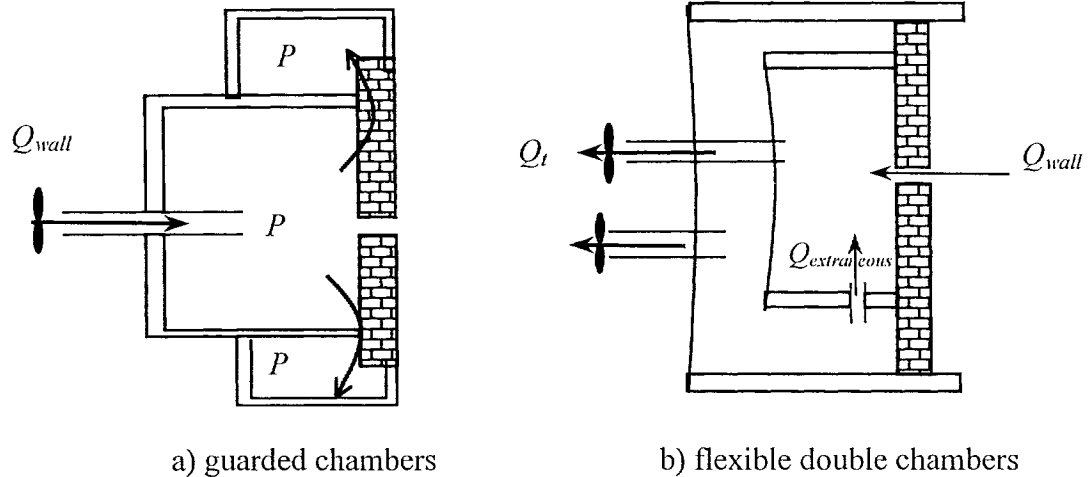
Figure 4.5 Schematic illustration of the double chamber setup

Considering the complexity and difficulty to setup several small balance chambers, a different test procedure called "double chamber method" was developed and shown in Figure 4.5b. An outer chamber was formed by taping a second layer of 10 mil (0.25mm) polyethylene sheet on the structural frame that houses the test specimen. This chamber covered the first inner chamber and enclosed the unintended leakage paths. Unlike the rigid chamber setup, the pressure difference across the flexible inner chamber cannot be zero. Due to the flexibility, any pressure change in one chamber will affect the pressure in the other. If the zero pressure difference was maintained, the inner polyethylene membrane would be in a free state. Any small pressure fluctuation can easily inflate or deflate the inner flexible chamber and change the air volume. Therefore, a sufficient pressure difference must always be maintained across the inner flexible chamber to maintain its constant volume. As a result, there will be a continuous air leakage between the two chambers across the extraneous leakage paths.

The detailed setup of double chamber depressurization test is shown in Figure 4.6. The outer chamber was depressurized by a second blower. The flow rate was regulated manually through a relieve valve on a T-connection, but was not measured. The airtightness was not very important either for this outer chamber. In addition to the instrumentation used in the single chamber tests, two additional pressure taps were installed in the space between the two flexible chambers at the same elevation levels as that installed inside the inner chamber to measure the pressure inside the outer chamber. Two ropes were also installed vertically from top to bottom of the structural frame to reduce the pressure load and tension on the outer membrane and to prevent the outer layer in contact with the inner membrane during depressurization tests.

4.2.4 Test procedure

The single chamber depressurization test was carried out first for each curtain wall system. The necessity of applying the double chamber method depends on if the presence of extraneous air leakage has been found in the test. As explained earlier, the vertical mullion caps at the junction of these two curtain wall systems is the main extraneous air leakage path (Figure 4.4). The pressure difference across the side of the vertical caps was monitored during the single chamber test. Depending on the magnitude of this pressure difference, the need of conducting a double-chamber depressurization was determined.
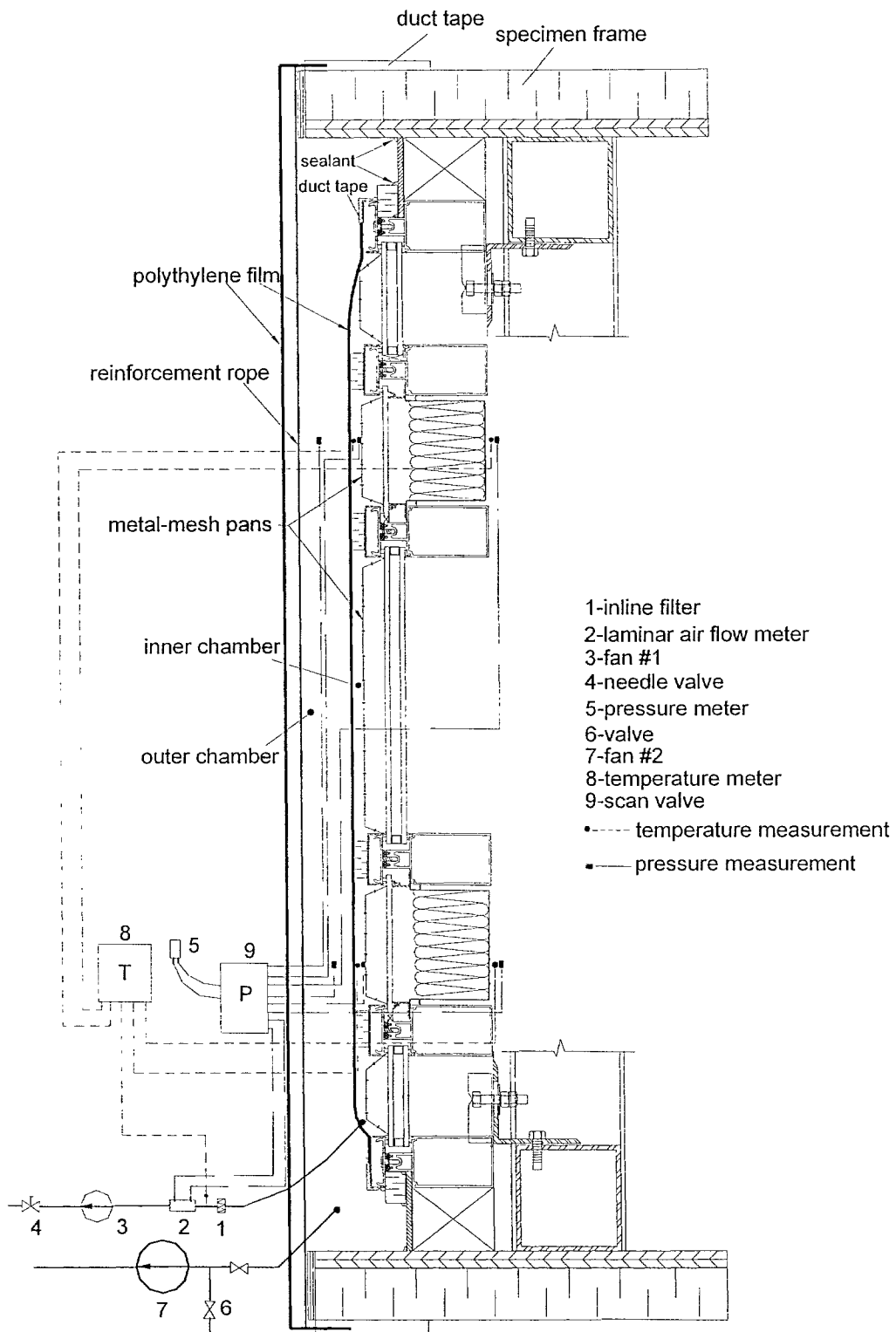
Figure 4.6 Setup of the double chamber depressurization air leakage test (vertical section, not to scale)

87

In accordance with standard ASTM E283, windows and other fenestration systems are normally tested under 75 Pa which corresponds to a wind speed at 6.7 m/s (25 mph). Curtain walls are normally required to be tested under 300 Pa due to their wide use in high-rise buildings. Therefore, the pressure difference across the test specimen was built up to as high as 400 Pa in the single chamber depressurization tests. In order to establish the air leakage characteristics of each curtain wall system, a series of pressure differentials were applied to the test specimen. They were 10, 20, 30, 40, 50, 75, 100, 150, 200, 250, 300 and 400 Pa. Since the airflow was regulated by adjusting the valves manually, the pressure differentials obtained had a tolerance of ± 5 Pa. To ensure the repeatability of the test results, the same test was repeated at least twice for each system. The pressure differential was increased from 10 Pa to 400 Pa for the first run and then was decreased from 400 to 10 Pa for the second run.

In the double chamber depressurization test, the pressure differences between the inner chamber and the outer chamber were maintained at values between 10 to 50 Pa. The pressure differences across the test specimen were maintained from 10 Pa to 300 Pa. The pressure inside the inner chamber was established first, and then the outer chamber. All of the readings were taken after the pressures in both chambers had stabilized. It normally took around 10 minutes for them to be stable.

4.3 Analyses of results

The power law equation is normally used to describe the air leakage characteristics for building envelope component, as expressed in equation 4.1:

$$Q = C\Delta P^n \qquad (4.1)$$

where,

Q = volumetric air flow rate, L/s;

C = flow coefficient, L/(s·Pa^n), depending on the geometry of the opening and the Reynolds number of the flow;

ΔP = pressure differential across the building envelope, Pa; and

n = exponent constant between 0.5 to 1.0 depending on the geometry of the opening.

The correlation between air leakage rate and pressure differential in the form of equation 4.1 can be established by a least square regression analysis on the measured data for single chamber tests. The predicted airflow rate can be converted to an equivalent leakage area (ELA) for the purpose of building envelope airtightness ratings in some cases. The ELA is calculated at a reference pressure of P_{ref} by the following equation in accordance with standard ASTM E779 (ASTM, 1999):

$$ELA = C \; P_{ref}^{\,n-\frac{1}{2}} \cdot \sqrt{\frac{\rho}{2}} \qquad (4.2)$$

Reference pressure P_{ref} includes 4, 10, 25, 50, and 75 Pa. The reference pressure of 4 and 10 Pa are normally used for residential buildings because they are closer to the pressure differences that actually induce air exchange. However, the predicted air leakage rate at 4 and 10 Pa by using the established correlation 4.1 are subject to significant uncertainty because they are outside the range of measured values (ASHRAE, 1997). In this thesis, the air leakage characteristics of curtain walls tests are represented by the power law equations and the air leakage rate at 300 Pa pressure difference.

4.3.1 Air leakage characteristics of system A

The pressure inside the small chamber enclosed by the sides of vertical caps of system A and B (Figure 4.4) was measured at maximum of 2 Pa when the depressurization pressure in the inner flexible chamber was 400 Pa, which indicated minimum air leakage throughout the perimeter. During the test, the perimeter tapes were checked frequently and a smoke pencil was used to identify possible leakage locations. No noticeable air leakage was observed. Therefore, it is safe to assume that no extraneous air leakage occurred through the perimeter of the single flexible chamber. The measured results using the single depressurization chamber were used to evaluate the air leakage characteristics of system A.

The air leakage rates measured under different pressure differentials were converted to that under standard conditions (21.1°C and 101.3 K Pa barometric pressure) and are listed in Table 4.1. The pressure differentials and temperatures measured at bottom and top two levels did not show a significant difference and were within ±0.5 Pa and ±0.5°C, respectively. The curves for air leakage rates vs. pressure differentials are plotted in Figure 4.7. The "upward run" means that the depressurization starts from 10 Pa and finishes at 400 Pa. The magnitudes of pressure differentials gradually decrease from high to low levels in the "downward run". The "upward run " curve matches very well with the "downward run" curve, which ensures the good repeatability of depressurization tests. A least square analysis was performed to obtain the power law equation. In reporting the air leakage test result, it is common to round the exponents to one or two decimals. The rearranged power law equation is shown in Table 4.2.

Table 4.1 Measured air leakage rates under different pressure differentials for system A using single flexible chamber setup[*]

Upward run		Downward run	
Pressure differential (Pa)	Air Flow Rate (L/s)	Pressure differential (Pa)	Air Flow Rate (L/s)
10.7	0.2388	400.0	2.6823
19.9	0.3603	304.5	2.2623
28.3	0.4615	250.4	1.9802
39.6	0.5758	199.5	1.7067
48.4	0.6601	149.6	1.4174
73.8	0.8875	102.8	1.1098
97.8	1.0769	74.4	0.8941
145.9	1.4096	47.8	0.6601
194.6	1.7015	40.0	0.5575
241.9	1.9670	31.0	0.4707
301.8	2.2221	21.1	0.3624
400.0	2.6823	11.6	0.2375

[*]All of the pressure is relative to the ambient pressure, and the negative sign is omitted for simplicity purpose.
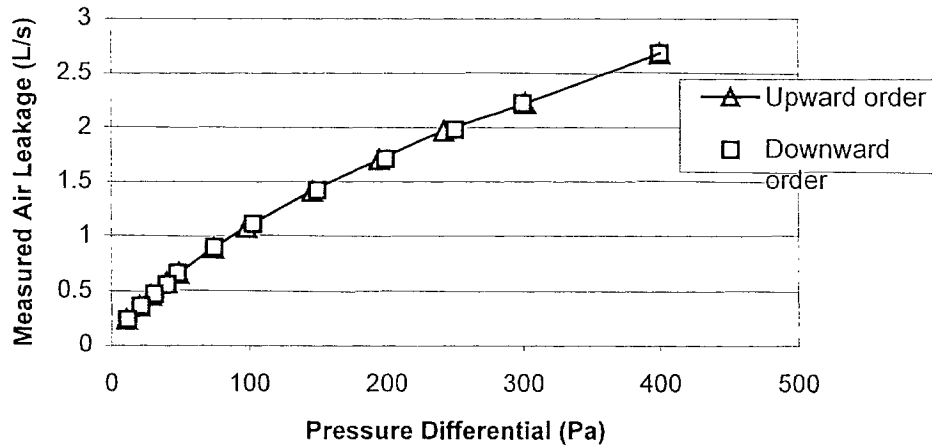
Figure 4.7 Data plot for single-chamber depressurization air leakage test on system A

Table 4.2 Air leakage characteristic and air leakage rate measured for system A

Leakage Characteristics	Air leakage rate (L/s) @300 Pa	Specimen area (m^2)	Air leakage rate @300Pa ($L/s \cdot m^2$)	Manufacturer's specification @300 Pa ($L/s \cdot m^2$)
$Q=0.04904(\Delta P)^{0.87}$	2.2492	12.78	0.176	0.3

91

4.3.2 Air leakage characteristics of system B

The single air chamber test was conducted for system B following the same test procedure as that for system A. The test results are listed in Table 4.3. The measured data show that the pressure inside the small chamber enclosed by the side of the vertical mullion caps varies proportionally with the pressure difference across the single chamber. The pressure inside the small chamber reached as high as 80 Pa when the pressure difference across the flexible chamber was 300 Pa, which indicates a certain amount of air leaks through the perimeter at the junction. The same checking procedure was repeated three times and the results were very close, which eliminates the possibility of significant erroneous readings. The relation curve between air leakage rate and pressure differential for system B is plotted in Figure 4.8.

Table 4.3 Measured air leakage rates under different pressure differentials for system B using single flexible chamber setup*

Pressure in single chamber (Pa)	Flow Rate (L/s)	Pressure in joint chamber (Pa)
10.6	0.6417	2.7
19.9	1.0230	4.8
30.4	1.3859	7.3
40.6	1.7041	9.8
50.5	1.9881	12.3
74.7	2.6087	18.7
99.1	3.1609	24.5
149.2	4.1787	37.5
200.8	5.1148	51.5
250.3	5.9267	65.4
299.2	6.6910	78.9

*All of the pressure is relative to the ambient pressure, and the negative sign is omitted for simplicity purpose.

$$Q = 0.1269P^{0.6979}$$
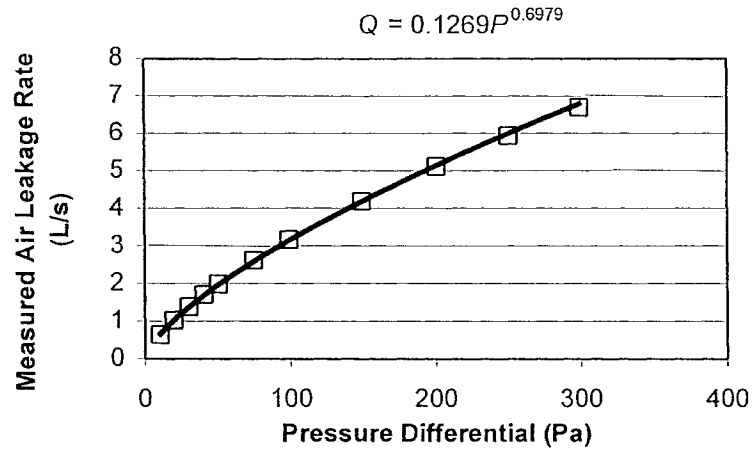
Figure 4.8 Data plot for single-chamber depressurization air leakage test on system B

To eliminate the extraneous air leakage, a double chamber test procedure was applied to system B. As explained earlier in section 4.2.3, a sufficient pressure difference must always be maintained across the inner flexible chamber. The magnitudes of pressures in the outer chamber were maintained always lower than those in the inner chamber and the pressure differentials across the inner chamber membrane were maintained between 10 to 50 Pa. Pressures and flow rates of the inner chamber as well as the pressures in the outer chamber were measured, as listed in Table 4.4. Both inner chamber and outer chamber were depressurized, so the pressures listed in Table 4.4 are all negative. For simplicity purpose, the negative signs are omitted. The pressures listed in Table 4.4 are the average of the two values at two levels of heights.

93

Table 4.4 Measured data in double chamber setup for system B*

Inner chamber pressure P_i (Pa)	Outer chamber pressure P_o (Pa)	Pres. diff. across inner chamber P_e (Pa)	Flow rate from inner chamber Q_t (L/s)
230.8	221.4	9.4	2.9742
93.0	76.7	16.3	1.9223
207.8	187.2	20.7	3.0110
89.9	68.6	21.3	1.9277
79.8	52.5	27.3	1.9382
187.3	156.5	30.9	3.0373
71.0	38.8	32.2	1.9565
60.0	20.7	39.3	1.9643
163.2	118.8	44.4	3.0637
148.5	94.9	53.6	3.0742

*Negative signs in P, P_2, and Q_t are omitted.

Due to the presence of pressure differences across the inner air chamber in double-chamber tests, the measured air flow rate from the inner chamber is actually composed of air leakage through both the tested specimen and the extraneous air leakage paths. Therefore, the extraneous air leakage characteristics are estimated together with the wall leakage parameters simultaneously. The estimated total flow rates out of the inner chamber, $\hat{Q}_t$, can be expressed as a summation of the predicted specimen leakage and extraneous air leakage in the following equation:

$$\hat{Q}_t = C_i \cdot P_i^{n_i} + C_e \cdot P_e^{n_e} \tag{4.3}$$

where,

P_i = pressure in the inner chamber, Pa;

P_o = pressure in the outer chamber, Pa;

$P_e = P_o - P_i$, pressure difference across the inner chamber, Pa;

C_i = flow coefficient for the test wall specimen;

n_i = exponent constant for the test wall specimen;

C_e = flow coefficient for the perimeter of the inner chamber;

n_e = exponent constant for the perimeter of the inner chamber.

The unknown parameters in the above equations are the coefficients and exponents of the power law relations for both specimen and the perimeter leakage. A least square regression analysis was performed to estimate test parameters. In the regression analysis, the sum of the squared discrepancies between the measured total flow rate (Q_t) and the estimated value ($\hat{Q}_t$) was calculated as a function of the four unknown parameters, via:

$$S(C_i, n_i, C_e, n_e) = \Sigma\left(Q_t - \hat{Q}_t\right)^2 = \Sigma\left[Q_t - \left(C_i P_i^{n_i} + C_e P_e^{n_e}\right)\right]^2 \qquad (4.4)$$

The estimated parameters are obtained by minimizing this S() function. The data used for the least square regression analysis include the data from the depressurization test on the double chamber setup and those from the single chamber test. The pressures of the second chamber are considered to be zero for the single chamber data. The combined new set of measured data is shown in Table 4.5.

The estimated result is:

$$\hat{Q}_t = 0.07466 \cdot P_i^{0.6597} + 0.04543 \cdot P_e^{0.7890} \qquad (4.5)$$

To round the exponents to two decimals, the flow coefficients were re-estimated and equation 4.5 becomes:

$$\hat{Q}_t = 0.07902 \cdot P_i^{0.65} + 0.04268 \cdot P_e^{0.80} \qquad (4.6)$$

95

The leakage characteristic for the curtain wall system B is the first term on the right side of the above equation, i.e.:

$$Q_w = 0.07902 \cdot P_i^{0.65} \; (\text{L/s}) \tag{4.7}$$

The comparison between the measured and the predicted air leakage for the test specimen and the extraneous air leakage is shown in Figure 4.9. The air leakage characteristic and air leakage rate measured for system B under 300 Pa are given in Table 4.6.

Table 4.5 Data used for regression analysis

	Inner chamber pressure P_i (Pa)	Outer chamber pressure P_o (Pa)	Pres. diff. across inner chamber P_e (Pa)	Flow rate from inner chamber Q_t (L/s)
1	230.8	221.4	9.4	2.975
2	10.6	0.0	10.6	0.642
3	93.0	76.7	16.3	1.922
4	19.9	0.0	19.9	1.023
5	207.8	187.2	20.6	3.012
6	89.9	68.6	21.3	1.928
7	79.8	52.5	27.3	1.938
8	30.4	0.0	30.4	1.387
9	187.3	156.5	30.8	3.037
10	71.0	38.8	32.2	1.957
11	60.0	20.7	39.3	1.965
12	40.6	0.0	40.6	1.703
13	163.2	118.8	44.4	3.063
14	50.5	0.0	50.5	1.988
15	148.5	94.9	53.6	3.075

Table 4.6 Air leakage characteristic and air leakage rate measured for system B

Leakage characteristics	Air leakage rate (L/s) @300 Pa	Specimen area (m^2)	Air leakage rate @300Pa (L/s·m^2)	Manufacturer's specification @300 Pa (L/s·m^2)
$Q=0.07902(\Delta P)^{0.65}$	3.2201	12.78	0.252	N/A

measured, specimen $\bullet$	$Q_t - C_e \cdot P_e^{n_e}$	——	estimated, specimen	$C_i \cdot P_i^{n_i}$
measured, EAL $\blacksquare$	$Q_t - C_i \cdot P_i^{n_i}$	— — —	estimated, EAL	$C_e \cdot P_e^{n_e}$
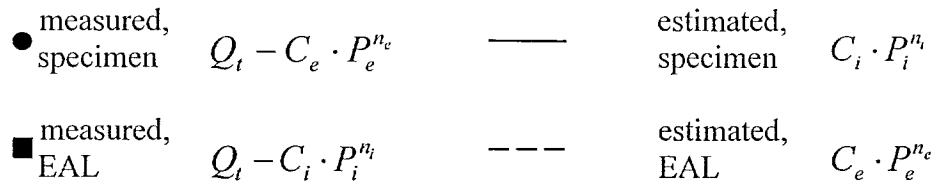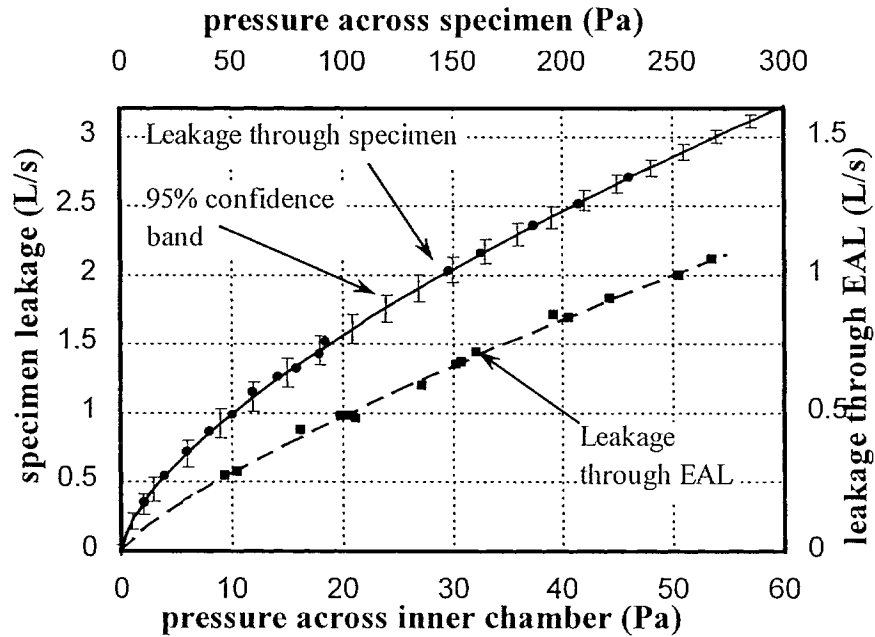
Figure 4.9 Measured vs. estimated leakage rates for specimen system B and extraneous air leakage (EAL denotes extraneous air leakage)

4.4 Conclusion

The air leakage characteristics of the two full-scale curtain wall systems were measured separately. A different test procedure and data processing method from the standard ASTM E283 were developed to overcome the difficulties in using the standard fan

97

pressurization method. A flexible single chamber test was carried out on system A since it had a negligible perimeter leakage. The air leakage rate measured under 300 Pa is 0.176 L/ s·m², which is smaller than the manufacturer's specification of 0.3 L/s·m².

Double chamber tests were required on system B due to the relatively high extraneous air leakage through the perimeter of the inner flexible chamber. A least square analysis was performed to estimate the air leakage characteristics for the test specimen together with the perimeter leakage simultaneously. The results show that system B has an air leakage rate of 0.252 L/s·m² at 300 Pa and is leakier than system A. This is due to the different spandrel back-pan designs. As shown in Figure 3.4 (b) in chapter 3, the return of the steel back-pan is shifted to the interior to reduce its thermal bridge effect. The continuity of the air barrier relies on the bead of sealant.

The use of a more economical flexible chamber setup instead of rigid chamber has been proved to be successful in measuring large-scale curtain wall specimen. The test procedure and data processing method developed for flexible double chamber measurements offer a realistic alternative when the ASTM standard method cannot be employed. This could be applied in principle to other situations where the standard ASTM calibration procedure cannot be implemented.

Chapter 5

Thermal performance tests

5.1 Introduction

The complexity in the configurations of metal curtain walls makes it necessary to treat curtain walls as integrated systems instead of separate sections. A large-scale metal curtain wall specimen including two different systems were installed in an environmental chamber and were subjected to different steady-state and cyclic test conditions including the introduced air infiltration. The approach of measuring extensive temperatures was chosen over measuring an average U-value. The advantages of detailed temperature measurements include: 1) the effect of design details on thermal performance of curtain walls can be revealed directly by temperature comparison; 2) condensation resistance can be calculated directly; 3) recorded temperatures can be used to analyze other performance such as thermal comfort analysis and determination of film coefficients; 4) extensive temperature measurements can also be used to validate current and future simulation programs; 5) detailed temperatures can provide insight information on understanding the heat transfer mechanism in curtain walls.

Two techniques were used to measure the temperatures. One is the thermocouple measurement. Thermocouples were installed throughout the test specimen and provided three-dimensional temperature profiles. The other is the infrared thermography

measurement. It offers the advantages of rapid visualization and large contiguous sets of surface temperatures. However, it can only map visually accessible surface temperatures and has a lower accuracy, typically of $\pm 1^{\circ}C$ to $\pm 2^{\circ}C$. These two techniques can supplement each other. The detailed test procedure and results are presented in this chapter.

5.2 Experimental setup and procedure

The test setup is shown in Figure 3.2. The parameters monitored include temperature, relative humidity, and air velocity. Temperature is the main parameter. This section focuses on the temperature monitoring by thermocouples. The tests conducted by the infrared camera are discussed in section 5.4.

5.2.1 Instrumentation

A total of 704 type-T (copper-constantan) thermocouples were installed throughout the test specimen, on the baffle surface, on the interior surfaces of hot box and cold box, and for the indoor and outdoor air temperatures. The thermocouple wires employed are premiere grade 30-gauges (NBS special limits of error). The installation of the sensors was concentrated in the region between the two horizontal beams (Figure 3.3), which represents one standard floor and is the main part of this study. For comparison purpose, the locations of the thermocouples installed on system A were symmetrical to the locations of the thermocouples installed on system B. For each system, thermocouples were symmetrically installed on the upper part and the lower part to record the impact of the stratification in hot box as a result of the temperature differences across the specimen.

100

For mullion surfaces, thermocouples were installed symmetrically on the jamb mullion surface and regular middle mullion surface (Figure 3.3) to monitor the effect of different boundary conditions.

- **Sensors on frames**

Thermocouples were installed on the aluminum mullion surfaces, inside aluminum channels, and across the mullion section. Figures 5.1 and 5.2 show the typical sensor locations across the horizontal and vertical mullion tubes. Simulation results from FRAME and the existing study conducted by Han et al. (1992) were consulted to determine the locations of the thermocouples across the mullion section. Natural convection exists within the air cavity formed by the mullion nose and the pressure plate due to the temperature gradient. Temperatures on the warm side surface, on the cold side surface and in the air cavity were also monitored to evaluate the contribution of natural convection. Several thermocouples were located inside the vertical mullion channels as well to monitor the stack effect inside the tube.

(a) system A   (b) system B
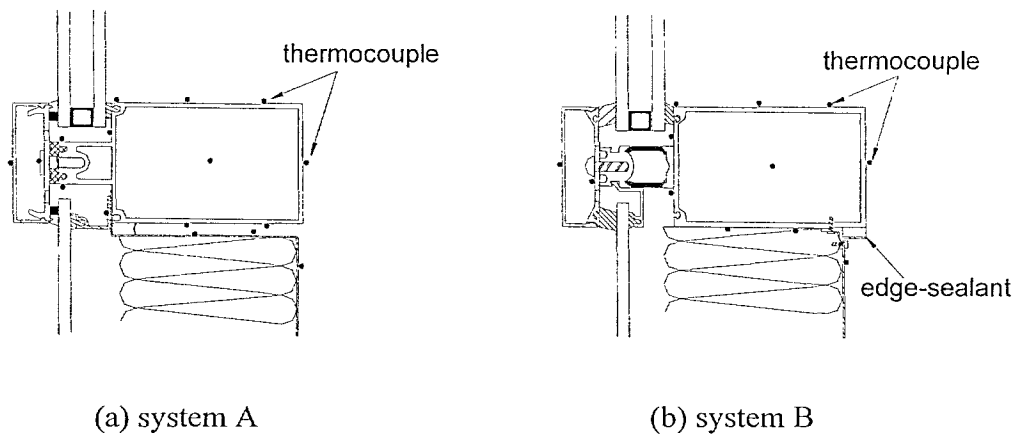
Figure 5.1 Sensor locations on a horizontal mullion section and edge-of-spandrel

system A   system B
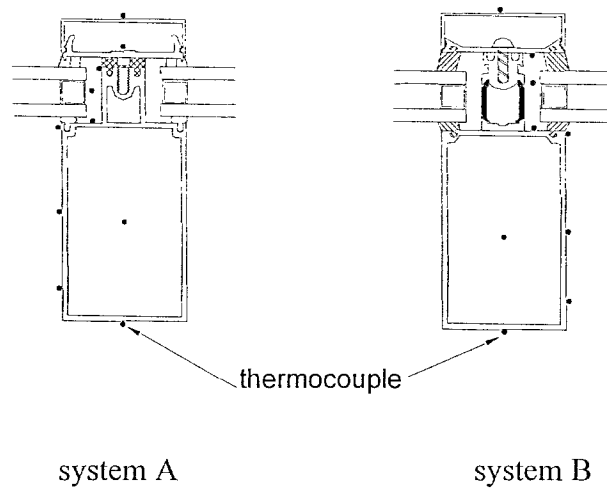
Figure 5.2 Sensor locations on a vertical mullion section

- **Sensors on spandrel panels**

Three layers of thermocouples were installed across the spandrel panel. The first layer was on the interior surface of the steel back-pan, the second layer was on the exterior surface of the 101.4mm (4") rigid fiberglass insulation, and the third layer was on exterior surface of the spandrel glass. The sensor locations were the same for the three surfaces. A few sensors were installed at the return of the steel back-pan of system A as shown in Figure 5.1a to monitor its thermal bridge effect

- **Sensors on glazing panels**

Thermocouples were installed on both the exterior and the interior surfaces of the glazing panels. In addition to meeting the requirement of AAMA standard (1998), additional sensors were added at the edge-of-glass region as shown in Figure 5.3 to monitor the condensation potential.

Figure 5.3. Sensor locations on a glazing surface

- **Sensors for monitoring test conditions**

The inside and outside air temperatures close to the test specimen were measured by thermocouples located 75mm (3") away from the wall surface. Six thermocouples were distributed evenly across the specimen height between the two horizontal beams on each side of the wall to record the indoor and outdoor air temperatures for each wall system. In addition, the temperatures on the baffle surface in the cold box and on the interior wall surfaces of the cold and hot boxes were measured.

Installation details for thermocouple junctions depend on the target medium and were designed to measure accurately and to cause minimum interference to the local heat exchange conditions. For air temperature measurements, each thermocouple junction was shielded from radiation heat exchange with the surrounding by a ϕ12.7mm ($\frac{1}{2}$") by 50mm (2") long tube made of aluminum tape. For metal surfaces, each thermocouple

103

junction was attached using a square piece of aluminum tape. Heat sink compound, a piece of mica and a piece of clear tape were used underneath each aluminum tape to avoid electrical contact to the metal surfaces. For non-metal surfaces, each thermocouple was attached using construction tape with a drop of heat sink compound to provide a high-quality thermal contact. The 50mm (2″) to 75mm (3″) length of the leading wire from junctions were taped on the surfaces for all surface thermocouples.

The extensive use of thermocouples provides three-dimensional temperature monitoring on the main components of the curtain wall. Due to the limited amount of DAQ channels (400 channels) at the time this test was carried out, the sensors were divided into two groups, each group for one wall system. These two groups were alternatively connected to the DAQ system and data was collected in turn after the steady-state condition was reached. To verify and ensure identical test conditions for both systems during measurement, three indoor air temperatures for system A, three indoor air temperatures for system B and the four hot box interior surface temperatures were monitored continuously. The temperature readings from DAQ channels were calibrated by an isothermal bath system.

Relative humidity (RH) sensors were installed in the spandrel glass cavities, the indoor air space close to the edge-of-glass and the indoor air space close to the wall surface. The air movement measurement inside the hot box and the air velocity measurement inside the cold box were conducted in different tests and will be described in Chapter 6.

5.2.2 Test procedure

The thermal performance tests used several different test conditions including different steady-state winter conditions, cyclic winter conditions, and steady-state CSA winter condition with introduced air infiltration, as listed in Table 5.1. The adoption of the worst condition of -32°C is to study the condensation potential of these two different curtain wall assemblies. The cyclic test evaluates the thermal response of metal curtain walls when subjected to the periodic variation of the outside temperature. The test with added air infiltration is to evaluate the effect of air leakage on indoor surface temperatures and on the condensation resistance factor. The indoor temperature was maintained at 21°C for all tests. The relative humidity in the hot box was maintained below 25% during all the tests.

Each of the tests listed in Table 5.1 except for the test with introduced air infiltration consists of three stages: start-up to reach steady state, maintain steady state, and data collection. It took 6 to 8 hours for the test specimen to start up and reach steady state. The test specimen was maintained in the steady state for 12 consecutive hours before taking measurements. In the data collection stage, measurements were taken over a period of 12 hours or more. The variations in the temperatures measured during this stage were within ± 0.1°C for the steady-state tests.

A 150 Pa pressure differential was introduced across the test specimen by depressurizing the hot box when the CSA winter condition had been maintained for 12 hours. The depressurization lasted for 4 hours. The temperatures were monitored before, during and after the depressurization until temperatures returned to the initial values stabilized before

the depressurization. The adoption of 150Pa is based on the field test by Ganguli (1988), which found that the pressure differential induced by the stack effect and mechanical systems could be as high as 150 Pa at the 24th floor under a 40°C temperature differential. Infrared thermography was used to monitor the effect of air leakage as well and the test procedure and results are presented in Section 5.4.

Table 5.1 Test conditions

#	Tests	Hot box conditions	Cold box conditions T_o	Remarks
1	Steady-state tests	21°C	-5 °C	
2			-10°C	
3			-18°C	CSA winter condition
4			-24°C	Montreal design condition (99%)
5			-32°C	Worst condition—annual extreme daily mean minimum temperature
6	Cyclic test	21°C	-12-6sin(t/12π) (°C)	Sinusoidal profile based on weather files from the Montreal weather station
7	Impact of air infiltration	21°C, -150Pa	-18°C	150 Pa across the test specimen, induced air infiltration

5.3 Test results and analyses

The results presented in this section include three parts: surface temperature distributions on glazing panel and mullion section under steady-state and cyclic winter conditions, measured condensation resistance factors following the AAMA procedure, and effect of air leakage on temperature distributions and on condensation resistance factors.

5.3.1 Temperature profiles on glazing surfaces

The detailed measurement on glazing surfaces, especially at the edge-of-glass, allows for the generation of highly illustrative temperature contours. In Figure 5.4, the two-dimensional temperature contours on the interior surface of glazing panel G_{a1} and G_{b1} are

106

presented. These contours were generated based on the measured data under CSA winter

conditions -18°C outdoor and 21°C indoor.

(a) Glazing panel G_{al} (b) Glazing panel G_{bl}
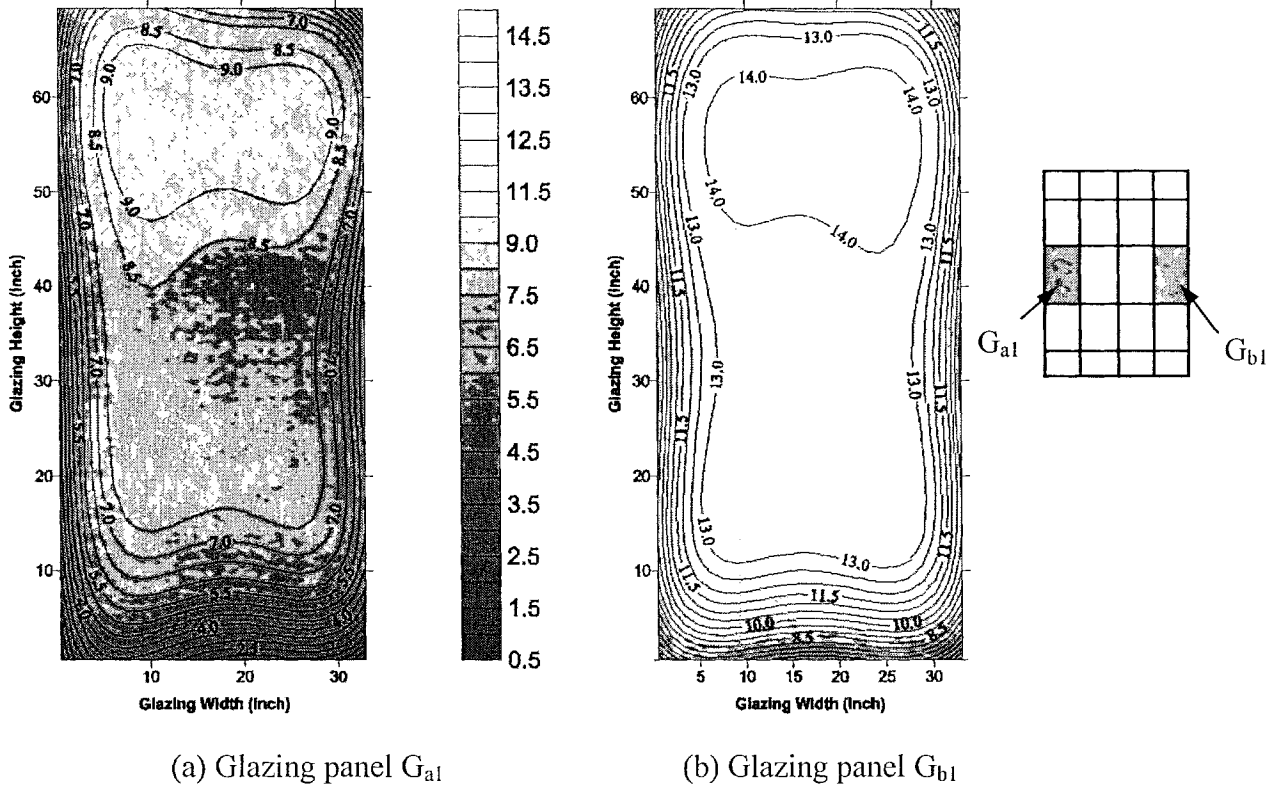
Figure 5.4 Two-dimensional temperature contours on interior surfaces of glazing panels
under test condition: -18°C outdoor and 21°C indoor

These contours can show the general distribution pattern of surface temperatures.

Examinations of the contours provide findings similar to existing studies (Wright, et al.,

1998; Elmahdy, et al., 1996; Griffith, et al., 1996). The lighter color for the high

performance glazing panel in system B shows much warmer surface temperatures. Both

surfaces are warmer at the upper parts and colder at the lower parts due to the convection

within the glazing cavity. The temperatures at the corners of the edge-of-glass regions

are lower than those at the centerlines. The lower parts, especially the lower corners of the glazing units, are, therefore, most susceptible to condensation.

To provide direct performance comparison between the two types of glazing panels, Figure 5.5 shows the interior surface temperature profiles for glazing panels G_{a1} and G_{b1} under CSA winter conditions along the vertical centerlines. The height of the glazing panel is 1.778m (70"), y=0 is at the bottom sight-line and y=70 is the top sight-line of the glazing panel. The temperature differences on the glazing surfaces between these two systems are also shown in Figure 5.5 by dashed lines. Figure 5.5 indicates that the high-performance glazing unit has much warmer surface temperature on the interior and much colder surface temperature on the exterior, thus much larger temperature difference across the glazing panel. The temperature comparison between the two types of glazing units shows that the temperature difference is smaller at edge-of-glass region, and larger in the center-of-glass region. It also indicates that the difference is greater on the interior surface than that on the exterior surface. At the center-of-glass region, the high-performance glazing panel has an average of $5.5^{\circ}C$ higher temperature on the interior and an average of $4^{\circ}C$ lower temperature on the exterior than the standard glazing panel does.
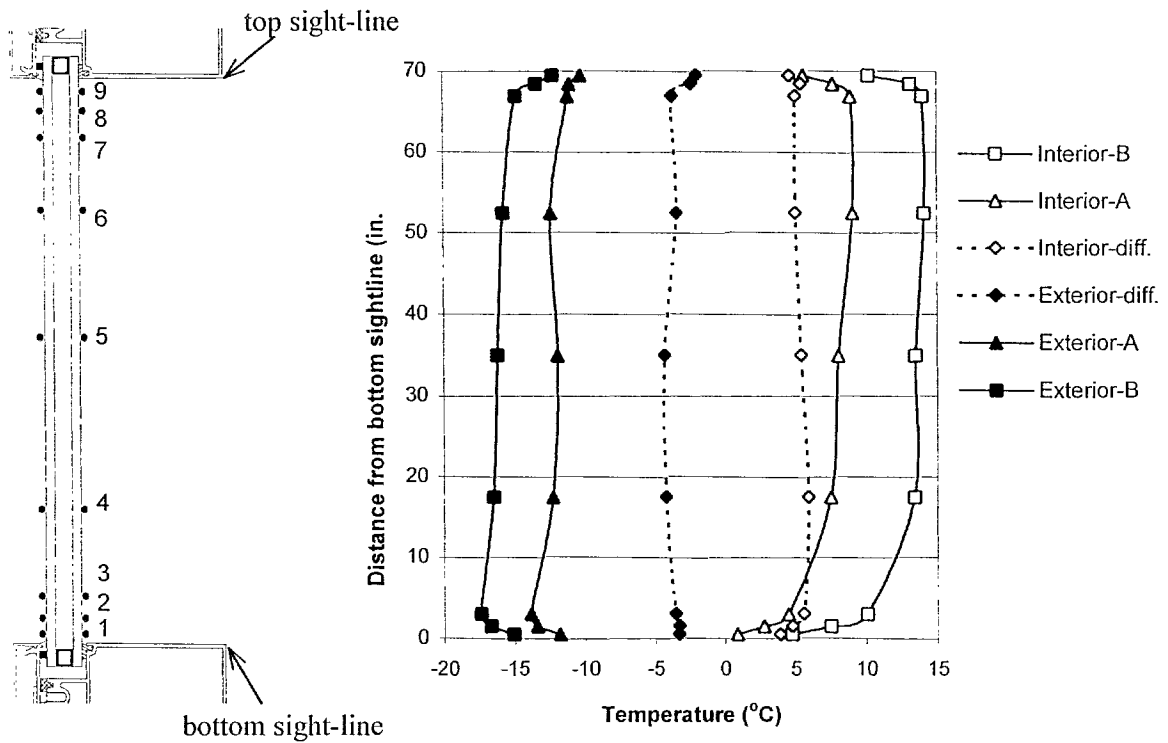
Figure 5.5 Vertical surface temperature profiles on the glazing panels under CSA winter condition: -18°C (outside) and 21°C (inside)

The average temperatures on the interior surface of glazing panels under various outdoor conditions are plotted in Figure 5.6. Each data point is the area-weighted average of all the measurements on glazing surface. A linear relationship is obtained between the surface temperature and the outdoor air temperature. The slope for glazing panel in system B is 0.22 and is 0.32 for glazing panel in system A. These values indicate that under the same outdoor temperature variation, the change in the average surface temperatures is less in system B, which implies that a higher thermal resistance is provided by high performance glazing units. The difference gets larger with the outdoor temperature getting colder, as shown in Figure 5.6.

$T_{(average, A)} = 0.318T_{(outdoor)} + 14.1$ $T_{(average, B)} = 0.219T_{(outdoor)} + 17.5$
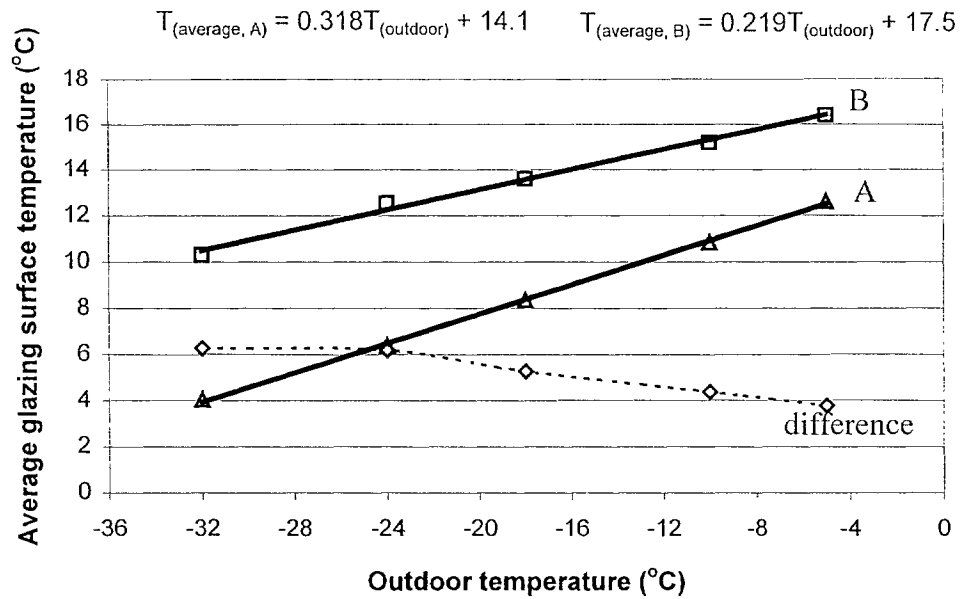
Figure 5.6 Average glazing surface temperatures in relation to outdoor air temperatures

To facilitate the comparisons under different test conditions, the glazing surface temperatures were normalized based on a scale that the outdoor temperature is 0.0 and the indoor temperature is 1.0. The normalized interior surface temperatures along the vertical centerline of glazing panel G_{a1} and G_{b1} are listed in Table 5.2 and Table 5.3.

Table 5.2 Normalized temperature readings along the interior surface of glazing panel G_{a1} under different test conditions

Conditions		Distance from the bottom sight-line								
		½″	1½ ″	3″	¼ height	½ height	¾ height	67″	68½ ″	69½ ″
$T_{outdoor}$	T_{indoor}	G_{a1}-1	G_{a1}-2	G_{a1}-3	G_{a1}-4	G_{a1}-5	G_{a1}-6	G_{a1}-7	G_{a1}-8	G_{a1}-9
-10°C		0.462	0.508	0.541	0.607	0.627	0.654	0.631	0.609	0.531
-18°C	21°C	0.466	0.512	0.549	0.622	0.637	0.663	0.653	0.630	0.566
-24°C		0.463	0.507	0.547	0.626	0.641	0.667	0.661	0.639	0.577
-32°C		0.473	0.515	0.556	0.637	0.650	0.675	0.670	0.648	0.585
Mean		0.466	0.511	0.548	0.623	0.639	0.665	0.654	0.632	0.565
Standard deviation		0.004	0.003	0.005	0.011	0.008	0.008	0.014	0.014	0.021
Coefficient of variance (%)		0.92	0.63	0.98	1.73	1.29	1.14	2.21	2.29	3.65

Notes: The coefficients of variance is: standard deviation / mean

110

Table 5.3 Normalized temperature readings along the interior surface of glazing panel G_{bl} under different test conditions

Conditions		Distance from the bottom sight-line								
		½″	1½″	3″	¼ height	½ height	¾ height	67″	68½″	69½″
$T_{outside}$	T_{inside}	G_{bl}-1	G_{bl}-2	G_{bl}-3	G_{bl}-4	G_{bl}-5	G_{bl}-6	G_{bl}-7	G_{bl}-8	G_{bl}-9
-10°C		0.548	0.618	0.676	0.755	0.760	0.777	0.762	0.741	0.646
-18°C	21°C	0.552	0.617	0.677	0.761	0.765	0.783	0.771	0.753	0.680
-24°C		0.557	0.620	0.681	0.766	0.773	0.790	0.780	0.764	0.692
-32°C		0.554	0.613	0.673	0.757	0.764	0.782	0.774	0.760	0.692
Mean		0.553	0.617	0.677	0.760	0.766	0.783	0.772	0.755	0.678
Standard deviation		0.003	0.003	0.003	0.004	0.005	0.005	0.006	0.009	0.019
Coefficient of variance (%)		0.59	0.41	0.42	0.55	0.62	0.59	0.84	1.16	2.78

Notes: The coefficients of variance is: standard deviation / mean

As shown in the tables, the normalized temperatures do vary but not significantly from one weather condition to another. The reason for the variation is probably because the surface film coefficients and the heat transfer coefficients in the glazing cavity change with the change of outdoor temperatures in addition to the measurement error. The coefficient of variance is less than 4% in system A and less than 3% in system B. Although it is small, the coefficient of variance does indicate that the variation is greater in system A than that in system B for all the points measured. This trend again indicates higher thermal resistance is provided by high-performance glazing panels, and surface temperature is less sensitive to the test conditions.

The normalized temperatures under the four test conditions are averaged for both the interior and exterior surfaces and are plotted in Figure 5.7. These profiles show the similar general pattern as observed from the 2-dimensional contours shown in Figure 5.4. This pattern depicts warmer temperatures at the upper part of the glazing and colder at the lower part, with significantly temperature variations at the edge-of-glass region and nearly uniform temperatures at the center-of-glass. The surface temperatures under other

111

non-tested conditions can be approximated using the normalized temperature index in order to predict the condensation potential for glazing units.
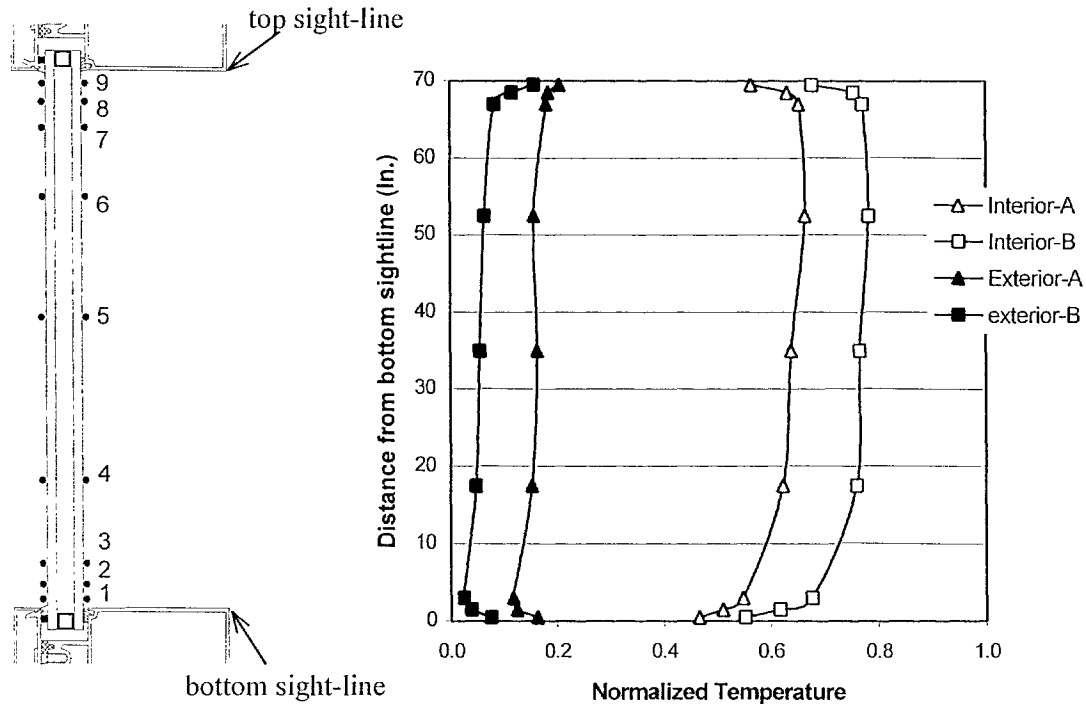
Figure 5.7 Normalized temperature profiles along the vertical centerline of glazing panel G_{a1} and G_{b1}.

5.3.2 Temperature distribution through mullion sections

The mullion sections presented here include three types: (i) the glazing meeting section that joins two glazing panels horizontally (ii) the spandrel meeting section that supports two spandrel panels horizontally and (iii) the sill section that joins a glazing panel and a spandrel panel vertically. The aluminum mullion tube works as a fin and temperature gradient exists along the surface. The exact gradients and surface temperature distributions vary with the types of the mullion sections and the design details of the mullions. In addition to the fin effect, the variation of local film coefficient is another important factor contributing to the temperature gradient along mullion surfaces. This is

112

demonstrated in both asymmetric temperature distributions on the mullion surface at the sill section and the differences among mullion temperatures at front surfaces of three different mullion sections. However, due to the differences in design details between the two systems, the extent of the differences varies. Figures 5.8 to 5.10 show the temperature distributions measured across these three types of mullion sections for both the standard wall system A and the improved wall system B, under -18°C outdoor and 21°C indoor test conditions.

In the standard wall system A, due to the lack of a sufficient thermal break, higher heat flow transfers through the mullion section and results in higher temperature gradient along the interior mullion surface compared to the improved wall system B (Figure 5.8a and Figure 5.8b). Meanwhile, the effect of local film coefficients is more prominent on the temperature distributions. For example, at sill section of system A, there is a distinct temperature difference between the upper and lower horizontal mullion surfaces, as shown in Figure 5.8a. At the lower horizontal mullion surface, the local film coefficient is lower due to the fact that the surface is exposed to the return of the back-pan which has much lower surface temperature than the indoor air and due to the fact that the air movement around this surface is restricted. This difference in film coefficients leads to a lower surface temperature of around 0.5°C at the lower surface. The effect of local film coefficients on mullion surface temperature is also illustrated by the temperature differences between different mullion sections. For three types of mullion sections, the glazing meeting section, the sill section, and the spandrel meeting section, the surface temperatures are different and depend on the numbers of surfaces facing the indoor air

and the return of the back-pans. The front surface temperatures, for example, were measured at 8.0°C, 5.5°C, and 4.4°C for glazing, sill and spandrel sections, respectively, as shown in Figure 5.9a, Figure 5.8a, and Figure 5.10a. The glazing mullion surface has a higher temperature of 3.6°C than the spandrel mullion surface due to the fact that all three surfaces of the glazing mullion are exposed to indoor air, while in the spandrel meeting section, only the front surface is exposed to the indoor air and the other two side surfaces are exposed to the return of the back-pan. The sill mullion surface has a temperature falling in between because its upper horizontal surface is exposed to the indoor air while its lower horizontal surface is exposed to the return of the back-pan.
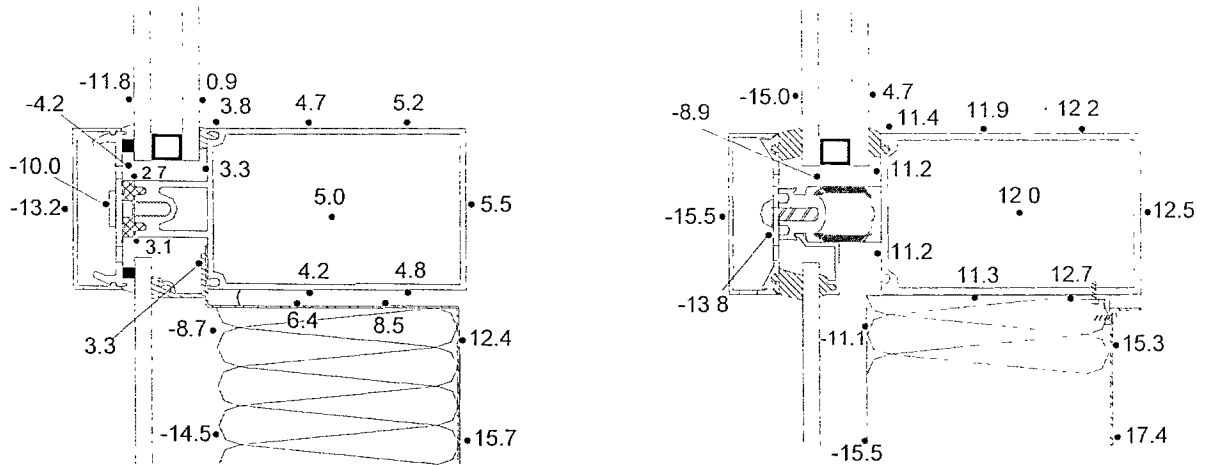
(a)Section 1: vision sill in system A   (b) section 2: vision sill in system B

Figure 5.8 Temperature distributions across sill sections under test condition: −18°C
outside and 21°C inside
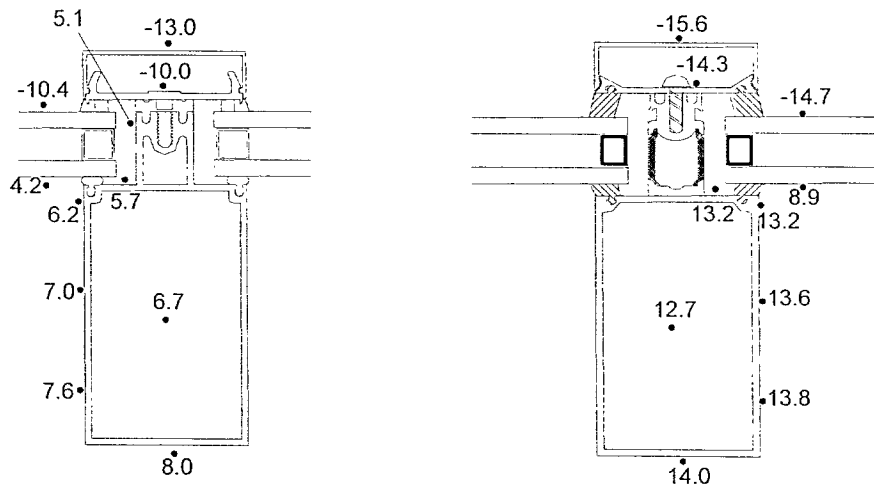
(a)Section 3: glazing mullion in system A   (b) section 4: glazing mullion in system B

Figure 5.9 Temperature distributions across glazing mullion sections under test condition: −18°C outside and 21°C inside
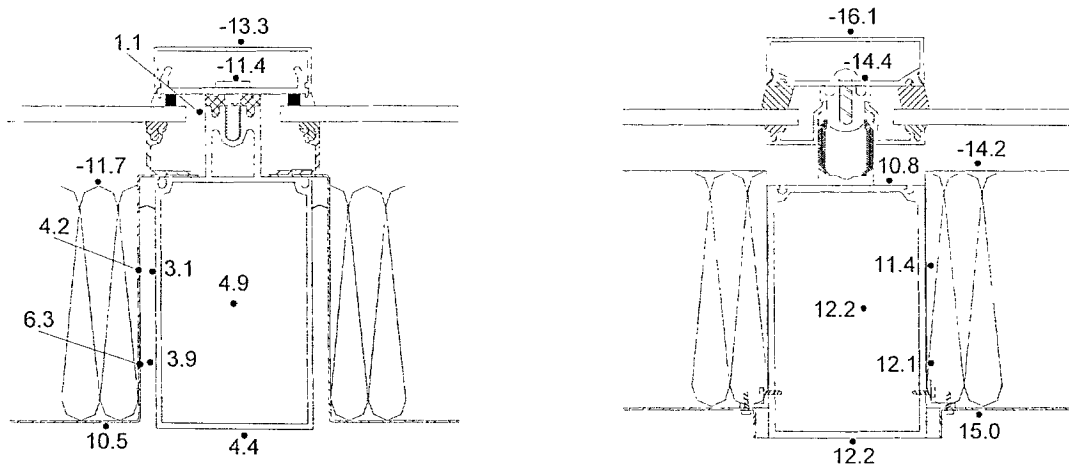
(a)Section 8: glazing mullion in system A   (b) section 9: glazing mullion in system B

Note: The section number indicated above is shown in Figure 3.3.

Figure 5.10 Temperature distributions across spandrel mullion sections under test condition:−18°C outside and 21°C inside

115

In system B, the larger thermal break dampens the heat flow through the mullion section and results in smaller temperature gradient along the mullion surfaces. The presence of the much larger thermal break also reduces the influence of local surface film coefficients on the temperature distributions. For example, the surface temperature at the spandrel mullion front surface was measured at 12.2°C (Figure 5.10b), which is only 1.8°C lower than that at the glazing mullion surface measured at 14.0°C (Figure 5.9b) compared to the difference of 3.6°C in system A. With the larger thermal breaks, a more uniform mullion surface temperature is achieved in system B.

The direct temperature comparison between system A and B clearly indicates the effect of the design details on the mullion performance. The temperature difference across the thermal break is increased from 12.7°C in system A to 25°C in system B at sill section (Figure 5.8) due to the use of larger reinforced nylon thermal breaks in the frame section of system B. Therefore, a 7°C higher temperature on the front surface of the sill mullion is achieved, and similarly, a 3.8°C colder temperature on the exterior surface of pressure plates is yielded. The enhanced frame configuration and the shift of the return of the back pan in system B achieved a 1.7°C improvement in the surface temperatures of the back-pan as shown in Figures 5.8. The thermal bridge effect of the return of the back-pan is indicated by the high temperature gradient along the return and also by the warmer temperature on the exterior surface of the insulation at edge-of-spandrel area (Figure 5.8a). With the revision of the back-pan design, the temperature on the exterior surface of the insulation at the edge-of-spandrel was reduced to −11.1°C, which is 2.4°C colder

116

than that in system A. The lower temperature in system B indicates that the thermal bridge effect is reduced and less heat is lost through this area.

5.3.3 Thermal responses under cyclic conditions

Metal curtain walls are light-weight building envelope systems and have little thermal mass. The daily variation of outdoor temperature and solar radiation may result in high fluctuation of wall surface temperatures due to its high conductivity and little thermal mass. The high fluctuation of surface temperature may affect the durability of the wall material, the indoor environment and the condensation potential. The dynamic performance of the wall was evaluated by subjecting it to a periodic variation of outdoor temperature. A sinusoidal profile based on weather files from the Montreal weather station was simulated in the cold box. The solar effect was not considered in this test.

The measured thermal responses of the selected points on curtain wall components are shown in Figure 5.11. Four representative points are chosen for each system (Figure 5.12): one at the surface of the vision sill mullion (Mullion-A and Mullion-B), one at the center of the interior glazing surface (Glazing-A1, Glazing-B1), one at the vertical centerline of the glazing and ½" (12.7mm) away from the bottom sight line (Glazing-A2, Glazing-B2), and one at the center of the back-pan surface (Spandrel-A, Spandrel-B).

These measured thermal responses reveal the performance difference between system A and system B. The magnitudes of the temperature variations are listed in Table 5.4. Components with higher thermal resistance have lower temperature variations. It has been found that in each system, the center-of-spandrel has the highest thermal resistance, while the edge-of-glass has the lowest thermal resistance. Each component in system B provides higher thermal resistance than the corresponding component in system A.

Dots on the lines correspond to peak temperatures
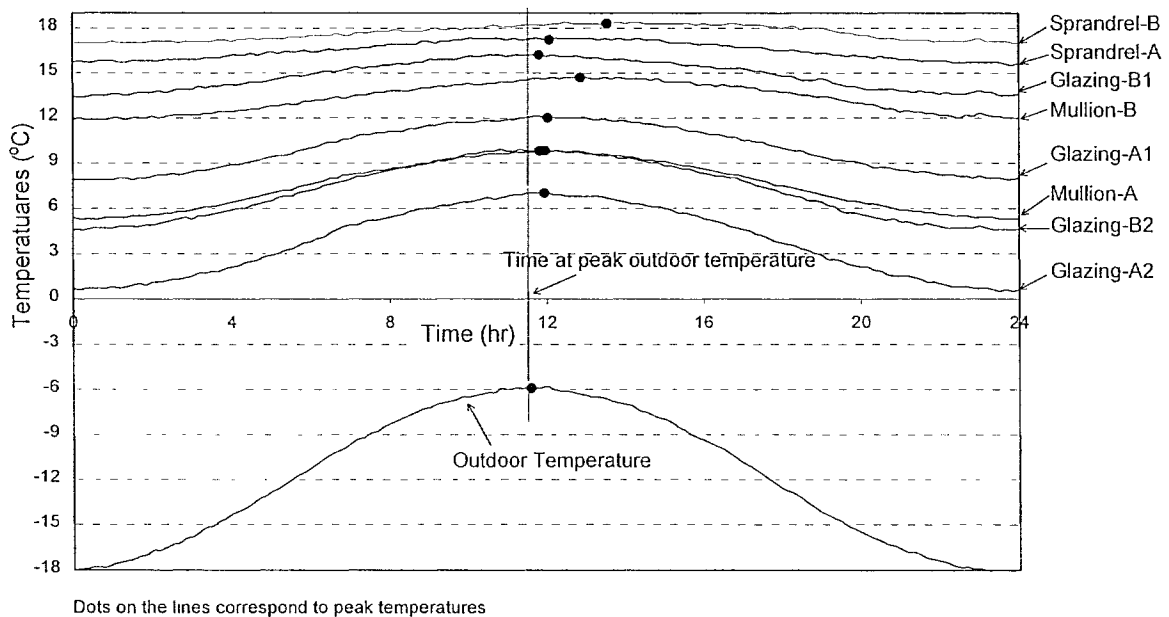
Figure 5.11 Thermal responses of curtain wall components to sinusoidal outdoor air temperatures
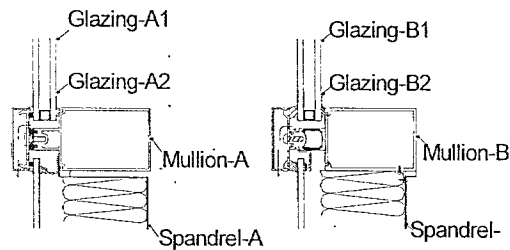
Figure 5.12 Locations of selected points shown in thermal response curves

118

The difference in the thermal responses is also evident in the time lag of the locations selected. The time lag at the particular location on the wall is a measure of its delayed temperature response to the outdoor temperature changes. A least square regression analysis technique has been employed for the estimation. The time lags obtained are listed on the last row in Table 5.4. Both of the measured temperature response curves and the time lag estimation indicate that the metal curtain wall offers little in term of thermal mass. The time lags to reach temperature peaks after the outdoor air temperature reaches its maximum are within half an hour for most of these points. The delays are longer only for the interior surface temperatures on the back-pan (Spandrel-B) and on the mullion (Mullion-B) in system B. These longer response delays further demonstrate the reduced thermal bridge effects by a larger thermal break in the improved system B.

Table 5.4 Temperature response and time lag under sinusoidal outdoor condition

Response characteristics	Outdoor air temp.	System A				System B			
		Mullion	Center-of-glass	Edge-of-glass	Center-of-spandrel	Mullion	Center-of-glass	Edge-of-glass	Center-of-spandrel
Max. temp. (°C)	-6.0	9.8	12.1	7.0	17.3	14.6	16.2	9.9	18.4
Min temp. (°C)	-18.0	5.3	7.9	0.5	15.5	11.9	13.4	4.6	17.0
magnitude (°C)	6.0	2.3	2.1	3.3	0.9	1.4	1.4	2.7	0.7
time lag (hr)		0.37	0.44	0.35	0.49	1.28	0.22	0.23	1.97

5.3.4 Condensation Resistance Factor (CRF)

Condensation resistance is an important factor in evaluating thermal performance of fenestration systems. The measured surface temperatures were used to calculate the condensation resistance factors for frame (CRF$_f$) and glazing (CRF$_g$) under different test conditions following AAMA procedure described in section 2.2.3. The glazing panel G$_{al}$

119

in system A with its surrounding mullions, and the glazing panel G_{b1} in system B with its surrounding mullions are considered. The predetermined temperature measurement locations are shown in Figure 5.13.
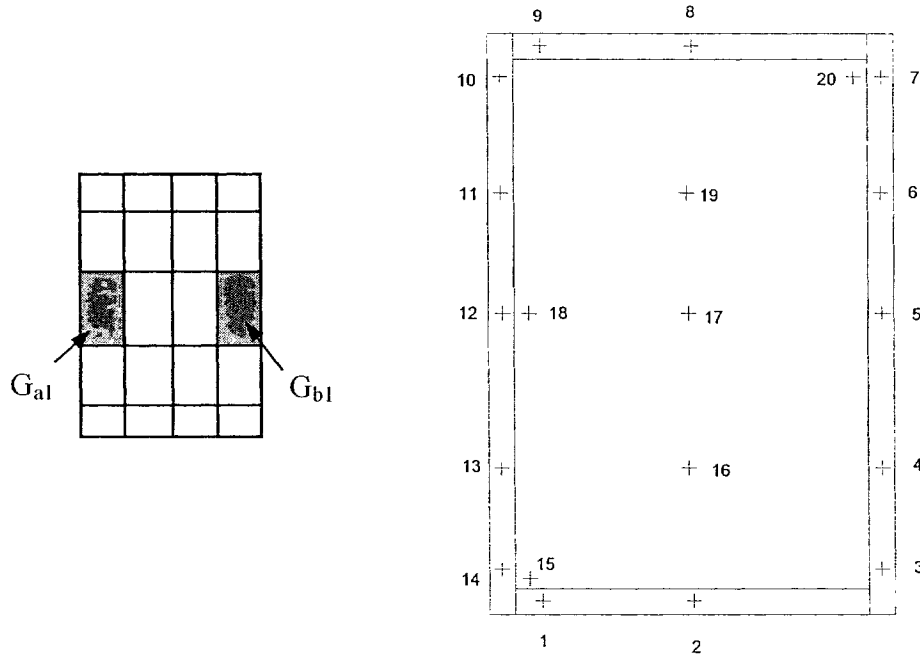
Figure 5.13 Locations of temperature measurements used to calculate the condensation resistance factor

Table 5.5 Measured CRF under various test conditions

	CRF	Test conditions T_o/T_i (°C)				
		-5/21	-10/21	-18/21	-24/21	-32/21
System A	CRF_g	58	59	59	60	60
	CRF_f	59	60	61	62	62
System B	CRF_g	70	71	72	72	71
	CRF_f	75	76	78	78	78

Notes: in accordance with AAMA, all numbers are rounded to whole numbers

The calculated CRF for frame and glazing are listed in Table 5.5. The values indicate that in system A, the aluminum frame has a condensation resistance similar to that of the glazing panel, while in system B, the condensation resistance of the frame is higher than

120

that of the high performance glazing panel. In general, the improved system provides a much higher condensation resistance than the standard system. It should be noticed that the condensation resistance factors determined for the glazing are based on the average value of six locations on the interior surface (shown in Figure 5.13). However, condensation is a local phenomenon. It occurs where the surface temperature is below the dew-point temperature of the surrounding air. The evaluation of condensation risk based on these CRF values assumes that a small amount of condensation is acceptable. Temperature distributions on glazing surfaces shown in section 5.3.1 and on frame surfaces shown in sections 5.3.1 indicate that the bottom edge-of-glass has the lowest surface temperature, especially at the corner, and these places are the most likely locations for condensation to occur. Figure 5.14 shows the frost formed at the bottom edge-of-glass of glazing panel G_{a2} (Figure 5.14a) in system A and G_{b2} (Figure 5.14b) in system B. The frost shown in these photos had accumulated for two days under the test condition of –32°C in cold box. There were about 6 cm high frost formed at the edge-of-glass of the standard glazing units in system A. In contrast, only about 1 cm frost formed at the edge-of-glass of the high-performance glazing units in system B. Frost was observed on the entire edge-of-glass region, but less on the upper part of the glazing panels. No condensation was observed on frame surfaces.
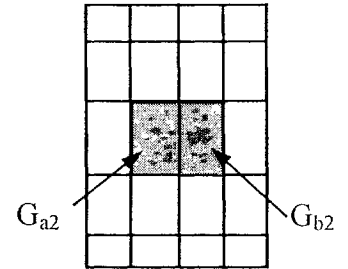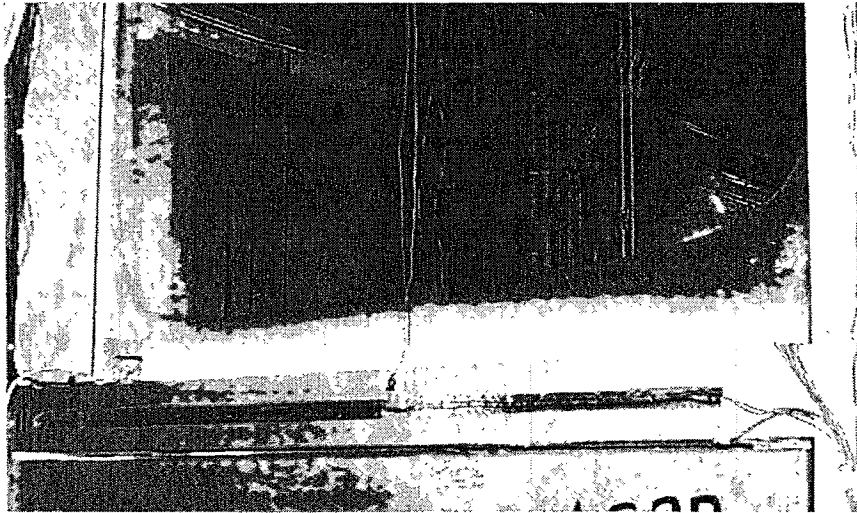
(a) Glazing panel G_{a2} in system A
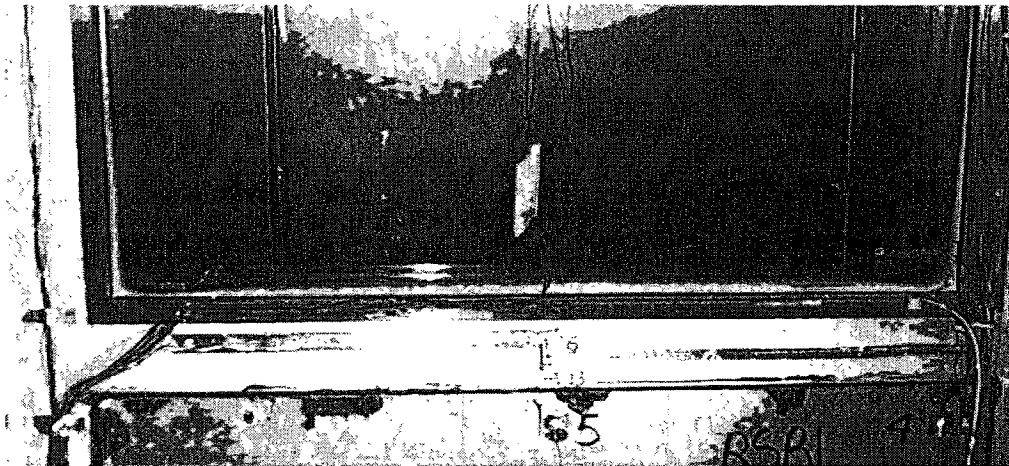
(b) Glazing panel G_{b2} in system B

Figure 5.14 Frost formed on glazing panels

5.3.5 Effect of air infiltration on condensation potential

As discussed in section 2.2.3 of Chapter 2, in the standard tests (AAMA, 1998; and CSA, A440) to determine condensation resistance for fenestration systems, the air leakage effect is eliminated by sealing the cracks and maintaining zero pressure difference across the test specimen. In real operating conditions, fenestration systems experience a continuously varying pressure difference induced by wind, stack effect, and mechanical

122

systems. The resulting air infiltration and exfiltration can change the temperature distribution of the fenestration system and, thus, the condensation resistance. Tests were designed and carried out to study the thermal response of the walls to the introduced air infiltration and the influence of infiltration on the condensation potential of the walls.

Pressure differentials across the specimen were introduced by depressurizing the hot box. The transient thermal responses of the walls tested to the presence and absence of air leakage were monitored. The analysis of the measured data are carried out in three steps: 1) identify temperature response patterns; 2) deduce air leakage paths; 3) evaluate the impact on the condensation resistance factor.

5.3.5.1 Temperature response patterns

Temperature responses to air infiltration are analyzed from the measurements made during three phases of the test: 1) two hours before the beginning of the depressurization; 2) during the four-hour depressurization; and 3) after the depressurization stops and until the temperature returns back to the initial value before depressurization was introduced. By examining the transient temperature variations, three typical temperature response patterns are identified. They are the synchronized temperature response profile, the delayed temperature response profile, and no-response temperature profile.

1. Synchronized temperature response profile

In this pattern, the temperature response follows the depressurization process. The temperature starts to drop when the blower starts. After a certain period of time it stabilizes at a constant value until the blower stops. Then it returns back to the initial

value. Before the depressurization starts, the wall assembly is at steady-state and the temperatures throughout the specimen remain constant. When a pressure differential is applied, cold air is driven through some cracks to the warm side. During infiltration, the cold air washes through the wall assembly and absorbs heat from the surfaces along its way. A transient process starts along the air leakage paths and propagates to parts away from the paths. Eventually a new steady-state condition can be achieved and maintained after a certain time. When the pressure differential is removed, temperatures start to move back to the original level.

2. Delayed temperature response profile

For this type of response profile, the temperature remains unchanged at the beginning of the depressurization for a certain period of time and then it drops slowly until it reaches a new constant value. It keeps this value for a while even after the termination of depressurization before it rises back to its original value (Figure 5.15). This type of temperature response profile occurs at some distance of the air leakage paths with a time lag of about one to one and a half hour. The magnitude of the temperature drops is small, around 0.2~0.5°C.

3. No-response temperature profile

The temperature at zones far away from air leakage paths remains unchanged during the entire test sequence, i.e. before, during and after the depressurization. The recorded temperature variations are within 0.1°C, and are not obviously related to the depressurization process. The temperature at the center of a glazing unit, for example, follows this pattern.
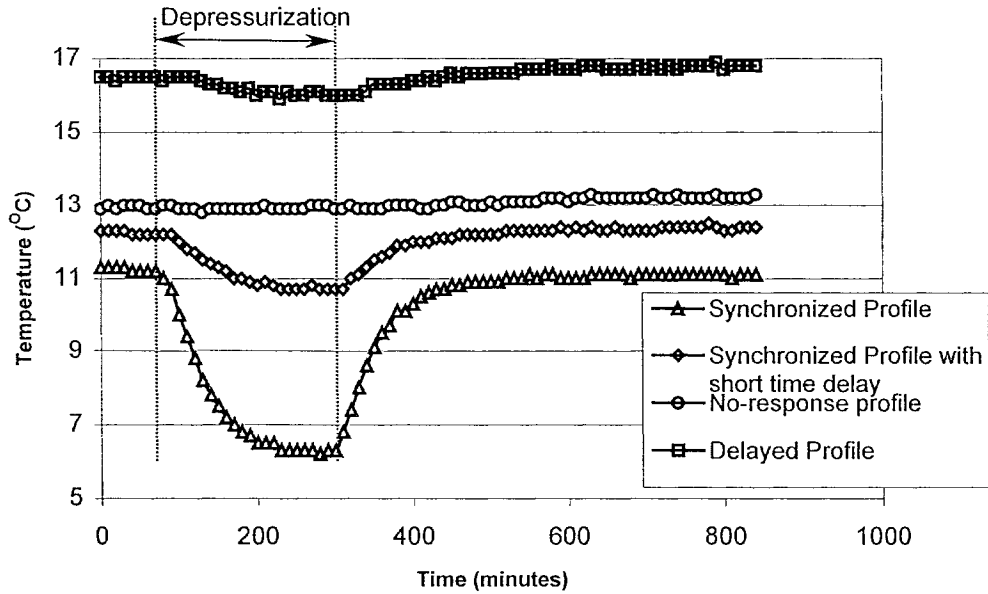
Figure 5.15 Typical temperature response patterns to depressurization

As shown in Figure 5.15, a synchronized profile shows that temperature starts to drop as soon as the blower is turned on. The other synchronized profile shows a short time delay (10 to 20 minutes) before the temperature drops, and has a smaller temperature variation. The magnitude of the temperature variation and the response time depend on the amount of air leakage and the distance from the leakage source. The direct ingress of the cold air causes quick drop of temperatures along its paths. The temperatures at the vicinity of the leakage paths follow the change, but with smaller magnitude. This type of temperature response profile can be used to identify the air leakage paths.

5.3.5.2   Locations of air leakage paths in system A

A distribution of temperature response patterns across wall system A is indicated in Figure 5.16 and the magnitudes of temperature variations are listed in Table 5.6.

125

M9 △ S1△ S2△ S3△ △ M12 △ S7
△ S8
△ S9
△ S4

M8 △ S5△ S6△ □ □

△ M11 □ M13 —

M7 △ △G1 △ G3 △ □ □
G2

M6 △ □ —

glazing section

M5 △ △G4 — — — —

jamb mullion

middle mullion

M4 △ — — —

G_{a1} G_{a2}

M3 △ △G5 — — □ —

△ M10 □ —

M2 △ △ △ △
S10 S11 S12 △ S16

△ S13 △ S17

△ S18

M1 △ △ △ □ □
S14 S15

M-mullion
S-spandrel panel
G-glazing panel

△ synchronized profile
△ synchronized profile with short time delay
□ delayed profile
— no response

spandrel section

S_{a3} S_{a4}
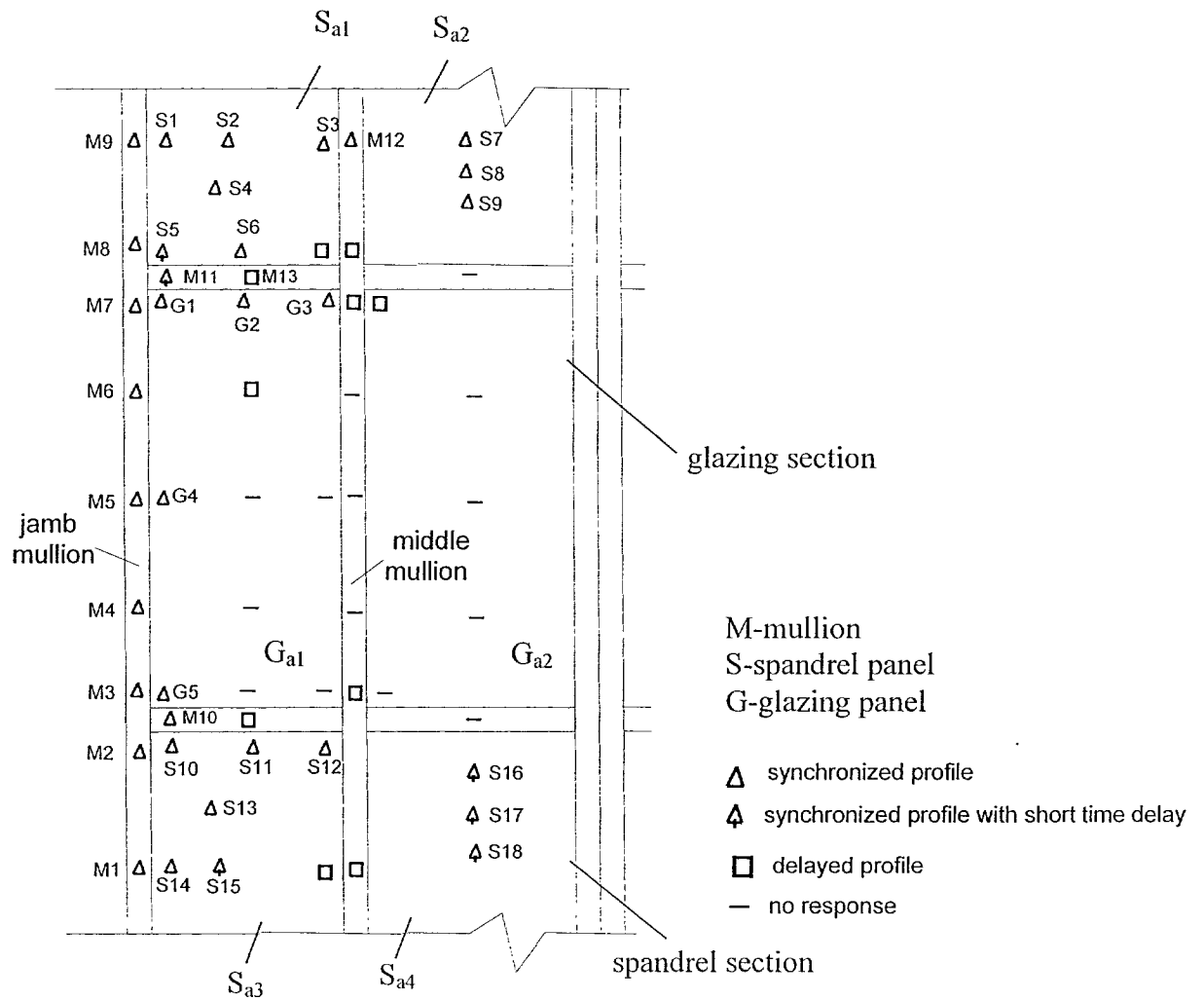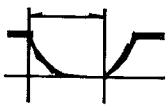
Figure 5.16 Distribution of temperature response patterns on the interior surface of system A

Table 5.6 Magnitude of temperature variation in system A

Synchronized response profile	Temperature variation (°C)										
depressurization	M_1	M_2	M_3	M_4	M_5	M_6	M_7	M_8	M_9	M_{10}	M_{11}	M_{12}
	3.3	3.9	4.7	5	3.3	2.5	1.6	3.1	4.2	1.8	1.5	0.9
	S_1	S_2	S_3	S_4	S_5	S_6	S_7	S_8	S_9	S_{10}	S_{11}	S_{12}
	2.6	3.2	1.6	2.5	1.5	1.4	1.7	1.5	1.3	2.7	0.5	0.8
	S_{13}	S_{14}	S_{15}	S_{16}	S_{17}	S_{18}	G_1	G_2	G_3	G_4	G_5
	1.2	2.5	1.1	0.5	0.5	0.5	1.5	0.8	0.9	1.1	2.2

Except for a few locations at the edge-of-glass on glazing panel G_{a1}, most of the glazing panel surfaces are characterized with no-response profiles. This condition indicates that there is no impact on this area from air leakage in adjacent areas during the four-hour depressurization. Also in the middle section of the glazing mullion (Figure 5.16), the temperatures remain constant during the test. A few locations at the middle spandrel mullions, however, are characterized by the delayed profiles. These profiles have delays between 60 to 90 minutes and the magnitudes of the temperature variation are small, around $0.2^\circ C \sim 0.5^\circ C$. Most of the synchronized temperature response profiles are located on the vertical jamb mullion, and the steel spandrel panels. For simplicity, only these locations are labeled and the magnitudes of temperature variations are listed in Table 5.6.

Three typical air leakage locations are identified for system A. The first type exists at the mullion jamb section, which is the junction between the specimen and the holding frame as shown in Figure 3.4e in Chapter 3. Although this section was carefully taped and sealed, tiny air leakage passages may exist and develop due to the movement by thermal and pressure loads. The direct ingress of cold air causes the mullion surface temperature to drop by as much as $5^\circ C$ (Point M_4 in Figure 5.16). This air leakage path also affects its vicinity. For example as shown in Figure 5.17, the location at M_8 is on the air leakage path and has a temperature drop of $3.1^\circ C$, while the location M_{11} at the vicinity has a temperature drop of $1.4^\circ C$ with a 20 minute delay. The temperature at point M_{13}, which is further from the jamb section, has a longer delay of 70 minutes and it drops only slightly by $0.5^\circ C$.
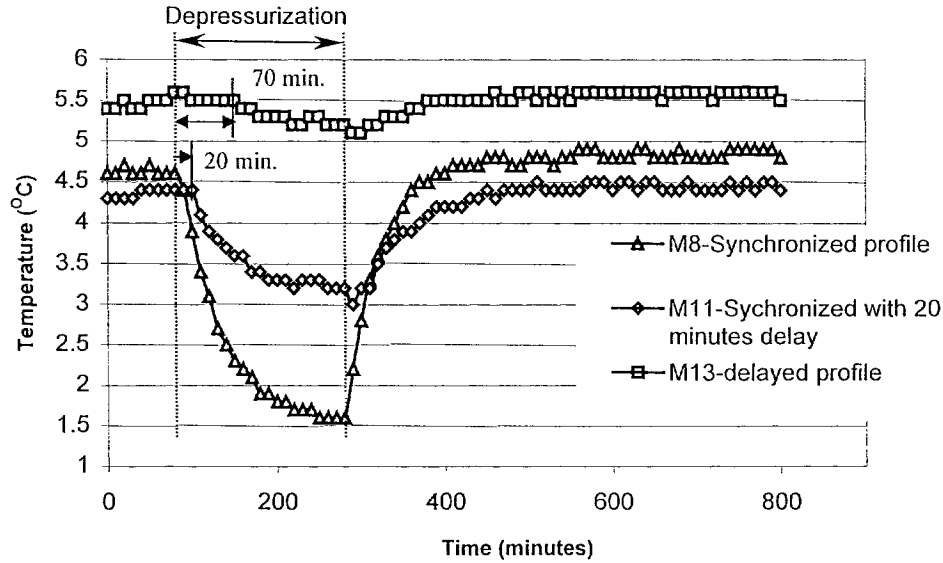
Figure 5.17 Selected temperature response profiles on mullion surfaces in system A

The second typical location for the synchronized temperature response profile and possible air leakage paths was found on the steel back-pan surfaces of spandrel panels S_{a1} and S_{a3} (Figures 5.16). There are two possible reasons for the temperature drop. First, cold air may find its way through the insulation, and get in through cracks at the joints between the spandrel panel and the mullions. By examining the temperatures on the exterior surface of the insulation, it was found that most of the surface remained at constant temperature except for point S_1 and point S_{10} (Figure 5.16) which were close to these joints and have a temperature variation of about $0.6°C$. The fact that most of the insulation surface remains at constant temperature implies that there is no significant amount of cold air passing through at the perimeter of the insulation panels. The second reason for the temperature drop is that the sharp temperature drop on the jamb mullion surface causes the temperature drop on the back-pan surface due to the high conductivity of aluminum and steel. The steel back-pan is connected directly to the flange of the

128

aluminum mullion (Figure 5.1). The closer the point is to the jamb mullion, the greater the temperature drop. For example, the temperature at point S_{14} drops by $2.5^{\circ}C$, while the temperature at point S_{15} drops by $1.1^{\circ}C$.

The third typical location for the synchronized temperature response profile is at the pin location of the top spandrel panel S_{a2} (Figure 5.16). Large temperature drops were found at points S_7 to point S_9 compared to the symmetrical locations points S_{16} to point S_{18} at the bottom spandrel panel S_{a4} (Figure 5.16). In the insulated spandrel panel, illustrated in Figure 5.18, steel pins are normally used to hold the rigid fiberglass insulation to the steel back-pan by punching them into the back-pan. Thermocouples were installed on both ends of the pin and their vicinities to monitor the effect of thermal bridge. The temperatures measured on the interior metal surface do not show significant differences since these pins have relatively small diameters ($\varnothing$2mm) and the high conductivity of metal results in small temperature gradient. However, the temperature at the head of the pin (S_7) is significantly higher than the temperature at its vicinity (S_8) on the exterior surface of the insulation. (Figure 5.19b). It was noted that during the installation, some of these pins were loosened leaving small holes (with diameter less than 1mm) on the back-pan surface (Figure 5.18). These holes were not deliberately blocked during the test since they may also exist in the site installation. Theses holes cause air leakage and temperature drop as shown in Figure 5.19. For example, the sharp temperature drop at point S_7 ($1.7^{\circ}C$) indicates the existence of such a hole. This leakage affects point S_8 in the vicinity region as well. Pinholes also cause the temperature drop at the corresponding points on the exterior surface of the insulation as shown in Figure 5.19b.
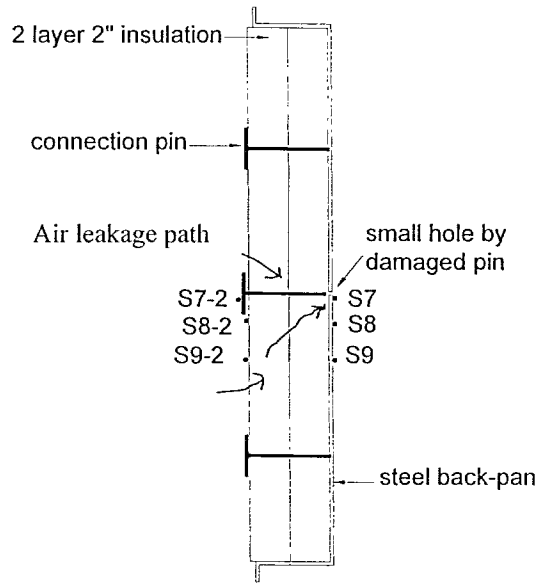
Figure 5.18 Insulated spandrel panel S_{a2}
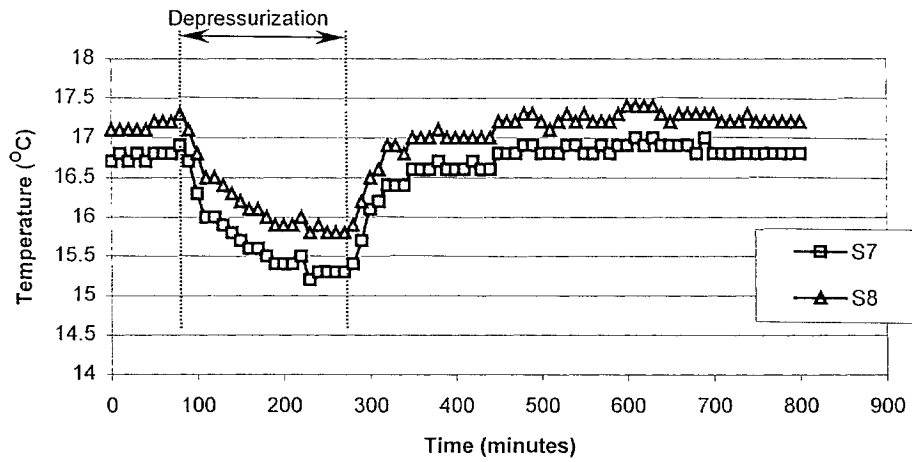
Figure 5.19a) Temperature response profiles on the interior back-pan surface of spandrel panel S_{a2} during depressurization due to the presence of a pinhole
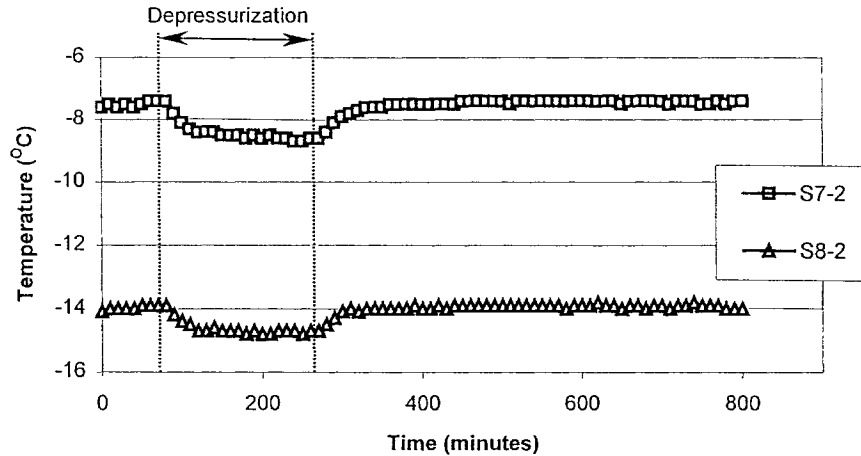
Figure 5.19b) Temperature response profiles on the exterior surface of the insulation in spandrel panel S_{a2} during depressurization due to the presence of a pinhole

In summary, the significant air leakage paths are along the mullion jamb section and through pinholes.

5.3.5.3   Locations of air leakage paths in system B

The distribution of temperature response patterns to air leakage is shown in Figure 5.20. The temperature variation magnitudes are listed in Table 5.7 for the wall system B. Similar to system A, the synchronized response pattern exists mainly along the jamb mullion, and the perimeter of the spandrel panels. There is no impact on the center-of-glazing and on the glazing mullion.
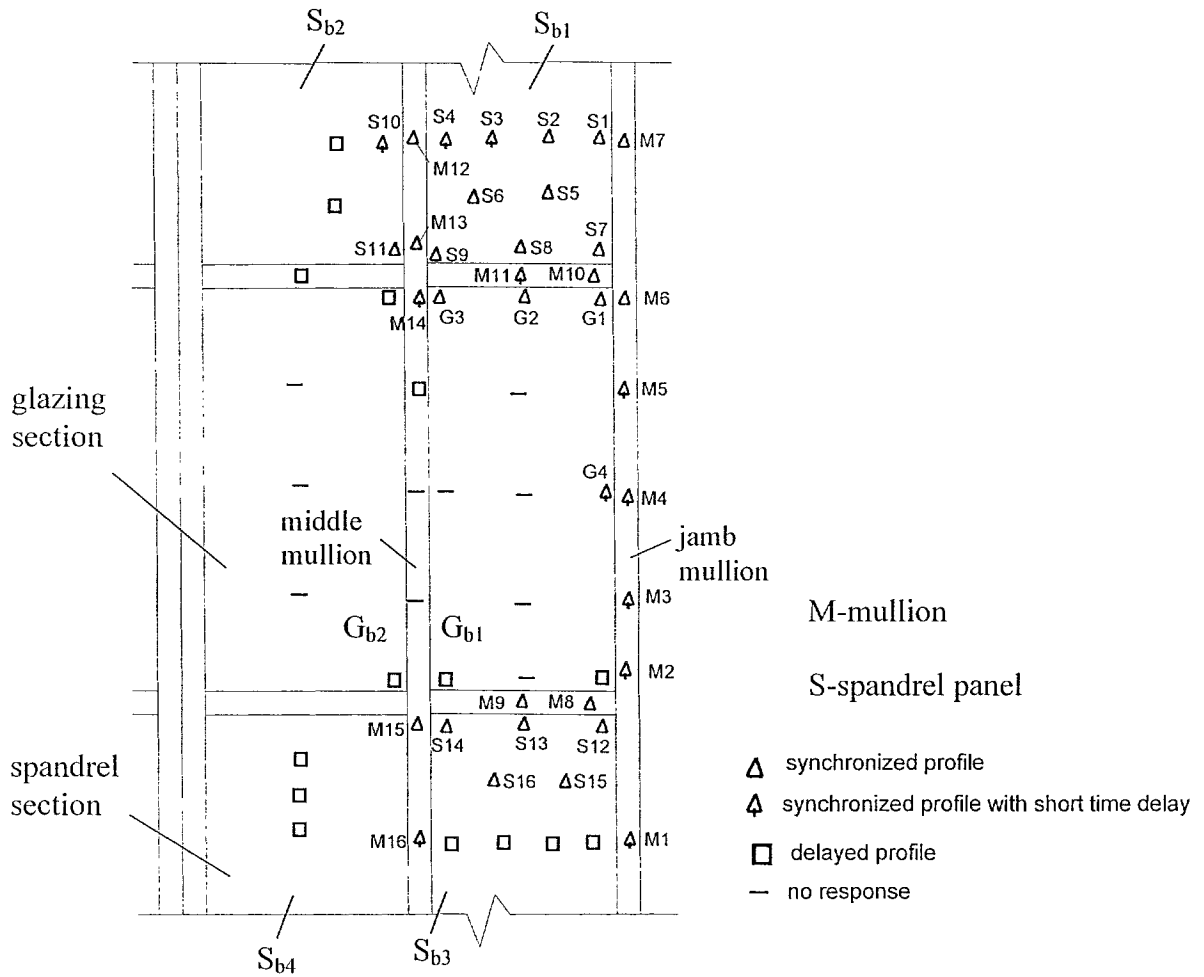
Figure 5.20 Distribution of temperature response patterns on the interior surface of system B

glazing section
middle mullion
jamb mullion
spandrel section

M-mullion
S-spandrel panel

△ synchronized profile
♦ synchronized profile with short time delay
□ delayed profile
— no response

Table 5.7 Magnitude of temperature variation in system B

Synchronized temperature response profile	Temperature variation magnitude (°C)									
depressurization	M_1	M_2	M_3	M_4	M_5	M_6	M_7	M_8	M_9	M_{10}
	1.3	1.3	1.5	1.7	2.1	2.6	4.9	1	0.9	1.9
	M_{11}	M_{12}	M_{13}	M_{14}	M_{15}	M_{16}	S_1	S_2	S_3	S_4
	0.9	0.9	1.3	0.5	0.5	0.3	3.5	2	1.5	1.3
	S_5	S_6	S_7	S_8	S_9	S_{10}	S_{11}	S_{12}	S_{13}	S_{14}
	1.3	1.3	2.1	1	0.6	0.5	0.8	1.9	1.9	0.7
	S_{15}	S_{16}	G_1	G_2	G_3	G_4				
	1.9	1.4	1.7	0.8	0.8	0.5				

In the revised back-pan design in system B (Figure 5.1), the continuity of the air barrier is achieved by the edge sealant on the interior. The integrity of this seal needs to be maintained over the service life of the curtain wall especially around corners. Some cracks were noted at the top perimeter of the spandrel panel S_{b3} likely due to workmanship or to excessive thermal and pressure loads. The temperature response profiles for point S_{13} and for its corresponding location S_{13}-exterior on the exterior surface of the insulation are shown in Figure 5.21. The discernible temperature drop at the exterior surface of the insulation indicates air leaks at these locations.
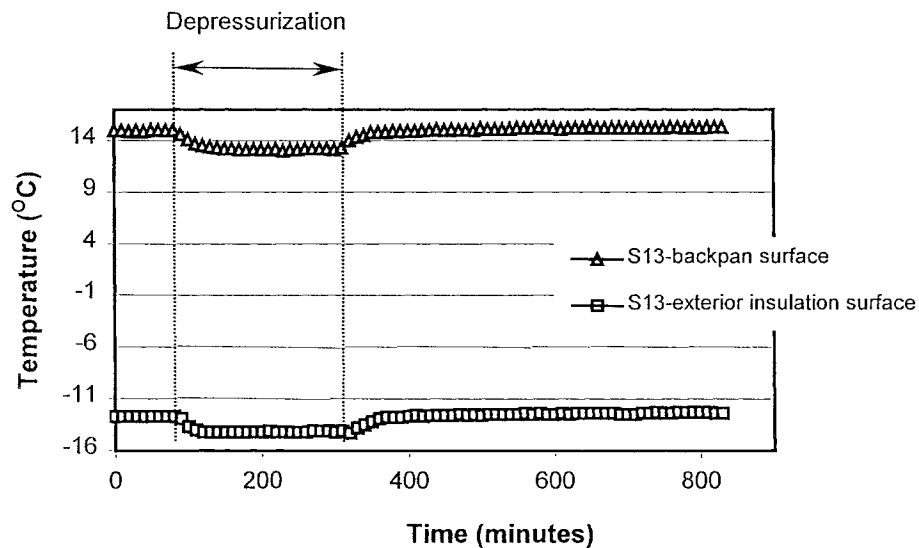
Depressurization

Figure 5.21 Temperature response profiles on the exterior surface of the insulation in spandrel panel S_{b3} due to depressurization

Note: Point S_{13}-exterior insulation means that the thermocouple is installed at exactly the same location as S_{13} but on the exterior surface of the insulation.

The procedures of fabrication and installation for the spandrel panels of system B used in this research project also affect the thermal response to air leakage. As shown in Figure 5.22a. the factory-fabricated spandrel panel consisted of the steel back-pan and only the

133

center block of insulation, while the edge insulation was installed in situ manually after the spandrel panel was connected to the main mullion grid. The stripes of edge insulation were held in place by friction. This "hybrid" procedure may introduce gaps between the center-insulation and the edge-insulation if the size of the edge-insulation is not large enough. In metal curtain wall design, the pressure equalized rainscreen principle is applied and outdoor air is allowed to flow in the chamber enclosed by the back-pan and the spandrel glass. If gaps in the back-pan insulation are present, then cold air may be in contact with the steel back-pan and could increase the heat loss through the spandrel panel. To monitor this effect, a small gap (around 5 mm) was left deliberately between insulation blocks in the top spandrel panel S_{b2} (Figure 5.22b). Thermocouples were installed on the exterior surface of the first layer of the insulation, the exterior surface of the second layer of the insulation, and the interior surface of the steel back-pan. The temperature variation profiles at these points are shown in Figure 5.23 and the temperature variation magnitudes are listed in Table 5.8.
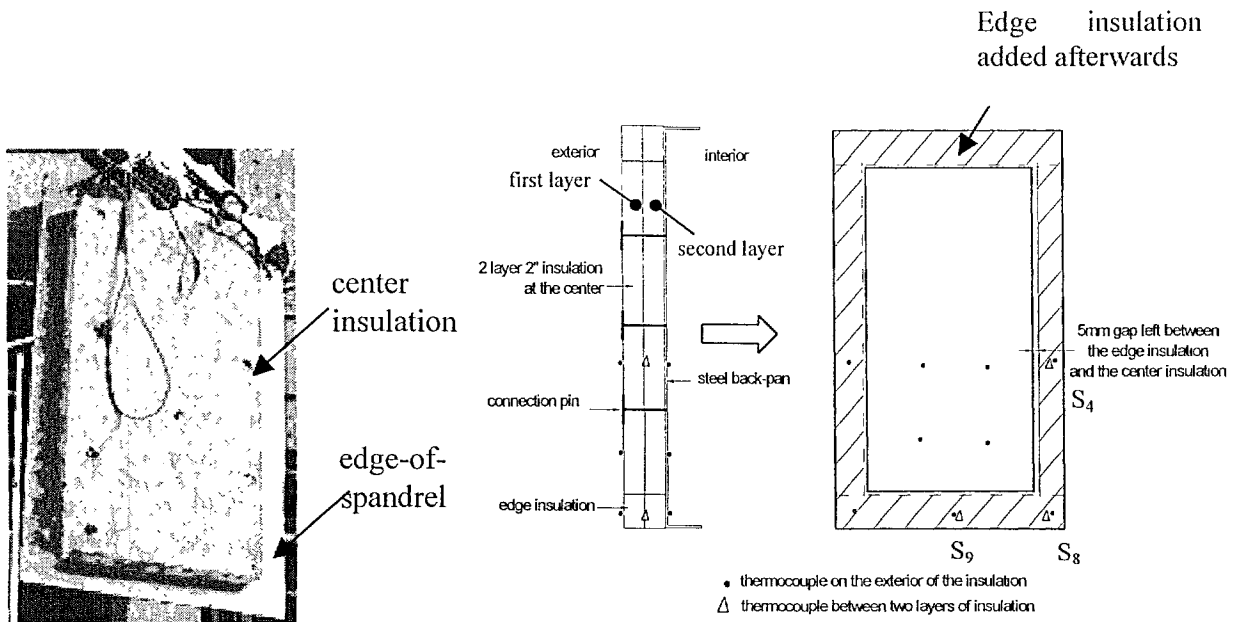
Figure 5.22a Insulated spandrel panel in system B

Figure 5.22b Configuration of spandrel panel S_{b1}

134

Table 5.8 Temperature variation magnitudes on the exterior surface of the insulation in spandrel panel S$_{b2}$

Sensors	Exterior surface of the first layer of insulation			Exterior surface of the second layer of insulation		
	S$_4$-1	S$_8$-1	S$_9$-1	S$_4$-2	S$_8$-2	S$_9$-2
Temperature variation (°C)	8.8	4.4	3.0	2.3	0.8	1.0
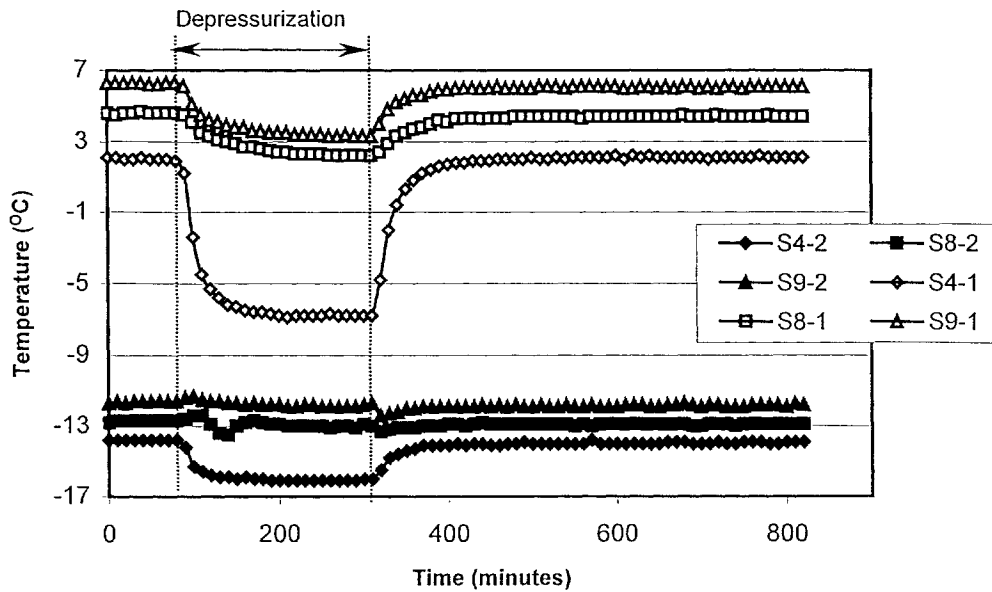
Figure 5.23 Synchronized temperature response profiles on the exterior surface of the insulation in spandrel panel S$_{b2}$ with gaps in insulation

In summary, the typical air leakage paths found in system B are along the jamb mullion section and the perimeter of the spandrel panels.

5.3.5.4   Effect of air leakage on the condensation resistance

The Condensation Resistance Factor is defined based on the average value of temperatures measured from the pre-determined locations on a glazing unit and its surrounding frames (Figure 5.13). The changes in the surface temperatures will affect the

CRF. However, air leakage is a local phenomenon and its effect on temperature responses is more prominent locally. Therefore, two indicators are used. The Temperature Index (TI) defined by equation 2.4 in section 2.2.3 is used to indicate the local effect of air leakage, and Condensation Resistance Factor (CRF) defined by equations 2.5 & 2.6 is used to indicate the global effect of air leakage.

The glazing panel G_{a1} in system A with its surrounding mullions and the glazing panel G_{b1} in system B with its surrounding mullions are considered. Table 5.9 lists the calculated Temperature Index with and without air leakage for each location indicated in Figure 5.13. These results show that the air leakage effect is concentrated on the joint sections. There is no obvious impact on the center-of-glass area, and the temperature index changes are within 1 unit. For the frame, the effect of the air leakage on the jamb mullion surfaces is significant. The maximum Temperature Index change in system A is 13, and is 7 in system B. The calculated CRFs are listed in Table 5.10. For system A, the CRF for glazing decreases by 2, and the CRF for frame decreases by 4. The reduction of CRF for glazing is mainly due to the temperature drops at the edge-of-glass. With introduced air leakage the frame section has the same resistance to condensation as the glazing area. For system B, the CRF decreases by 1 unit for glazing and by 3 unit for frame.

The maximum relative humidity that the fenestration system can stand before condensation forms will decrease with the reduction of Condensation Resistance Factor due to the presence of air infiltration. Figure 5.24 shows the effect of air infiltration on

this maximum relative humidity under different outdoor temperatures. The reduction by 4 in the frame CRF of system A due to air infiltration causes a 4% reduction to the relative humidity before condensation would occur on the frame. For system B, the CRF for the frame is reduced by 3, which corresponds to around 4% lower relative humidity as well.

Table 5.9 Surface temperatures and Temperature Index with and without air leakage

| | | System A | | | | | System B | | | | |
| | Location | Without air leakage | | With air leakage | | ΔTI | without air leakage | | With air leakage | | ΔTI |
		Temp. (°C)	TI	Temp. (°C)	TI		Temp. (°C)	TI	Temp. (°C)	TI	
Frame	1	4.6	57	2.8	53	5	11.8	76	10.8	73	3
	2	5.3	59	5.3	59	0	12.3	77	11.4	74	2
	3	5.9	61	5.6	60	1	12.8	78	12.5	77	1
	4	6.3	61	6.1	61	0	13.7	80	13.2	79	1
	5	7.7	65	7.7	65	0	14.1	81	14.1	81	0
	6	8.1	66	8.1	66	0	14.5	82	14.2	82	1
	7	6.5	62	6.1	61	1	12.8	78	12.3	77	1
	8	5.4	59	5.1	58	1	13.5	80	12.6	78	2
	9	4.4	57	3.2	54	3	12.6	77	10.7	73	5
	10	4.5	57	3	53	4	12.0	76	9.4	69	7
	11	5.0	58	2.7	52	6	12.3	77	10.2	72	5
	12	4.5	57	1.2	49	8	12.6	77	10.9	73	4
	13	4.2	56	-0.8	44	13	12.3	77	10.8	73	4
	14	3.8	55	-0.9	43	12	11.6	75	10.3	72	3
Glazing	15	0.7	47	-1.5	42	6	5.4	59	5.1	58	1
	16	7.3	64	7.3	64	0	13.6	80	13.6	80	0
	17	8.2	66	8.2	66	0	13.8	80	13.4	79	1
	18	1.8	50	0.8	48	3	8.8	68	8.3	67	1
	19	9.1	69	9.1	69	0	14.7	83	14.6	83	0
	20	3.1	54	2.3	51	2	7.2	64	6.4	62	2

Table 5.10 Measured CRF under CSA test condition with and without introduced air leakage

| Systems | CRF without air leakage | | CRF with air leakage | |
	CRF_g	CRF_f	CRF_g	CRF_f
A	59	61	57	57
B	72	78	71	75

Note: all numbers are rounded to whole numbers in accordance with the AAMA standard,.
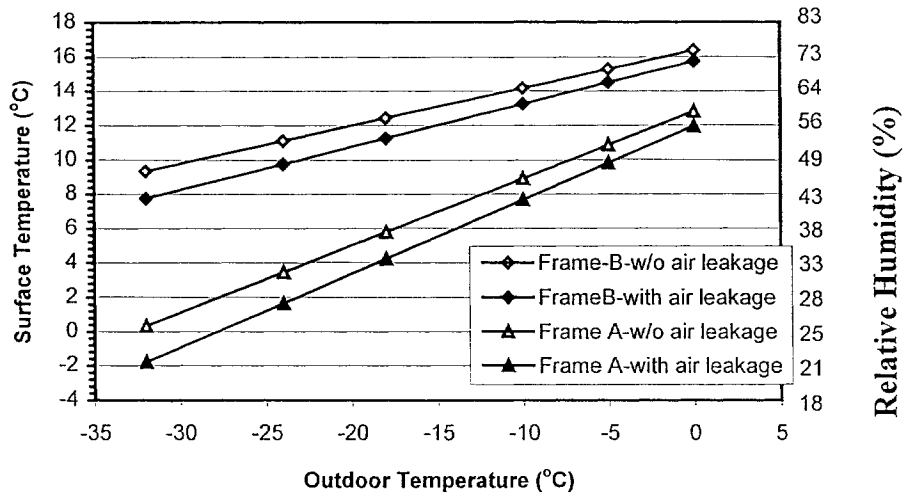
Figure 5.24 Maximum relative humidity before condensation occurs on frames in system
A and B with/without air leakage
(note: the indoor air temperature is at 21°C)
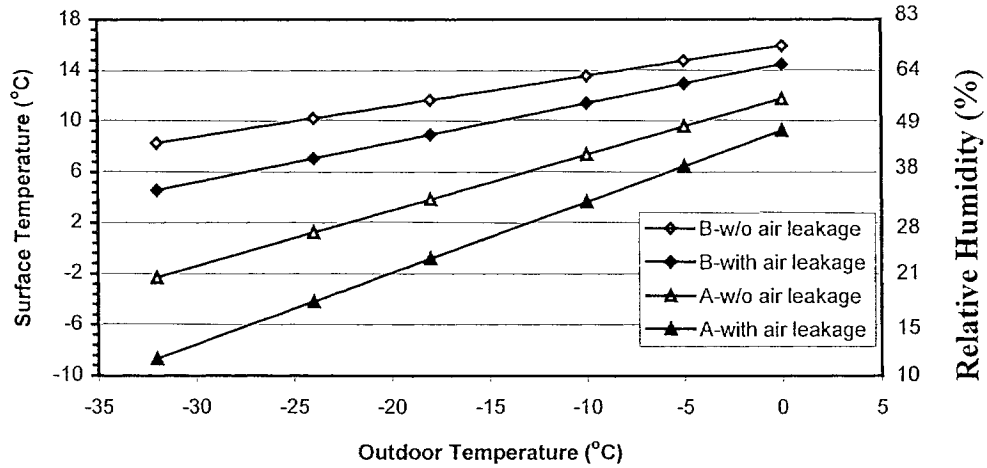
Figure 5.25 Maximum relative humidity before condensation occurs at the locations with
maximum temperature variation in system A and B with/without air leakage
(note: the indoor air temperature is at 21°C)

In summary, the analysis on condensation resistance indicates that the tested curtain walls
have good air tightness. The impact of air leakage on the condensation resistance of
glazing units is not significant either locally or globally, while it is substantial for the

138

mullion frame with the current test setup. For the frame section, the local values of maximum TI changes are as much as 13 in system A and 7 in system B. These changes correspond to a 9% decrease to the relative humidity before condensation occurs at this specific location. Globally, the CRF changes by 4 in system A and by 3 in system B, which corresponds to 4% lower relative humidity before an amount of non-acceptable condensation occurs on frame.

5.4 Infrared Thermography

The infrared scanning was conducted to monitor the surface temperature profiles with and without the presence of air infiltration. The objectives are to visualize the thermal bridge effects, to supplement the 3-dimensional thermocouple measurements, to help identify the location of air leakage and to evaluate the effect of air leakage on local surface temperature. The external reference technique was employed in this Infrared Thermography test setup to increase the accuracy of the measurements.

5.4.1 Experimental setup for IR imaging

The experimental setup for the IR Thermography is shown in Figure 5.26. The IR system includes infrared imager, temperature-controlled external reference emitter, and post-data processing software.
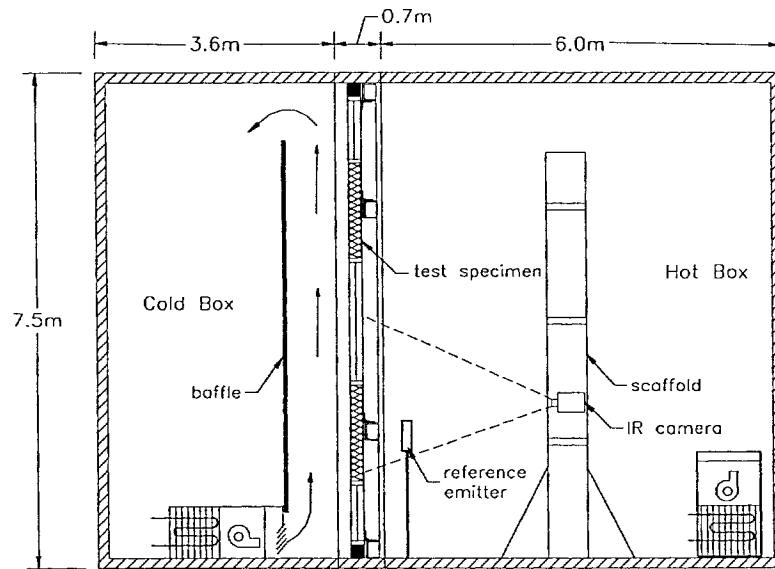
Figure 5.26 Diagram of Infrared Thermography setup

5.4.1.1 Infrared imager

The infrared camera used in the tests employs a scanning system to measure the individual energy fluxes emitted and reflected by a large number of elements over a surface. The radiation flux received by the infrared detector generates an electrical voltage signal, whose amplitude is proportional to the temperature for each point across the surface being scanned by the camera. The output voltage signals for all the individual points are then processed and transferred to the display monitor to form a thermal image. The thermal image can be stored on a floppy disk or on a videocassette for further post-processing. The specifications of the scanner used in this experiment are listed in Table 5.11.

Table 5.11 Specifications of the Infrared camera

Infrared detector	Mercury/Cadmium/Telluride
Spectral range	2-5μm
Absolute accuracy	± 2% or ± 2°C
Relative accuracy	± 0.1 °C

5.4.1.2 Reference emitter

A reference emitter is a temperature-controlled device with a known surface emittance and temperature (Griffith, 1995 and Türler 1997). The thermal image of the reference emitter is included in the Thermography image of the test specimen. Since the surface temperature and surface emittance of the reference emitter are known, the deviation between the temperature read from the infrared image and the temperature by direct contact measurement can be used to correct the infrared readings for the test specimen. A customized reference emitter with a temperature-controlled liquid system was fabricated for the infrared Thermography measurement. The construction detail follows the method developed by Türler (1997) and is described in Appendix B.1.

5.4.1.3 Determination of surface emittance

The accuracy of the infrared measurement is affected by many factors including the surface emittance, background radiation, ambient relative humidity, and the optical length. The correct surface emittance is critical to interpret the thermal image correctly. The true surface emittance depends not only on the specimen material, but also its surface condition and temperature. The surface emittance to be determined in the curtain wall test specimen includes anodized aluminum alloy, architectural glass, galvanized steel, and stainless steel. A literature survey was carried out to obtain the emissivity for these materials. The emissivity of architectural glass used in buildings is 0.84. The information for aluminum and steel is rarely reported, and even when it is reported, the values vary greatly among sources. Therefore, it is more suitable in this case to measure directly the surface emittance. The emissivity measurement was also performed for

stainless steel, which is used to cover the interior surface of the hot box, in order to determine the radiation film coefficient from the test specimen to the hot box surfaces. The emittance of a surface can be determined by bringing the unknown material to the same temperature as a known material and scanning these two surfaces at the same time. The general procedure to measure surface emittance described by Türler (1997) is included in Appendix B.2.

The external reference emitter system was used to measure the surface emittance and the setup is shown in Figure 5.27. Enamel black paint was used as the reference material and the literature-suggested value for emissivity is 0.90. This value was confirmed by comparing the black paint to a piece of glass with emissivity of 0.84. A piece of 2-mm-thick clear glass was glued to the isothermal plate with half of the surface covered with the black paint. After the emittance of the black paint was confirmed as of 0.9, each sample was sealed to the isothermal plate and measured with half of the surface covered with the black paint.
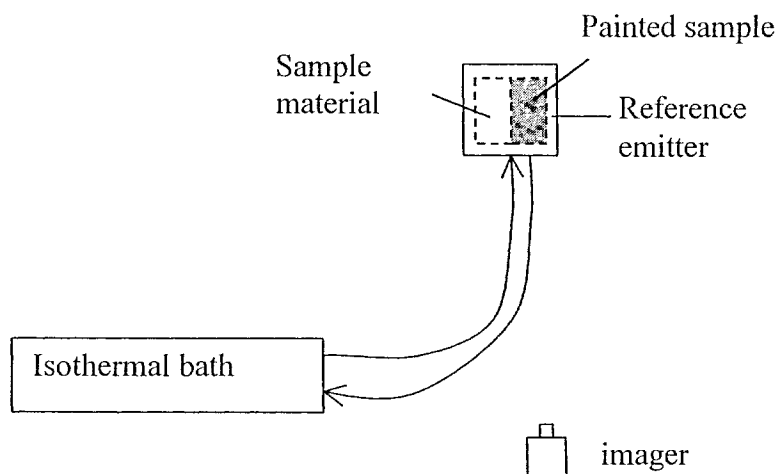
Figure 5.27 Setup of emittance measurement

142

The surface emittance measurements were carried out in a small room inside the laboratory. The air temperature and relative humidity were recorded during the measurements. The enclosure surface temperatures were measured by infrared thermometer and thermocouples. It was found that the background temperature was uniform during the tests and was maintained around 24°C. The equivalent background radiation was verified by taking IR images of the isothermal plate covered by low emissivity aluminum tape (ε= 0.09). The isothermal plate temperature was controlled at 15°C and 40°C. The sample surface temperature was monitored by a 30-gauge type T thermocouple. Several measurements with different scales and center temperatures were performed and the readings were averaged. The measured results are shown in Table 5.12.

Table 5.12 Measured surface emittance

Materials	Emittance
Architectural clear glass (literature)	0.84
Black enamel paint	0.90
Finished aluminum mullion	0.72
Steel	0.20
Stainless steel	0.30

5.4.2 Test conditions and procedure

The infrared scanning was conducted under CSA winter condition before and during the depressurization. The relative humidity inside the hot box was maintained under 25% to avoid condensation on the specimen surface. Moisture condensation on the specimen surface being imaged will alter the surface emittance and change the infrared radiation characteristics. The IR scanning focused on the joint section, where air infiltration may occur. By comparing the thermal images, the impact of air leakage are evaluated. The

test sequence is shown in Figure 5.28. Thermocouple readings were recorded continuously throughout the test.

Steady-state, $\Delta P=150$

Steady-state, $\Delta P=0$

IR measurement | 1 hour | 1 hour | 1 hour | 1 hour | 1 hour
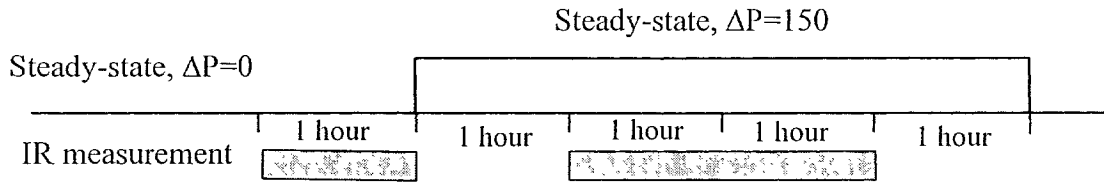
Figure 5.28 Infrared Thermography measurement sequence for air leakage effect

Infrared images were taken from a scaffold platform setup in the hot box at a height between the two horizontal beams as show in Figure 5.26. The IR scanner, supported by a tripod, focused 3 m away and had a view angle offset from normal to the wall surface to prevent the reflections of the cold scanner lens. To avoid the influence of the operator, a thick plastic curtain surrounded the scaffold section, where the imaging was being taken.

The external reference emitter was positioned close and parallel to the specimen surface and stayed in the focus range of the camera while the camera was focused primarily on the specimen. The reference emitter surface temperature was set to within $\pm$ 5°C of the surface temperatures under imaging. A piece of sample material, either glass or aluminum, was sealed to the emitter surface with heat sink compound. The sample surface temperature was measured by a thermocouple. The wall surface was marked with low-emittance aluminum tape to identify the spatial location. The background radiation was evaluated by scanning the reference emitter covered with low-emittance aluminum tape before and after the IR measurements on the test specimen. The infrared images were taken with three different lens, 20°, 12° and 7°. The 20° lens was used for covering

144

half of a glazing panel or half of a spandrel panel. The 12° lens was used for closing up measurement—approximately ¼ panel. The 7° lens was used to capture the detailed frame surface temperatures. To improve the accuracy, multiple images were taken for the same view with different span and center temperature settings on the camera. The results were obtained by averaging these images. When imaging the wall surface, the emittance was set to 1.0. The temperatures read from the thermal images were corrected by giving the correct emittance input in the post-processing software.

The air temperature, and relative humidity were recorded during the infrared measurement. The environmental chamber conditions and the regular measurements of the installed sensors were taken by the data acquisition system. The steel back-pan surface was painted to avoid the significant error in the IR measurement due to its low emittance.

5.4.3 Test results and analyses

5.4.3.1 Data processing procedure

A post-processing software (Irwin 5.1 by AGEMA) was used to extract the temperature readings from the thermograms. The temperatures from the thermograms were adjusted by the surface emittance and background radiation. The background radiation was evaluated by scanning the reference emitter covered with the aluminum tapes.

$$T^4_{\varepsilon=1.0,smpl} = \varepsilon_{smpl}T^4_{smpl} + (1-\varepsilon)T^4_{background} \tag{5.1}$$

$$T^4_{background} = \sum_{i=1}^{n} F_i\varepsilon_iT_i^4 \tag{5.2}$$

where

$T_{e=1.0,\ smpl}$ = equivalent blackbody temperature of the test specimen, K;

ε_{smpl} = emittance of the test specimen, dimensionless;

T_{smpl} = surface temperature of the test specimen, K;

$T_{background}$ = equivalent blackbody temperature of the background, K;

n = number of background enclosure surfaces;

ε_i = emittance of each enclosure surface, dimensionless;

F_i = view factor between enclosure surface and the test specimen, dimensionless;

T_i = surface temperature of each enclosure surface, K.

The averaged surface temperature of the reference emitter was adjusted following the above procedure. The corrected temperature was compared to the direct contact measurement by thermocouples and the deviations were used to scale the rest of the infrared data for the test specimen, shown in equation 5.3.

$$T = T_{IR,smpl} - (T_{IR,\mathrm{Ref}} - T_{DC,\mathrm{Ref}}) \qquad (5.3)$$

where

$T_{IR,\ smpl}$ = temperature of test specimen corrected by emittance and background, K;

$T_{IR,\ Ref}$ = temperature of the reference emitter corrected by emittance and background, K;

$T_{DC,\ Ref}$ = temperature of the reference emitter measured by direct contact thermocouple, K;

T = final temperature of the test specimen, K.

5.4.3.2 Temperature distributions without air leakage

Figure 5.29 shows the thermograms for the top half of the glazing panels G_{a2} and G_{b2}. It shows that the surface of G_{b2} is much warmer than that of G_{a2} and the upper surfaces are warmer than the bottom surfaces. These findings correspond to the thermocouple measurements. The horizontal temperature profiles on the interior surfaces at the middle height of glazing panels G_{a2} and G_{b2} extracted from the thermograms are shown in Figure 5.30. The difference between IR measurements and thermocouple measurements are within 1°C for the center-of-glass. Higher discrepancies exist for the edge-of-glass region.
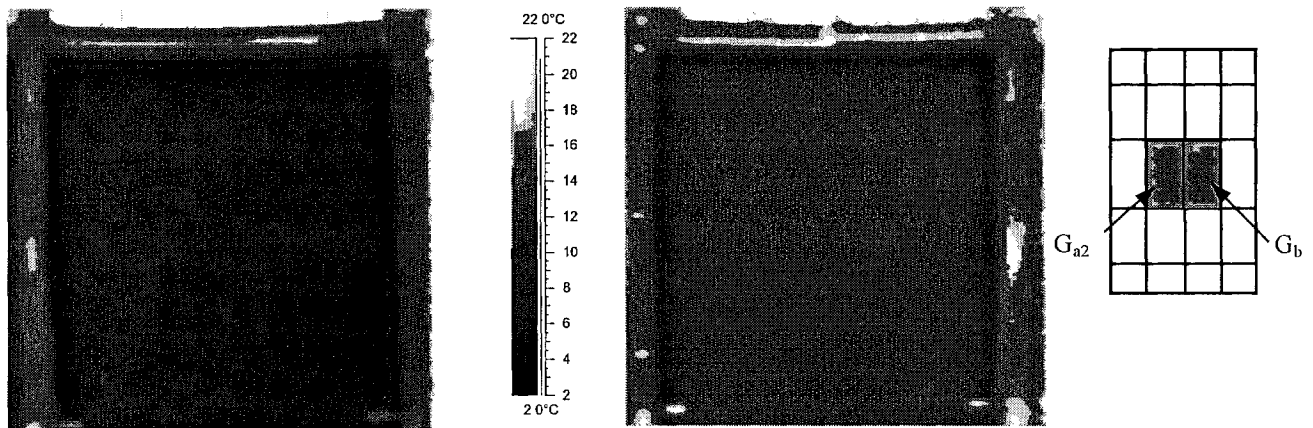
Figure 5. 29 Thermogram for glazing panel G_{a2} and G_{b2} under CSA winter condition
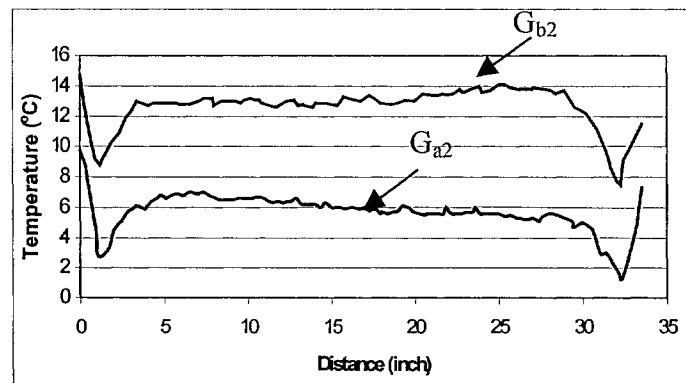
Figure 5.30 Extracted horizontal temperature profiles on glazing surface G_{a2} and G_{b2}

147

The IR measurements found that the temperatures on the vertical mullion surfaces are higher than that on the horizontal surfaces (Figure 5.32a). On the vertical mullion, the temperature in the glazing section is higher than that in the spandrel section. In general, the mullion surface temperature is lower at the corner than it is in the center section. This pattern concurs with the thermocouple measurements and is due to the effect of different aluminum surfaces exposed to indoor air and different local film coefficients. Approximately 3°C to 5°C higher temperature was captured on the mullion surface in system B than that in system A. This difference is lower than that measured by thermocouples. The thermocouple measurements show about 6°C to 7.8°C difference between the frame surfaces in the two wall systems.

The surface temperature on the back-pan of system B is slightly warmer than that in system A, but it is not obvious in the thermogram shown in Figure5.31 due to the large temperature range. .

a) System A   b) system B
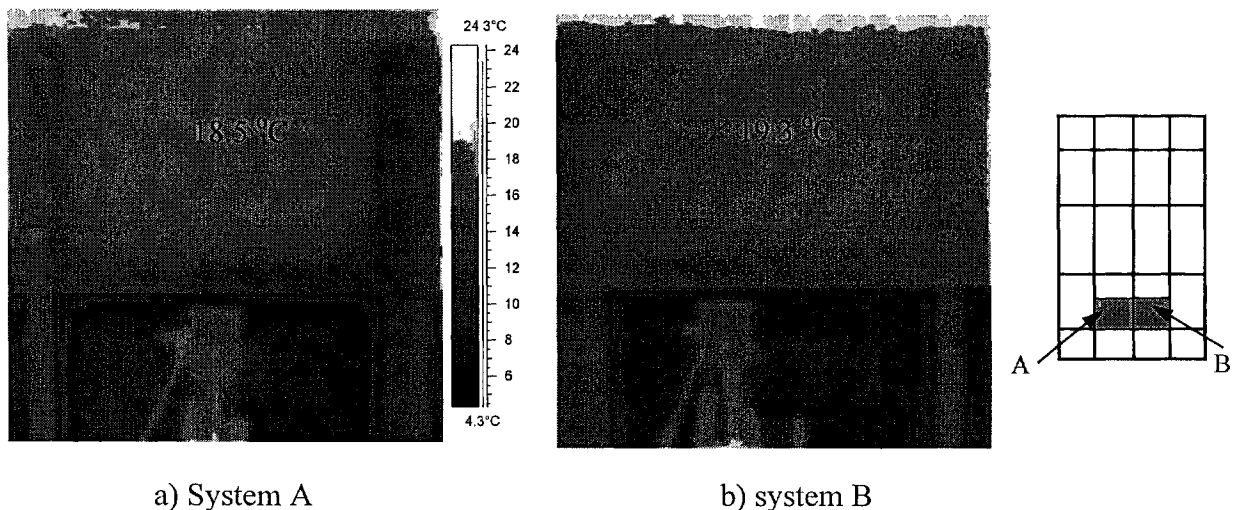
Figure 5.31 Thermograms for spandrel panels

5.4.3.3   Effect of air infiltration

The infrared scanning for evaluating air leakage effect focused on the joint section only since these are the most likely places for air leakage paths. The relatively high airtightness of metal curtain walls, and the high conductivity of metal made the air leakage paths not very obvious in the thermograms. However, the effect of air leakage were qualitatively indicated by comparing the surface temperature before and during the depressurization. The relative humidity in the hot box was maintained under 25% before the depressurization and condensation was observed at the edge of glazing panels in system A, but no noticeable condensation at the edge of the middle glazing panels in system B. No condensation was observed on the mullion surface. The test was carried out in mid-August. When the depressurization was started, the humid air from the laboratory outside the environmental chamber was pulled into the hot box and the relative humidity was increased to 35%. Both the air infiltration and the increased relative humidity contributed to more condensation at the edge-of glazing panels for system A, even on the mullion surface at the bottom.

A few typical thermograms before and during the depressurization for mullion sections are shown in Figure 5.32 to 5.34. The mullion surface temperature before the depressurization is labeled in Figure 5.32a, but not during the depressurization because the accumulation of condensation on the mullion surface altered the surface emissivity, which made the readings not meaningful anymore.

149
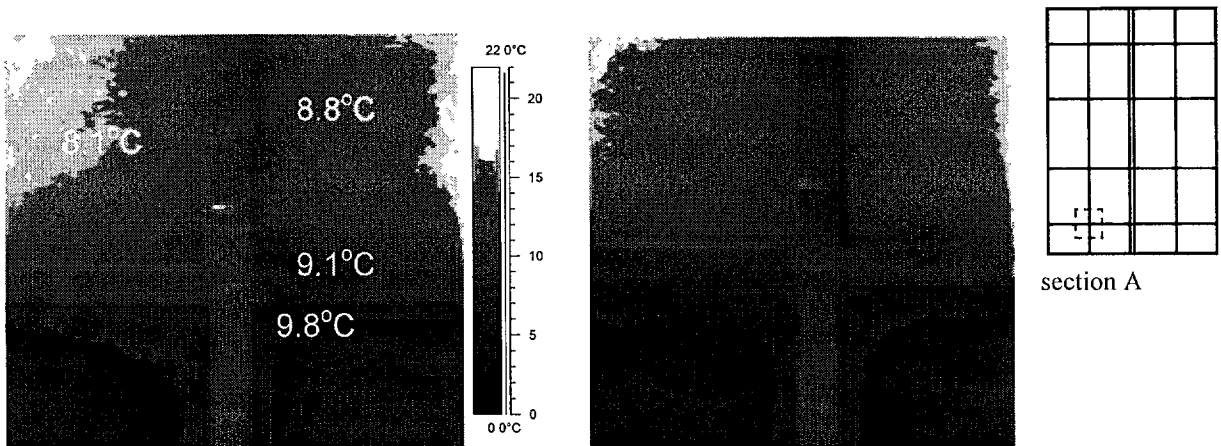
(a) before depressurization   (b) during depressurization

Figure 5.32 Thermograms for section A before and during depressurization

The lower surface temperature in Figure 5.33b reveals the effect of air leakage but not significantly. The temperature at point C drops dramatically, which implies cold air passed through at this location and the visual observation proved that there was a small crack at the sealant. Figure 5.34 shows section AB, which is the joint section between these two systems. The difference between these two systems is obviously revealed by the surface temperatures. Condensation formed on the mullion surface in system A during depressurization, but not on the mullion surface of system B.

(a) before depressurization   (b) during depressurization
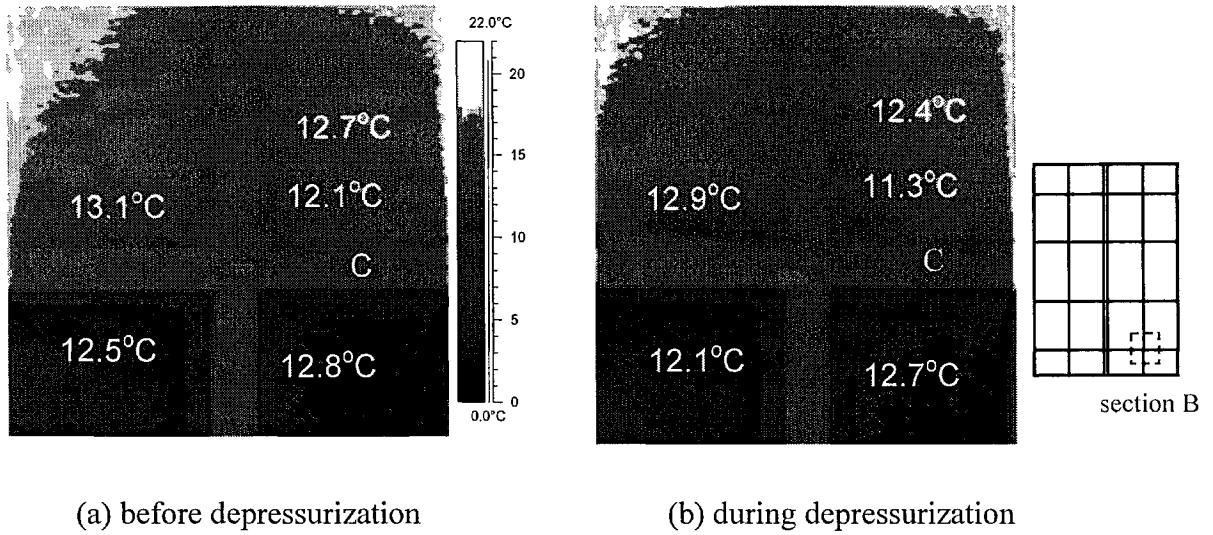
Figure 5.33 Thermograms for section B before and during depressurization

(a) before depressurization   (b) during depressurization
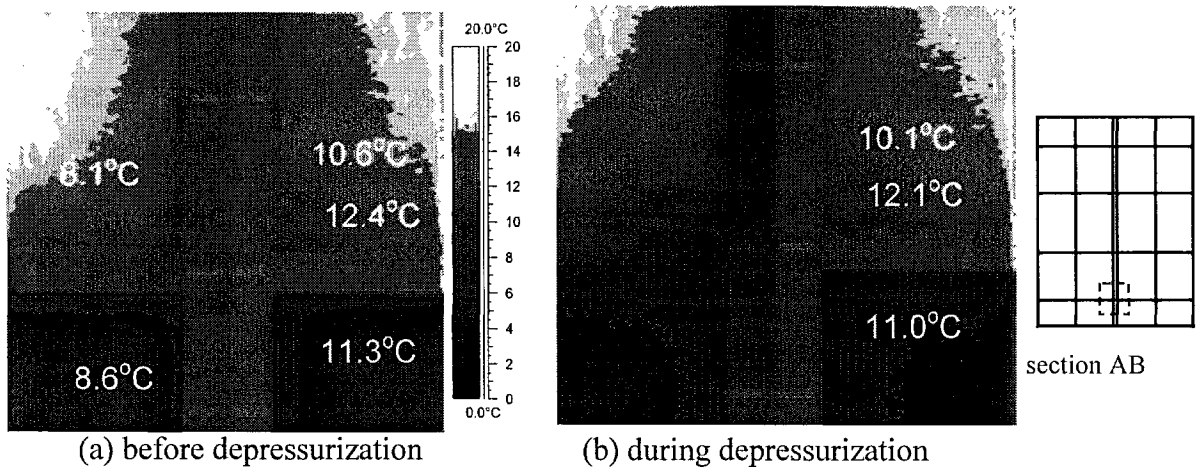
Figure 5.34 Thermograms for section AB before and during depressurization

In summary, the large size of the test specimen, the complex configuration, and the large temperature variation have made it difficult to obtain accurate IR measurement in this

test. The use of the reference emitter has improved the accuracy of the IR measurements. The results clearly showed the relative performance of these two curtain wall systems and the thermally improved curtain wall system provides better thermal performance.

Due to the high airtightness of the curtain wall specimen and high conductivity of aluminum, the air leakage paths cannot be clearly identified in the IR images. However, the effect of air leakage has been indicated by the change of the surface temperature. The perimeters along the spandrel panels are more likely the potential air leakage paths.

5.5 Conclusion

The analysis on extensive temperature measurements demonstrates the effect of design details on the thermal performance of metal curtain walls. For example, the high performance glazing panels have a $5.5^{\circ}C$ warmer surface temperature. The larger thermal break in system B results in 6 to $7.8^{\circ}C$ higher surface temperature on the frame and $1.7^{\circ}C$ higher temperature on the back-pan surface under CSA winter conditions. The temperature distribution is also sensitive to local film coefficients. The sensitivity decreases when the components are better insulated. High performance glazing units provide 20% higher condensation resistance than standard double IGU, and frames with larger thermal breaks provide 30% higher condensation resistance than regular frame systems. The cyclic tests confirmed that better performing frames have smaller temperature variations and longer time lags to outdoor air temperature swings.

The study on the effect of the introduced air infiltration has identified the potential air leakage paths for metal curtain walls under tests, and provided information on the increased condensation risks. The results suggest that the curtain walls tested have good airtightness and the impact of the introduced air infiltration on the condensation resistance factor is insignificant on the glazing unit but considerable on the frame.

The infrared thermography measurements also confirmed the relative performance of these two curtain wall systems in parallel with the direct temperature measurements. Due to the high airtightness of the curtain wall specimen and high conductivity of aluminum, the air leakage paths were not clearly shown in the IR images. However, the effect of air leakage was indicated by the change of the surface temperature. The perimeters along the spandrel panels are more likely the locations of air leakage paths.

Chapter 6

Determination of surface film coefficients

6.1 Introduction

The indoor and outdoor film coefficients are necessary information for the correct interpretation of test results and for comparisons in results between laboratories. The accurate determination of the surface coefficients is important for obtaining accurate results in computer simulations. In standard test methods of ASTM C1199 (2000) a Calibration Transfer Standard (CTS) panel is used to determine an average surface film coefficient. The surface film coefficient determined from a CTS may be different from values in actual tests for fenestration systems since the thermal resistance and surface temperatures of an actual fenestration system are much lower than the CTS. In addition, frames or sashes of the actual fenestration system alter the local flow and local film coefficient. The CTS is a flat plate without frame and the flow pattern developed along its surface is different than that developed along the actual fenestration products.

The CTS method to quantify the surface film coefficient is not used in this research project because of two reasons. First, the full-scale two-storey high wall sample makes CTS measurement difficult and expensive. Secondly, CTS measurements give only an average surface coefficient, while the local heat transfer and local film coefficient are the interests of this study. The approaches to determine the surface film coefficients

154

employed include a direct measurement for the indoor local convection coefficient, calculation for the outdoor convection coefficient using the correlation recommended by ASHRAE based on the measured air velocity, and calculation of local radiation coefficient with known surface temperatures and surface emittance. The details are discussed in the following sections.

6.2 Indoor convection heat transfer coefficient

As reviewed in section 2.3.3.1, the convection coefficient varies over the fenestration surface and is lower near heads and sills due to flow stagnation. The use of one constant film coefficient in simulations is one of the reasons for the discrepancies in temperature distributions between simulations and tests. An approach to directly measure the local convection coefficient over the interior glazing surfaces is adopted in this study. A similar method was used in studies by Griffith, et al., (1998b).

6.2.1 Theoretical foundation

Based on the classic free convection theory (Raithby and Hollands, 1975), the boundary layer formed over a vertical plate includes both a fluid boundary layer characterized by a velocity profile and a thermal boundary layer characterized by a temperature profile. Typical temperature and velocity profiles over a cool vertical plate are shown in Figure 6.1. One feature of the free natural convection is that the boundary layer can be divided into the inner and outer regions by a local maximum in the air velocity profile. In the inner region, viscous and buoyancy forces are balanced and there is no momentum transfer perpendicular to the wall. In the outer region, buoyancy and acceleration forces

are balanced and momentum transfer exists. As there is no mass transfer within the inner region, pure conduction heat transfer can be reasonably assumed. Therefore, the temperature profile can be linearly approximated within the inner region and Fourier's equation for heat transfer can be used to calculate the heat flux:

$$q_c = k(\frac{DT}{Dy})$$

(6.1)

The local convection film coefficient can be obtained using the following equation:

$$h_c = \frac{q_c}{(T_\infty - T_{surf})}$$

(6.2)

where

q_c = heat flow delivered to the surface by convection (W/m^2),

h_c = convection film coefficient (W/m^2·K),

k = thermal conductivity of still air (W/m·K),

T = air temperature (K),

y = distance from plate (m),

T_∞ = mainstream air temperature (K),

T_{surf} = surface temperature (K).

The inner region can be identified by finding the location of the maximum air velocity if the typical air velocity profile can be obtained by measurements. Then, the local convection coefficients can be calculated using equations 6.1 & 6.2 with the measured linear air temperature distribution profile within the inner region. Therefore, the important parameters to be measured accurately are air velocity, air temperature and the increment of the corresponding distances from the glazing surfaces.

156
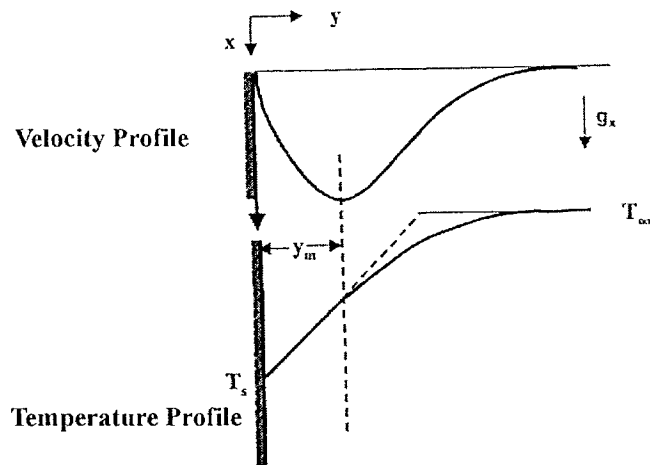
Figure 6.1 Velocity and temperature profile within the free-convection boundary layer
(Raithby & Hollands, 1975)

6.2.2 Experimental setup

A customized 3-dimensional computer controlled traverse system has been designed and
built to carry out the measurements within a very close region to the glass surface (within
10mm). The sketch of the setup is shown in Figure 6.2. The 3-D traverse system can
reach a space volume of 4.1m long, 1.8m high and 0.3m deep near the glass surface and
can cover the entire test specimen horizontally and the middle glazing section vertically.
It can be programmed and controlled by a computer to position and measure along pre-
programmed 3-dimensional routes.

Three step motors were used to control the movement of the axes with high resolutions.
For the depth axis, the movement can be as small as 0.004 mm. This high spatial
resolution is important in the experiment since the inner region of the boundary layer is
very close to the glass surface and the calculation of convection coefficient depends on

157

the temperature gradient, which requires the precise measurement of the distance between two points.

A low velocity omni-dimensional hot sphere anemometer was used to measure the air velocity. To reduce the impact of the sensor on the natural convection flow, the anemometer chosen has a small tip with a diameter of 0.75 mm. The specification of the anemometer is shown in Table 6.1. A 30-gauge copper and constantan thermocouple was used to measure the air temperature. Although the accuracy of thermocouples is within ±0.5°C, the resolution and repeatability of thermocouples in temperature measurements is within ±0.1°C.

Table 6.1 Specifications for omni-dimensional anemometer

Parameter	Specification
Range	0.01~1 m/s
Accuracy	± 1.0% full scale, ± 1.5% reading
Auto temperature compensation	30°C
Reaction Time	100ms

The wall surface may not be perfectly flat due to the thermal expansion and contraction, or the installation alignment. To provide precise distance positioning and to protect the sensors against touching the surface, a mechanical surface detector was integrated into the measurement device. This detector is made of a thin steel rod that is mechanically connected to a limit switch. When the depth axis moves towards the surface, the limit switch is activated as soon as the tip of the steel rod touches the surface and the axis motion is stopped. The wall surface is defined as the origin of the coordination in depth direction. The surface detector, thermocouple and the anemometer were mechanically fixed together and were attached to the depth axis, as shown in Figure 6.3. The wall

surface is not flat because of the presence of frames and spandrel panels. To avoid any possible damage to the anemometer, two limit switches for each axis were installed. With these limit switches, the probe can move only within a pre-defined area. The position of these limit switches can be manually located before each test.
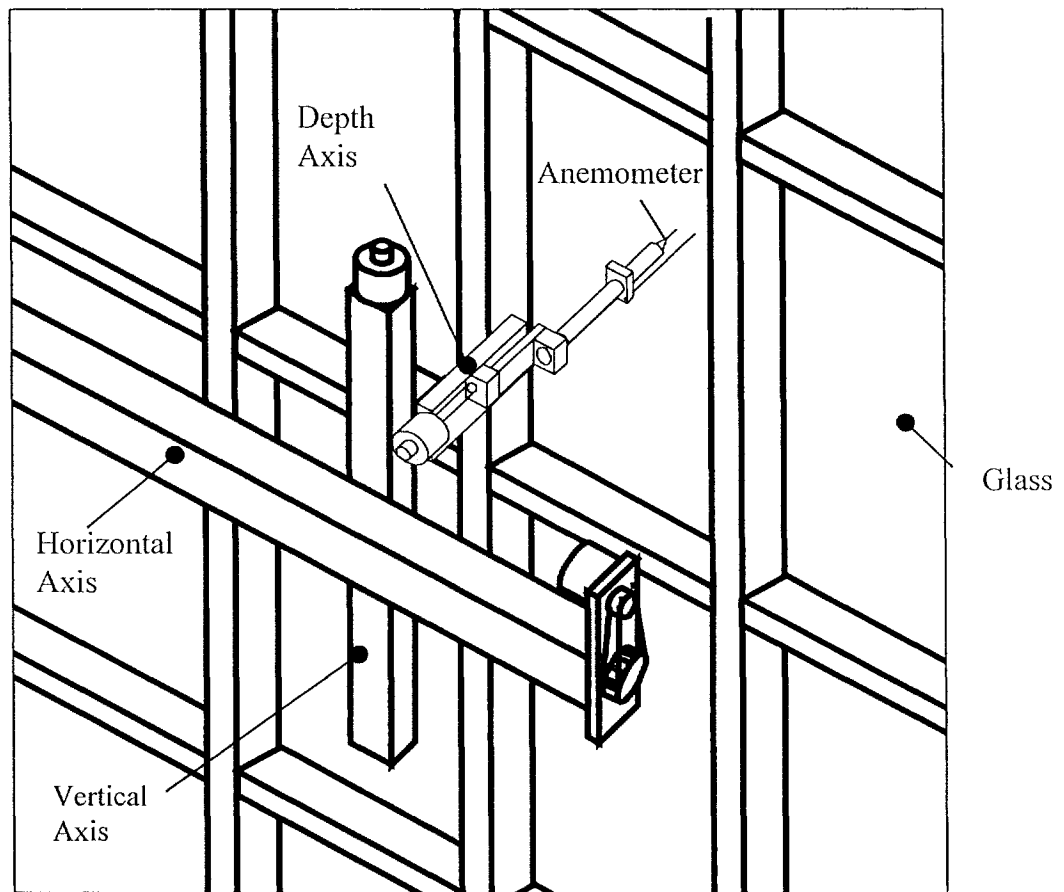
Figure 6.2 Layout of the 3-dimensional traverse system for air velocity and temperature measurements
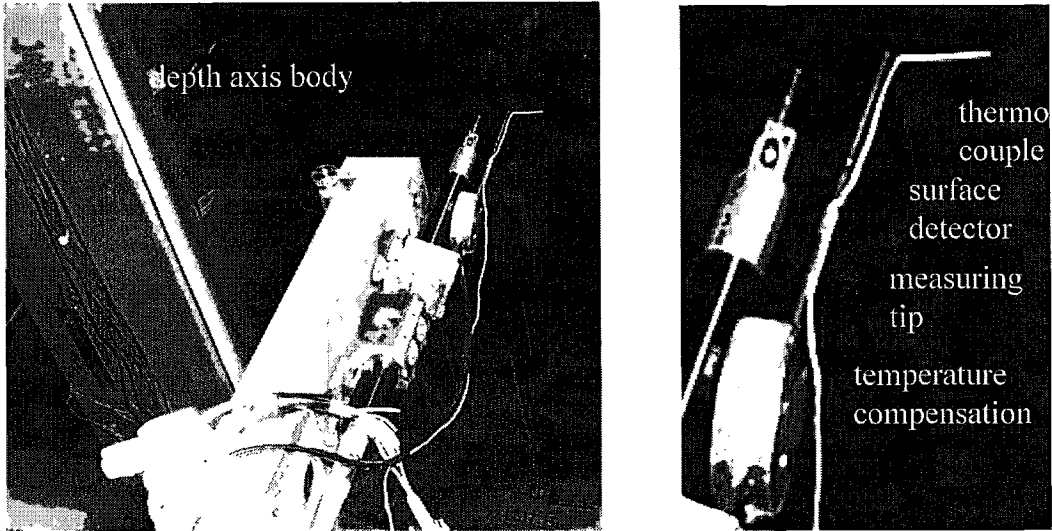
Figure 6.3. Sensors and surface detector of the measurement device

A customized program was developed using a high-level data acquisition software (Labview 5.1, from National Instruments inc.). This program can position the probe, perform measurements and store data automatically. Figure 6.4 shows the axis movement control interface. The operation sequence of moving probe and taking measurements is defined by macros. There are six types of macros and their functions are listed in Table 6.2.
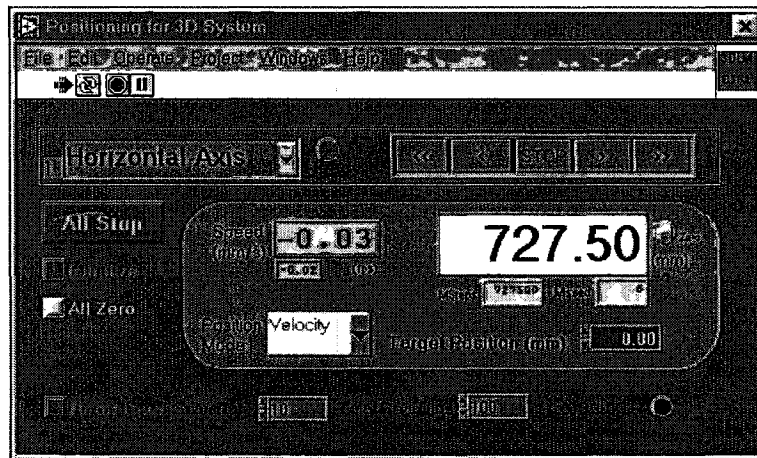
Figure 6.4 Movement control interface in 3-dimensional automatic measurement program

Table 6.2 Types of Macros and their functions

Macro Type	Description of function
Go to Home	Move the depth axis to the wall surface, where is defined as the origin for the depth axis
Move relative	Move a specific axis by a specified distance relative to the current position,
Move absolute	Move a specific axis to a specified position
Measurement	Perform the measurement with defined scan rate (Hz), number of scans, and duration of the scan
Wait	Wait for specified seconds.
Loop	Perform repeated actions

An example of the complete macro is shown below.

```
0: +  Wait 1 seconds
1: | Axis 3 Goto Home
2: +  + Wait 10 seconds
3: |  | Measurementrate 20, scans 3000
4: |  | Axis 3 Move Relative by 0.30 mm
5: | Axis 3 Loopto #2 N=14
6: +  + Wait 10 seconds
7: |  | Measurementrate 20, scans 3000
8: |  | Axis 3 Move Relative by 0.50 mm
9: | Axis 3 Loopto #6 N=9
10: +  + Wait 10 seconds
11: |  | Measurementrate 20, scans 3000
12: |  | Axis 3 Move Relative by 1.00 mm
13: | Axis 3 Loopto #10 N=9
14: +  + Wait 10 seconds
15: |  | Measurementrate 20, scans 3000
16: |  | Axis 3 Move Relative by 5.00 mm
17: | Axis 3 Loopto #14 N=9
18: +  + Wait 10 seconds
19: |  | Measurementrate 20, scans 1200
20: |  | Axis 3 Move Relative by 10.00 mm
21: | Axis 3 Loopto #18 N=7
22: | Axis 2 Move Relative by 127.00 mm
23:Axis 2 Loopto #0 N=13
```

When defining the macro sequence for a test, the measurement points can be previewed

graphically before the test.   For example, Figure 6.5 shows the corresponding

measurement locations for the macro listed above. The graphic preview is very useful to

check the correctness of the planned test. When the correct macro sequence are defined, the positioning, measurement and data storage can be performed automatically by the program. Real-time measurements can be graphically displayed as shown in Figure 6.6. The data recorded at each planned location include the time of the measurements, location of the sensors, and statistics of the measured air velocities and air temperatures. The instantaneous values of velocities and temperatures were also recorded in separate data files for each location for potential post-processing.
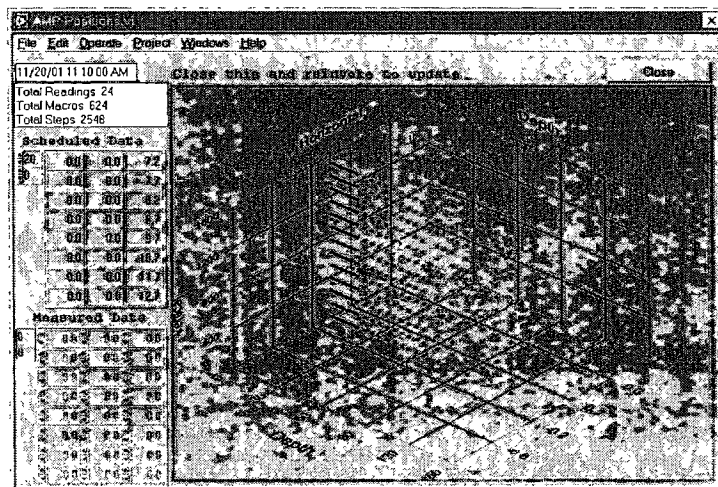
Figure 6.5. An example of graphical display of measurement locations
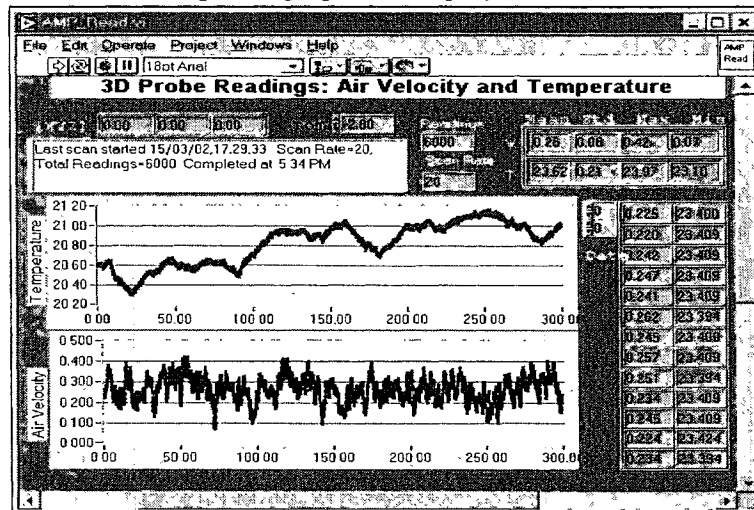
Figure 6.6 An example of real-time display of measured air temperature and air velocity

162

6.2.3 Test procedure

The suitable sampling frequency and measurement duration need to be determined to ensure that the measurements can capture the dynamic characteristics of the airflow. Air velocities and temperatures at one location near the glazing surface were measured for 10 minutes under the test condition of $-18°C$ outside and $21°C$ inside. A spectrum analysis for air velocities was conducted and the results are shown in Figure 6.7. The power density function decreases slowly up to frequencies of 0.1 Hz and then decreases rapidly with the frequency. At 0.5Hz the power density is more than 100 times smaller than the value at the lowest analyzed frequency of 0.005Hz. In this case, the air velocity fluctuations with a frequency up to 0.3 Hz make the greatest contribution to the power spectrum. Figure 6.8 shows the spectral analysis for the air temperature with similar frequency patterns. To measure the flow characteristics at low frequencies, a longer sampling period will be better, but it takes more time. Considering the amount of measurements to be done and the time it requires, the sampling period of 1 minute and the sampling frequency of 20 Hz were chosen based on the spectrum-power analysis.
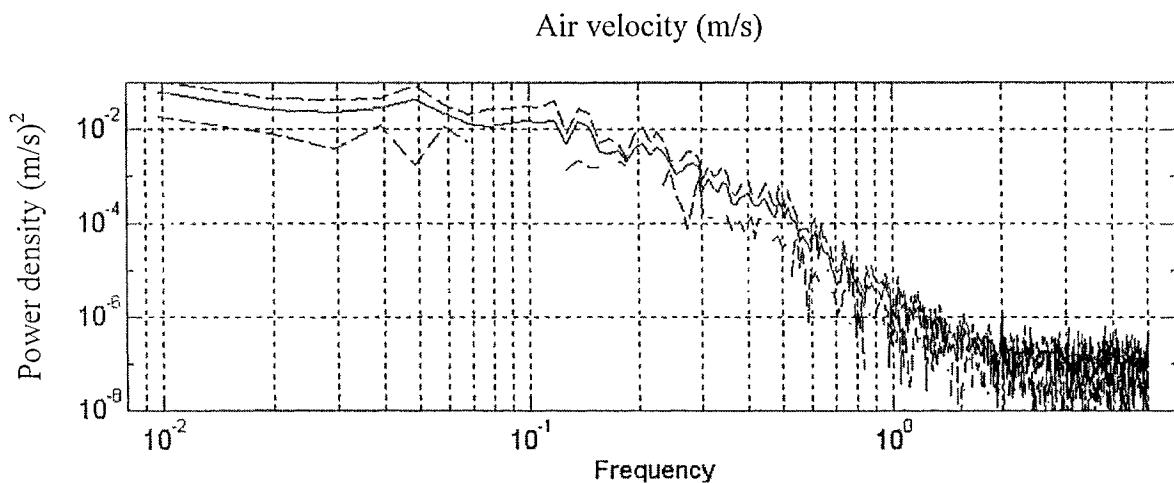
Figure 6.7 Power density function for air velocity measured under CSA winter condition
(dashed lines show the upper and lower confidence bounds)
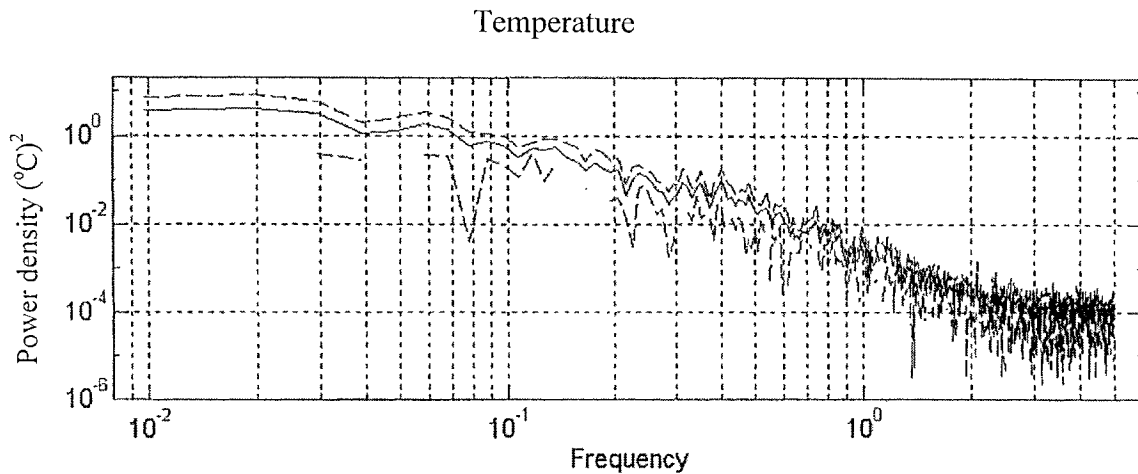
Temperature

Figure 6.8. Power density function for air temperature measured under CSA winter condition (dashed lines show the upper and lower confidence bounds)

The measurements include three stages: move the probe to the pre-defined position, wait and take measurements. Since the depth axis movement is very slow (2 mm/s), the waiting period is specified to be 10 seconds.

The boundary layer measurements were performed for the glazing panels, mullion surfaces, and spandrel panels with the glazing surface being the main focus. Over the glazing surface, the measurement grids were placed more closely at edge-of-glass region since the local film coefficients at this region is one of the main interest of this study. The glazing panel is 1.778m high. The measurements were taken vertically between 12.7mm and 1650mm from the bottom sight-line with 12.7mm (1") interval for the first 127mm, and with 127mm (5") interval for the rest of the panel. Along the depth direction of a location over the glazing panels, measurements extend from 1 mm to 110 mm from the surface. Measurements were taken every 0.3mm for the first 5mm from the surface, and the spatial resolution of measurement grid gradually decreases to 5 mm at the distance of 50 mm. From 50mm to 110mm, the measurements were taken every

10mm. On average, it took about one hour to complete the measurements for one location.

6.2.4 Test conditions

Most of the measurements were carried out under CSA winter condition, which is −18°C outdoor and 21°C indoor. The indoor relative humidity was kept under 25% to avoid condensation at the edge of the glass since the presence of any water or frost may affect the probe and the measurements. Besides the CSA winter condition, two more winter conditions of −24°C, and −32°C in the cold box, and 21°C in the hot box were simulated. Under these two conditions, only the vertical profiles for the glazing panels were measured. The 3-dimensional temperature measurements across the wall assembly were recorded during the convection coefficient measurements. The recorded glass surface temperatures were used to calculate the convection coefficient.

6.2.5 Results and analyses

The measurements were performed 3-dimensionally over each glazing panel. However, the result analyses presented in this thesis focus on the measurements along the vertical centerlines of glazing panel G_{a1} in system A and glazing panel G_{b1} in system B. The determined local convection coefficient will be used in 2-dimensional FRAME simulations. The labeling of the glazing panels is shown in Figure 3.3 of chapter 3.

The results presented in this section include the velocity and temperature profiles measured for the boundary layer and the local convection film coefficients calculated

using the measured data for each wall system. The measured results are also compared between different test conditions for both wall systems.

6.2.5.1   System A

Figure 6.9 shows the selected air velocity profiles in the direction normal to the glass surface at four different distances from the bottom sight-line along the vertical centerline of glazing panel G_{a1} under CSA winter condition. The measured air velocity profiles indicate the existence of a maximum air velocity in the region near to the glass surface. When the cold air flows down the glass surface, the air velocity increases and the inner boundary gets thicker. For example, at distance of 1270mm from the bottom sight-line, the maximum air velocity is 0.47m/s and occurs at 2.7mm from the surface, which at distance of 204mm from the bottom sight-line, the maximum air velocity increases to 0.63 m/s and occurs at 4.4mm from the glass surface. The maximum air velocity occurs within 2.5mm~5mm for the center-of-glass region. At the bottom, the inner boundary layer gets as thick as 12mm. When the measurements extend to 1650mm from bottom sight-line, which is 127mm (5") from the top sight-line, the air velocity decreases to 0.13m/s for the first 20mm from the glass surface and then gradually increases to the velocity of the mainstream air flow (Figure 6.9). The different air velocity profiles at distance of 1650mm suggest that the airflow is in the re-circulation region after the head frame.
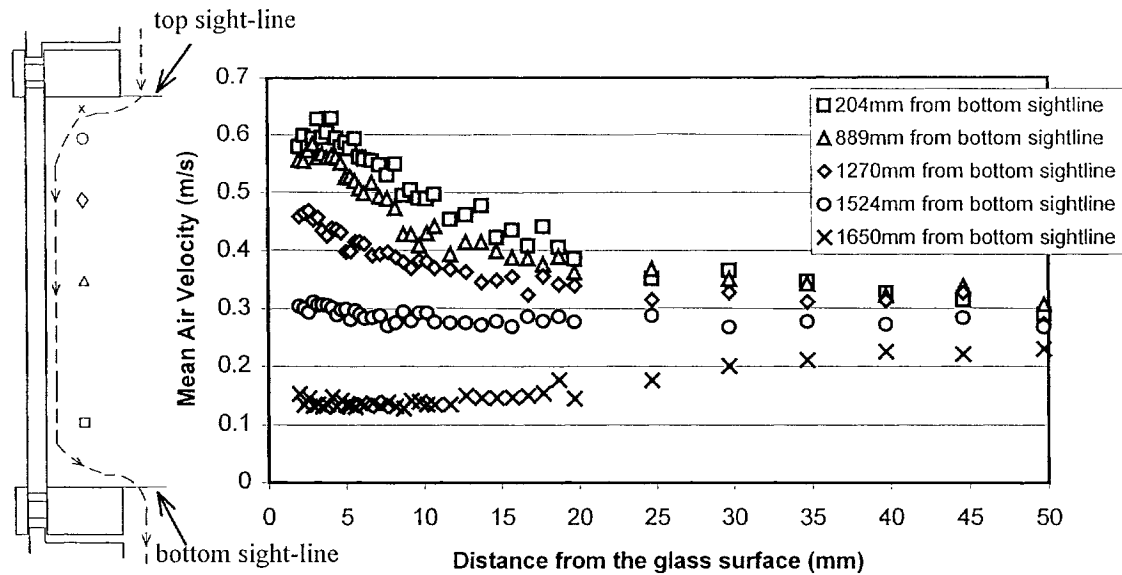
Figure 6.9 Selected air velocity profiles in the direction normal to the glass surface at four different distances from the bottom sight-line along the vertical centerline of glazing panel G_{a1} under CSA winter condition

Figure 6.10 shows the corresponding temperature profiles at these five different locations. The temperature profiles indicate good linearity in regions very close to the glass surface. The temperature gradient increases slightly with the increase of the distance from the bottom sight-line except for the location of 1650mm from the bottom sight-line. As indicated in Figure 6.9, the airflow is in the re-circulation region and has lower convection film coefficient at 1650mm from the bottom sight-line. These findings comply with the free convection theory.
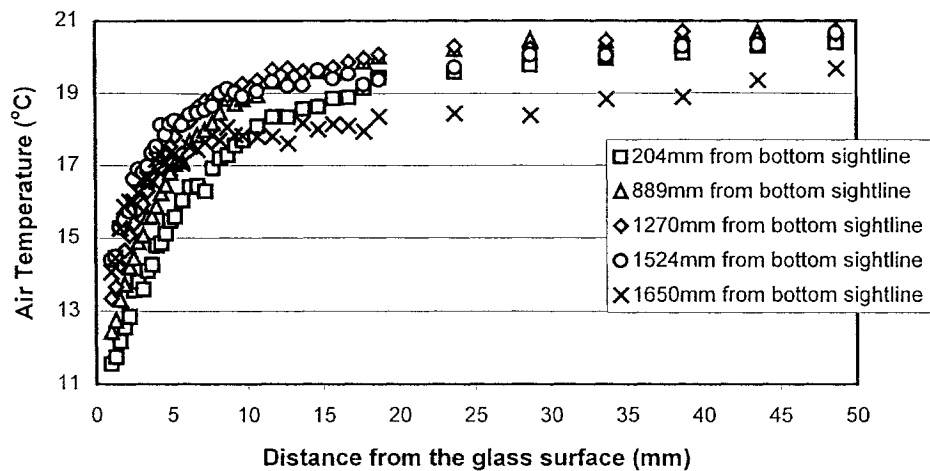
Figure 6.10 Selected air temperature profiles in the direction normal to the glass surface at four different distances from the bottom sight-line along the vertical centerline of the glazing panel G_{a1} under CSA winter condition

Selected vertical profiles of air velocities at three distances from the surface along the vertical centerline of glazing panel G_{a1} are shown in Figure 6.11. From these profiles, the development of the boundary layer along the glazing surface is clearly shown. For an isothermal plane without sills, the air velocity increases with the distance from the top of the plate. However, for a real window with head and sill, flow stagnation occurs at these places, which can be indicated by much lower velocities as shown at the bottom and top in Figure 6.11. For the airflow at 3mm away from the surface, it starts slowing down at about 400 mm above the sight-line and the air velocity decreases to about 0.2m/s at 12.7mm from the sill. For the air flow at 10mm away from the surface, the flow pattern is same, but it starts slowing down at about 300mm above the sight-line. The air velocity in the mainstream, which is shown in Figure 6.11 as 104mm, is almost uniform along the glazing surface except for the bottom. At the bottom, the airflow is redirected to flow off

168

the frame and the air velocity increases to 0.45 m/s. At the top, in the stagnation flow

region, the measured air velocity is as low as 0.13m/s.
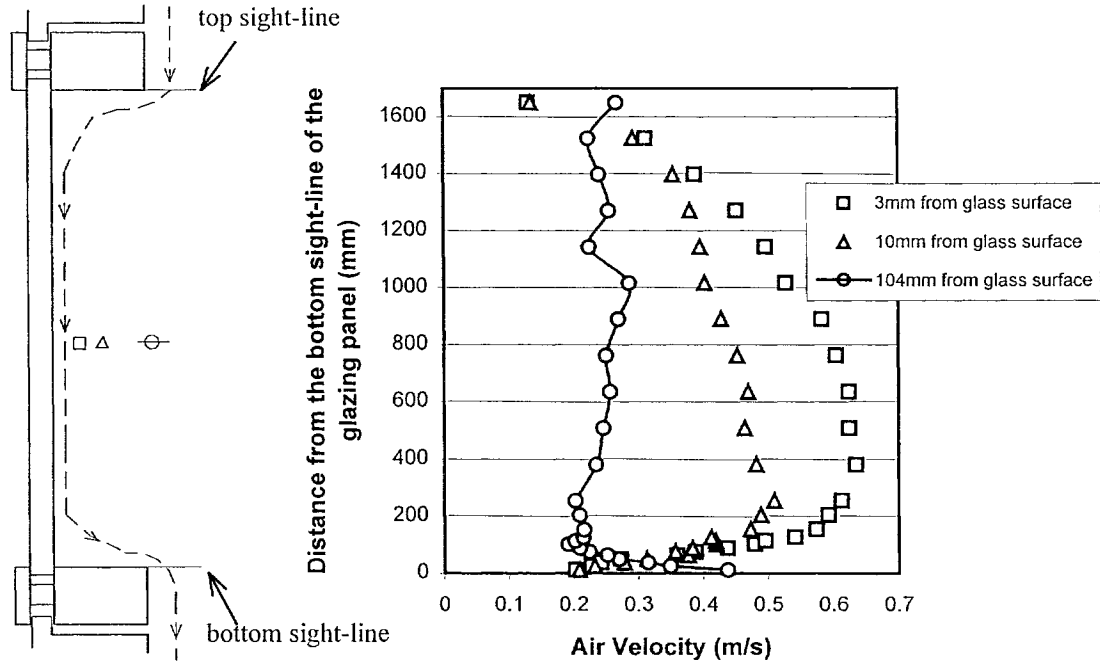
Figure 6.11 Selected vertical profiles of air velocity at different distances from the
surface along the centerline of glazing panel G_{a1} under CSA winter condition

The measured air velocity and temperature profiles in the boundary layer indicate that

natural convection dominates along the glazing surface under the test conditions, and

pure conduction can be reasonably assumed in the inner region. Thus, Equations 6.1 &

6.2 can be used to determine the local convection coefficient. The first seven

measurements, positioned within 3mm from the surface, were used to calculate the

temperature gradient within the inner boundary region. The thermal conductivity of air

was evaluated based on a linear interpolation of two literature values for k, 0.02408

W/m·K at 0°C and 0.02614 W/m·K at 26.85°C (Liley 1968) by using the air temperature

at the middle point. The surface temperatures measured by thermocouples are limited to

nine points along the centerline, as shown in Figure 5.3 of chapter 5. A linear interpolation was employed to obtain the surface temperatures where direct measurements were not available. The calculated local convection coefficients along the vertical centerline of glazing panel G_{al} are shown in Figure 6.12.
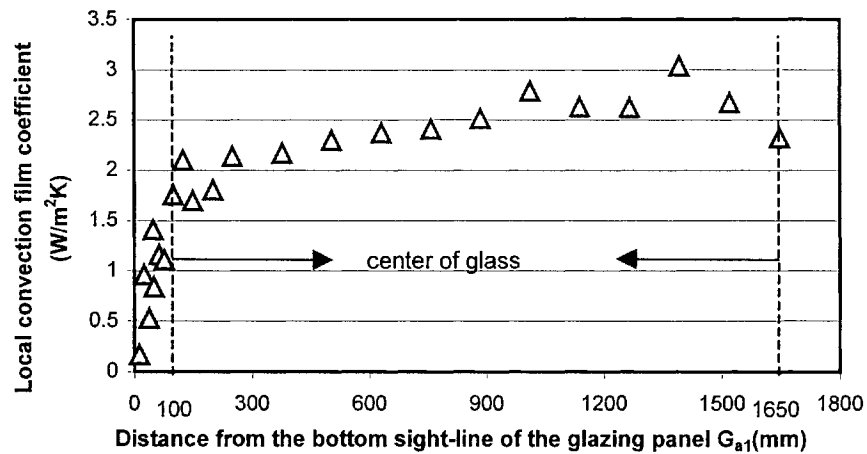
Figure 6.12 Local convection film coefficients along vertical centerline of glazing G_{al}

The results in Figure 6.12 reveal the trend of the local convection film coefficients along the vertical centerline of the glazing surface. In the center-of-glass region as indicated in Figure 6.12, the convection coefficients increase slightly with height and reach a value as high as 3 $W/m^2 \cdot K$, and then drops down to 2.32 $W/m^2 \cdot K$ when the re-circulation region after the head frame is approached at height of 1650mm. Within the 100mm of the bottom edge-of-glass area, the convection coefficients drop significantly when the airflow approaches the frame. The value reaches about 0.17 $W/m^2 \cdot K$ at 12.7mm from the bottom sight-line.

The outdoor conditions affect the development of natural convection and the resulting convective heat transfer coefficients over the interior glazing surface. The measured air

170

velocities and calculated convection film coefficients under three test conditions are compared. Figure 6.13 shows the vertical air velocity profiles under the three test conditions at 3 mm away from the surface along the centerline of glazing panel G_{a1} in system A. It clearly indicates that the natural convection becomes stronger and the air velocity gets greater when the temperature differences between the glass surface and the room air increases due to the decrease of the outdoor temperatures. Figure 6.14 shows the measured local convection coefficients along the vertical centerline of glazing panel G_{a1} at center-of-glass region under these three test conditions. It indicates that the interior convection film coefficient slightly increases when the outdoor temperature drops. However, it is within the range of $2\sim3\,\text{W/m}^2\cdot\text{K}$ at the center-of-glass region under the conditions tested. At the top of the glazing panel, where the natural convection starts, there is no noticeable difference among the convection film coefficients measured under the three conditions.
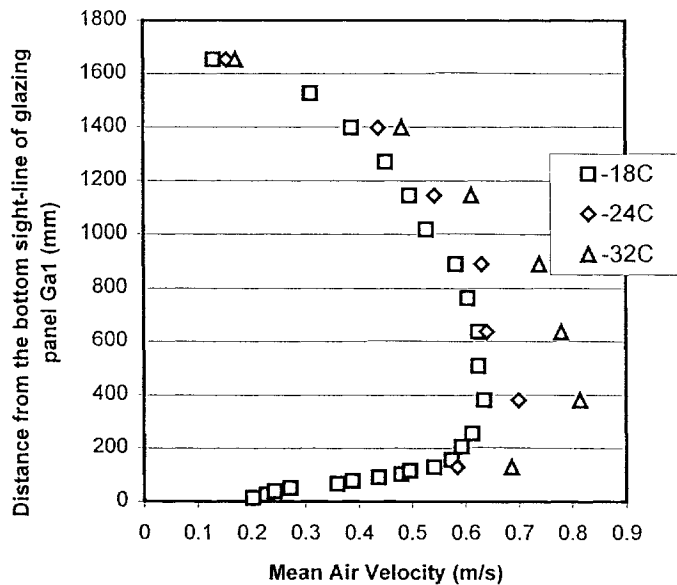
Figure 6.13 Vertical air velocity profiles at 3mm from the surface along the vertical centerline of glazing panel G_{a1} in system A under three different test conditions

171
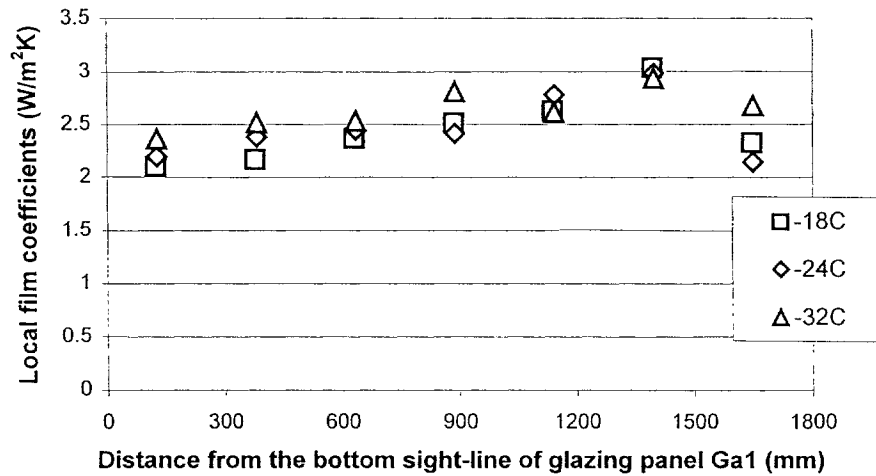
Figure 6.14 Local convection film coefficients along the vertical centerline of glazing panel G_{a1} in system A under three test conditions

6.2.5.2 System B

The same analysis is applied to glazing panel G_{b1} in system B. Air velocity profiles and air temperature profiles in the direction normal to glass surfaces at three different distances from the bottom sight-line along the centerline of the glazing panel G_{b1} are shown in Figure 6.15 and Figure 6.16. Both the air velocity and air temperature profiles have similar patterns to that in system A, which indicates that the free convection dominates in the boundary layer. However, the air velocity developed along the glazing surface is smaller and the inner boundary layer is thicker than that in system A because of the higher surface temperature and smaller temperature differences between the glazing surface and the ambient air. The maximum air velocity ranges from 0.2m/s to 0.39 m/s and occurs within 3~6mm from the glass surface. The local convection film coefficients along the vertical centerline are shown in Figure 6.17. It has similar but slightly different pattern to that of system A (Figure 6.12). The air velocity patterns along the vertical centerline of glazing panel G_{b1} under CSA winter conditions are shown in Figure 6.18 at

172

different distances from the glass surface.
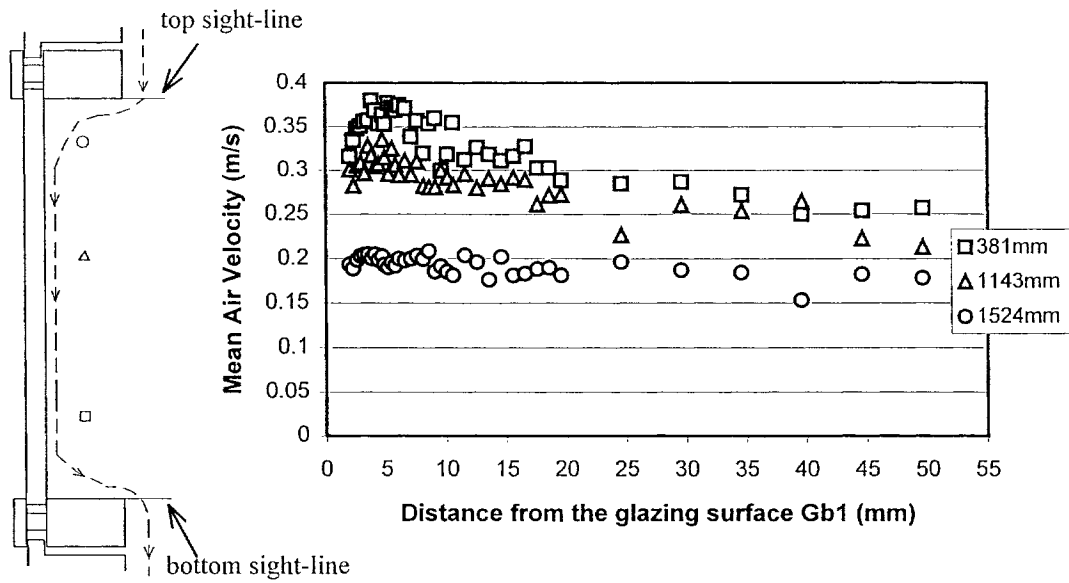
Figure 6.15 Selected air velocity profiles in the direction normal to glass surface at three different distances from the bottom sight-line along the vertical centerline of glazing panel G_{b1} in system B under CSA winter condition
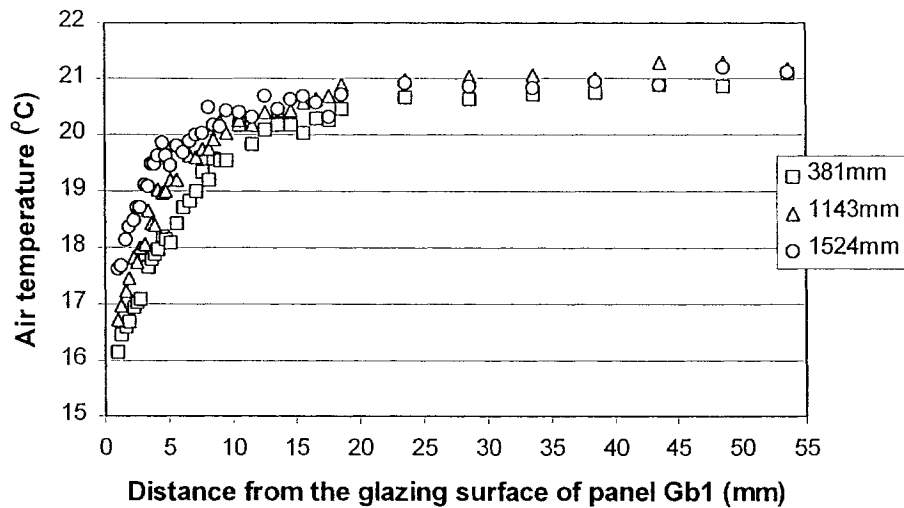
Figure 6.16 Selected air temperature profiles in the direction normal to the glass surface at three different distances from the bottom sight-line along the vertical centerline of the glazing panel G_{b1} in system B under CSA winter condition
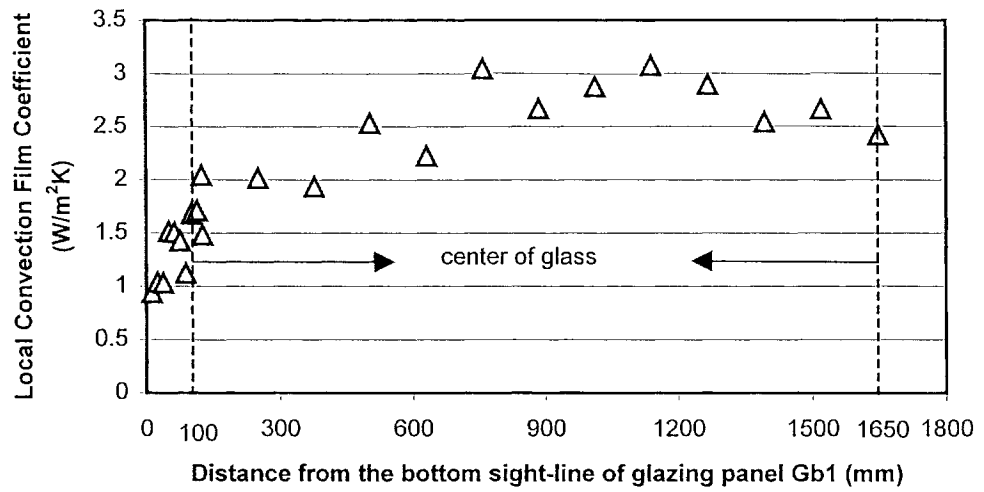
Figure 6.17 Local convection film coefficients along vertical centerline of glazing panel G_{b1} in system B under CSA winter condition
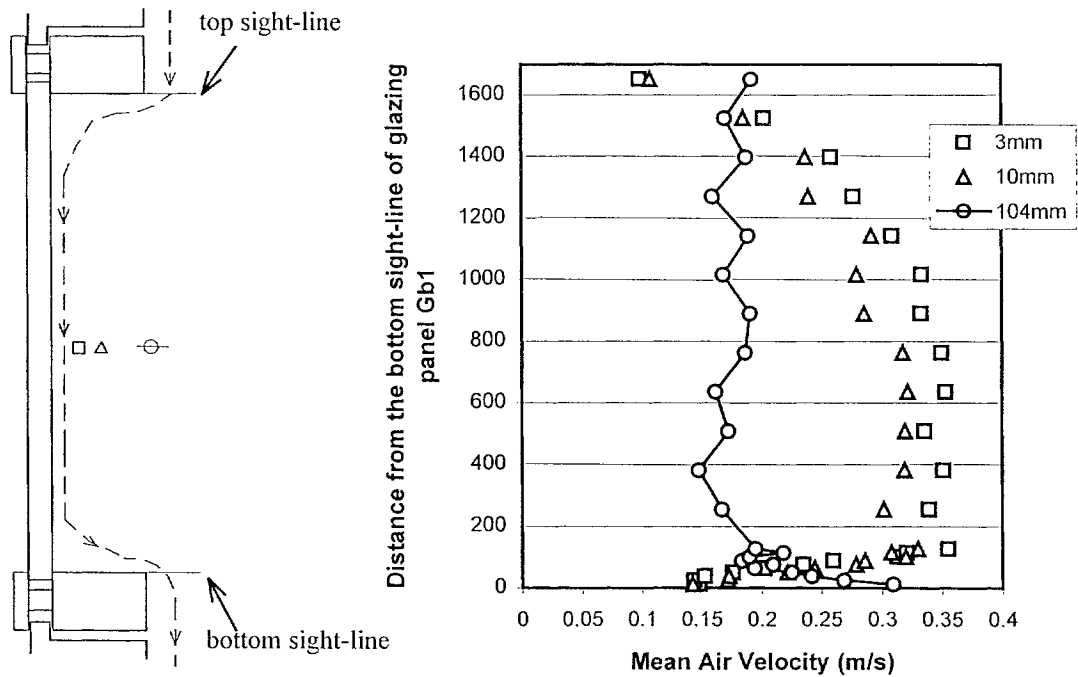
Figure 6.18 Selected vertical profiles of air velocity at different distances from the surface along the centerline of glazing panel G_{b1} under CSA winter condition

174

The effect of different outdoor conditions on the air velocities and local convection coefficients along glazing surface is indicated in Figure 6.19 and Figure 6.20 for system B. Similar to that in system A, with the increase of the temperature difference between the glass surface and the room air stronger natural convection is developed indicated by higher air velocity in the inner boundary layer. The convection coefficients slightly increase with lower outdoor temperature.
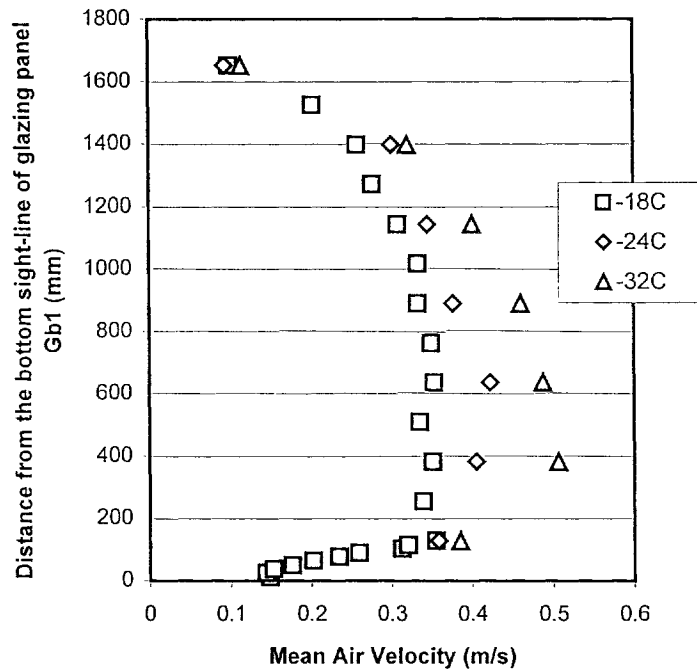
Figure 6.19 Vertical air velocity profiles at 3mm from the surface along the vertical centerline of glazing panel G_{b1} in system B under three different test conditions
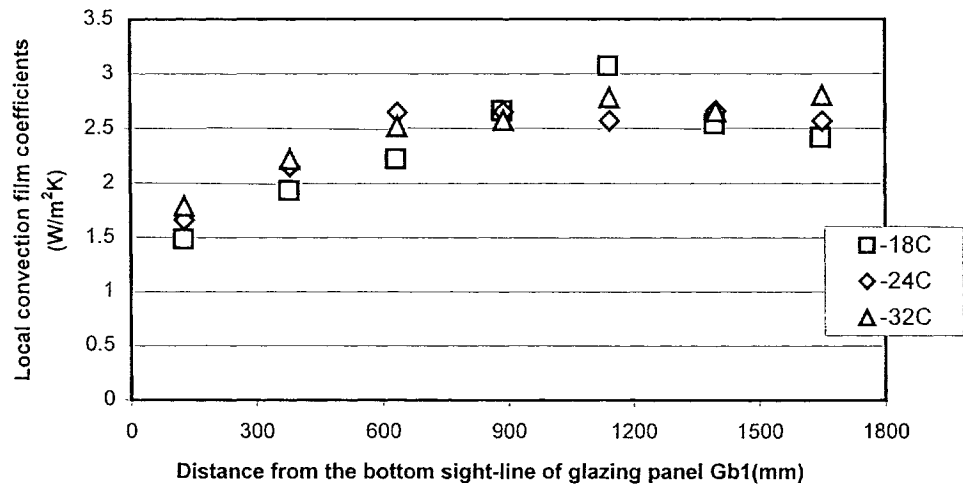
Figure 6.20 Local convection film coefficients along the vertical centerline of glazing panel G_{b1} in system B under three test conditions

6.3 Outdoor convection film coefficient

To estimate the outdoor convection film coefficients, the following correlations from ASHRAE standard 142P (ASHRAE,1996) are used:

$$h_{c,o} = 8.07V^{0.605}, \quad V > 2\text{m/s} \tag{6.3}$$

$$h_{c,o} = 12.27, \quad V \leq 2\text{m/s} \tag{6.4}$$

The air velocity profile in the cold box was measured by a hand-held air velocity meter. The air velocity distribution is not uniform in the cold box because the blower is located at the center of the cold chamber, and it extends to cover the two panels of the test specimen in the center. The measurements show that the air velocity is higher along the center joint of the two wall systems than that along the perimeters. The average of the measured air velocities is 5.5m/s for the center range and 3.1m/s for the perimeter. Then the corresponding convection coefficients based on the average velocity for each region will be 22.6 W/m²·K and 16.0 W/m²·K, respectively.

6.4 Radiation film coefficient

6.4.1 Standard calculation procedure

The radiation heat transfer coefficients can be evaluated based on the measured surface temperature, known surface emittance, and the enclosure geometry according to the procedure outlined by ASTM standard C1199 (2000). Several assumptions are made in deriving this calculation procedure, including: a) each surface of the enclosure is assumed to be at a uniform temperature; b) surface where the assumption of a uniform temperature is not valid is considered as several small uniform temperature areas; and c) all surfaces are assumed to be diffuse gray and opaque, and the air in the enclosed space is neither absorbing nor emitting.

The total radiation heat transfer energy that leaves a surface per unit time and per unit area is called radiosity, J. The total radiation heat transfer energy received by a surface per unit time and per unit area is called irradiation, G. The net radiative heat exchange for the ith surface, $q_{r, i}$, is equal to the difference between radiosity and irradiation of that surface, i.e.

$$q_{r,i} = A_i (J_i - G_i) \tag{6.5}$$

The radiosity is the sum of the energy emitted by the surface, and the energy reflected. It can be written as:

$$J_i = E_i + \rho_i G_i \tag{6.6}$$

where $E_i = \varepsilon_i \delta T^4$ is the radiative energy emitted by the surface, ε_i is the emittance of the surface, T is the surface temperature in K, δ is Stefan-Boltzmann constant and ρ_i is the

177

reflectance of the surface. For a diffuse-gray opaque surface, $\rho=1-\alpha$, α is the absorptance

of the surface, and $\alpha=\varepsilon$.

Substituting equation 6.6 into 6.5, the net radiation heat transfer can be expressed as:

$$q_{r,i} = \frac{E_{bi} - J_i}{(1-\varepsilon_i)/\varepsilon_i A_i} \qquad (6.7)$$

Once the radiosity for each surface, J_i, is obtained, then the radiation film coefficient for

each surface, $h_{r,i}$, can be calculated as:

$$h_{r,i} = \frac{q_{r,i}}{A_i \Delta T} = \frac{E_{bi} - J_i}{(1-\varepsilon_i)\Delta T/\varepsilon_i} \qquad (6.8)$$

The procedure to obtain J_i is described below.

Equation 6.6 can be re-written as:

$$J_i = \varepsilon_i E_{bi} + (1-\varepsilon_i)G_i \qquad (6.9)$$

By definition, the irradiation of surface i is:

$$A_i \bullet G_i = \sum_{j=1}^{n} F_{ji} \bullet A_j \bullet J_j \qquad (6.10)$$

where, F_{ji} is the view factor from surface j to surface i. Using the reciprocity relation for

view factors, $A_i \bullet F_{ij} = A_j \bullet F_{ji}$, and substituting equation 6.10 into equation 6.9, the radiosity

becomes:

$$J_i - (1-\varepsilon_i)\sum_{j=1}^{n} F_{ij} \bullet J_j = \varepsilon_i E_{bi} \qquad (6.11)$$

For any number of surfaces, the radiosities can be determined by solving a system of n

simultaneous equations. In the matrix form, equation 6.11 becomes:

$$[K] \bullet \{J\} = \{E\} \qquad (6.12)$$

where,

178

$$\{J\} = \begin{bmatrix} J_1 \\ J_2 \\ \cdot \\ \cdot \\ \cdot \\ J_n \end{bmatrix} \qquad\qquad (6.13)$$

$$\{E\} = \begin{bmatrix} \varepsilon_1 \delta T_1^4 \\ \varepsilon_2 \delta T_2^4 \\ \cdot \\ \cdot \\ \cdot \\ \varepsilon_n \delta T_n^4 \end{bmatrix} \qquad\qquad (6.14)$$

$$[K] = \begin{bmatrix} 1 & -\rho_1 F_{12} & \cdot & \cdot & \cdot & -\rho_1 F_{1n} \\ -\rho_2 F_{21} & 1 & \cdot & \cdot & \cdot & -\rho_2 F_{2n} \\ \cdot & & \cdot & & & \cdot \\ \cdot & & & \cdot & & \cdot \\ \cdot & & & & 1 & \cdot \\ -\rho_n F_{n1} & & \cdot & \cdot & \cdot & -\rho_n F_{n(n-1)} & 1 \end{bmatrix} \qquad\qquad (6.15)$$

6.4.2 Indoor radiation film coefficient

The volume enclosed by the hot box and the test specimen is illustrated in Figure 6.21. Each of the interior surfaces of the hot box is assumed to have a uniform temperature equal to the room air temperature of 21°C. Each panel of the test wall is considered as an individual element with a uniform temperature. The four glazing panels are highlighted in Figure 6.21 and the radiation heat transfer analysis for each of these four panels was carried out. Each glazing panel is assumed to have a uniform temperature equal to the area-weighted average from the measurements. All of the interior surfaces of the hot box except for the floor are finished with stainless steel. The surface emittance used in this analysis is listed in Table 6.3. These values are from the measurements described in

chapter 5. For long wave radiation analysis, the insulated glazing unit can be assumed as opaque.
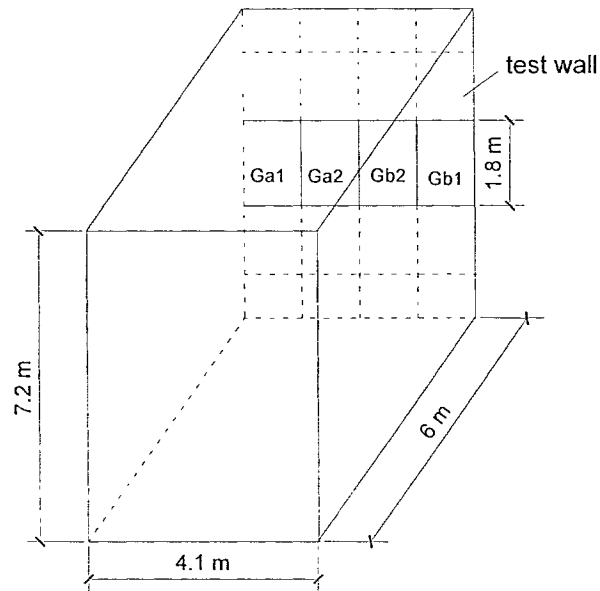
Figure 6.21 Geometry of the enclosure analyzed

Table 6.3 Surface properties used in radiation heat transfer analysis

Surfaces	Emittance	Absorptance
Glazing panels	0.84	0.16
Finished aluminum mullions	0.72	0.28
Stainless steel wall surfaces	0.30	0.70
Floor	0.90	0.10

All the stainless steel wall surfaces can be reasonably assumed to have the same temperature and the same emittance, therefore, they can be considered as one fictitious surface so that the analysis can be simplified by dealing with only three surfaces: glazing surface, floor and the fictitious surface. The simplified model is shown in Figure 6.22.

180
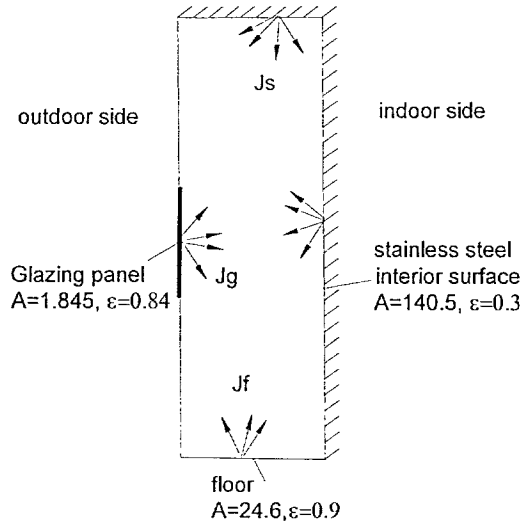
Figure 6.22 A simplified radiation model for specimen under tests

To calculate the indoor radiation heat transfer coefficient, the view factors among the involved surfaces have to be determined first in order to construct matrix K to solve matrix J (equation 6.12). The detailed procedure to determine the view factors is described in Appendix C.1. The calculated results show that the view factors for the four glazing panels (G_{a1}, G_{a2}, G_{b1} and G_{b2}) with respect to the other two surfaces (hot box floor and the fictitious surface) are the same within the acceptable numerical precision (less than 1%). Since the small glazing panels face a large enclosure, their relative horizontal positions have no significant effect on the view factors. The general view factors for glazing panel to other surfaces are listed in Table 6.4. The local radiation film coefficients for the four glazing panels, therefore, depend only on the temperatures of the glazing surfaces. Since the temperature difference between the two glazing panels in each wall system is within 0.5°C, only one value is calculated for a glazing panel in each system.

181

With known surface temperatures, surface emittance, and view factors, matrices K and E were constructed and matrix J was solved. Finally the radiation film coefficients are obtained using equation 6.8 and the results are listed on the first data row of Table 6.5.

Table 6.4 View factors among glazing panel, floor and the fictitious wall

	Glazing Panel	Floor	Fictitious wall
Glazing Panel G_{a1}	0	0.00822	0.99178
Floor	0.00062	0	0.99938
Fictitious wall	0.01302	0.17496	0.81202

Table 6.5 Estimated radiation film coefficients for glazing panels

	Glazing Panel in system A	Glazing panel in system B
Detailed calculation	4.46	4.58
Simplified calculation	4.54	4.67
Difference (%)	1.87	1.88

A simplified calculation, which assumes the glazing surface is facing a black body, was also carried out and the results are shown on the second data row of Table 6.5. The difference between the detailed and simplified calculations is within 2%. This implies that for a small surface exposed to a large enclosure, the enclosure can be treated as a black body even though the enclosure has a low surface emissivity. This conclusion can be applied to other components of the tested wall to estimate the local radiation film coefficient by a simple calculation.

6.4.3 Outdoor radiation film coefficient

A simplified procedure was used to calculate radiation film coefficients of the exterior specimen surfaces in the cold box. The basis for this simplification is that the temperature difference between wall surface and the air is very small, and the wall surface is facing a flat baffle plate made of stainless steel. The radiation heat exchange

between the wall surface and the baffle is assumed to be between two parallel plates and

the calculation formulae for the coefficient is:

$$h_{r,o} = q_r / \Delta t = \cfrac{1}{\cfrac{1}{\varepsilon_g} + \cfrac{1}{\varepsilon_b} - 1} \delta(T_{surf}^4 - T_b^4)/(T_{surf} - T_o) \qquad (6.16)$$

where, ε_g is the emittance of glass, ε_b is the emittance of the stainless steel baffle, 0.3,

and T_b is the temperature of baffle surface, assumed to be at air temperature in K.

The average temperature of -14.3°C on the exterior surface of glazing panels is used for

this calculation. The outdoor radiation film coefficient using equation 6.16 is estimated

at 1.09 W/m²·K under CSA winter condition.

6.5 Estimation of surface film coefficients using thermal network analysis

The convective and radiative heat transfer coefficients were determined individually for

indoor and outdoor surfaces in above sections. To provide a comparison for the

estimation results, a thermal network analysis was employed to simultaneously calculate

these coefficients based on the fundamental heat transfer process across the glazing units.

For a glazing unit in the tested specimen, one-dimensional heat transfer can be reasonably

assumed at the center-of-glass area. With measured temperatures on the interior and

exterior surfaces, a thermal network analysis can be used to estimate the interior surface

film coefficient and the exterior surface film coefficient. The physical model developed

for this thesis is illustrated in Figure 6.23.
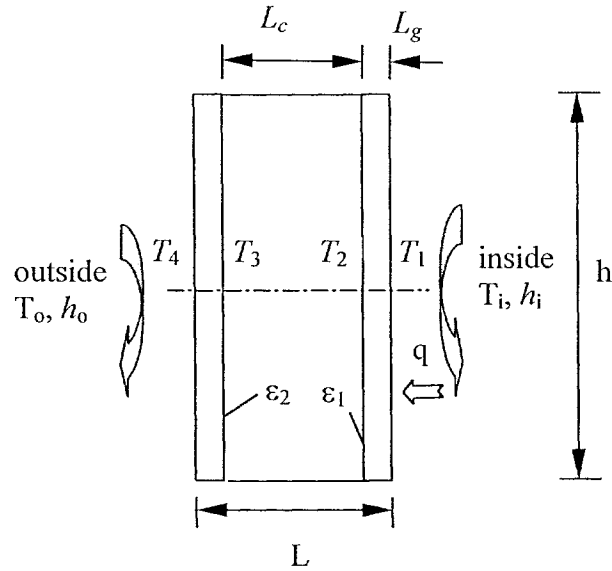
Figure 6.23 Physical model for thermal network analysis, h=1.67m, L_g=6.4mm, L_c=12.7mm

The heat flux through the center-of-glass can be expressed in a set of equations:

$$q = h_i(T_i - T_1)$$ (6.17)

$$q = \frac{T_1 - T_2}{k_g / L_g}$$ (6.18)

$$q = h_c(T_2 - T_3)$$ (6.19)

$$q = \frac{T_3 - T_4}{k_g / L_g}$$ (6.20)

$$q = h_o(T_4 - T_o)$$ (6.21)

Thermal conductance for the glazing cavity, h_c, is composed of convection and radiation, and can be expressed as:

$$h_c = h_{cc} + h_{cr}$$ (6.22)

184

$$h_{cc} = \frac{Nu \cdot k_{gas}}{L_c} \qquad (6.23)$$

$$h_{cr} = \frac{\delta(T_2^2 + T_3^2)(T_2 + T_3)}{\frac{1}{\varepsilon_1} + \frac{1}{\varepsilon_2} - 1} \qquad (6.24)$$

According to Elsherbiny et al.(1982), the Nusselt number, Nu, for natural convection within closed spaces can be calculated:

$$Nu = (1 + (C_1 \cdot Ra^{C_2})^{C_3})^{1/C_3} \qquad (6.25)$$

For the glazing cavity considered, the aspect ration A is 132 and Ra is less than 10^4. In this condition, the coefficients used in equation (6.25) are $C_1=0.0607$, $C_2=1/3$, $C_3=18$. The Rayleigh number, Ra, is defined as:

$$Ra = Gr \cdot \Pr = \frac{\rho^2 \cdot g \cdot \beta \cdot \Delta T \cdot l_c^3 \cdot C_p}{\mu \cdot k} \qquad (6.26)$$

The Rayleigh number depends on the temperature difference between these two glazing walls, the average temperature of the gas in the cavity, and the properties of the filling gas, and the thickness of the cavity. The properties of the filling gas, e.g. the density, ρ, conductivity, k, are functions of the temperature. The properties information for air and Argon is obtained from ASHRAE standard 142P (1996) and listed in Table C.1 in Appendix C.

The procedure to solve the problem is to assume an initial value for the constant heat flux, q, first. With the assumed q and the known temperatures T_1, and T_4, T_i, and T_o, a new set of surface temperatures can be calculated. By assigning the calculated

temperatures for the interior glass surface and the exterior glass surface to be equal to the measured values, the right heat flux q can be obtained. This can be done using the solver function in Microsoft Excel. To facilitate the calculation, the assumed initial value of q was estimated using equation $q=U(T_i-T_o)$. The overall heat transmittance U-factor for each glazing panel was obtained using the VISION program. In the glazing panels G_{a1} and G_{a2} in system A, the filling gas is air and the emissivity of cavity surface $\varepsilon_1=\varepsilon_2=0.84$. In the glazing panels G_{b1} and G_{b2} in system B, the filling gas is Argon and the surface emissivity $\varepsilon_1=0.1$, and $\varepsilon_2=0.84$. The final results calculated for each glazing panel are shown in Table 6.6 and Table 6.7.

Table 6.6 Temperatures on glazing surfaces at center-of-glass area (^{o}C)

Glazing panels	T_i	T_1	T_2	T_3	T_4	T_o
G_{a1}		8.0	7.3	-11.6	-12.3	
G_{a2}		7.6	6.9	-13.2	-13.9	
G_{b1}	21.0	13.5	13.1	-14.6	-15.0	-18.0
G_{b2}		13.2	12.8	-15.4	-15.8	

Notes: T_i, T_1, T_4, T_o are measurements from the tests. T_2, T_3 are analytical results.

Table 6.7 Calculated surface film coefficients for glazing panels

Glazing panels	Calculated results for glazing cavity				q (W/m^2)	h$_i$ (W/m^2·K)	h$_o$ (W/m^2·K)
	Ra	Nu	h$_{cc}$ (W/m^2·K)	h$_{cr}$ (W/m^2·K)			
G_{a1}	5887	1.11	2.09	3.27	103.0	7.63	18.07
G_{a2}	6344	1.13	2.13	3.24	107.8	7.75	26.24
G_{b1}	9887	1.30	1.67	0.45	58.9	7.36	19.62
G_{b2}	10155	1.32	1.68	0.45	60.5	7.28	27.48

The results indicate that the film coefficient on the exterior surface is not uniform for different glazing units. The differences between the two glazing panels in the same wall system is caused by the non-uniformity of the air velocity distribution in the cold box as

explained in section 6.3. The higher air velocity for the center region than that at the perimeter results in a higher convection film coefficient. The interior surface film coefficients for the glazing panels in system A are slightly higher than that in system B due to the higher temperature difference between glazing surface and the room air for system A.

The estimated film coefficients from the thermal network analysis are compared to the values determined individually by measurements and calculations, as listed in Table 6.8. The measured exterior convection film coefficient is the average of the values for the two panels in each wall system. The outdoor film coefficients listed in Table 6.8 by thermal network analysis are also the averaged values for both panels in each wall system. The results from measurements and thermal network analysis agree within 10% for indoor side and within 14% for outdoor side. Therefore, the average surface film coefficients in the environmental chamber under the current test setup can be reported as $7.0 \text{W}/ \text{m}^2 \cdot \text{K}$ for room side and $20.4 \text{W}/ \text{m}^2 \cdot \text{K}$ for the outdoor side.

Table 6.8 Surface film coefficients in the environmental chamber under current test setup (W/m^2·K)[*]

	Interior				Exterior				
	Determined individually			Thermal network	Diff. (%)	Determined individually			Thermal network	Diff. (%)
	h_c	h_r	h_i	h_i		h_c	h_r	h_o	h_o	
System A	2.46	4.46	6.92	7.63	10.3	19.32	1.09	20.41	22.16	7.9
System B	2.48	4.58	7.06	7.36	4.3	19.32	1.09	20.41	23.55	13.4

*The comparison is over the measured values

6.6 Conclusion

An experiment setup and procedure was developed to estimate the local convection film coefficients by measuring air velocity and temperature in the boundary layer of the wall surface. The values obtained for local convection coefficients are reasonable and the trends and magnitudes are in agreement with theory. The results have confirmed the feasibility and reliability of the setup in performing velocity and temperature measurements with high spatial resolution. This setup could be used to provide data for further convection coefficient and indoor air movement studies.

The indoor radiation film coefficients were analyzed by a detailed radiation heat transfer model using measured surface temperatures. The local convection film coefficients measured in this test, and the local radiation film coefficients estimated using the procedure described in this chapter can be used as more realistic boundary conditions to validate the reliability of computer programs in predicting the temperature distributions for curtain wall systems. The details are described in Chapter 8.

The average surface film coefficients were obtained and reported as $7.0 \text{W/ m}^2 \cdot \text{K}$ for indoor and $20.4 \text{W/ m}^2 \cdot \text{K}$ for outdoor under the current test setup in the environmental chamber.

Chapter 7

Measurement of cold draft induced by glazing surfaces

7.1   Introduction

Metal curtain walls typically have a large continuous glazing area. In cold winter, the cold draft induced by the large cold glazing surface may cause thermal discomfort to the occupants in the perimeter zone. The temperature, velocity, and turbulent intensity of the cold draft are the significant factors contributing to the local percentage dissatisfied (PD). This chapter describes the test procedure and results of measuring the air temperature and air velocity of the cold draft induced by two curtain wall systems. The effect of the cold draft on the local thermal sensation of occupants was evaluated in accordance with the procedure recommended by ASHRAE standard 55 (ASHRAE, 1992).

7.2   Experimental setup and procedure

A rudimentary living space was simulated by adding to the wall specimen a temporary floor on the indoor side. This floor was created by placing a fiberboard panel on top of the movable platform. The floor was at the height of the lower horizontal beam, which is six feet above the hot box floor, as shown in Figure 7.1. The temperature difference between the glazing surface and the room air under winter testing conditions induces the air to move downward along the glazing surface. When this air current meets the aluminum frame, it is forced away from the glazing surface to the frame edge and

continues to flow downward along the spandrel panel. When this cold air stream hits the floor, it changes its direction and penetrates into the occupied zone. During this movement, the cold air mixes with the warm room air. Consequently, as the cold air temperature gradually increases its downward force gradually decreases. The maximum air velocity that develops at the bottom of the glazing surface depends on the height of the surface and on the temperature difference between the surface and the indoor air. Normally, it is not this maximum velocity that affects the thermal sensation of the occupant, but the maximum air velocity and minimum air temperature in the occupied zone, in which it penetrates.
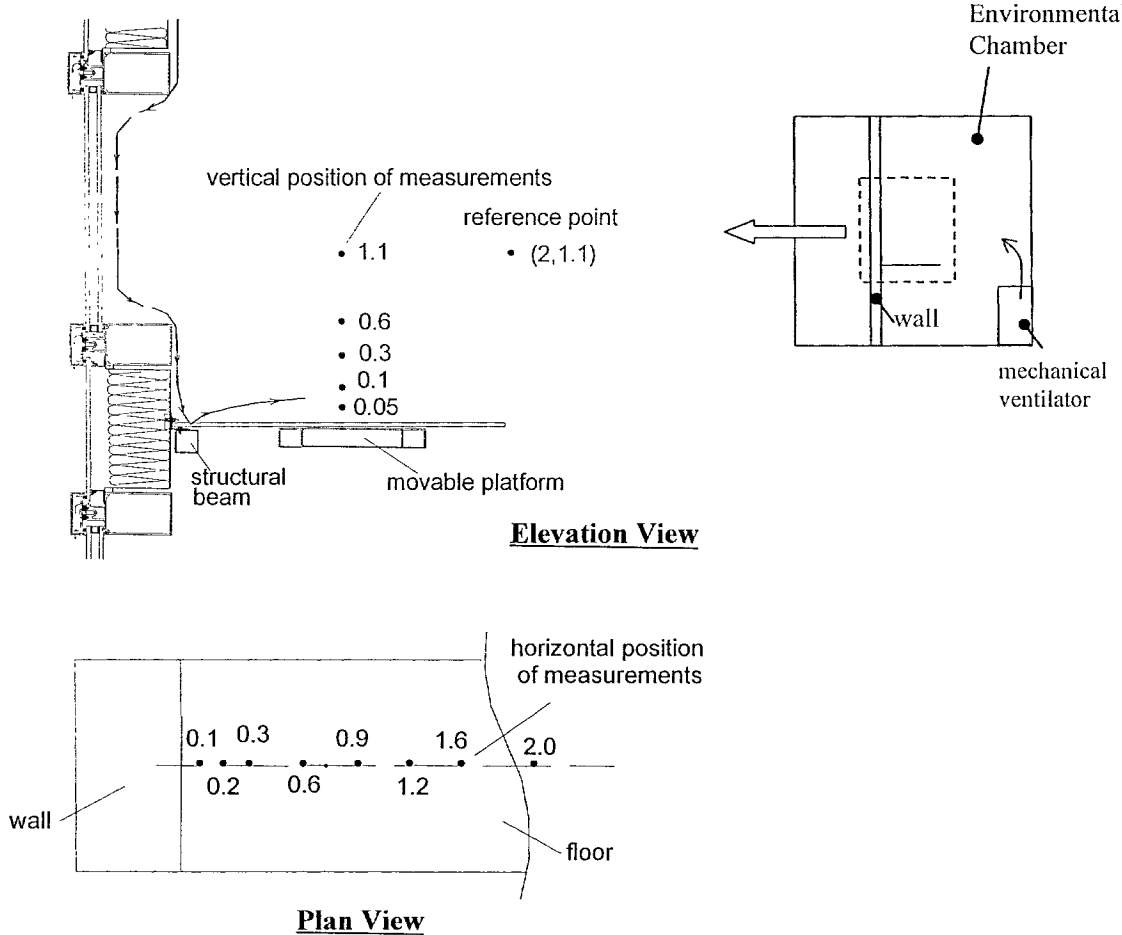
Figure 7.1 Test setup for cold draft measurement (not to scale, dimensions in m).

190

The route of the cold draft includes two segments: the portion from the edge of frame to the floor and the portion along the floor to the occupied zone. Two sets of measurements were carried out to characterize the two segments of the cold draft movement. The first part is to determine the cold draft trajectory for segment one. The 3-dimensional traverse system described in section 6.2.2 was used to measure the air temperature and air velocity along the vertical centerline of the frame and spandrel panel surfaces. The traverse system can automatically position a 30 gauge type T thermocouple and a low-velocity (0.01~1.00 m/s) omni-directional anemometer at a programmed distance away from the wall surface. As shown in Figure 7.2, the measurements were taken at 7 locations, two locations at the frame section, one at the edge-of-spandrel panel, and the other fours along the spandrel panel. The measurements were up to 135mm away from the wall surface. The sampling frequency was 20 Hz and the sampling period was 1 minute for each measurement.
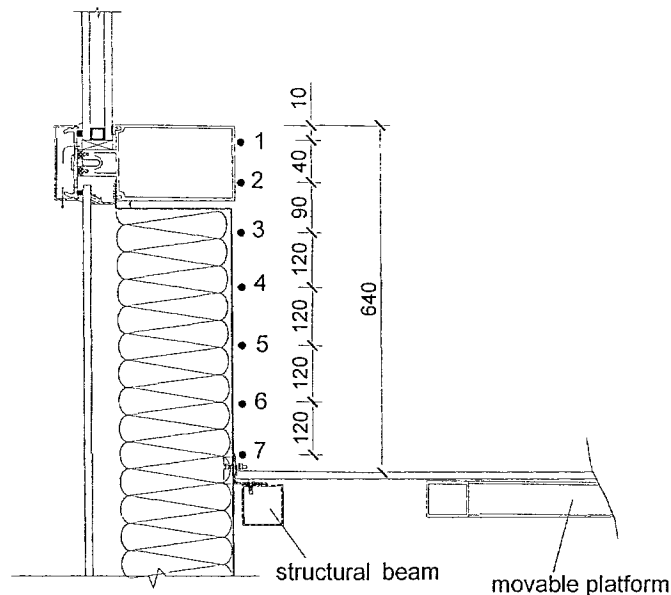
Figure 7.2 Locations of measurements to determine cold draft trajectory (not to scale, dimensions in mm)

191

The second part is to evaluate the effect of the cold draft on occupants' local thermal sensation after the cold flow hits the floor and moves into the occupied zone. The third axis of the 3D traverse system was removed from the system and was attached to a small metal stand to carry out the air temperature and air velocity measurements (Figure 7.3). Measurements were taken at different distances away from the wall surface and at different heights from the floor. The height of the probe from floor and the distance from the wall was adjusted manually.

In accordance with ASHRAE Standard ANSI/ASHRAE 55, the occupied zone starts at 0.6m away from the wall surface. The height of 0.1m from floor represents the ankle level of the body, the height of 0.6m represents a seated person, and the height of 1.1 m represents a standing person. Therefore, the measurement grids were designed as: distance from wall surface, D=0.1m, 0.2m, 0.3m, 0.6m, 0.9m, 1.2m, 1.6m, 2m and the height from the floor, H=0.05m, 0.1m, 0.3m, 0.6m, 1.1m. The reference point in the occupied zone was located at 1.1 m above the floor and 2 m away from the wall. The measurement locations are shown in Figure 7.1. The sampling frequency was 20 Hz, but the sampling period was much longer, as of 5 minutes.

The tests were carried out for two conditions: CSA winter condition, −18°C in the cold box and 21°C in the hot box; and Montreal worst winter condition, −32°C in cold box and 21°C in the hot box. The relative humidity in the hot box was maintained under 25%. The measurements for system A and system B were carried out separately after the test conditions had reached steady-state.

192
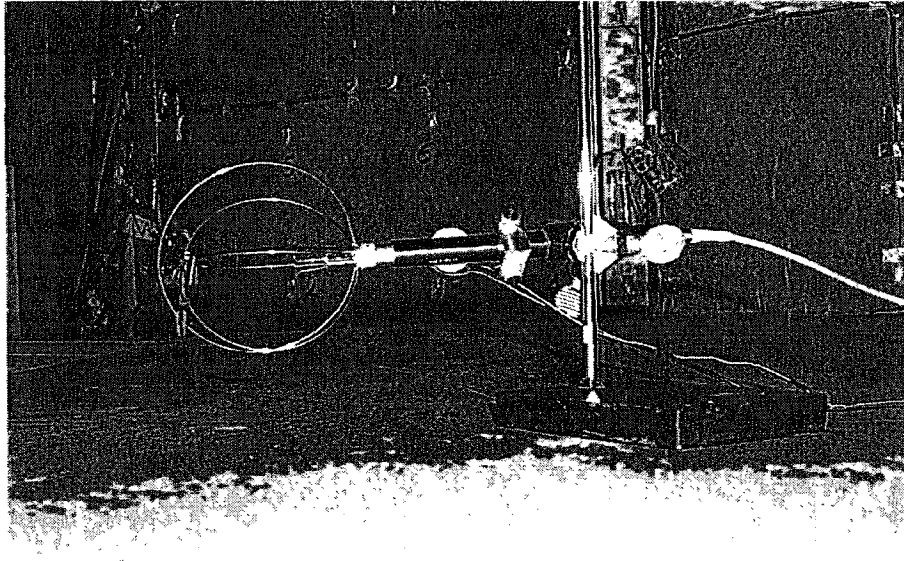
Figure 7.3 Photo of the setup for cold draft measurement along the floor

As illustrated in Figure 7.1, a terminal air supply unit is located at the end of the hot box in the Environmental Chamber to regulate the indoor test conditions. The air supply unit is located 6 m away from the tested walls. The indoor air movement induced by the mechanical ventilator may interfere with the air movement along the floor due to the cold draft. To monitor the influence of this unit, the air velocity and air temperature along the floor were measured before the temperature differential was built up across the tested walls.

7.3   Results and discussion on cold draft and its effect on local thermal sensation

The measurement results are presented in three parts. The first part concentrates on the trajectory of the cold draft from the frame edge to the floor. The second part discusses the air velocity and air temperature measured along the floor in the occupied zone. The third part analyzes the impact of the cold draft on the thermal comfort using the procedure described by ASHRAE standard 55 (ASHRAE, 1992)

193

7.3.1 Trajectory of cold draft

The trajectory of the cold draft is identified by finding the corresponding distance from the wall surface for the maximum mean air velocity at each location indicated in Figure 7.2. The air velocity profiles in the direction normal to the wall surface for each location are shown in Figure 7.4 and Figure 7.5 for each curtain wall system under Montreal worst winter condition. These measurements show that the maximum air velocity at the edge of the mullion can reach a level as high as 1 m/s for system A under Montreal worst winter condition (-32°C outdoor) due to the very low surface temperature, which is approximately 3.8°C at the center-of-glass. For system B, the maximum air velocity at edge of the mullion is 0.68m/s under Montreal worst condition. The smaller air velocity in system B is due to the much better thermal performance of the glazing panel, that is a much higher surface temperature of approximately 10°C at the center of glass as compared to 3.8°C for system A under Montreal worst condition.
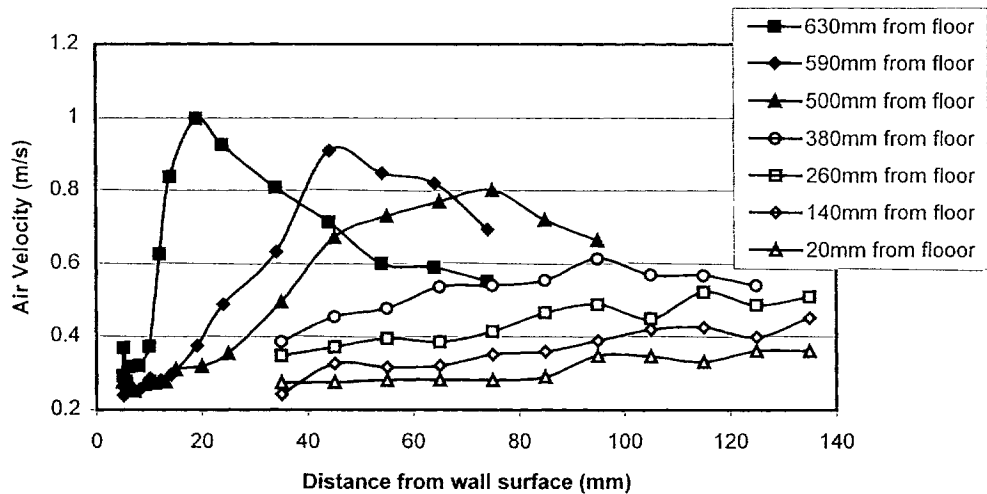
Figure 7.4 Air velocity distribution along spandrel panel surface in system A under -32°C/21°C condition

194
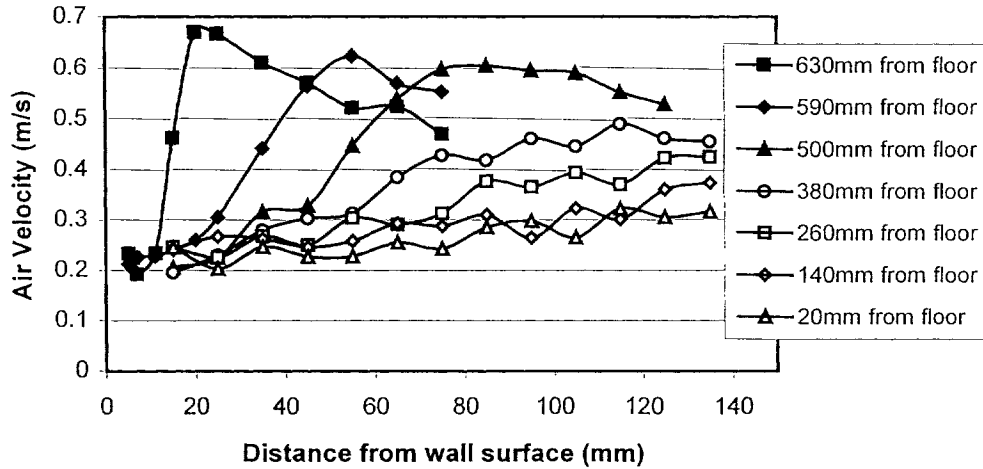
Figure 7.5 Air velocity distribution along spandrel panel surface in system B under -32°C/21°C condition

The maximum moving range of the depth axis in the traverse system was 140mm, and the measurements taken were up to 135mm from the wall surface. As shown in Figure 7.4 and Figure 7.5, the maximum air velocities were not clearly observed for locations 6 and 7 which locate 140mm and 20mm from floor, respectively. However, the trends show that the air velocities were getting steady after the distance of 135mm. The measured maximum velocity and its corresponding distance from the wall surface for system A and system B are listed in Table 7.1. The mean maximum velocity and its corresponding temperature profiles of the downward cold airflow are plotted in Figure 7.6a and Figure 7.6b. These figures show that stronger cold draft is formed along the wall surface of system A, which is indicated by higher velocity and lower air temperature compared to that in system B. When the cold airflow moves downwards, it gets mixed with the room air and the velocity gradually decreases and the temperature gradually increases.

195

Table 7.1 Maximum mean air velocity and its corresponding distance from wall surface for each wall system under Montreal worst winter condition

Locations	System A		System B	
	Maximum air velocity (m/s)	Corresponding Distance (mm)	Maximum Air Velocity (m/s)	Corresponding Distance (mm)
1	0.997	20	0.670	20
2	0.911	45	0.624	55
3	0.801	75	0.605	85
4	0.614	95	0.491	115
5	0.523	115	0.425	135
6	0.452	135	0.374	N/A
7	0.361	N/A	0.317	N/A

(a)   (b)
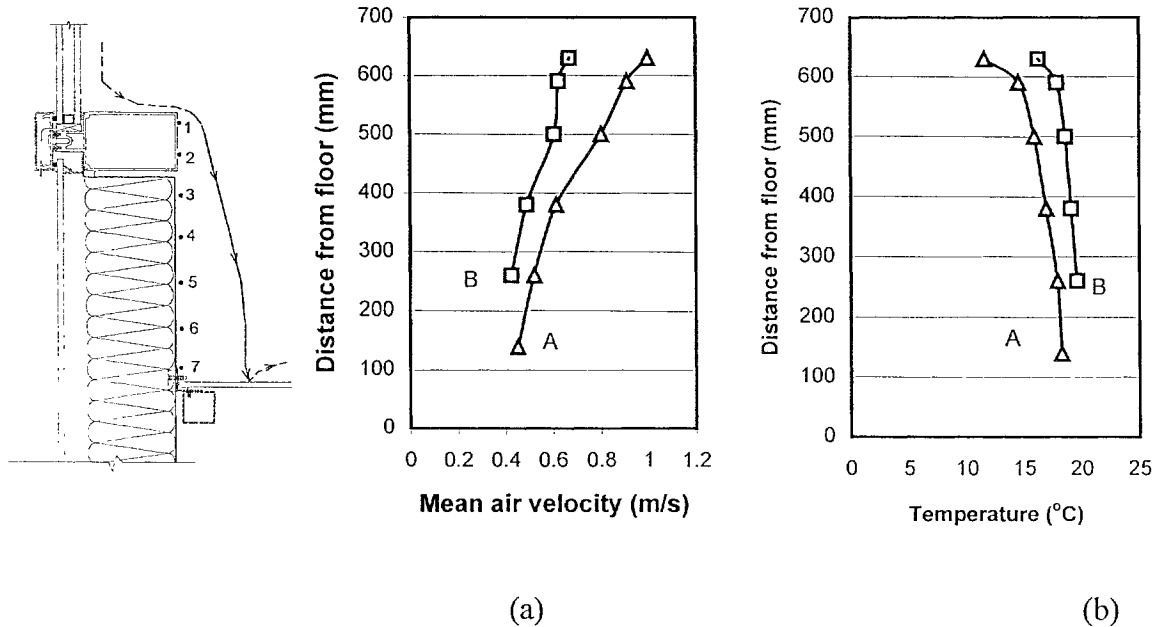
Figure 7.6 Mean maximum air velocity and its corresponding temperature profile of the downward cold airflow along spandrel panel surfaces

The air velocity profiles in the direction normal to the wall surface for each location under CSA winter conditions are shown in Figure 7.7 and Figure 7.8 for curtain wall system A and B. The measurements were performed up-to a distance of 85 mm under this test condition and maximum mean air velocities were observed for the top three locations. It has been found that although the values of the maximum air velocities are

196

different under these two test conditions , the corresponding distances are the same. The

maximum air velocity at the edge of the mullion is 0.82m/s and 0.60m/s for system A,

and B, respectively under CSA winter condition.
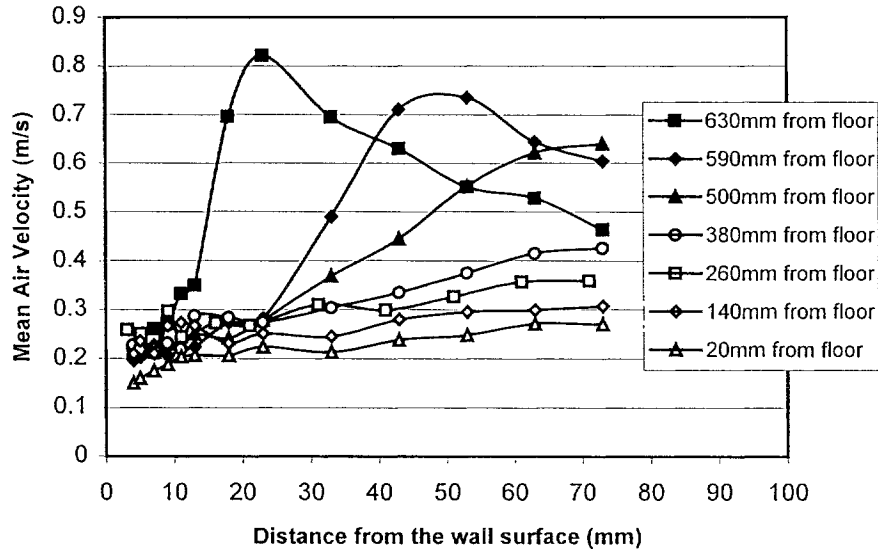
Figure 7.7 Mean air velocity along spandrel panel surface in system A under CSA winter
condition: -18°C/21°C
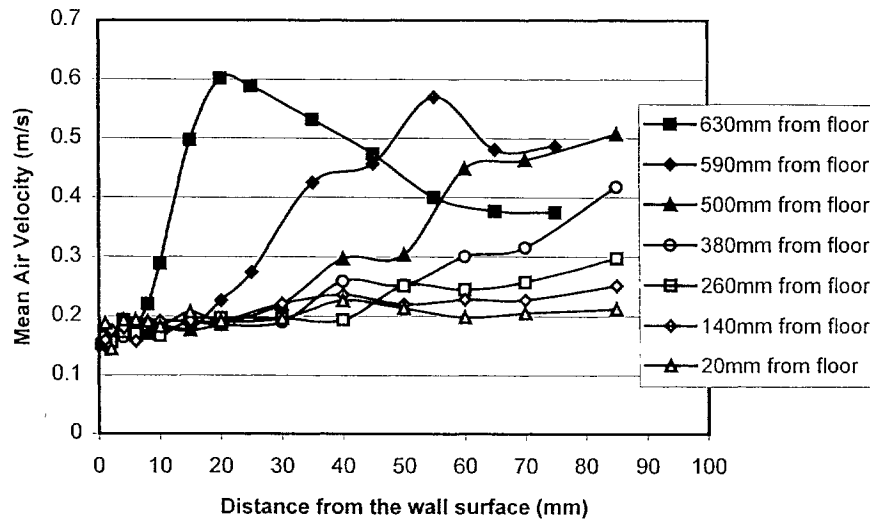
Figure 7.8 Mean air velocity along spandrel panel surface in system B under CSA winter
condition: −18°C/21°C

197

The trajectories of the cold draft identified for each wall system are plotted in Figure 7.9. A polynomial regression analysis was performed using Excel and the equations obtained are listed below. Using these equations, the location for cold draft hitting floor are estimated as 150mm from the wall surface for system A and 170mm from the wall surface for system B. Although much stronger cold draft was formed along the glazing surface of system A due to the much lower surface temperature, the shape of the trajectories for the two systems are similar (Figure 7.9) and the corresponding distances at the maximum velocity for each location are within 20 mm. This similarity implies that the trajectory of the cold draft induced by the cold glazing surface depends more on the geometry of the frame than the air velocity within the measured range (0.6 m/s to 1 m/s). In this test, the frame depth is 101.6mm (4") for both wall systems.
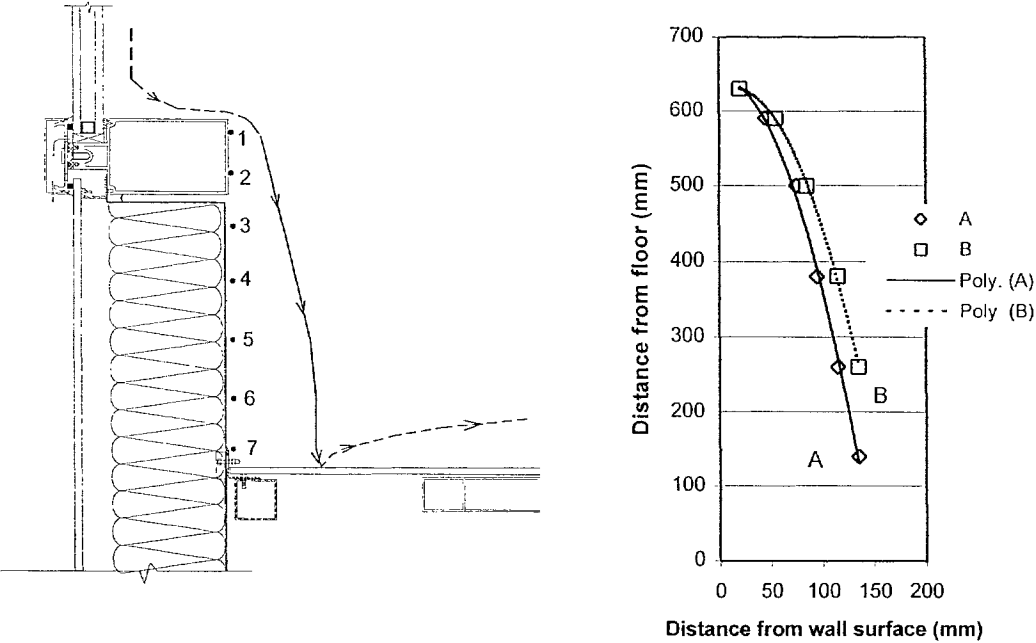
A: $H = -0.028D^2 - 0.0289D + 645.58$, $R^2=0.9971$; B: $H = -0.0252D^2 + 0.7174D + 625.69$, $R^2=0.9994$
D is the corresponding distance from wall surface at the maximum air velocity, in mm, and H is the distance from the floor in mm.

Figure 7.9 Cold draft trajectory along the spandrel panel surfaces

198

The presence of frame reduced the velocity of the cold draft from 0.997m/s to 0.361m/s (Figure 7.6a) before it hits the floor and deflected the flow from the wall surface by about 150mm. These observations imply that the presence of frame may reduce the cold draft effect on occupants.

7.3.2 Air velocity and temperature along floor

The study in this section deals with the movement of the cold draft along the floor and its effect on occupants' local thermal sensation. The influence of the mechanical ventilator on the air movement induced by the cold glazing surface and on the prediction of the percentage of dissatisfied (PD) due to draft is discussed.

7.3.2.1 Effect of mechanical air supply system

The presence of the mechanical air supply in the hot box may interfere with the air movement of cold draft along the floor in the test room, as mentioned earlier. To evaluate the impact of the mechanical system only, the mean air velocity profiles above the floor were measured at the same measuring locations with maintaining room temperatures in both chambers on the indoor and outdoor sides of the specimen. The mechanical air supply unit locates 6m away from the wall, 1.68 m from the floor, and has a supply velocity of 2.6m/s. The distribution of air velocities measured is shown in Figure 7.10. The value of air velocity depends on the distances from both the wall surface and the floor.
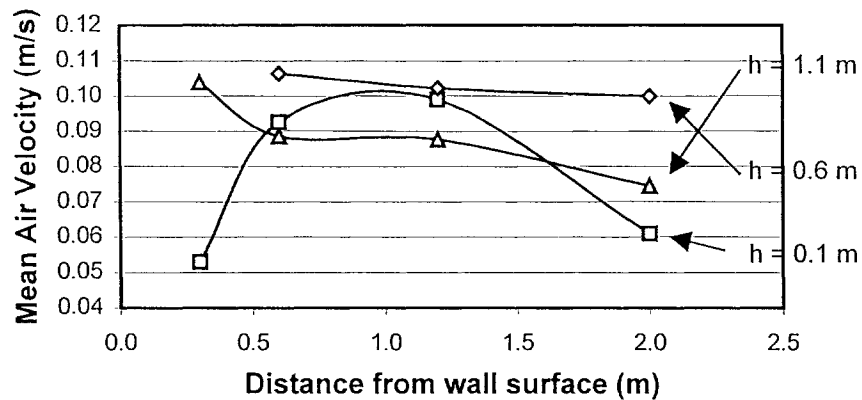
Figure 7.10 Air velocity distribution at different distances from wall surface at three different heights from floor when air supply fan in hot box is on but without introducing temperature difference across the test specimen

The pre-measurements indicate that the mechanical air supply fan results in 0.05~0.11m/s air velocity in the region above the floor when no cold draft is formed. When the natural convection along the wall surface is developed, the air velocity and air temperature measured along the floor are the combined results of the mechanical supply and the cold draft. If the mechanical supply fan is turned off, the effect of pure natural convection can be measured. However, the room air temperature cannot be maintained constant without the mechanical air supply unit, thus the cold draft won't be stable. To get the information how much the mechanical supply fan can affect the measurements, a short period of 25 minutes measurements with the supply fan off were conducted after the test specimen had been stabilized under CSA winter conditions. The measurements were taken at a height of 0.1m from the floor and at distances of 0.3m, 0.6m, 1.2m, and 2 m away from the wall surface. The room air temperature dropped by around 2.3°C during this 25-minute measurement, and the glazing surface temperature dropped by around 1°C. The measured air velocity and air temperature without the supply fan are compared to the

200

measurements for the cold draft when the supply fan was on, as shown in Figure 7.11 for system A and in Figure 7.12 for system B.

These figures indicate that without the interference from the mechanical air supply unit, the velocity of the cold draft gradually decreases when it moves along the floor. When the supply fan is on, a much higher air velocity is yielded from the combined effect of the natural convection airflow induced by the cold glazing surface and the forced convection airflow by the mechanical ventilator. A simple subtraction was performed between the values of air velocity measured with and without fan. The difference is compared to the air velocity measured when no temperature difference has been established across the wall. As shown in Figure 7.11 and Figure 7.12, there are big differences between these two curves, that indicates the influence of the mechanical air supply can not be considered by simple arithmetic addition or subtraction due to the fact that velocity is a vector. The pattern of the air velocity profile measured when both natural and forced convection flow take effect is similar to that measured when no cold draft exists but only mechanical ventilator is on. The similarity implies that the effect of the mechanical air supply dominates the flow characteristics along the floor area.
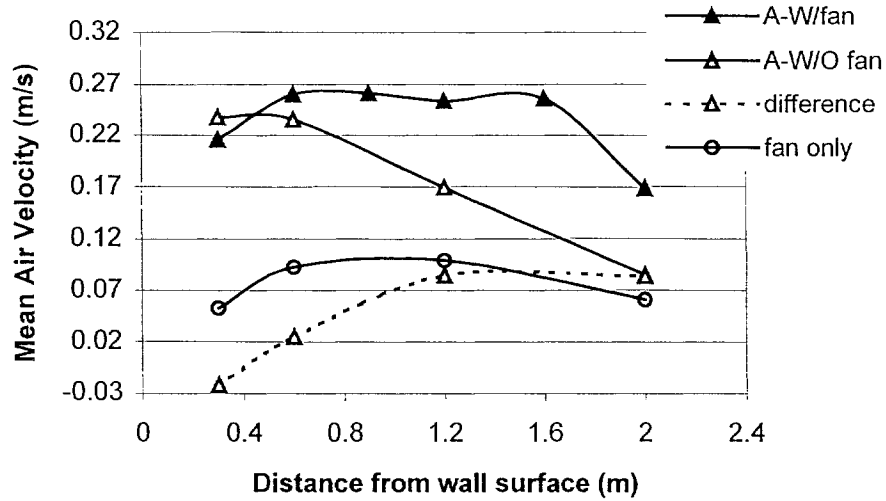
Figure 7.11 Comparison between air velocities measured at 0.1m above floor with/without mechanical supply fan under CSA winter condition for system A.
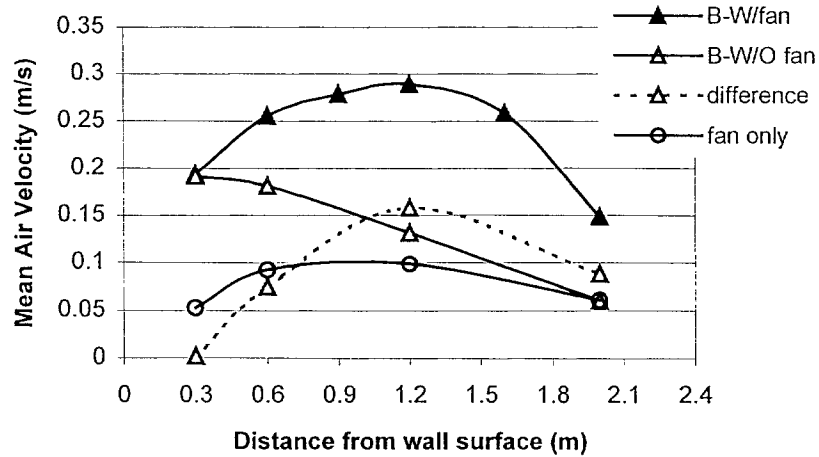
Figure 7.12 Comparison between air velocities measured at 0.1m above floor with/without mechanical supply fan under CSA winter condition for system B.

Notes: In both Figure 7.11 and Figure 7.12, the "Difference" curve is obtained by simply subtracting the velocity value with fan on from the velocity value without fan. "Fan only" curve refers to the measurements without temperature differential across the wall

The comparison between the velocities measured for two curtain wall systems is shown in Figure 7.13. This figure clearly shows that without the interference of the mechanical

202

supply fan, a stronger cold draft exists along the floor in system A due to its much colder glazing surface compared to system B. The mean air velocity measured for system A is 0.05m/s greater than that measured for system B. However, the difference is significantly reduced by the presence of the mechanical supply fan. The air temperatures measured along the floors are shown in Figure 7.14. The air temperatures measured with the supply fan off decrease with the distance from the wall surface. This is because without the supply air, the room temperature was not maintained at $21^{\circ}C$ during the measurements. It was recorded that the room temperature dropped about $2.3^{\circ}C$. The measurements started at distance of 0.3m from the wall surface. While the measuring points were moved away from the wall surface, the room reference temperature gradually dropped. A linear drop of room temperature was assumed and the temperature readings were simply adjusted based on the time interval between the measuring points and the first measurement at distance of 0.3m from the wall. The adjusted readings are shown in Figure 7.14 as "estimated" curves. No considerable difference between air temperatures measured for the two curtain wall systems is observed under both conditions with and without supply fan. However, a large difference exists between measurements with and without supply fan. The supply fan accelerates the mixing between the cold downward airflow and the room air, and results in about $1^{\circ}C$ higher in temperature for the cold airflow moving along the floor.
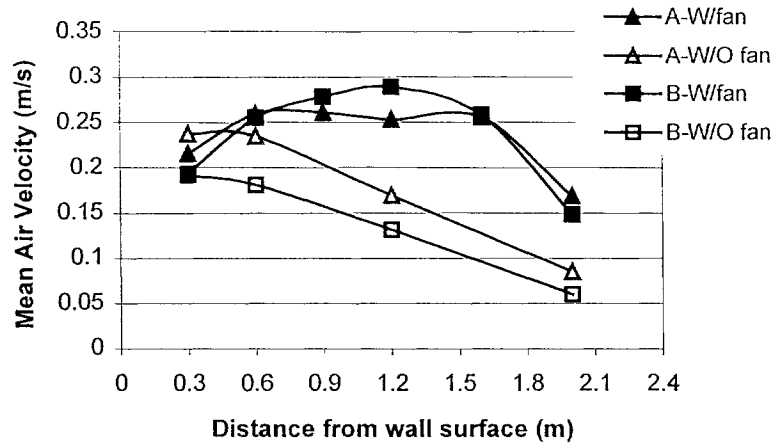
Figure 7.13 Comparison between air velocities measured at 0.1m above floor for two curtain wall systems under CSA winter condition
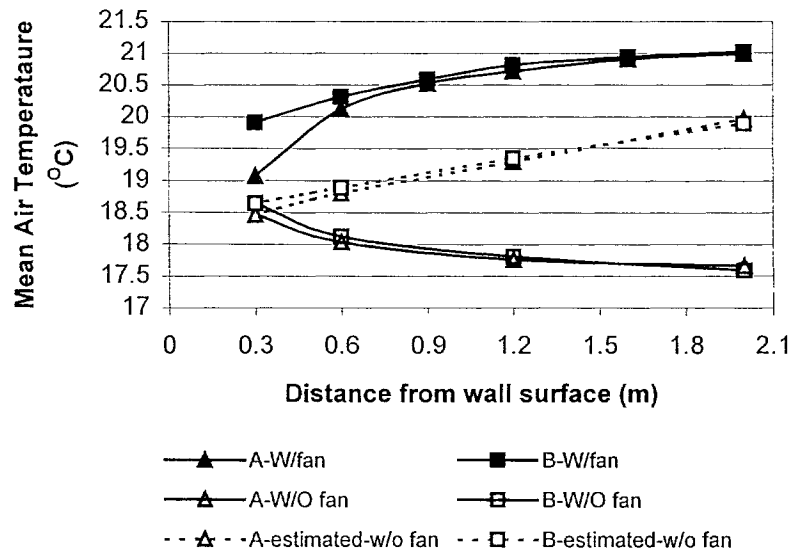
Figure 7.14 Comparison between air temperatures measured at 0.1m above floor for two curtain wall systems under CSA winter condition

From the comparisons, it is clear that the presence of the mechanical air supply system results in higher air velocity and higher air temperature for the cold airflow moving along the floor. The impact of the cold draft on occupant comfort depends not only on the

mean air velocity but also on air temperature and turbulent intensity. The effect of air

temperature and air velocity is opposite on the occupant comfort. To indicate the

influence of the mechanical air supply system in term of local draft sensation, the

procedure recommended by standard ANSI/ASHRAE 55 (ASHRAE, 1992) was followed

to calculate PDs in the occupied zone for both conditions with and without supply fan

using the following equations:

$$PD = (34 - T_a)(\bar{v} - 0.05)^{0.62}(0.37\bar{v}Tu + 3.14) \tag{7.1}$$

$$Tu = SD_v / \bar{v} \times 100 \tag{7.2}$$

where, T_a is local air temperature in °C, $\bar{v}$ is the mean air velocity in m/s, Tu is the

turbulent intensity in %, and SD_v is the standard deviation of velocity measurements in

m/s. The calculated results are presented in Figure 7.15.
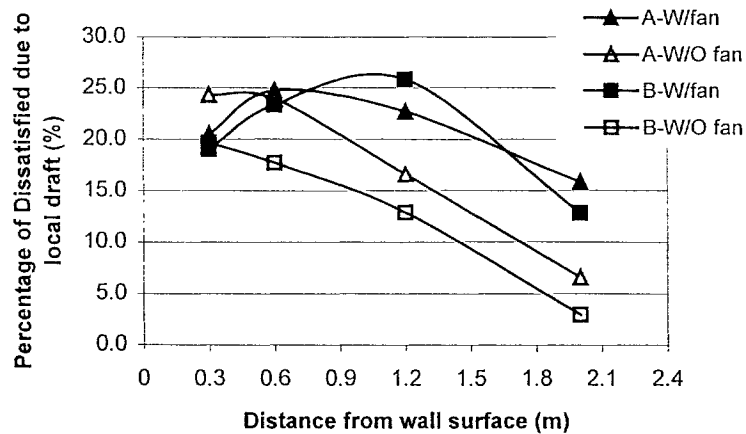
Figure 7.15 Percentage of the Dissatisfied evaluated for two curtain wall systems at 0.1m
above floor under conditions with and without mechanical supply fan.

Figure 7.15 shows that the percentage dissatisfied evaluated for wall system A is about

5% higher than the percentage dissatisfied evaluated for wall system B when the

mechanical system is off. The ASHRAE requirements that the risk of cold draft shall be

less than 15% in the occupied zone cannot be met until 1.0m away from the wall surface for system B and 1.4m away from the wall surface for system A. With the influence of the mechanical system, the percentage dissatisfied is increased by about 10%. The ASHRAE requirements can only be met when the occupant moves about 2.0m away from the wall surfaces.

7.3.2.2 Cold draft measurements and its effect on local thermal sensation

In reality, mechanical systems are operating when the occupant is present in commercial buildings. Based on the above PD analysis, the presence of the mechanical system imposes the occupants to higher risk of draft due to the combined effect from both the cold draft induced by glazing surface and the mechanical system. To represent more realistic performance of curtain walls, most of the measurements and analysis were performed with mechanical system on. To ensure the repeatability, two sets of measurements under the same temperature conditions were taken twice at different times. The results show no considerable difference between the two tests, and the average values were used for the analysis.

The measured air velocities and temperatures along the floor at different heights under CSA winter condition are shown in Figure 7.16 and Figure 7.17 for system A, and in Figure 7.18 and Figure 7.19 for system B.
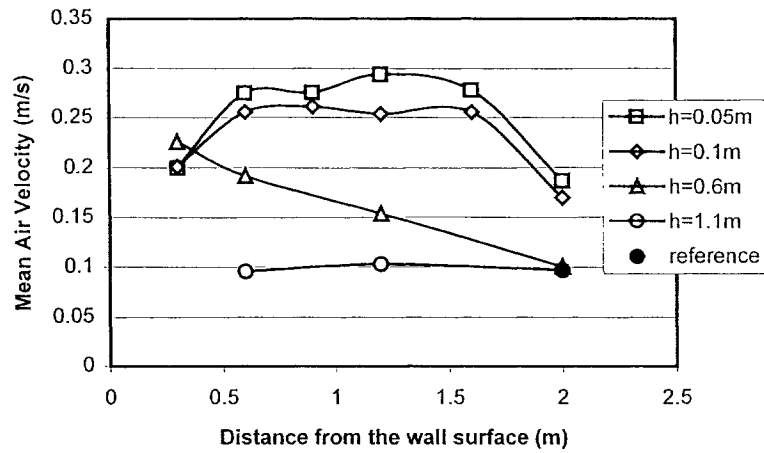
Figure 7.16 Mean air velocity measured at different heights from floor under CSA winter condition for system A
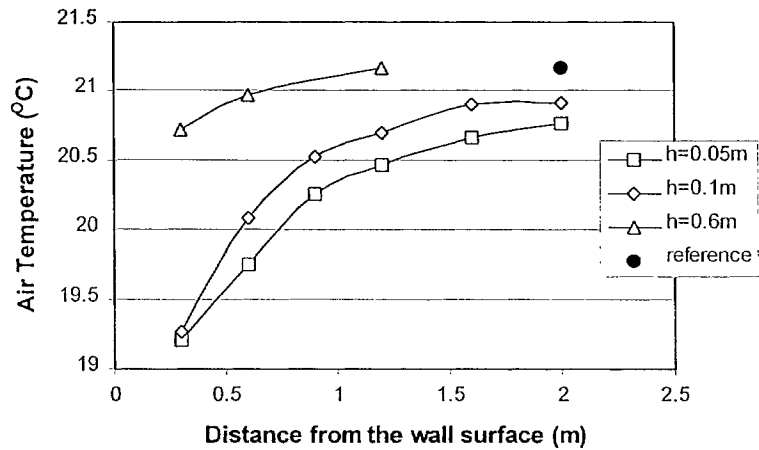
Figure 7.17 Mean air temperature measured at different heights from floor under CSA winter condition for system A

As the height from the floor increases, the air velocity gradually decreases. The air velocity decreases to approximately 0.1m/s at a height of 1.1 m (Figure 7.16). In this test setup, the distance between the sight-line of the glazing panel and the floor is 0.64m. The air movement at 1.1m above floor is out of the functioning territory of the cold draft and the measured velocity of 0.1m/s is the result of the mechanical supply fan as shown in

207

Figure 7.10. For the readings at height of 0.6m, the first air velocity is very high because this point is very close to the edge of the sill, where the cold draft flows down. The pattern of the air velocity distributions at each height from floor takes a very similar shape as that measured at the same corresponding height without the temperature gradient between the glass surface and the room air with the fan on as shown in Figure 7.10. This similarity implies that the effect of the mechanical air supply dominates the flow characteristics along the floor area as analyzed in section 7.3.2.1.

The air temperature gradually increases to the reference temperature when the cold air moves into the occupied zone along the floor. It can also be noticed that at the near floor level (0.05m and 0.1m above floor), the temperatures have much greater gradient than that at the height of 0.6m.
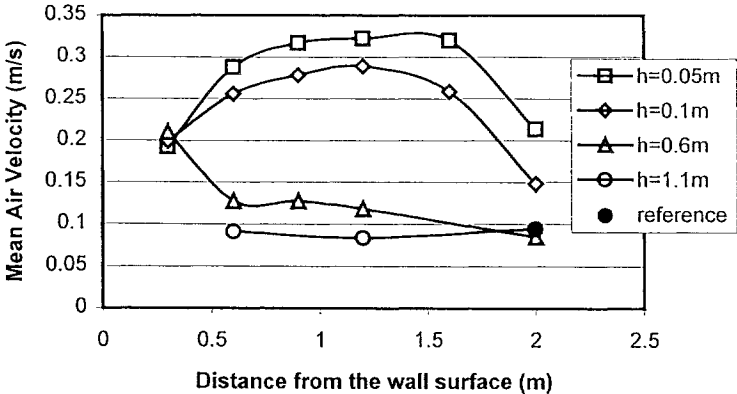
Figure 7.18 Mean air velocity measured at different heights from floor under CSA winter condition for system B
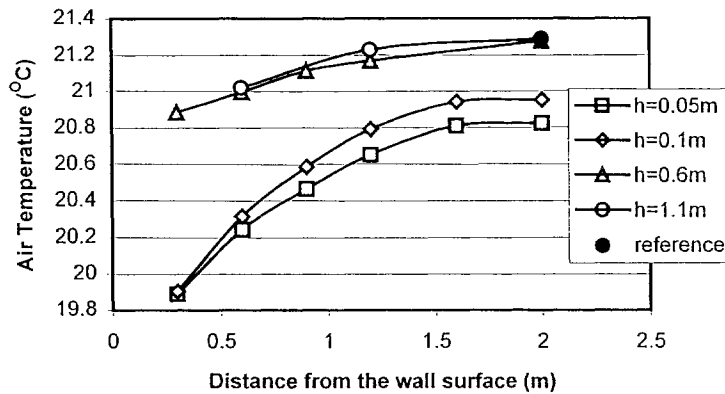
Figure 7.19 Mean air temperature measured at different heights from floor under CSA winter condition for system B

The measured air velocity and temperature under condition of –32°C outside and 21°C inside are shown in Figure 7.20 to Figure 7.23 for system A and B. The patterns are similar to those under CSA winter condition. The measurements were taken at slightly different locations. The difference includes: a) the measurements at a height of 1.1 m were removed since in the previous sets of measurements the measured values were almost uniform as of 0.1m/s in the direction normal to the wall surface; b) a set of measurements at height of 0.3 m from the floor were added to investigate more closely the impact of cold draft between the ankle and seated heights.

The measured profiles in Figure 7.20 to Figure 7.23 show more complete details for the cold draft from near the wall surface to the occupied zone. At the height of 0.6m, the air velocity measured at 0.1m from the wall reaches as high as 0.475m/s and the velocity decreases with distance. The reason for such high velocities is because the closer to the wall surface, the closer to the trajectory of the cold draft at the height of 0.6m. Based on the analysis in section 7.3.1, the cold draft is deflected from the wall surface when the

cold air flows downward. For example, the air velocity at a height of 0.3m reaches its maximum value at the second location, 0.2m from the wall surface, as shown in Figure 7.20. Due to the same reason, the temperatures measured at height of 0.3m and 0.6m from floor have much lower temperature at the distance of 0.1m and 0.2m from the wall surface, as shown in Figure 7.21.
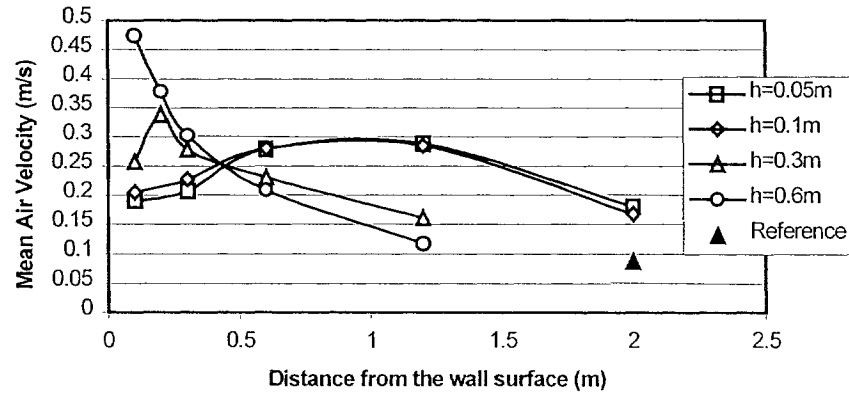
Figure 7.20 Mean air velocity measured at different heights from floor under –32°C outdoor condition for system A
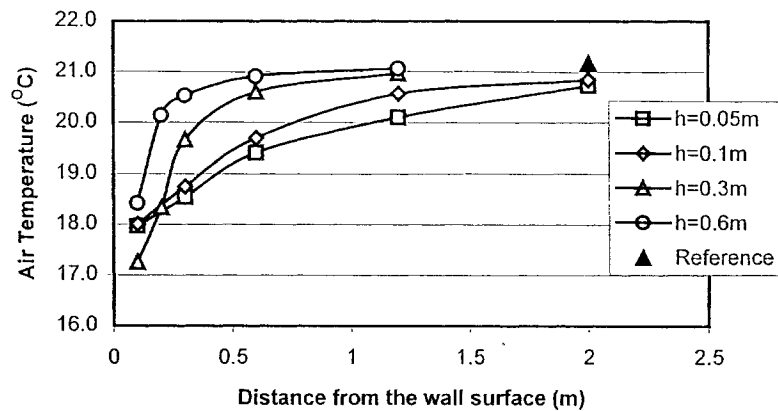
Figure 7.21 Mean air temperature measured at different heights from floor under –32°C outdoor condition for system A

The air velocity and temperature measured under Montreal worst winter conditions is about 0.02m/s higher and 0.8°C lower than that measured under CSA winter condition at

ankle level, which implies that higher percentage of dissatisfied will be experienced by occupants under colder outdoor temperature.
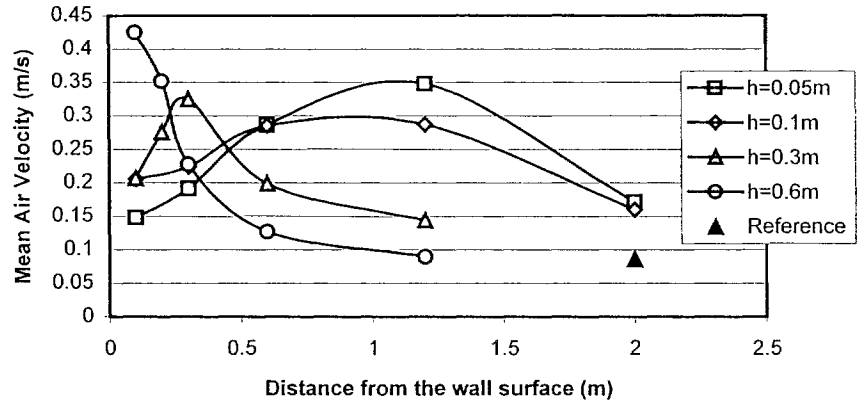
Figure 7.22 Mean air velocity measured at different heights from floor under –32°C outdoor condition for system B
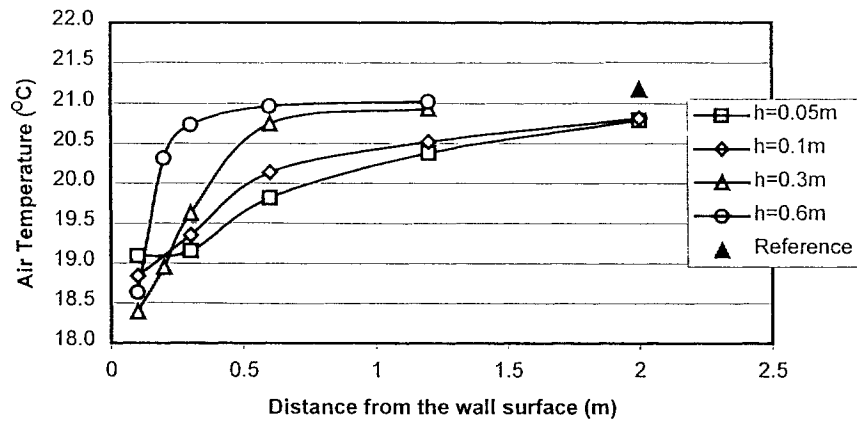
Figure 7.23 Mean air temperature measured at different heights from floor under –32°C outdoor condition for system B

The PD in the occupied zone at three levels of 0.1m, 0.6m and 1.1 m from the floor are calculated for both systems based on measurement data taken under two different test conditions. The results are listed in Table 7.2. The PDs at ankle level under two test

conditions are plotted in Figure 7.24 for system A and in Figure 7.25 for system B. The results show that there is higher risk of cold draft under colder test conditions. The ASHRAE requirement cannot be met until the occupants seat about 2m away from the wall surface under both test conditions for both wall systems.
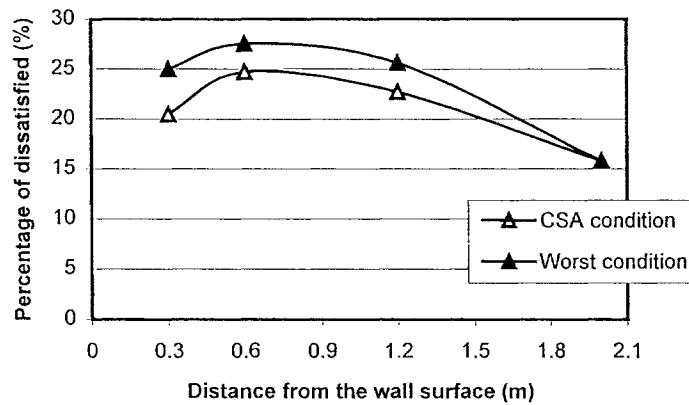
Figure 7.24 PD evaluated at ankle level under two test conditions for system A
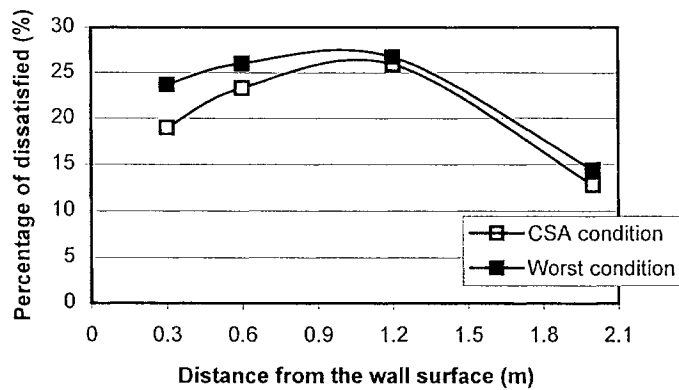
Figure 7.25 PD evaluated at ankle level under two test conditions for system B

Table 7.2 Percentage of Dissatisfied in the occupied zone under different test conditions for both curtain wall systems

Locations		Test Conditions			
		$T_o=-18°C, T_i=21°C$		$T_o=-32°C, T_i=21°C$	
Height from floor (m)	Distance from wall surface (m)	System A	System B	System A	System B
0.1	0.3	20.5	19.0	25.0	23.7
	0.6	24.7	23.3	27.5	26.0
	1.2	22.7	25.9	25.6	26.7
	2	15.8	12.8	15.8	14.4
0.6	0.3	27.9	26.8	33.0	29.1
	0.6	22.9	14.4	28.3	14.2
	1.2	17.5	12.3	12.6	8.4
	2	9.2	6.7		
1.1	0.6	8.5	9.5		
	1.2	10.0	7.3		
	2	9.4	8.4	7.5	7.5

The PDs calculated for the seated person level, 0.6m from the floor, under CSA winter conditions are plotted in Figure 7.26 for both wall systems. The ASHRAE requirement can be met by system B, but not by system A until about 1.5m away from the wall surface. At the standing level, 1.1m from the floor, the PDs are less than 10% for both systems (Table 7.2). Although the presence of the mechanical system significantly reduces the difference between the wall systems, the results do indicate that system B performs better than system A in term of risk of local draft. The wall surface temperature would have to be raised by means of perimeter heating or air from the HVAC system in order to meet ASHRAE requirements.

Percentage of dissatisfied (%)

30
25
20
15
10
5
0

—A— A-CSA condition
—☐— B-CSA condition

0   0.5   1   1.5   2   2.5

Distance from wall surface (m)
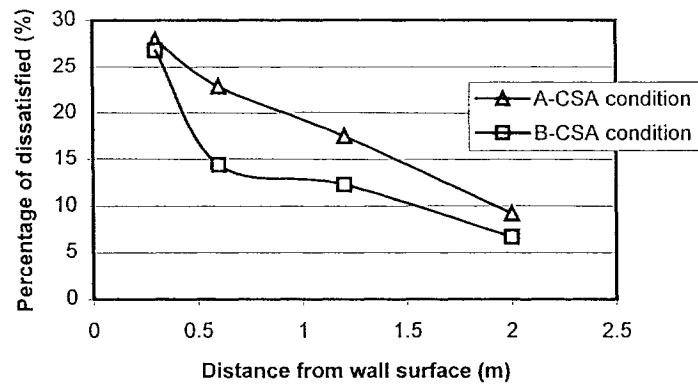
Figure 7.26 PDs evaluated at seating level under CSA winter conditions for both wall systems

7.4   Conclusion

The measurements of air velocity and temperature for the cold draft induced by two curtain wall systems were performed from the edge of frame to 2m in the occupied zone along the floor. The first part of the measurements identified the trajectory of the cold draft after it flows down the frame and before it hits the floor. The results indicate that a stronger cold draft is formed along the wall surface of system A due to its much colder glazing surface temperature compared to system B. With the presence of the frame, the cold flow is deflected away from the wall surface, and mixed with the room air before it moves into the occupied zone. The identified shapes of the trajectories are very close for the two systems although system A develops stronger cold draft.

The second part of the measurements in the occupied zone indicates that the presence of the mechanical system accelerates the mixing for the cold draft with the room air and results in higher air velocity and higher temperature. However, on the meantime, the presence of a mechanical system increases the percentage of dissatisfied by about 10% at

ankle level, and also significantly reduces the difference between the two curtain wall systems.

In reality, mechanical systems are operating when the occupant is present in commercial buildings. To represent more realistic performance of curtain walls, measurements were performed with a mechanical system on under two test conditions. The results of PD analysis indicate that at ankle level, ASHARE requirement cannot be met until the occupants seat about 2m away from the wall surface under both test conditions and for both curtain wall systems. Although the presence of the mechanical system reduces the different between the wall systems, the results do indicate that system B performs better than system A in term of risk of cold draft. This study suggests that the surface temperature of curtain walls needs to be raised to a comfort level.

Chapter 8

Evaluation of critical factors affecting thermal performance by simulations

8.1 Introduction

The overall thermal transmittance of metal curtain walls and the contribution of performance enhancement through the use of high performance glazing units are significantly affected by the performance of frame and spandrel panels as shown by existing studies reviewed in Chapter 2 and by the calculations demonstrated in Chapter 1. Simulation techniques are employed in this chapter for more detail studies on the heat transfer processes through metal curtain walls. A holistic approach was used in simulations for evaluating the effect of the design details in glazing, frame and spandrel panels on the U-factor of metal curtain walls. This approach, referred to as the integrated method in this thesis, treats metal curtain walls as integrated systems. The estimation results by the integrated method were compared to those by the conventional method and CSA method in calculating the overall U-factor for different metal curtain wall systems.

Computer simulation programs FRAME/VISION have been validated by physical tests and recommended by the standards to calculate U-factors for fenestration systems. However, the reliability of these programs to predict the condensation resistance performance is still under study. The simulation procedure is still under development. The existing studies (Wright, 1996; McGowan, 1995 and 1998) concluded that a large

discrepancy existed between the simulation and test results in predicting the local temperature distribution at edge-of-glass and frame area. Two main possible reasons believed to be responsible for the discrepancy are, first, the assumption of one constant surface film coefficient in the simulations and second, the omission or inaccurately reported locations of measurements (McGown, et al.,1998). The extensive 3-dimensional temperature measurement in this research makes it possible to do more accurate and thorough comparison between the simulations and the experimental results. More realistic boundary conditions obtained through actual testing and detail analysis were applied in simulations and results were compared to measurements.

8.2 Integrated simulation approach

For decades, the thermal performance of the entire metal curtain wall has been evaluated and represented only by the performance of the vision panel for product comparison purpose. In current curtain wall practice, for the purpose of estimating energy consumption, only the U-factor for center-of-spandrel is considered without taking into account the effect of edge-of-spandrel and frame. The new edition of CSA A440.2 (1998) recommends taking the spandrel panel into account when evaluating the overall thermal performance of metal curtain walls, but "The properties for curtain walls shall be determined separately for the vision panel and the spandrel panel."(CSA, 1998). As shown in Figure 8.1, the dimension to determine the U-factors extends to the outside of the mullion for product comparison purpose. For energy calculation purpose, the dimension is from centerline to centerline. The sections to be simulated are jamb

sections (Figure 8.1a and 8.1b), and are assumed with an adiabatic boundary condition for the frame/wall junction.

The significant thermal bridge effect of the return of the steel back-pan makes the assumption of adiabatic boundary condition for the frame-wall joint unrealistic. A holistic approach was developed to treat curtain walls as integrated systems. As shown in Figure 8.2, the dimensions to determine the overall U-factor for the wall are the horizontal and vertical distances between the centerlines of the mullions. The sections to be simulated for this calculation include the sill section which consists of the edge-of-glass, mullion, and edge-of-spandrel (Figure 8.2a), the intersection of the vision panels (Figure 8.2b), and the intersection of the spandrel panels (Figure 8.2c). Thus, the boundary conditions used in the simulation are the real conditions experienced by the curtain wall sections. This integrated method was used in this chapter for both the thermal transmittance evaluation and temperature distribution prediction.

(a) Vision panel jamb section

(b) Spandrel panel jamb section
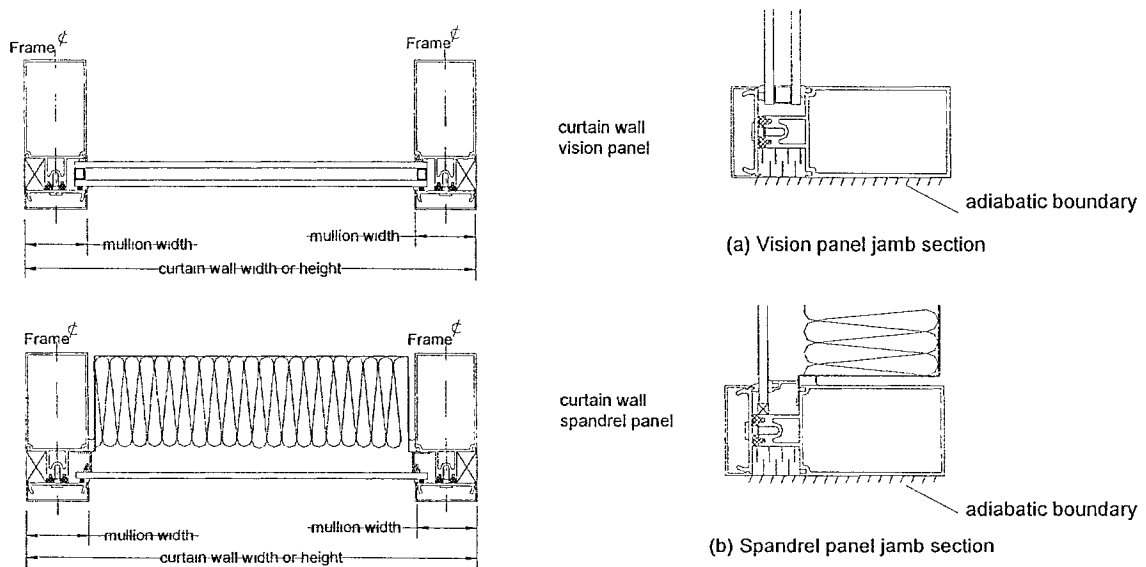
Figure 8.1 CSA method to determine the U-factor for metal curtain walls

edge-of-glass

center-of
glass

vision panel height

2

1

edge-of-spandrel

center-of
spandrel

3

spandrel panel height

curtain wall height

(a) 1-sill section   (b) 2-intersectin of vision panels

(c) 3-intersection of spandrel panel
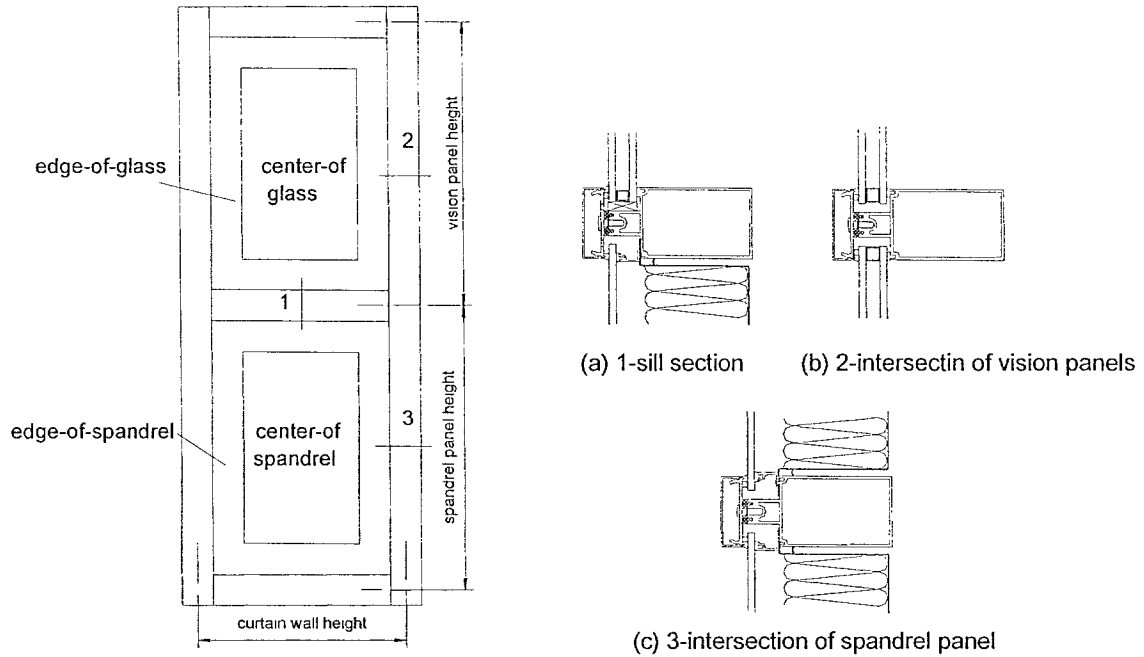
Figure 8.2 Integrated method to determine the overall U-factor for metal curtain walls

8.3 Effect of design details on U-factors

Three main thermal bridges exist at the joint section of curtain walls, including the conventional aluminum spacer at the edge of the glazing, the steel screws used to fasten the pressure plates to the frame, and the return of the steel back-pan. The heat flux plotted in Figure 8.3 clearly shows that heat flow concentrates on these thermal bridges. The effect of design details on both the component U-factor and on the overall U-factor for curtain wall assemblies sized 1.22m by 3.66m are discussed in the following sections.
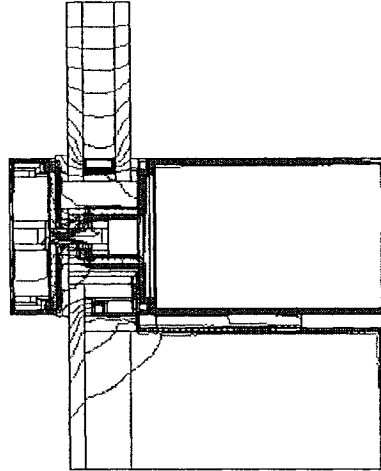
Figure 8.3 Heat flux plot for a joint section

8.3.1 Simulation configurations

The section simulated is the sill section, which consists of the edge-of-glass, the frame and the edge-of-spandrel altogether. The design details examined include two different types of glazing units, two types of spacers, two types of frame configurations, two types of different back-pan designs, and different spacing of screws. All the design details studied in this chapter are based on the overall structures of the two curtain wall systems tested in the environmental chamber. Five different configurations were obtained by combining individual design details and are listed in Table 8.1. The configuration details regarding the dimension and the composition of the vision panel, frame, and spandrel panel are given in Table 3.1 of Chapter 3.

The standard insulated glazing unit (IGU) uses double clear glass with conventional aluminum spacer and has a U-factor of 2.76 W/(m^2·K) at the center-of-glass obtained from VISION simulations. A high-performance IGU has low-E coating (ε=0.1) on the

exterior surface of the inner pane, Argon gas filling within the glazing cavity, and thermally broken spacer. It has a U-factor of 1.53 W/(m²·K) at the center-of-glass. The spandrel panel is composed of 6.4mm thick exterior clear glass and 101.6mm high-density mineral fiber insulation with a 19mm air gap in between. The U-value of the center-of-spandrel is 0.34 W/(m²·K).

Table 8.1 Detailed configurations simulated

	Configurations			A	B
1	clear double glazing unit with conventional aluminum spacer	Regular backpan design	screw spacing at 150mm	√	√
2			screw spacing at 76mm, 230mm, 300mm and 450mm	√	
3		Revised backpan design with screw spacing of 150mm		√	√
4	double glazing unit with low-E coating, Argon gas, and thermally broken spacer	Regular backpan design with screw spacing at 150mm		√	√
5		Revised backpan design with screw spacing at 150mm		√	√

Two types of back-pan designs were simulated. One is the regular design (Figure 8.4a), the other is the revised design (Figure 8.4b), which shifts the connection to the interior flange of the mullion tube to eliminate the thermal bridge created by the return of the back-pan. The screws are made of stainless steel.

8.3.2 Simulation procedure

Programs FRAME and VISION were used to carry out the simulations using CSA winter conditions. The outdoor surface film coefficient uses the standard value of 30 W/m²·K, and the indoor surface film coefficient uses 8.3 W/m²·K for the frame and edge-of-spandrel areas. The edge-of-glass sections in FRAME simulations are imported from VISION simulations and have a constant surface film coefficient value same as that for

the center-of-glass. The value of film coefficient obtained from program VISION is a function of the temperature difference between glass surface and room air (ASHRAE, 1996).

The boundary conditions assigned for the sill sections are shown in Figure 8.4a for the regular back-pan design and in Figure 8.4b for the revised back-pan design by heavy dashed lines. Adiabatic conditions were assumed for all the "cut" surfaces at edge-of-glass and edge-of-spandrel. For the frame area in regular back-pan design, there is a gap of around 6.4mm between the lower horizontal surface of the mullion and the surface of the return of the back-pan. The boundary conditions along these two surfaces was defined according to CSA A440.2, which states that "if a frame cavity extends at least five times the width of its opening into the frame, then the air cavity beyond the five-times width can be considered stagnant". Therefore, the surfaces of the first 32mm length of this segment comply with indoor boundary conditions, as shown by heavy dashed line in Figure 8.4a; while the rest of the cavity is treated as regular air cavity. In the revised back-pan design, the standard indoor boundary conditions were applied to all of its exposed surfaces since no such a recessed cavity exists.

In the FRAME program, each section is defined by two location points. For example, in the regular back-pan design shown in Figure 8.4a, the edge of glass is defined by location points 2 and 3, fame section if defined by location points 3 and 4, and edge-of-spandrel is defined by points 4 and 5. The U-factor for each component is calculated based on the projection height between the two location points. The U-factor for each section in the

regular back-pan design can be obtained through one simulation run by defining the sill

section as a "wall junction". The "wall junction" attribute allows six location points, but

location point 2 &3, 4&5 must be vertically aligned.

adiabatic boundary conditon

inside
h_i=8.3
$W/m^2 \cdot K$

Outside
h_o=30 $W/m^2 \cdot K$
T_o=-18°C

32

63.5

63.5

6.4

63.5

6   5

adiabatic boundary conditon

(a) regular back-pan design (dimension in mm)

adiabatic boundary conditon

inside
h_i=8.3
$W/m^2 \cdot K$

Outside
h_o=30
$W/m^2 \cdot K$

63.5

63.5

63.5

(4)

5

adiabatic boundary conditon
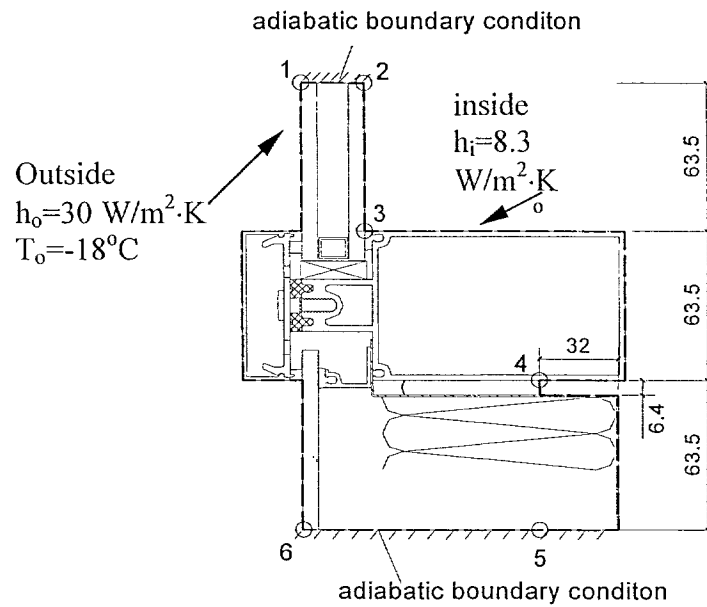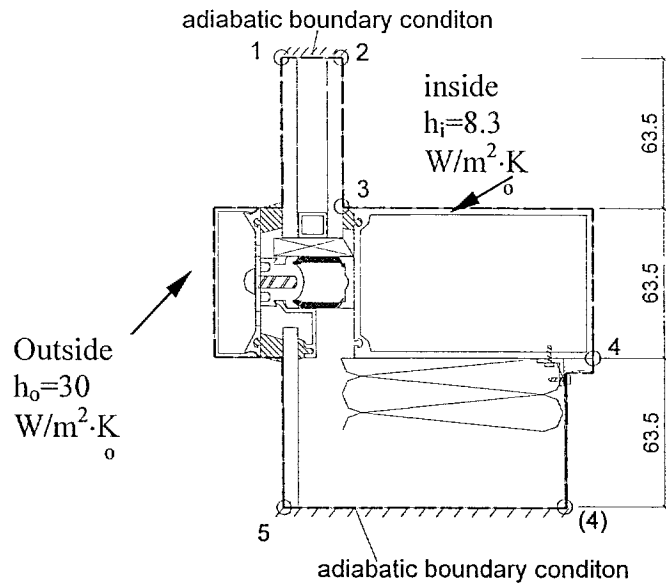
(b) Revised back-pan design (dimension in mm)

Figure 8.4 Boundary conditions assigned in simulations

223

In the revised back-pan configuration, however, no point on the spandrel "cut" surface can be vertically aligned with location point 4 due to the small recession of the back-pan. Therefore, a different simulation technique was used. The sill section was defined as "sill" attribute, which allows five location points only. Two simulation runs were required. In the first run, the location point 4 was defined at the bottom of the mullion and the obtained results include the U-factor for the edge-of-glass and the U-factor for the frame (U_f). In the second run, the location point (4) was defined at the bottom of the edge-of-spandrel, the calculated U-factor for the so-called "frame" (U_{f2}) in fact includes both the frame and the edge-of-spandrel sections. Then, the U-factor for the edge-of-spandrel was calculated by equation 8.1 since the projected height for frame and edge-of-spandrel is the same:

$$U_{es} = 2 \cdot U_{f2} - U_f \qquad (8.1)$$

where, U_{es} is the U-factor for edge-of-spandrel, W/m^2·K.

The fastening screws in the frame configuration of system A create thermal bridges. Both parallel path method and isothermal plane method were employed to consider the effect of screw on the U-factor. The parallel path method requires two runs, one with the stainless steel screw, and the other without. These two runs result in two sets of U-values for edge-of-glass, frame, and edge-of-spandrel, respectively. The U-value obtained from parallel path method is the area-weighted average of the U-factor simulated with screws (U_{screw}) and the U-factor simulated without screw (U_{air}), as expressed in equation 8.2.

$$U_p = a_{screw}U_{screw} + a_{air}U_{air} \qquad (8.2)$$

where, U_p is the component U-factor by parallel path method in W/(m$^2 \cdot$ K); a_{screw} is the area percentage with screw in %, a_{air} is the area percentage without screw,(1-a$_{screw}$) in %. The area percentage of the screw was calculated following the guideline of CSA A440.2, which states that for circular element such as bolts, the effective length of the bolts in the dimension perpendicular to the cross-section shall be taken as 0.79 (π/4) times the diameter.

In the isothermal plane method, the effective conductivity for the screw space is determined based on an area-weighted average of the screw conductivity (k_{screw}), and the no-screw conductivity (k_{air}). The space without screw is composed of two air spaces, a nylon thermal break section, and an aluminum section. The no-screw conductivity (k_{air}) can be obtained by dividing the inverse of the sum of the thermal resistance from each material in the space by the total length of the screw space. The effective conductivity of the screw space by isothermal plane method, k_{iso} (W/m·K), can be calculated by the following equation:

$$k_{iso} = a_{air}k_{air} + a_{screw}k_{screw}$$ (8.3)

The screw spacing studied ranges from 76mm (3") to 305mm (12") at interval of 76mm, 457mm (18") and 610mm (24"). The yielded effective conductivities at different screw spacing distances are listed in Table 8.2. Since the parallel path method and the isothermal plane method give the lower and upper bounds (ASHRAE, 1993), the average of these two results was used to represent the U-factor for each component with specific screw spacing distance.

225

In the frame configuration of system B, the use of reinforced nylon mullion nose reduces the thermal bridge effect of screws so much that the effect of screws is negligible. The pre-simulations show that the difference between the U-factors simulated with and without screws is less than 0.5%. Therefore, the effect of the screws can be omitted and all of the configurations simulated for system B have screws in the cross sections.

Table 8.2 Effective conductivity calculated for the screw space by isothermal plane method with difference spacing distances

Conductivity (W/ m·K)	Screw spacing (mm)					
	76	152	229	305	457	610
Stainless steel	14.3					
Screw space	0.0376					
Effective conductivity	2.418	1.225	0.830	0.632	0.434	0.334

The material conductivities used in the simulations were taken from the database in program FRAME and are listed in Table D.1 in Appendix D.

8.3.3   Simulation results

The U-factors obtained through FRAME simulations for curtain wall sills sections with various design details are presented and discussed in this section. The effect of these design details is indicated by comparing component U-factors and the total U-factors for the whole joint section, and also by heat flux plots.

8.3.3.1   Results for system A

The U-values with various design details for system A are listed in Table 8.3. The improvement is calculated over the base configuration with a standard IGU and regular back-pan design. The average of U-factors obtained from parallel path method and isothermal plane method is used for the comparisons. The U_{total} listed in Table 8.3 is the U-factor for the whole joint section of curtain walls.

The simulation results indicate that the U-factor for the edge-of-glass depends mainly on the spacer type and the U-factor for the center-of-glass. The configuration of the back-pan has little impact on it due to the high heat loss through the frame. The type of glazing unit has a small influence on the U-factor of the frame (2.5%) and on the U-factor of the edge-of-spandrel (2.4%). Although the use of high-performance IGU can lower the U-value at the edge-of-glass by 32%, its effect on the total U-value of the joint section is only 9.6%. The revision of the back-pan lowers the U-factor for the frame by about 14%, but it dramatically increases the U-factor for the edge-of-spandrel by about 50%. The net result on the total U-value of the joint section is 0%, which indicates that the shifting of the back-pan would not reduce the heat loss unless the conductance of the frame is improved, which is the case in system B.

Table 8.3 U-factors for various design details for system A *

		Baseline Regular back-pan Standard IGU	Case 1 Regular back-pan High-performance IGU		Case 2 Revised back-pan Standard IGU		Case 3 Revised back-pan, High-performance IGU	
		U-value $(W/m^2 \cdot K)$	U-value $(W/m^2 \cdot K)$	IM (%)	U-value $(W/m^2 \cdot K)$	IM (%)	U-value $(W/m^2 \cdot K)$	IM (%)
U_{eg}	Parallel	3.19	2.12		3.25		2.18	
	Isothermal	3.18	2.21		3.29		2.21	
	Average	3.18	2.17	31.8	3.27	-2.8	2.20	30.8
U_f	Parallel	7.56	7.31		6.49		6.33	
	Isothermal	8.91	8.74		8.18		8.06	
	Average	8.24	8.03	2.5	7.13	13.5	7.00	15.1
U_{es}	Parallel	1.92	1.87		2.84		2.78	
	Isothermal	2.21	2.16		3.52		3.52	
	Average	2.07	2.02	2.4	3.10	-49.7	3.07	-48.3
	U_{total}	4.50	4.07	9.6	4.50	0.0	4.09	9.1

* IM= improvement, IGU=insulated glazing unit, U_{eg} = U-factor of the edge-of-glass, U_f =U-factor of frame, U_{es} = U-factor of the edge-of-spandrel.

227

The effect of these details can also be illustrated directly by the heat flux density plot as shown in Figure 8.5. Three designs are compared in Figure 8.5. Each line in a plot represents one unit of heat flux (1 W/m) based on the projection height. The total heat flow through a component can be estimated by multiplying the number of heat flux lines through its boundary and the projection height of the component. In the simulation configurations, each of the three components has the same projection height of 63.5mm (2.5"). Therefore, the amount of heat flow can be compared directly by counting the number of heat flux lines or by observing the density of the lines. For example, Figure 8.5a shows the heat flux through the configuration with the standard glazing unit and regular back-pan. There are 10 heat flux lines through the edge-of-glass section, 7 lines through the edge-of-spandrel, and 20 lines through the frame section. After replacing the standard glazing unit with high-performance glazing unit the heat flow through edge-of-glass is reduced to 6 lines (Figure 8.5b), while the heat flow through the edge-of-spandrel and frame remains the same. When the back-pan design is revised (Figure 8.5c), the number of heat flux lines is reduced to 6 through the adapter and the edge-of-spandrel glass. However, a large amount of heat is transferred from the back-pan to the frame through the connector as shown in Figure 8.5c. This explains why shifting the return of back-pan dramatically increases the U-factor of the edge-of-spandrel. When the frame performance is poor, this revised design results in transferring of heat from back-pan to the frame, so the frame is warmed up and the U-factor of frame is reduced. However, the heat loss transferred through the return of the back-pan is now transferred through the frame. The net result is that the total amount of heat loss through the joint section remains the same, while the paths of the heat flow are re-distributed.

(a) standard IGU,   (b) high-performance IGU,   (c) standard IGU
    regular back-pan   regular back-pan,   revised back-pan
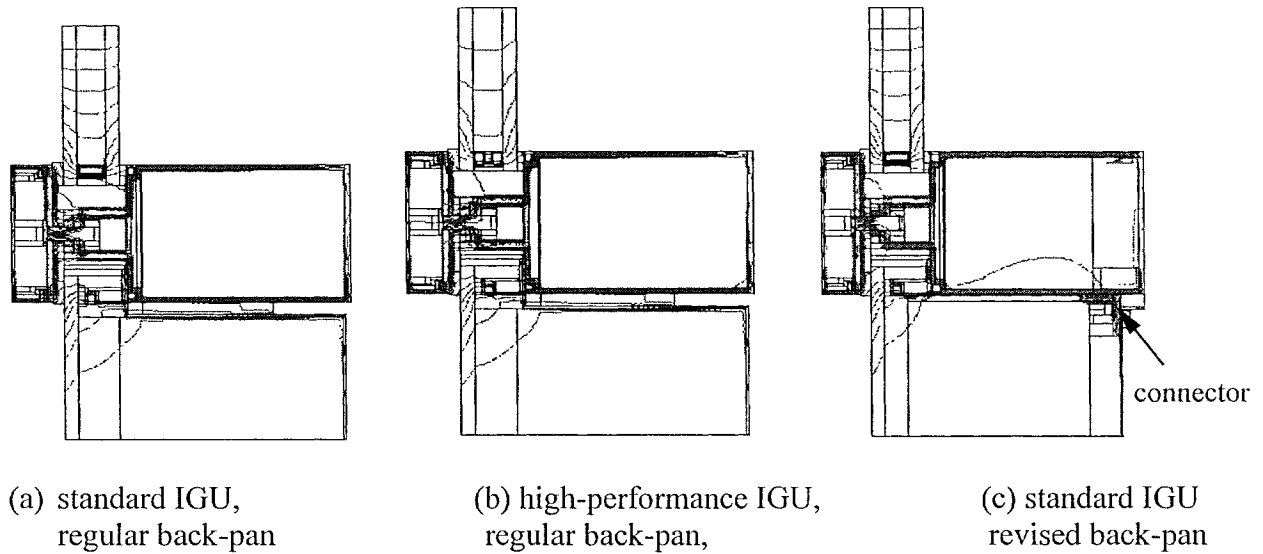
Figure 8.5 Heat flux plots for sill sections with different design details in system A

The effect of the spacing of stainless screws for system A with standard IGU and regular back-pan is shown in Table 8.4. The comparisons are made against the case without screws given in the last column of Table 8.4. The spacing varies from 76mm up to 457mm. As in the back-pan design, the spacing of the screws has little effect on the U-value at the edge-of-glass (1.2%). However, the effect of the screw spacing is significant on the U-factor for the frame and for the edge-of-spandrel (Figure 8.6). In practice, the pressure plates are normally pre-drilled every 76mm (3"). The standard spacing for screws is 152mm (6"). Sometimes at the corners, to increase the structural strength, screws are used at every 76mm. When the spacing is reduced to 76mm, the U-factor of the frame is increased by as much as 27% compared to the case without screws. When the spacing of screws is increased to 457mm, which is 3 times the standard spacing, the U-factor for the joint section can be reduced by 6.7%. It can be seen that the stainless steel screws at 152mm spacing increase the U-factor of the frame by 16 %. The thermal

229

performance of the frame may be improved by increasing the screw spacing, by using low-conductivity screw materials, and by breaking the thermal bridge.
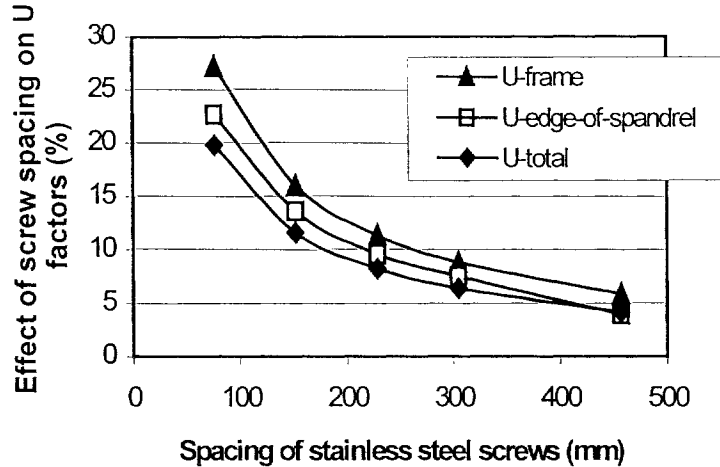
Figure 8.6 Impact of screw spacing on U-factor at joint section for system A

Table 8.4 Effect of screw spacing on U-factors (W/m²·K) for system A with standard IGU*

		Spacing of screws (mm)					
		76	152	229	305	457	No screw
Edge-of-glass	U-factor	3.22	3.18	3.18	3.18	3.18	3.18
	Difference (%)	1.2	0.0	0.0	0.0	0.0	
Frame	U-factor	9.03	8.24	7.90	7.72	7.51	7.10
	Difference (%)	27.2	16.0	11.3	8.8	5.8	
Edge-of-spandrel	U-factor	2.23	2.07	1.99	1.96	1.89	1.82
	Difference (%)	22.7	13.6	9.5	7.5	3.9	
Total	U-factor	4.83	4.50	4.36	4.29	4.20	4.03
	Difference (%)	19.8	11.6	8.2	6.4	4.1	
U_{total} Compared to the standard spacing 152mm (%)		-7.4	0.0	3.0	4.6	6.7	10.3

*compared to the base case "No screw".

8.3.3.2 Results for system B

The U-values with various design details for system B are listed in Table 8.5. The improvements are calculated over the base configuration with a standard IGU and regular

230

back-pan design. Similar to the findings for system A, the U-factor of the edge-of-glass depends mainly on the spacer type and the U-factor for the center-of-glass. With the improvement of the frame performance, the dependency of the U-factor at the edge-of-glass on the frame configuration is slightly greater than that in system A. The performance of the frame is also more sensitive to the type of glazing. The use of high-performance IGU lowers the total U-factor for the joint by about 20%, which is much greater than that for system A. The revised back-pan lowers the U-factor for the frame by 16% and the total U-factor for the joint section by 6%, These results indicate that when the frame performance is improved, the shifting of the back-pan connection can reduce the heat loss through the joint section.

Table 8.5 U-factors for various design details for system B *

	Baseline Regular back-pan Standard IGU	Case 1 Regular back-pan High-performance IGU		Case 2 Revised back-pan Standard IGU		Case 3 Revised back-pan, High-performance IGU	
	U-value $(W/m^2 \cdot K)$	U-value $(W/m^2 \cdot K)$	IM (%)	U-value $(W/m^2 \cdot K)$	IM (%)	U-value $(W/m^2 \cdot K)$	IM (%)
U_{cg}	3.24	2.10	35.2	3.07	5.3	1.93	40.4
U_f	3.46	3.18	8.1	2.9	16.2	2.67	22.8
U_{es}	0.91	0.85	6.6	1.19	-30.8	1.19	-30.8
U_{total}	2.54	2.04	19.7	2.39	5.9	1.93	24.0

* IM= improvement, IGU=insulated glazing unit, U_{cg} = U-factor of the edge-of-glass, U_f =U-factor of frame, U_{es} = U-factor of the edge-of-spandrel.

The heat flux density plots for three different designs in system B are shown in Figure 8.7. The amount of heat loss through the edge-of-glass area is the same as that in system A, but the number of the heat flux has been dramatically reduced from 20 to 7 for frame and from 7 to 3 for the edge-of-spandrel. The smaller number of heat flux through edge-

of-spandrel in system B indicates that when the frame performance is improved, the heat loss through the edge-of-spandrel can be significantly reduced. When the back-pan design is revised for system B (Figure 8.7c), the number of heat flux through the edge-of-spandrel is reduced by 1, that is the same as for system A (Figure 8.5c). However, the heat flow transferred from back-pan to the frame is not as significant as that in system A due to the high performance of the frame. Therefore, a net reduction of 6% in the total heat loss through the joint section is yielded.

| (a) standard IGU, IGU regular back-pan | (b) high-performance IGU, regular back-pan, | (c) high-performance revised back-pan |
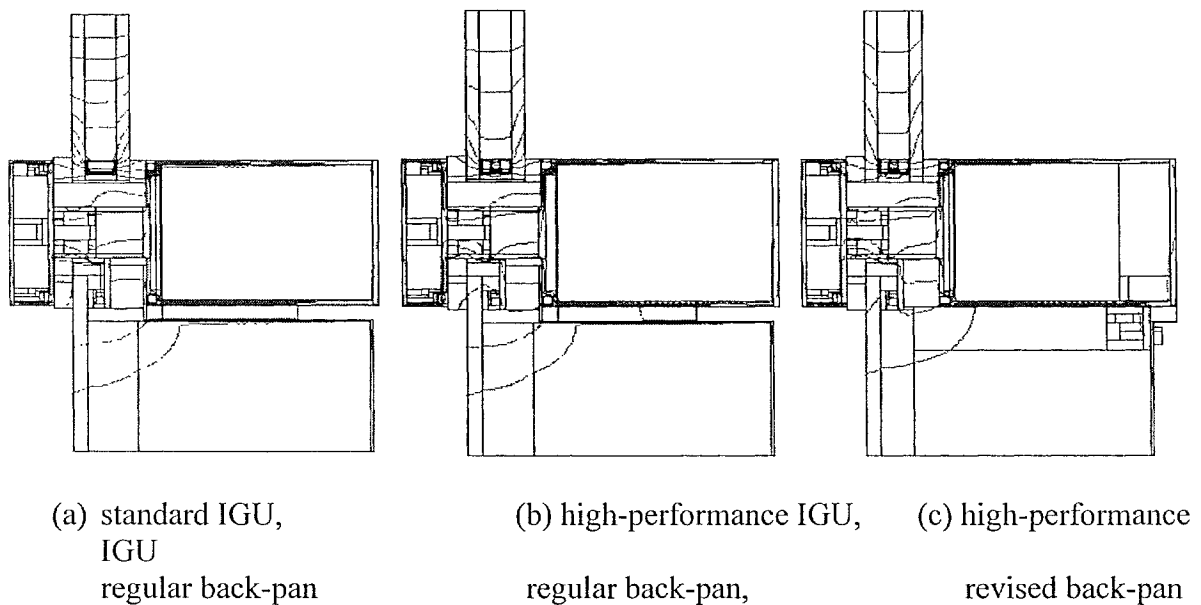
Figure 8.7 Heat flux plots for sill sections with different design details in system B

The comparison between system A and B is shown in Table 8.6. The use of the reinforced nylon as a larger thermal break in the mullion of system B reduces the U-factor of the frame by 58 to 63%, the U-factor of edge-of-spandrel by 56 to 62%, and the total U-factor of the joint section by 44 to54% compared to system A. With the higher

232

thermal resistance in the frame, the impact of spacer types on the U-factor of the edge-of-glass, frame, and edge-spandrel increases.

Table 8.6. Comparisons of U-factors between system A and system B[*]

| | With Regular Back-pan | | | | | | | | With Revised back-pan | | | |
| | Standard IGU | | | | High-performance IGU | | | | High-performance IGU | | | |
	U_{eg}	U_f	U_{es}	U_{total}	U_{eg}	U_f	U_{es}	U_{total}	U_{eg}	U_f	U_{es}	U_{total}
A	3.18	8.24	2.07	4.50	2.17	8.03	2.02	4.07	2.20	7.19	3.15	4.18
B	3.24	3.46	0.91	2.54	2.10	3.18	0.85	2.06	1.93	2.67	1.19	1.93
IM (%)	-1.9	58.0	56.0	43.6	3.2	60.4	57.9	49.4	12.3	62.9	62.2	53.8

*U_{eg} = U-value of edge-of-glass, U_{es} = U-value of edge-of-spandrel, U_f = U-value of frame, values are in $W/(m^2 \cdot K)$.

8.3.3.3 Effect of design details on the overall U-factor

To indicate the effect of the design details on the overall U-factor of curtain walls, four types of curtain wall designs are considered. The dimension of the curtain wall is 1.22m wide and 1.83m high at centerline of mullions for both vision panel and spandrel panel. This dimension is recommended by CSA A440.2 for the evaluation of thermal transmittance of curtain wall panels. The results shown in Table 8.7 indicate that by replacing the standard glazing unit with high performance glazing unit, the U-factor of the vision panel is reduced by 33% and the overall U-factor is reduced by 25%. By using frame system B, which has larger thermal breaks, the overall U-factor is reduced by 22%, which has almost the same effect as using high-performance glazing unit. When combining high-performance glazing unit with the high-performance frame system, the overall thermal U-factor is reduced by 48%.

Table 8.7 Overall U-factor for four types of curtain wall designs in W/($m^2 \cdot$ K)

	Frame configuration A		Frame configuration B	
	With Standard IGU	With High-performance IGU	With Standard IGU	With High-performance IGU
Visional Panel	3.38	2.25	2.95	1.78
Spandrel Panel	1.23	1.22	0.66	0.65
Total	2.31	1.74	1.81	1.21

8.4 Comparisons between different methods in calculating overall U-factors

The overall thermal transmittance determined by the conventional method, CSA method, and the integrated method are compared for two types of curtain wall designs. The results are shown in Table 8.8. The dimensions used in CSA method is from centerline to centerline since the purpose of the U-value calculation is for energy consumption estimation.

For system A with regular back-pan and standard IGU, the CSA method predicts about 25% lower U-value for the frame than the integrated method due to the simplified assumption of adiabatic condition for the frame/wall junction. The overall U-factor calculated by CSA method is 2.18 W/$m^2 \cdot$K, which is about 6% lower than that calculated by the integrated method. The small difference is because of the low percentage of frame, which takes only 8.5% of the total curtain wall area. For frame system B, the difference between these two methods is similar as of 5%. The conventional method, which does not consider the effect of edge of spandrel and frame, overestimates the overall performance by about 23% for system A and 17% for system B compared to the integrated method.

Table 8.8 Comparison between three methods calculating the overall thermal transmittance for metal curtain walls

		System A with regular back-pan and Standard IGU				System B with regular back-pan and high-performance IGU			
		U_{edge}	U_{center}	U_{frame}	U_{total}	U_{edge}	U_{center}	U_{frame}	U_{total}
Integrated method	Vision panel	3.17	2.76	9.33	3.38	2.03	1.53	3.53	1.78
	Spandrel panel	2.30	0.34	7.10	1.23	1.00	0.34	2.76	0.65
	Total	2.31				1.22			
CSA method	Vision panel	3.25	2.76	7.38	3.23	2.10	1.53	2.44	1.70
	Spandrel panel	2.62	0.34	5.33	1.13	1.14	0.34	2.10	0.62
	Total	2.18				1.16			
Conventional method	Vision panel	3.25	2.76	7.38	3.23	2.10	1.53	2.44	1.70
	Spandrel panel	0.34				0.34			
	Total	1.79				1.02			

8.5 Effect of realistic boundary conditions on temperature prediction

A set of boundary conditions have been assigned in FRAME simulations for the sill sections. The effect of realistic boundary conditions on the prediction of surface temperature distribution has been studied by comparing the simulations to the measured results. The simulation procedure and the results are discussed in detail in this section.

8.5.1 Procedure

The temperature of the interior glazing surface is influenced by the local film coefficients on both indoor and outdoor sides, but it is more sensitive to the interior surface heat transfer coefficients. Therefore, different sets of local film coefficients on the indoor side

have been used in FRAME simulations to study the accuracy of the program in predicting the temperature distribution at curtain wall sill sections. A constant film coefficient is used over the outdoor surface since its local effect is not significant on the prediction of the indoor surface temperatures.

Five sets of boundary conditions to be used for the study are:

1. **Standard conditions**

   Simulations are performed in accordance with the procedure to determine the U-factor with the standard constant boundary conditions for indoor and outdoor;

2. **Standard conditions with convection in glazing cavity**

   To evaluate the condensation resistance of glazing unit, a 2-D CFD (computational fluid dynamic) analysis can be carried out with the VISION program. When the glazing unit is imported into the FRAME program, the velocity files have been embedded at the edge-of-glass section. A heat transfer solution which accounts for the effect of fill gas convection can be generated by running the simulation under "convection" mode in the FRAME program. The sill sections are simulated under "convection" mode with standard film coefficients.

3. **Test conditions with convection in glazing cavity**

   The average film coefficients experienced by the test wall in the environmental chamber, which have been determined and reported in chapter 6, are assigned at the room side and the outdoor side. The sill sections are simulated under "convection" mode with the actual average film coefficients.

4. Convection in glazing cavity and locally varying film coefficient for the frame and the edge-of-spandrel

The local film coefficients along the frame surface and edge-of-spandrel surface are applied. The determination procedure is described in section 8.5.2 and the results are given in Table 8.10. The constant film coefficient is applied over the edge-of-glass area.

5. Convection in glazing cavity, locally varying film coefficients for both edge-of-glass, and frame and edge-of-spandrel sections

The local film coefficient along the edge-of-glass is determined and applied as well. The procedure is described in section 8.5.2 and the results are given in Table 8.10.

The locations of temperature measurements across the sill section are indicated in Figure 8.8. The measured temperatures were compared to the simulations at these locations. The edge-of-glass is extended to 76.4mm (3") instead of 63.5mm (2.5") since one temperature measurement was located at 63.5mm away from the bottom sight-line. The edge-of-glass is divided into 3 segments, each has a length of 25.4mm (1"), as shown in Figure 8.9. The upper surface of the frame is divided into 3 segments as well, and the length for each segment is shown in Figure 8.9. The vertical mullion surface plus the small segment on the lower horizontal surface is defined as one boundary segment. The small portion of the return of the back-pan and the vertical surface of the back-pan is defined as one boundary segment.

Figure 8.8 Locations of temperature measurements across sill section

Figure 8.9 Boundary segments defined at sill section

8.5.2 Determination of local film coefficients at sill section

The local convection film coefficient for edge-of-glass was measured and discussed in Chapter 6. The measured results are shown in Table 8.9. For the upper surface of the mullion, the local convection film coefficient is calculated using the correlation developed by Curcija and Goss (1993):

$$h_x = 0.1 + 1.75(\frac{x}{x_1})^{\frac{1}{3}}$$
(8.4)

where,

x = the horizontal distance from the beginning of the frame, m;

$x_1 = D\text{-}0.25 \cdot C_f$, D is the depth of the frame,

238

For the end region of the horizontal surface of the mullion, which is the segment VI shown in Figure 8.9, the following correlation is used:

$$h_x = 1.75 + 24\frac{1}{C_f^2}(x - x_1)^2 \qquad (8.5)$$

Where, C_f = conversion factor, C_f=1 for dimension in inches, and C_f=0.0254 for dimension in m.

For the vertical surface of the mullion, and the edge-of-spandrel, the following correlation is used according to the recommendation from Curcija and Goss (1993):

$$h_y = C_1\frac{k}{y}Ra_y^{0.25} \qquad (8.6)$$

The benchmarking values of constant coefficient C_1 is listed in Table 2.2 of Chapter 2. The value of 0.4425 from McAdams (1954) is used in this calculation. y is the vertical distance from the top of the glazing unit. The calculated results using the above equations for segment IV to VIII (See Fig. 8.9) are listed in Table 8.9.

The edge-of-glass region and the upper mullion surface can see each other, which reduces the radiation heat exchange to the room surfaces. The procedure described in section 6.4.1 is followed to estimate the local radiation film coefficients for segments I to VI. To determine the view factor between surfaces, the cross-string method is employed. The cross-string method is used to analyze two-dimensional structures with infinite extent in one direction, such as long attics, ducts and channels. For a three-sided enclosure as shown in Figure 8.10, the view factor can be calculated using equation 8.7 (Hagentoft, 2001).
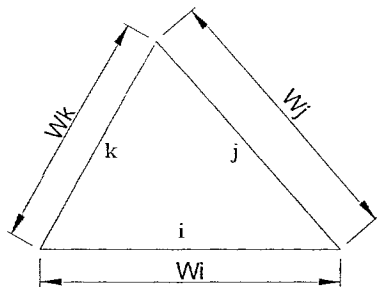
$$F_{ij} = \frac{W_i + W_j - W_k}{2W_i} \qquad (8.7)$$

Figure 8.10 View factor for a three-sided enclosure using cross-string method

The radiation analysis in section 6.4.2 found that the large room of the hot box can be considered as a black body with room air temperature. Therefore, the radiation exchange between edge-of-glass, upper mullion surface, and room can be simplified as a seven-element enclosure, shown in Figure 8.11.
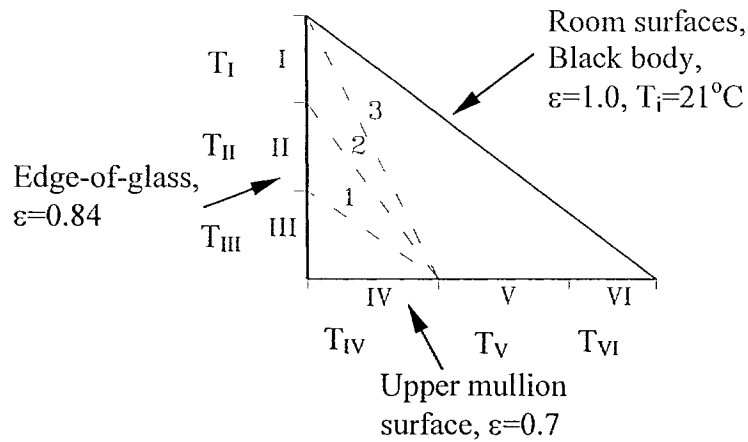
Figure 8.11 Radiation heat exchange model for edge-of-glass region

The temperature for each segment is represented by a constant value at the middle point of the segment. For example, segment IV has a uniform temperature of T_{IV}, which is the

240

average of the measured temperatures T_4 and T_5 (Figure 8.8). According to equation 8.7, the view factor F_{IV-III} is:

$$F_{IV-III} = \frac{L_{IV} + L_{III} - L_1}{2L_{IV}} \qquad (8.8)$$

where, L_i is the length of segment i and $i=I\sim VI$, 1, 2, ...as shown in Figure 8.11.

The view factor F_{IV-II}, F_{IV-I}, ... can be calculated following the same procedure. The view factor between IV and the room is:

$$F_{IV-room} = 1-(F_{IV-III} + F_{IV-II} + F_{IV-I}) \qquad (8.9)$$

The reciprocity relation and unity relation can be used to calculate view factors among these seven surfaces.

With known view factors and surface temperatures, the local radiation film coefficient can be obtained using equation 6.8 described in Chapter 6. The estimated results are listed in Table 8.9.

For the vertical surface VII and VIII (Figure 8.9), the simple calculation, which assumes a surface facing a black body, is used to calculate the radiation coefficient. The results are also listed in Table 8.9. The description for each boundary condition scenario and its corresponding surface film coefficient are also given in Table 8.9.

8.5.3 Results and discussion

The results for each boundary condition scenario are shown in Table 8.10 for system A and in Table 8.11 for system B. The temperature differences between measurement and

simulation are listed in the tables. For system A, when simulated using CSA standard condition with constant film coefficients, most of the temperature differences are in the range of 3°C. When the convection in glazing cavity is considered, the temperature difference between simulation and test is decreased to within 0.5°C (Scenario 2 & 3) for edge-of-glass area. However, the temperature difference at frame and edge-of-spandrel is still high at 3°C. When the actual average film coefficients determined for the environmental chamber presented in Chapter 6 is applied, there is not much improvement on the temperature prediction. In scenario 4, the film coefficient for edge-of-glass is maintained as the average value for center-of-glass, the local film coefficients obtained from estimation for mullion surface and edge-of-spandrel are applied. These more realistic boundary conditions result in much better agreement between test results and simulations. Most of the temperature differences are within 0.5°C. Although the local film coefficient for edge-of-glass has been determined for 3 individual segments and listed in Table 8.9, the previous simulations (Scenario 3) show that with the glazing convection mode, the application of an average film coefficient at edge-of-glass gives results close enough to the measurements (within 0.2°C). With the application of local film coefficients at frame (Scenario 4), the predicted edge-of-glass is slightly lower than the measurements (-0.6°C). If the localized film coefficient for edge-of-glass is used, which is lower than that for the center-of-glass, the predicted temperature of the glazing surface will become even lower. Therefore, it is not necessary to localize the film coefficient for the edge-of-glass for simplicity and accuracy purposes. In scenario 4, it is noticed that most of the temperatures obtained from simulations are lower than the measurements. Therefore, the convection film coefficient estimated for segment VI is

applied for the whole horizontal upper mullion surface. The results show that this adjustment brings the simulation values closer to the measured values.

For system B, using the glazing convection mode has a similar effect as that on system A, i.e. a better agreement between the simulation and measurement results are obtained for edge-of-glass area. However, the temperature discrepancies for mullion surface and edge-of-spandrel are very high, typically 4.5°C. When the localized film coefficients for mullion surface and edge-of-spandrel are applied (Scenario 4), the temperature discrepancies are brought down to within 2°C higher. In scenario 5, the convection film coefficient determined for segment 2 is applied for the entire edge-of-glass section, and the radiation film coefficient for center-of-glass is used. The results show that this adjustment predicts much lower values than the measurements for the edge-of-glass, but does not reduce the discrepancies for frame and edge-of-spandrel. The different effect of local film coefficients on frame system A and B is probably because that in system A, the frame surface temperature is more sensitive to the local film coefficients due to its weaker thermal breaks. When the more realistic film coefficient is applied, the simulation results are significantly improved. While for system B, with the significant increase in thermal resistance of the mullion itself, the interior film coefficient becomes less critical, however its performance is more sensitive to wind washing effect, and convection in the large frame cavities. These effects are not considered in current FRAME simulations.

8.6 Conclusion

The FRAME simulations carried out by an integrated method have identified the relative importance of the design details on the U-factor of curtain walls. It has been found that the frame configuration (e.g. the depth and materials of the thermal breaks in the frame section) has a significant impact on the U-factor. For example, the use of the reinforced nylon mullion nose as a larger thermal break can reduce the U-factor by as much as 60% for the frame and by 22% for the overall U-factor of a metal curtain wall panel sized 1.22m by 3.66m. The improved frame system offers almost the same performance improvement on the overall thermal transmittance as provided by replacing a standard IGU with a high-performance IGU. The effect of shifting the back-pan connection depends on the performance of the frame. For the standard curtain wall system, no improvement is made on the total U-value of the joint section from the revision of back-pan, but when the frame performance is improved, the total U-value at the joint section can be reduced by 6%. For the standard curtain wall system, the impact of the stainless steel screws is significant as well, and can increase the U-factor of the frame by 16% when the standard spacing of 152mm is applied.

It was also found that the CSA method predicted about 25% lower U-value for the frame section than the integrated method due to the simplified assumption of adiabatic condition for the frame/wall junction, however, the overall U-factor calculated by the CSA method was about 6% lower than that calculated by the integrated method. This result suggests that reasonably accurate results can be obtained by CSA method due to the small percentage of the frame (8.5% in the calculations presented in section 8.4). The

conventional method, which does not consider the effect of edge of spandrel and frame, underestimated the overall U-factor by about 23% for system A, and 17% for system B.

In the second part of this chapter, the effect of more realistic boundary conditions on the temperature prediction by FRAME for curtain wall sill section was studied. It was found that the application of more realistic boundary conditions provided simulation results closer to the measurements. For the edge-of-glass area, the consideration of the convection in the glazing cavity gives sufficiently accurate results, and it is not necessary to apply localized film coefficient at this region for the simplicity purpose. The mullion surface temperature on system A is very sensitive to the local film coefficient due to its weaker thermal breaks. The application of local film coefficients brings the simulated temperatures to be within $0.5^{\circ}C$ of the measurements on the mullion surface. While in system B, the difference between simulation and measurement is still as high as $2^{\circ}C$. The reason is probably because the better-insulated frame system B is less sensitive to local film coefficients but more sensitive to wind washing and air leakage effect, which was not taken into account in current FRAME simulations.

Table 8.9 Surface film coefficients in W/m²·K for various boundary condition scenarios

#	Test Conditions	Variant	Indoor h_i — Convection								Indoor h_i — Radiation								Outdoor h_o
			I	II	III	IV	V	VI	VII	VIII	I	II	III	IV	V	VI	VII	VIII	
1	Standard CSA conditions		8.30																30.0
2	Standard CSA conditions, convection in glazing cavity		8.30																30.0
3	Test conditions with convection in glazing cavity	System A	2.46								4.46								20.0
		System B	2.48								4.58								
4	Convection in glazing cavity, varying local film coefficient for frame and edge-of-spandrel	System A	2.46			1.12	1.58	1.75	2.01	1.73	4.46			2.30	2.98	3.28	3.74	3.32	20.0
		System B	2.48			1.12	1.58	1.75	1.74	1.57	4.58			1.90	2.88	3.28	3.87	3.37	
5	Convection in glazing cavity, varying local film coefficient for edge-of-glass, frame, and edge-of-spandrel	A, planed	1.16	0.52	0.17	1.12	1.58	1.75	1.95	1.68	3.68	3.40	3.08	2.30	2.98	3.28	3.74	3.32	20.0
		A, used	2.46				1.75				4.46								
		B, planed	1.51	1.03	0.94	1.12	1.58	1.75	1.69	1.53	3.90	3.70	3.48	1.90	2.88	3.28	3.87	3.37	
		B, used	1.03								4.58								

Note: The boundary condition segments I to VIII are shown in Figure 8.9.

Table 8.10 Comparisons of local temperatures in °C between measurements and simulations for system A

		1	2	3	4	5	6	7	8	9	10	11	12	13	14	15	16	17	18	19	20	21
Measured values		3.8	2.8	1.0	3.8	4.7	5.2	5.5	4.8	4.2	5.0	3.1	6.4	8.5	12.4	-8.7	3.1	2.7	-13.2	-11.8	-13.4	-13.8
Simula tions	1	+2.7	+3.2	+2.8	+2.7	+2.7	+2.9	+2.9	+3.0	+2.9	+2.6	+2.8	+2.7	+3.6	+2.8	-2.7	-1.5	+2.5	+1.3	-0.8	-0.8	-0.4
	2	+0.1	+0.2	-0.5	+2.6	+2.5	+2.7	+2.7	+2.8	+2.7	+2.4	+2.6	+2.6	+3.5	+2.7	-2.7	-1.7	+2.3	+1.1	-1.4	-1.0	-0.6
	3	0	+0.2	0	+2.7	+2.7	+2.8	+2.7	+2.9	+2.9	+2.4	+2.9	+2.5	+3.6	+2.4	-1.8	-1.0	+2.7	+3.3	+0.4	+0.3	+0.6
	4	0	+0.2	-0.6	-0.3	-0.5	-0.4	-0.4	-0.1	-0.1	-0.6	0	-0.4	+0.8	-0.4	-2.9	+3.4	-0.2	+2.3	+0.1	+0.2	+0.5
	5	0	+0.1	-0.5	0	-0.2	-0.1	-0.1	+0.1	+0.2	-0.4	+0.3	0	+1.1	-0.3	-2.6	+3.2	+0.1	+2.4	+0.1	+0.2	+0.5

Table 8.11 Comparisons of local temperatures in °C between measurements and simulations for system B[*]

		1	2	3	4	5	6	7	8	9	10	11	12	13	14	15	16	17	18	19	20	21
Measured values		9.2	7.5	4.8	11.4	11.9	12.2	12.5	12.7	11.3	12.0	11.2			15.3	-11.1			-15.5	-15.0	-16.5	-16.6
Simula -tions	1	+2.0	+3.7	+6.4	+4.6	+4.4	+4.2	+4.2	+3.8	+4.8	+4.3	+4.6			+1.8	-0.3			-0.5	-0.6	+1.0	+1.0
	2	-0.7	+0.1	0.0	+4.4	+4.2	+4.2	+4.0	+3.6	+4.6	+4.2	+4.4			+1.6	-0.3			-0.7	-0.5	-0.1	0
	3	0	+0.8	+0.8	+4.7	+4.5	+4.5	+4.3	+3.9	+4.9	+4.3	+4.7			+1.9	+0.2			+0.2	+0.5	+0.6	+0.6
	4	-0.5	+0.1	-0.1	+1.9	+1.7	+1.7	+1.5	+1.1	+2.0	+1.6	+1.9			-0.9	-0.6			-0.1	-0.4	-0.6	-0.6
	5	-3.4	-2.4	-2.1	+1.7	+2.5	+1.5	+1.4	+1.0	+1.9	+1.4	+1.8			-1.0	-0.6			-0.1	+0.2	+0.5	+0.6

1. Numbers 1 to 21 are referred to the locations of temperatures measured across sill section in both systems, shown in Figure 8.8. Due to the difference configuration in frame, temperature measurement location 12,13,16 and 17 do not exist in system B.
2. Number 1 to 5 in the first column refers to the five boundary condition scenario described in Table 8.9;
3. The values shown under "simulation" row are the difference between simulation results and measurements.

Chapter 9

Effect of thermal performance on thermal comfort and energy consumption

9.1 Introduction

The performance of the building envelope has a significant influence on energy efficiency in buildings. Metal curtain walls are characterized by a large portion of glazing to provide occupants with visual contact with the outdoors, and to provide natural daylights. It may, however, lead to higher energy consumption because of its high thermal conductance and cause thermal discomfort problem for the occupants at the perimeter zone. The concern on energy consumption, on the environment, and on the indoor thermal comfort has promoted the use of high performance glazing units. However, as concluded in chapter 8, the benefits of high-performance glazing units can be fully realized only when the performance of frame and spandrel panel is improved. This chapter evaluates the effect of different curtain wall systems on the indoor thermal comfort and on the energy consumption for a prototype office building.

9.2 Effect of thermal performance on occupant thermal comfort

The main parameters affecting occupant's thermal sensation include air temperature, mean radiant temperature, air velocity, relative humidity, occupant's clothing level and

activity level. It has been recognized that a large hot or cold surface, such as that of a window, can dramatically affect occupant's thermal comfort. The window surface can easily get either very hot in summer due to solar radiation or very cold in winter. The occupant seated close to a window may experience significant thermal discomfort due to the radiant heat exchange with the window or the cold draft induced by the cold glazing surface. In curtain wall buildings, large and continuous glazing areas may aggravate the discomfort problem for occupants at the perimeter zones. The impact of different curtain wall performance on occupant's thermal comfort was evaluated by using the PMV-PPD model. The thermal discomfort is considered only for the winter season in this study.

9.2.1 Evaluation procedure

ASHRAE Thermal Comfort Tool (ASHRE, 1995) was used for the evaluation. PMV standards for predicted mean vote, which is used to quality the mean response by a large group of people to a certain indoor environment. PMV is a function of four environmental parameters and two personal parameters. The four environmental parameters include ambient air temperature, relative humidity, air velocity, and mean radiant temperature. The two personal parameters include the level of metabolic activity, and the clothing insulation level.

PPD is the percentage of people dissatisfied at each PMV value. The correlation between these two indexes developed by Fanger (1982) are expressed as:

$$PPD = 100 - 95\exp(-(0.03353PMV^4 + 0.2179PMV^2)) \qquad (9.1)$$

It is impossible to specify a thermal environment that will satisfy everyone because of individual differences, but a thermal environment should be acceptable to at least 80% of the occupants, which means PPD should be less than 20% (ASHRAE 55, 1992).

The non-uniformity of the thermal environment, such as vertical temperature differences, radiant temperature asymmetry, warm or cold floors, and draft, may cause local discomfort. In the case of large cold glazing surface, the radiant temperature asymmetry and the cold draft induced by the cold surface are the significant factors for local discomfort. ASHRAE standard 55, requires the radiant asymmetry to be evaluated at 0.6m above floor for seated occupants, and at 1.1 m above floor for standing occupants. To limit the local discomfort, radiant temperature asymmetry in the vertical direction shall be less than $5^{\circ}C$ and in the horizontal direction less than $10^{\circ}C$. The cold draft should be evaluated at the head and foot levels (0.1m from the floor). The procedure to estimate the local discomfort from draft has been described in Chapter 7, and the results from the measurements has been shown in Table 7.2.

In this section, the thermal comfort as a result of using metal curtain walls in a hypothetical room was studied. The curtain wall systems evaluated are the two systems tested in the Environmental Chamber. A room with dimensions of 6m deep, 4m wide, and 3.0m high is modeled. The front-side wall shown in Figure 9.1 (4m wide by 3.0 m) is an exterior curtain wall and has a 1.8m high continuous glazing area. The other three walls are interior walls and both of the floor and the ceiling are not exposed to outdoor air. The PMV-PPD calculations assume that the occupant is dressed in average winter

clothing of 1.0 Clo, and has a metabolic rate of 1.0 met with light sedentary activity. The room air temperature in the occupied zone is maintained at 21°C and the relative humidity is 30%. The PPD is examined under the CSA winter condition (-18°C outside and 21°C inside).
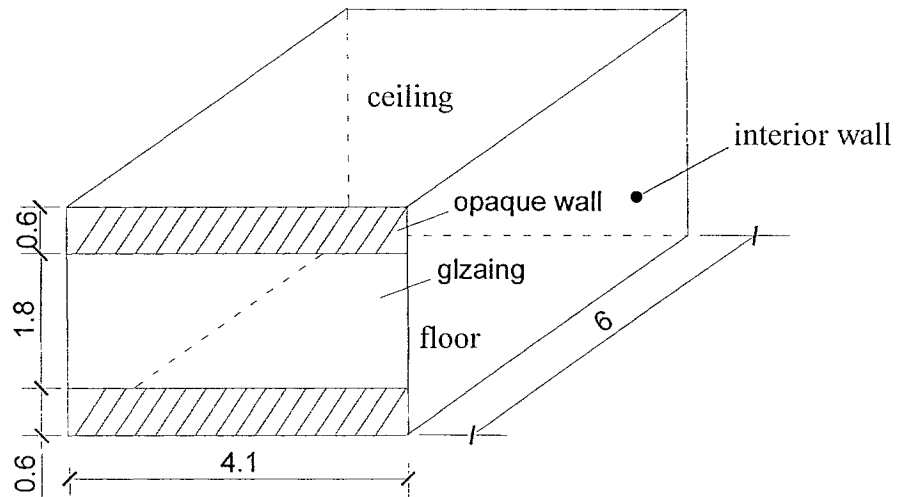
Figure 9.1 Geometry of the enclosure modeled for thermal discomfort evaluation
(dimension in m)

For PMV-PPD calculations, the mean radiant temperature (MRT) is an important parameter. The MRT is defined as the uniform surface temperature of an imaginary black enclosure in which an occupant would exchange the same amount of radiant heat as in the actual space with non-uniform surface temperatures (ASHRAE, 1997). The MRT is calculated as:

$$MRT^4 = F_{p-1}T_1^4 + F_{p-2}T_2^4 + \cdots + F_{p-N}T_N^4 \tag{9.2}$$

where, F_{p-N} is the angle factor from the occupant to surface N, and T_N is the temperature of surface N in K.

The mean radiant temperature for persons seated in the room (shown in Figure 9.1) at different distance from the wall surface is calculated using equation 9.2. For the exterior curtain wall, the glazing surface temperature used to calculate the MRT is an area weighted average value of the measured temperatures of frame, edge-of-glass and center-of-glass. The opaque wall surface temperature used for MRT calculation is the average value of the measured temperatures for spandrel panels. The used glazing and opaque wall surface temperatures are shown in Table 9.1. All other room surfaces are assumed to be at the room air temperature of 21°C.

Table 9.1 Average surface temperatures of curtain walls used for MRT calculation under CSA winter condition

Temperature (°C)	Test conditions	
	T_o= -18°C, T_i=21°C	
	System A	System B
Glazing surface	7.3	12.9
Spandrel surface	17	17.5

The radiant asymmetry is the difference in plane radiant temperatures between the window-facing and non-window facing directions and can be calculated using the following equation (ASHRAE, handbook 1997):

$$\Delta t_{pr} = t_{pr1} - t_{pr2} \qquad (9.3)$$

The plane radiant temperature t_{pr} is the uniform temperature of an enclosure in which the incident radiant flux on one side of a small plane element is the same as that in the actual environment. The plane radiant temperature describes the thermal radiation in one direction and its value thus depends on the direction. In comparison, the mean radiant temperature describes the thermal radiation for the human body from all directions. The plane radiant temperature can be calculated using the same equations (equation 9.1) but

the area factors are determined differently following the equations listed in chapter 8 of ASHRAE handbook of Fundamentals (1997).

9.2.2 Results

The PPD for a seated person, who is centered 0.6m from floor and located at the midway point of the glazing jambs, are calculated at different distances from the glazing surface under CSA winter condition. The measured mean air velocity, air temperature, and the calculated MRT at 0.6 m from floor are used to determine the PPD. The calculated results are listed in Table 9.2 for system A and Table 9.3 for system B.

The draft sensation evaluated at the ankle level in Chapter 7 is also given in Table 9.2 and Table 9.3. As concluded in chapter 7, the ASHRAE requirements, that PD should be less than 15% in the occupied zone, cannot be met by both systems at ankle level until 2m away from the wall surface under the test conditions presented in this thesis. Although the presence of the mechanical system significantly reduced the difference of cold draft effect between the two wall systems, the results do indicate that system B performs better than system A in term of risk of local draft.

ASHRAE requirements regarding horizontal radiant asymmetry can be met by system A at every point in the occupied zone at seated level but not at standing level. The radiant temperature asymmetry is as high as 11°C at a distance of 0.6m from the wall surface at standing level. The higher radiant temperature asymmetry at standing level is because the occupant is more exposed to the cold glazing surface than at seated level due to the

fact that the edge of the glazing is 0.6m above the floor (Figure 9.1). The ASHRAE

requirements can be met by system B at both seated and standing levels, as shown in

Table 9.3.

Table 9.2 Calculated radiant asymmetry, local draft sensation PD, and PPD at different distances from glazing surface in system A

	Distance from glazing surface (m)			
	0.3	0.6	1.2	2.0
Glazing surface temperature (^{0}C)	7.3			
V (m/s)	0.23	0.19	0.15	0.10
T_a (^{0}C)	20.7	21	21.1	21.2
MRT (^{0}C)	17.5	18.1	19.0	19.8
PPD (%)	49	40	30	21
Draft sensation PD (%)	20.5	24.7	22.7	15.8
Radiant temperature asymmetry at h=0.6m (^{0}C)	8.5	7.8	6.1	4.2
Radiant temperature asymmetry at h=1.1m (^{0}C)	12.7	11	7.8	4.9

Table 9.3 Calculated radiant asymmetry, local draft sensation PD, and PPD at different distances from glazing surface in system B

	Distance from glazing surface (m)			
	0.3	0.6	1.2	2.0
Glazing surface temperature (^{0}C)	12.9			
V (m/s)	0.21	0.127	0.118	0.085
T_a (^{0}C)	20.9	21	21.1	21.1
MRT (^{0}C)	18.7	19.1	19.7	20.1
PPD (%)	33	26	22	18
Draft sensation PD (%)	19.0	23.3	25.9	12.8
Radiant temperature asymmetry at h=0.6m (^{0}C)	5.5	5	3.9	2.7
Radiant temperature asymmetry at h=1.1m (^{0}C)	7.6	6.6	4.8	3.1

As shown in Figure 9.2, PPD significantly decreases as the occupants move away from

the wall surface. However, the requirements by ASHRAE standard 55 that PPD shall be

less than 20% cannot be met by either wall system until 2m away from the wall surface

under the test conditions presented in this thesis with the heating system located 6m away

from the walls. This suggests that both curtain wall systems require perimeter-heating elements to counteract the cold draft and to raise the surface temperature in order to provide an acceptable thermal environment. However, the results do clearly indicate that the better thermal performance of system B provides better thermal comfort index. As indicated in Table 9.2 and 9.3, the high performance wall can improve the thermal sensation by 14% at the beginning of the occupied zone (0.6m from wall surface), which implies that less peripheral heating would be required for system B to provide acceptable thermal environmental in the perimeter zone.
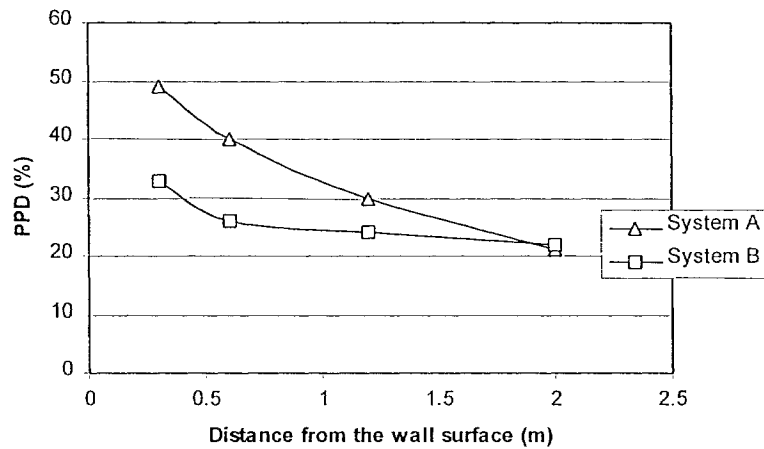
Figure 9.2. Calculated PPD for a seated occupant at different distances from curtain wall surface

9.3 Effect of thermal performance on energy consumption

The effect of different metal curtain wall systems on the energy consumption of a prototype office building was evaluated using a simplified simulation model developed by Cornik and Sander (1995). The purpose of this energy simulation is to investigate the effect of thermal characteristics of the building envelope on the energy consumption and to provide information on system selection in the preliminary design stage rather than an

accurate evaluation of energy consumption of an in-service building. Thus, the correlation-based simulation model is sufficient enough to provide a quick and simple way to represent the effect of different metal curtain wall designs.

The two frame systems and two types of glazing units tested in the environmental chamber were chosen and, by combining the different design details, four curtain wall designs were evaluated. The climate effect has also been studied by conducting the simulations for four different cities (Montreal, Toronto, Edmonton, and Vancouver) located in four different climate zones. As shown in section 8.4 of chapter 8, the conventional method, which does not consider the effect of edge of spandrel and frame, estimated a lower overall U-value for system A by about 23% and for system B by 17% compared to the integrated method. The effect of the underestimation in overall U-factor by the conventional method on the energy consumption evaluation was studied for Montreal weather condition.

9.3.1 Simplified energy consumption correlation model

The simplified correlation model developed by Cornik and Sander (1995) is composed of a set of regression equations derived from a database of 5400 DOE2.1 simulations for 25 Canadian locations. Approximate energy consumption of a building can be simulated using these correlations with minimum inputs of building parameters. The model served as the basis for the prescriptive and trade off procedure in the Modeling National Building Energy Code (MNBEC, 1997). This model predicts annual energy use within 10% of the DOE-2.1E simulations. The results from 25 locations modeled by DOE-2.1E

256

were used to generate climate correlations to predict heating and cooling requirements for locations not in the database.

9.3.1.1 Assumptions

This model simulates only the four exterior zones facing the cardinal orientations instead of a whole building. The following assumptions are made:

- No inter-zone heat transfer;

- Fixed infiltration rate of 0.25 L/s per square meter of building envelope;

- Heating setback at 15°C and cooling off when unoccupied;

- Variable-air-volume (VAV) system with terminal re-heat;

- Internal loads on a 6 day office type schedule;

- 13°C supply air for cooling;

- Free cooling (enthalpy-controlled air-side economizer); and

- Minimum ventilation as prescribed by ANSI/ASHRAE 62-1989 requirements at 9.4 L/s·person.

The building envelope is characterized by three parameters: thermal transmittance, U, solar gain parameter, V, and an internal gain parameter, W. These parameters are defined as:

$$U = (A_w * U_w + A_{wall} * U_{wall})/A_t \quad \text{W/m}^2\text{·K} \tag{9.4}$$

$$V = A_w * SC_g / A_t \quad \text{dimensionless} \tag{9.5}$$

$$W = I * A_{floor} / A_t \quad \text{W/m}^2 \tag{9.6}$$

where

A_{wall} = opaque wall area, m^2;

A_w = window wall area including frame, m^2;

A_t = gross wall area, $A_{wall} + A_g$, m^2;

A_{floor} = floor area associated with envelope, typically 4.5m deep, m^2;

U_{wall} = opaque wall U-factor, $W/m^2 \cdot K$;

U_w = window U-factor, including frame, $W/m^2 \cdot K$;

SC_g = window shading coefficient, dimensionless;

I = design heat gain from lights, people, and equipment, W/m^2 floor area.

9.3.1.2 Heating energy estimation

The heating load predicted by this model can be expressed as:

$$H = L \cdot SGRF \cdot IGRF \cdot GIF \quad (MJ/m^2 \cdot yr) \qquad (9.7)$$

The symbol L denotes the annual heat loss. It is a linear function of U with the slope and intercept dependent on climate. It can be expressed as:

$$L = b_0 + b_1 U \qquad (MJ/m^2 \cdot yr) \qquad (9.8)$$

where, b_0 is a constant, representing HVAC system, infiltration and ventilation losses $(W/m^2 \cdot K)$ and b_1 is the intercept of the linear relationship between U-value and the heat loss, L. These two coefficients vary slightly with building orientations and depend on the climate.

SGRF stands for solar gain reduction factor and is a function of V. It can be expressed as:

$$SGRF = L_v / L = 1/(1 + \alpha_1 * X + \alpha_2 * X^2 + \alpha_3 * X^3) \qquad (9.9)$$

258

where, L_V is the annual heat loss minus solar heat gain, MJ/m^2·yr;

X=V/L;

α_1, α_2, α_3 are coefficients, which are dependent on orientation and location.

IGRF stands for internal gain reduction factor and is a function of W. It can be expressed as:

$$IGRF = L_w / L = \exp(\beta_1 * Y + \beta_2 * Y^2 + \beta_3 * Y^3) \qquad (9.10)$$

where, L_w is the annual heat loss minus the internal gains, MJ/m^2·yr;

Y=W/L; and

β_1, β_2, β_3 are coefficients, which are orientation independent and location dependent.

GIF stands for solar gain and internal gain interaction factor. It is independent to the building orientation, and is not strongly dependent on location. It can be expressed as:

$$GIF = \exp(\delta_0 + \delta_1 * \gamma + \delta_2 * \gamma^2 + \delta_3 * \gamma^3) \qquad (9.11)$$

where, $\gamma=1$, if SGRF & IGRF=1, otherwise

$$\gamma = (1 - SGRF * IGRF)/((1 - SGRF) + (1 - IGRF)) \qquad (9.12)$$

$$\delta_0 + \delta_1 + \delta_2 + \delta_3 = 0$$

9.3.1.3 Cooling energy estimation

The yearly cooling load predicted by this model can be expressed as:

$$C = C_0 + \Delta C_0 \quad (MJ/ \ m^2 \cdot yr) \qquad (9.13)$$

C_0 is the base cooling load. It is a linear function of V and W, and is dependent on climate and orientations. It can be expressed as:

$$C_0 = \max(C_{min}, a_0 + a_1 * V + a_2 * W)$$
(9.14)

where, C_{min} is the minimum cooling load for a particular climatic location and a_0, a_1 and a_2 are the climate and orientation dependent coefficients.

ΔC_0 is the adjusting term to account for the effect of U on the cooling load. In a cold climate, such as Canada, when U is increased, more heat is lost through the envelope: the heating load is increased and the cooling load is decreased. But the envelope transmission losses for cooling tends to be relatively small when compared to the base cooling load.

$$\Delta C_0 = a_3 * U * (1 - C_{min} / C_0)$$
(9.15)

where a_3 is a climate and orientation dependent coefficient as well.

9.3.1.4   Climate correlations

The coefficients in the heating and cooling load equations were derived from the DOE2.1-E simulations for the 25 Canadian cities in the database. Climate correlations were developed based on the basic climatic data such as heating-degree days, cooling-degree days and the amount of solar radiation in order to apply this model to other Canadian locations. The details regarding the development of climate correlations can be found in Cornik and Sander (1994).

9.3.2 Simulation procedure by the simplified model

The prototype building simulated is a 20-storeys high office building with dimension of 30m by 30 m. The floor-to-floor height is 3.66m. The glazing wall ratio is 50%. Only the perimeter zones facing four cardinal orientations were considered and the depth of the perimeter zone is 4.5m. The input for this model includes the thermal characteristics of building envelope, U, V, internal gain W, and a series of climate-dependent correlation coefficients. Four cities located in four different climate zones were chosen for the simulations. They are Montreal, Toronto, Edmonton, and Vancouver. The climate-dependent correlation coefficients for 25 Canadian cities were taken from Cornik and Sander (1994).

The integrated method described in section 8.2 was used to determine the overall U-factor for four different curtain wall systems. The dimension of each curtain wall section is 1.22m wide and 1.83m high in accordance with the recommendation of standard CSA A440.2 (CSA, 1998). The solar heat gain coefficient (SHGC) for the vision panel includes two parts: $SHGC_g$ for glass and $SHGC_f$ for frame. The solar heat gain coefficient for the glass, $SHGC_g$, was obtained from the VISION program, and the $SHGC_f$ for the frame was calculated using equation 9.16 (CSA, 1998).

$$SHGC_f = 0.0051U_f \qquad (9.16)$$

where, U_f is frame U-value in W/m$^2 \cdot$ K.

The internal gain parameter W was determined in accordance with ASHRAE 90.1 (ASHRAE,1992). The determined parameters U, V, and W are listed in Table 9.4 for each design. The determined parameters U, V, and W using three different methods for

curtain wall design 1 which has frame system A and standard IGU, are also listed in

Table 9.4.

Table 9.4 Input parameters for energy consumption simulations

			Integrated method		CSA method		Conventional method		W
			U	V	U	V	U	V	
A	1	Standard IGU	2.31	0.45	2.18	0.44	1.79	0.44	
	2	High performance IGU	1.74	0.31					30.2
B	3	Standard IGU	1.80	0.44					
	4	High performance IGU	1.21	0.29					

9.3.3 Results and Discussion

The estimated energy consumption by the different curtain wall designs under Montreal

weather condition are listed in Table 9.5 and shown in Figure 9.3.

Table 9.5 Energy consumption estimated under Montreal weather condition (MJ/m²·yr)

Configuration	Heating Load	Cooling Load	Total	Saving (%)[*]
1:basecase	3349.6	1617.1	4966.7	0
2	2960.0	1297.9	4257.9	14.3
3	2664.0	1195.9	3859.9	22.3
4	2257.1	1313.4	3570.5	28.1

*The comparisons are against to the base case: configuration 1

Table 9.6 Energy consumption comparison between three calculation methods under Montreal weather condition for curtain wall design configuration 1

Method	Heating Load	Cooling Load	Total	Difference (%)[*]
Integrated method	3349.6	1617.1	4966.7	base case
CSA method	3165.2	1636.3	4801.5	-3.3
Conventional method	2624.2	1693.7	4317.9	-13.1

*The comparisons are over the integrated method and units for the values are MJ/m²·yr.

Table 9.5 shows that by replacing the standard glazing units with high-performance glazing units in frame system A, the energy consumption can be reduced by 14.3%. By replacing the frame system A with frame system B, the energy consumption can be reduced by 22%, which is even higher than using high performance glazing units. This reduction in energy consumption indicates again the importance of improving the performance of the frame. When the high performance frame is combined with the high performance glazing unit, the energy consumption can be reduced by 28%.

Figure 9.3 Annual energy consumption for a prototype office building with four different curtain wall designs under Montreal weather condition

The three methods to calculate the overall U for metal curtain walls were compared in section 8.4 of chapter 8. It was found that the overall U-factor calculated by the CSA method for the purpose of energy calculation is within 5% of the results calculated by the integrated method. However, the conventional method gave about 23% lower U-factor.

263

Table 9.6 collates the energy consumption values obtained from using these three different methods for the curtain wall design configuration 1 (Table 9.4, frame A with standard glazing) under Montreal weather condition. Comparisons shown in the last column of Table 9.6 are made with respect to the integrated method. It shows that the CSA method underestimates the energy consumption by 3.3%, and the conventional method underestimates energy consumption by 13.1%. The comparison indicates the importance to take into account the effect of the edge-of-spandrel and frame for the spandrel panel evaluation.

The estimated energy consumptions of the prototype office building for Toronto, Edmonton, and Vancouver climates are shown in Figures 9.4 to 9.6 respectively. These figures show similar trends as that in Figure 9.3 under Montreal weather conditions. By using the high performance frame system, the energy consumption can be reduced by about 15% for most of the cities studied. This reduction is similar to that obtained by using high-performance glazing units. Sometimes, the energy saving is even higher, e.g. for very cold regions such as Edmonton and Montreal. In Edmonton, the main energy consumption is from heating. By reducing the overall U-factor, the heating load can be reduced. At the same time, using standard glazing units allow more solar heat gains, which can reduce the heating load as well. In the case of Vancouver, the heating load and cooling load is similar, using high performance frame system can slightly decrease the heating load, but it significantly increases the cooling load as compared to the design with frame system A and high performance glazing units.

264
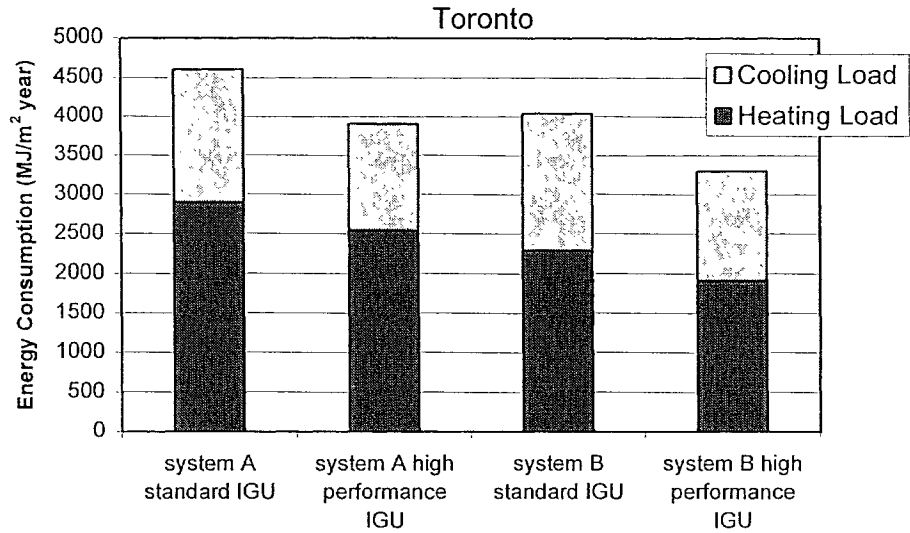
Figure 9.4 Estimated annual energy consumption for a prototype office building with four different curtain wall designs under Toronto weather condition

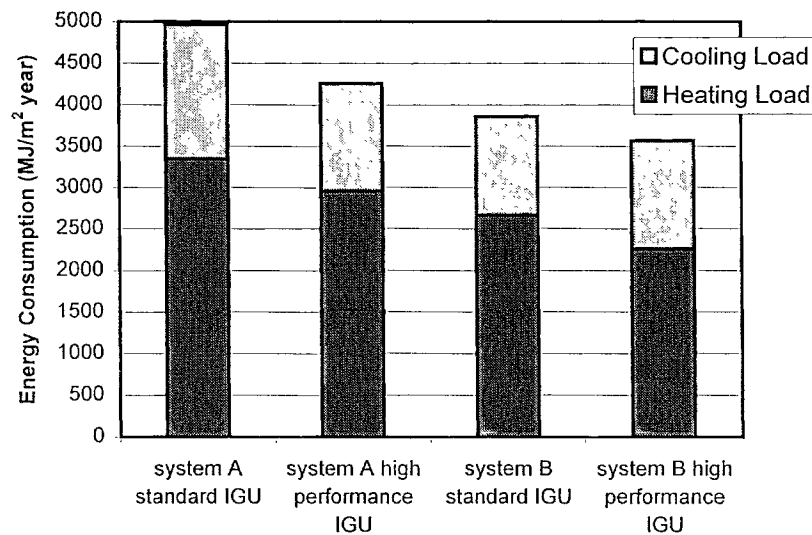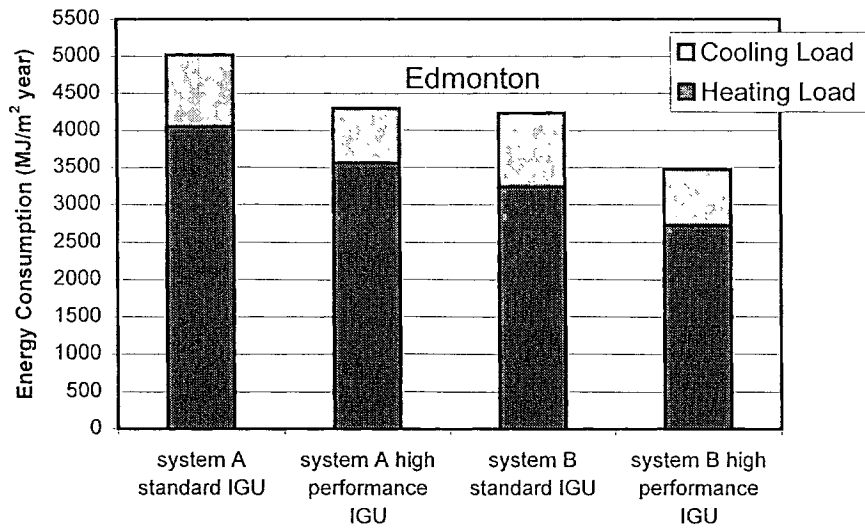Figure 9.5 Estimated annual energy consumption for a prototype office building with four different curtain wall designs under Edmonton weather condition
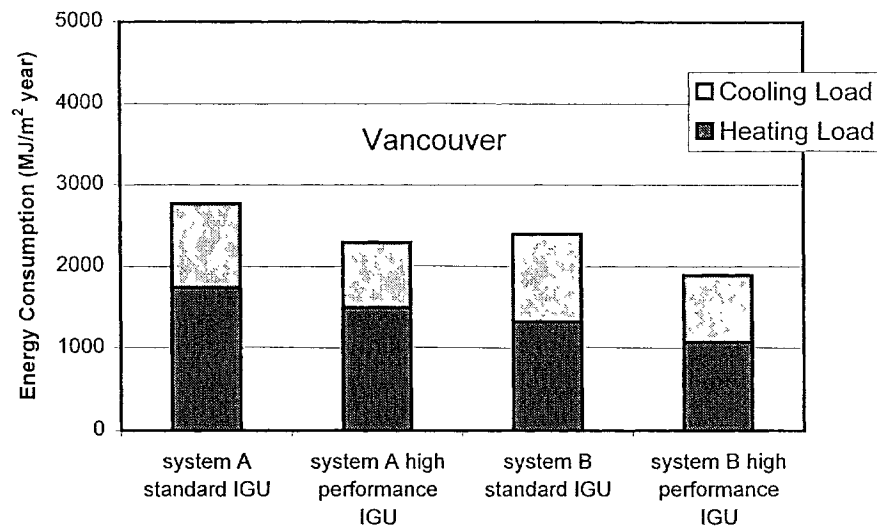
Figure 9.6 Estimated annual energy consumption for a prototype building with four different curtain wall designs under Vancouver weather condition

9.4 Conclusion

The effect of different curtain wall systems on thermal comfort and energy consumption has been studied. The surface temperatures measured on the walls and the air temperature and velocity measured for the cold draft were used for the PMV-PPD thermal sensation analysis. It was found that for the curtain wall systems tested in the current setup and conditions presented in this thesis, a perimeter heating system or any type of HVAC system to warm up the wall surface are necessary in order to meet the requirement of ASHRAE standard 55. Nevertheless, the results clearly indicate that the high performance curtain wall can provide better thermal comfort for occupants at the perimeter zone.

A simplified correlation energy simulation model was used to study the effect of different curtain wall designs on energy consumption for a prototype office building under

266

different climates. The results indicate the importance to improve the performance of the frame to achieve better energy performance. By simply replacing the frame system A with frame system B, the energy consumption can be reduced by 22% for Montreal climate conditions, which is even higher than using high performance glazing units. For most heating-dominated cities studied in Canada, the use of high performance frame system can reduce total energy consumption by about 15%. The current practice without accounting for the frame and edge-of-spandrel underestimates energy consumption by 13% for the prototype office building.

Chapter 10

Conclusion

10.1 Contributions of the research thesis

The work of this thesis was designed to establish the overall performance of curtain walls by testing full-scale specimens under field conditions reproduced in a large-scale environmental chamber. The work was undertaken on the premise that an holistic approach would yield a more realistic representation of the overall performance of curtain walls as compared to that obtained from existing approaches that attempt to determine this performance from characteristics of the various components of the curtain wall. Because of its length and complexity the research work was broken down into a series of steps including: full-scale air leakage tests, thermal performance tests, measurement of local convection film coefficients, measurements of cold draft induced by the glazing surfaces, evaluation of the impact of design details on U-factors, effect of local film coefficients on temperature prediction, the effect of thermal performance on the occupants and on energy consumption, and the development of test and laboratory facilities to carry these measurements with accuracy. The findings and contributions for each of these categories are highlighted below.

1. Full-scale air leakage tests

The air leakage rates for the two curtain wall systems were measured separately and the results are 0.176 L/m²·s for system A and 0.252 L/m²·s for system B under 300 Pa pressure difference. The method established herein enabled the accurate establishment of the air leakage characteristics for large-scale curtain walls. The work suggests that the air-tightness of system B could be improved by improving the design detail of the back-pan.

2. Thermal performance tests

Extensive temperature measurements throughout the test specimen were performed under different steady-state and cyclic conditions including the introduced air infiltration. It has been found that the temperature distribution depends on the configuration of the wall and the local film coefficients. High performance glazing units provide 20% higher condensation resistance than standard double IGU, and frames with larger thermal breaks provide 30% higher condensation resistance than regular frame systems. The temperatures on the better-insulated components are less sensitive to the variation of local film coefficients. The cyclic tests confirmed that better performing frame has smaller temperature variation and longer time lag to outdoor air temperature swings. The air infiltration study suggests that the curtain walls tested have good airtightness and the impact of the introduced air infiltration on the condensation resistance factor is insignificant on glazing unit but considerable on frame.

3. Measurement of local convection film coefficients

It has been found that the profile of these coefficients is a function of the wall components, of the details, and of the contour of the entire wall, which leads to the

conclusion that such local convection film coefficients can only be established through the type of tests described herein in order to obtain more realistic boundary conditions for thermal simulation programs.

4. Measurement of cold draft induced by glazing surfaces

The cold draft induced by the glazing surface is an important factor in determining the overall performance of the curtain wall in respect to comfort of the occupants and the design of the HVAC system. Extensive measurements have been taken and draft profiles have been drawn for both systems A and B. It was found that the velocity of the air washing down the surface of the glazing varies inversely with the temperature of the glazing. The temperature of the interior surface of system B, for example, is higher than that of system A because system B is better insulated. Consequently the draft velocity in system B is less than in system A, which results in a reduced area of discomfort in the vicinity of the curtain wall of system B. It was noted from the data that the difference in air velocity and air temperature of the cold draft induced by two different glazing surfaces was reduced when air supply was provided from a mechanical unit at the end of the hot box. The introduction of this air represents the impact of ventilation systems typically present in commercial buildings and the importance of designing the air distribution from mechanical systems to counteract the cold drafts caused by the cold glazing surfaces. The results indicate that high performance glazing units provide a better thermal comfort index than standard glazing units. It was found that the surface temperature of both wall systems would have to be raised in order to meet the thermal comfort requirement of ASHRAE standard 55.

5. Effect of design details on U-value

The FRAME simulation results indicate that the material and depth of the thermal break in the frame is critical for curtain wall performance. The frame U-value can be decreased by 60% by using a larger thermal break. This reduction results in 22% lower overall U-value for a typical curtain wall, which has almost the same effect as using a high-performance IGU. The revision of back-pan design does not improve the overall U-factor for curtain wall system A due to the high heat loss through frame section. When the frame performance is improved in system B, the U-value for edge-of-spandrel is reduced significantly by 56% and more positive effect (6%) can be yielded from the revision of the back-pan. The stainless steel screws contribute 16% for the frame U-factor in the standard design of system A.

It has also been found that the CSA simulation procedure predicted about 25% lower U-value for the frame than the integrated method due to the simplified assumption of adiabatic condition for the frame/wall junction. The overall U-factor calculated by CSA method is about 6% lower than that calculated by the integrated method due to the small percentage of the frame area (8.5%) in the calculations. However, the conventional method, which does not consider the effect of edge of spandrel and frame, underestimates the overall U-factor by about 23% for system A, and 17% for system B.

This work has identified the significant effect of frame configuration on the overall performance of curtain walls, which enhanced the findings from thermal performance

tests. The relative importance of the design details formulated using the integrated method in the simulations led to suggestions on improving curtain wall design.

6. Effect of local film coefficients on temperature prediction

It was found that the application of more realistic boundary conditions increased the accuracy in predicting temperatures by FRAME simulations. The application of local film coefficients brings the simulated temperatures to be within $0.5^{\circ}C$ of the measurements on the mullion surface for system A. However, in system B the difference between simulation and measurement is still as high as $2^{\circ}C$. The reason is probably because the better-insulated frame system B is less sensitive to local film coefficients but more sensitive to wind washing and air leakage effect, which was not taken into account in current FRAME simulations. For the edge-of-glass area, the consideration of the convection in glazing cavity gives sufficiently accurate results, and it is not necessary to apply localized film coefficient at this region for simplicity purpose.

It should be noticed that the three-dimensional effect of screws was approximated two-dimensionally in FRAME simulations. The temperature measurements showed that the coldest places occur at corners. Therefore, it would be preferable to have a three-dimensional simulation program which can represent more accurately the three-dimensional heat transfer of screws and corners in order to more accurately predict the condensation performance of curtain walls.

7. Effect of thermal performance on the occupants and on energy consumption

It was found that better insulated wall systems provide better thermal comfort index for occupants in the perimeter zone and consume less energy. A simplified energy calculation for a prototype office building indicates the importance of improving frame performance to achieve better energy performance. By simply replacing the frame system A with frame system B, the energy consumption can be reduced by 22%, which is even higher than using high performance glazing units. In order to meet ASHRAE thermal comfort requirements, the surface temperature of both wall systems needs to be raised by means of a perimeter heating or ventilation system.

8. Development of test and laboratory facilities to carry these measurements with accuracy

On the individual tests, innovative adoption and improvements have been made to apply the existing testing methodology and standards to accommodate the specific full-scale testing setup and requirement. A more economical and accurate procedure has been developed to measure the air leakage characteristics for airtight large-scale metal curtain walls. A large-scale 3-dimensional computer-controlled traverse system has been built to investigate heat transfer processes in the boundary layer over the full-size curtain wall sections. The results have confirmed the feasibility and reliability of the setup in performing accurate measurements with high spatial resolution. This setup could be used to provide data for further convection coefficient studies and for CFD studies.

In summary, this thesis work represents the first comprehensive experimental testing program ever conducted on full-scale curtain wall specimens to establish the overall

performance of curtain walls under more realistic conditions. The application of thermal simulation programs supplements and enhances the value of the experiment work. Results from extensive testing and simulations are synthesized to provide a profound insight in the performance of curtain walls. This research also represents the first comprehensive investigation on the impact of the innovative solutions the industry is currently using and developing to improve the metal curtain wall system. The combined experimental and analytical investigation have revealed the intricate links among the components, the overall wall assembly performance and the impact on the energy use and indoor comforts; and, therefore, provided solid technical information for the manufacturers on the productive direction of future R&D and for designers on the selection of curtain wall systems to achieve energy-efficient buildings with healthy and comfort indoor environment. Extensive testing has provided a valuable set of experimental data to validate the current and future computer simulation programs.

10.2 Recommendations for further work

This research work has covered a broad range of areas and fields related to the performance of metal curtain walls. It has opened up a number of potentially fruitful research work that could benefit the metal curtain wall industry in particular and the building envelope and many other building engineering fields in general.

1. The experimental implementation for thermal performance evaluation can be extended to integrate into the test setup that an outdoor and indoor environment is completed with simulated solar radiation and mechanical ventilation systems. A three dimensional cutout of a typical office room can be built on the current test setup. A

possible test arrangement along a concept developed by Dr. Fazio, is shown in Figure 10.1. The energy consumption, thermal comfort, and condensation potential could be studied with different mechanical systems and operation schedules, and different lighting strategies under simulated seasonal and diurnal outdoor conditions. Different innovative building envelope designs could be tested. The optimization between building envelope and ventilation system could be formulated to achieve energy-efficient buildings with healthy and comfortable indoor environment. The experimental data could then be used to validate the energy consumption simulation programs.
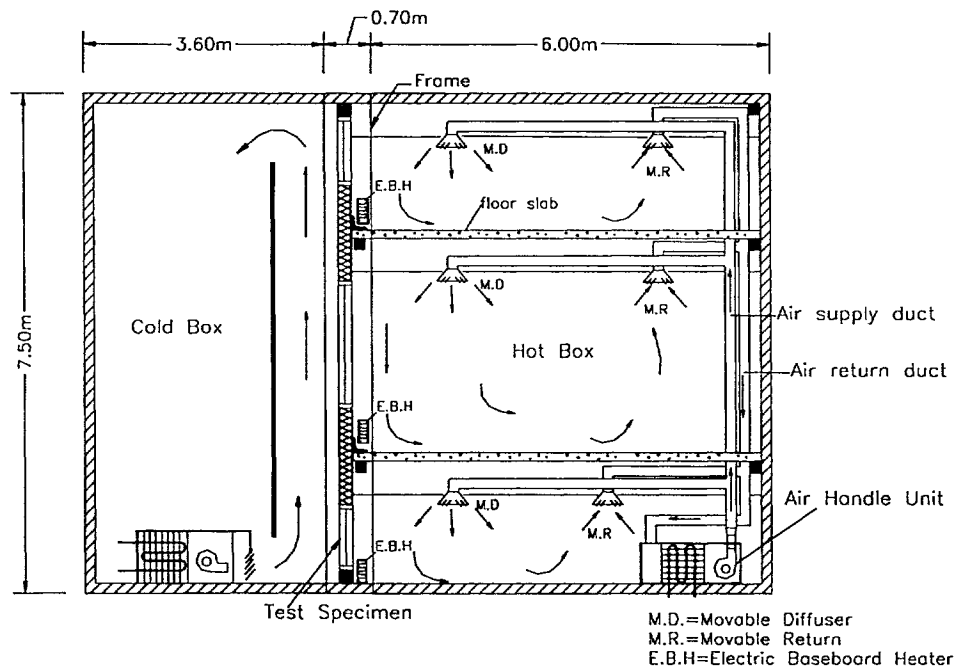
Figure 10.1 A potential experimental setup for future work

2. The indoor air movement studies could be extended to study the effect of frame geometry on the local convection film coefficients, on cold draft in the occupied zone, and on the condensation risk at edge-of-glass using the test setup established in

275

this thesis. The experimental data then could be used to validate computer simulation programs in energy consumption and thermal comfort.

3. The measurements of air velocity and air temperature in the boundary layer of curtain wall could be extended and used to validate CFD models in predicting indoor airflow.

4. The qualitative investigation carried out on the effect of air infiltration on condensation resistance can be extended to establish quantitative correlations between the amount of air leakage and the condensation resistance factor. Through additional testing conducted under varying air leakage conditions, a more general correction factor could be derived to calculate the condensation resistance under different thermal conditions and air infiltration levels. Such a general condensation factor can predict more precisely the condensation occurrence and related effect.

5. Further study could also focus on developing a more realistic 3-dimensional model to take into account the wind washing effect, air leakage effect, and more realistic convection effect in frame tube to predict the condensation risks for fenestration systems. This model could be validated by the extensive data obtained in this thesis and additional data obtained from the potential tests mentioned in item 4.

10.3 Related publications

Fazio, P., J. W. Rao, and H. Ge (2002). Measuring air leakage characteristics with flexible double air chambers. Journal of Architectural Engineering, Vol. 8 No.3, September, pp.89-95.

Ge, H., and P. Fazio (2002). Evaluation of critical factors affecting the thermal performance of metal curtain walls by simulations. Proceedings of eSim 2002, Sept. 11-13, Montreal, pp.112-119.

Ge, H., P. Fazio and J.W. Rao (2001). Experimental study of temperature distribution across two curtain wall systems. Proceedings of Thermal Performance of the Exterior Envelopes of Buildings VIII, ASHRAE, Florida, Dec.2-7.

Ge, H., and P. Fazio (2001). Study on thermal performance of curtain walls using infrared thermography. Proceedings of International Conference on Building Envelope Science and Technology, Ottawa, June, Vol.1, pp. 231-235.

Fazio, P., H. Ge and J.W. Rao (2001). Measuring air leakage of full-scale curtain wall sections using a non-rigid double air-chamber method. Proceedings of International Conference on Building Envelope Science and Technology, Ottawa, June, Vol.2, pp.269-273.

Ge, H., and P. Fazio (2001). Performance comparison of two different curtain wall systems. Proceedings of the Whole Life Performance of Building Façade, Bath, April 18-19, pp.193-201.

Ge, H., and P. Fazio (1999). Experimental study on thermal performance of metal curtain walls. Proceedings of the 3rd International Symposium on HVAC, Nov., Shenzhen, China.

Reference

AAMA. 1979. Aluminum curtain wall design guide manual. American Architectural Manufacturers Association.

AAMA. 1994. Standard test method for metal curtain wall for water penetration using dynamic pressure. Standard 501.1, American Architectural Manufacturers Association.

AAMA. 1998. Voluntary test method for thermal transmittance and condensation resistance of windows, doors and glazed wall sections. Standard 1503, American Architectural Manufacturers Association.

Arasteh, D., 1989. An analysis of edge heat transfer in residential windows. Thermal Performance of Exterior Envelopes of Buildings IV, Atlanta. American Society of Heating, Refrigerating and Air-conditioning Engineers, Inc. pp.376-387.

ASHRAE. 1992. Thermal environmental conditions for human occupancy. ANSI/ASHRAE standard 55-1992. American Society of Heating, Refrigerating and Air-conditioning Engineers, Inc.

ASHRAE. 1993. Handbook of Fundamentals, ASHRAE, Atlanta.

ASHRAE. 1995. Thermal comfort tools. American Society of Heating, Refrigerating and Air-conditioning Engineers, Inc.

ASHRAE. 1996. Standard method for determining and expressing the heat transfer and total optical properties of fenestration products. Standard 142P ASHRAE, Atlanta.

ASHRAE.1997. Handbook of Fundamentals, ASHRAE, Atlanta.

ASTM. 1993. Standard test method for field measurement of air leakage through installed exterior windows and doors. Standard E783, American Society for Testing and Materials, Philadelphia, PA.

ASTM. 1993. Standard test method for steady-state thermal performance of building assemblies by means of a guarded hot box. Standard C236-89, American Society for Testing and Materials, Philadelphia.

ASTM. 1996. Standard test method for thermal performance of building assemblies by means of a calibrated hot box. Standard C976-90, American Society for Testing and Materials, Philadelphia.

278

ASTM. 1999. Standard test method for determining air leakage rate by fan pressurization. Standard E779, American Society for Testing and Materials, Philadelphia, PA.

ASTM. 1999. Standard test method for determining rate of air leakage through exterior windows, curtain walls, and doors under specified pressure difference across the specimen. Standard E283-91, American Society for Testing and Materials, Philadelphia.

ASTM. 2000. Standard test method for measuring the steady-state thermal transmittance of fenestration system using hot box methods. Standard C1199, American Society for Testing and Materials, Philadelphia.

ASTM. 2000. Standard test method for water penetration of exterior windows, skylights, doors and curtain walls by uniform static air pressure difference. Standard E331, American Society for Testing and Materials, Philadelphia.

ASTM. 2000. Standard test method for water penetration of exterior windows, skylights, doors and curtain walls by cyclic static air pressure difference. Standard E547, American Society for Testing and Materials, Philadelphia.

ASTM. 2000. Standard test method for determining rate of air leakage through exterior windows, curtain walls and doors under specific pressure and temperature difference across the specimen. Standard E1424-91, American Society for Testing and Materials, Philadelphia.

Athienitis, A.K., 1998. Building thermal analysis. Concordia University, 3rd edition.

Baskaran, A. and Brown, W.C. 1992. Performance of a pressure equalized rainscreen wall under cyclic loading. Journal of Thermal Insulation and Building Envelope, Vol. 16, pp. 183-193.

Batchelor, G.K. 1954. Heat transfer by free convection across a closed cavity between vertical boundaries at different temperatures. Quarterly of Applied Mathematics, Vol.12, pp.209-233.

Bernier, M.A., 1997. Effects of glass plate curvature on the U-factor of sealed insulated glazing units. ASHRAE Trans., vol.103, part 1, pp. 270-277.

Branchaud, T.R. 1997. Two-dimensional finite element analysis of laminar and turbulent convective heat transfer over the exterior surface of a fenestration system. M.S. thesis, University of Massachusetts, Amherst.

Brooks, A.J. 1998. Cladding of Buildings. E & FN SPON, 3rd edition.

Brooks, A.J., 1992. Performance criteria for curtain wall are confusing and even misleading at times. Journal of Architecture, March, pp.37.

Brown, W.C., Rousseau, M.Z. and Dalgliesh, W.A. 1991. Field testing of pressure equalized rainscreen walls, ASTM STP 1034, Exterior Wall Symposium, Precast Concrete, Masonry and Stucco, Chicago, ILL, pp.59-69.

CANMET. 1993. The determination of fenestration thermal performance using simulated solar irradiance. Part 1, CANMET report DSS No. 06455-23440-0-9469.

Carmody, J., S. Selkowitz and L. Heschong. 1996. Residential windows: a guide to new technologies and energy performance. W.W. Norton & Company, Inc.

Carpenter, S. 1992. Thermal performance of window framing system. Thermal performance of the exterior envelopes of buildings V. Clearwater Beach, FL, pp.345-348.

Carpenter, S., and A. McGowan. 1993. Effect of framing systems on the thermal performance of windows. ASHRAE Transactions, Vol. 99 (1), CH-93-7-1 pp.907-914.

Carpenter, S. and A.H. Elmahdy. 1994. Thermal performance of complex fenestration systems. ASHRAE Transactions, Vol. 100(2), OR-94-20-1, pp.1179-1186.

Churchill, S.W., and H. Ozoe. 1973. A correlation for laminar free convection from a vertical plate. Transactions of the ASME, Journal of Heat Transfer: 540-541.

Cornick S., D. M. Sander. 1994. Development of heating and cooling equations to predict changes in energy use due to changes in building envelope thermal characteristics. IRC Report 656, NRCC, Ottawa.

Cornick, S.M. and Sander, D.M., 1995. A simplified energy model for analysis of building envelope thermal characteristics. Proceedings of Thermal Performance of the Exterior Envelopes of Buildings VI, pp.687-695.

CSA. 1990. Windows. CAN/CSA A440-M90. Canadian Standard Association.

CSA. 1998. Energy performance of windows and other fenestration systems. CAN/CSA A440.2-1998. Canadian Standard Association.

Curcija, D., and W.P. Goss. 1993. Two-dimensional natural convection over the isothermal indoor fenestration surface—finite element numerical solution. ASHRAE Transactions, Vol.99(1), pp.274-287.

Curcija,D., and W.P. Goss. 1995. Two-dimensional forced convection perpendicular to the outdoor fenestration surface—FEM Solution. ASHRAE Transactions, Vol.101 (1), pp. 201-209.

Curcija, D., Yie Zhao, and W.P.Goss. 1998. Effect of realistic boundary conditions in computer modeling of condensation resistance for fenestration systems. Thermal performance of the exterior envelope of buildings VII, pp.405-414.

De Abreq, P.F., R.A. Fraser, H.F. Sullivan, and J. L. Wright. 1996. A study of insulated glazing unit surface temperature profiles using two-dimensional computer simulation. ASHRAE Transactions, Vol. 102(2): pp.497-507.

De Abreu, P.F., 1996. Modeling the thermal performance of windows using a two-dimensional finite volume model. Ph.D. thesis from University of Waterloo.

Desmarais, G., D. Derome, and P. Fazio. 1998. Experimental setup for the study of air leakage patterns. Thermal performance of the exterior envelope of buildings VII. Atlanta: American Society of Heating, Refrigerating and Air-conditioning Engineers, Inc. pp. 99-108.

Drennen, R.C., 1994. High-rise Curtain wall adds to fire-fighting challenges. Journal of Fire Engineering, June, 1994, pp.81-85.

Eckert, E.R.G. and W.O.Carlson. 1961. Natural convection in an air layer enclosed between two vertical plates with different temperatures. International Journal of Heat and Mass Transfer, Vol. 2, pp. 106-120.

Elder, J.W., 1965. Laminar free convection in a vertical slot. Journal of Fluid Mechanics, Vol.23, pp.77-98.

Elmahdy, A.H. 1990. A universal approach to laboratory assessment of the condensation potential of windows. Proceedings of the 16th annual conference of the solar energy society of Canada, pp.165-173.

Elmahdy, A.H., and Th. Frank. 1993. Heat transfer at the edge of sealed insulating glass units: comparison of hot box measurements with finite-difference modeling. ASHRAE Transactions, Vol. 99(1), pp.915-922.

Elmahdy, A.H., 1995. Air leakage characteristics of windows subjected to simultaneous temperature and pressure differentials. Proceedings of Window Innovation' 95, Toronto, Ont., Canada, pp. 146-163.

Elmahdy, A.H. 1996. Surface temperature measurement of insulating glass units using infrared thermography. ASHRAE Transactions 102 (2), pp. 489-496.

Elmahdy, A.H. 2001. To seal or not to seal? A critical look at the effects of air leakage on the condensation resistance of windows. Proceedings of whole-life performance of façade, Bath. pp. 143-152.

El-Sherbiny, S.M., G.D. Raithby, and K.G.T. Hollands. 1982. Heat transfer by natural convection across vertical and inclined air layers. ASME Journal of Heat Transfer, Vol. 104, pp. 96-102.

Endean, K.F. 1995. Investigating rainwater penetration of modern buildings. Brookfield, Vt.:Gower. Aldershot, Hampshire, England.

Enermodal Engineering Ltd.1990. FRAME/VISION window performance modeling and sensitivity analysis. Institute for Research in Construction, National Research Council of Canada, Ottawa.

Enermodal Engineering Ltd., 1994. Thermal performance of complex fenestration systems: skylights, greenhouse windows and curtain walls, CANMET Report.

Enermodal Engineering Ltd., 1995. FRAMEplus toolkit, version 4.0. Enermodal. Kitchener, Ontario.

Fanger, P.O. 1982. Thermal Comfort. Robert E. Krieger Publishing Company, Malabar, FL.

Fazio, P., Athienitis, A., Marsh, C. and Rao, J. 1997. Environmental chamber for investigation of building envelope performance. Journal of Architectural Engineering, Vol. 3, No. 2, pp. 97-102.

Fazio, P., D. Derome, D. Gerbasi, A. Athienitis, and S. Depani. 1998. Testing of flat roofs insulated with cellulosic fiber. Proceedings of the Thermal Performance of the Exterior Envelopes of Buildings VII Conference. Atlanta: American Society of Heating, Refrigerating and Air-conditioning Engineers, Inc. pp. 5-11.

Furler, R., P. Williams, F.K. Kneubuhl. 1988. Experimental and theoretical study on energy balance of windows. Ph.D. thesis 8580, ETH Zurich, Switzerland, NEFF report 177.1.

Ganguli, U. and Quirouette, R.L. 1987. Pressure equalization performance of a metal and glass curtain wall. IRC Paper No. 1542, NRCC 29024, National Research Council of Canada, Ottawa.

Ganguli, U. and Dalgliesh, W.A. 1988. Wind pressures on open rain screen walls: Place Air Canada. Journal of Structural Engineering, Vol. 114, No.3, pp. 642-656.

Garden, G.K. 1963. Rain penetration and its control, Canadian building digest (CBD) 40, National Research Council of Canada, Division of Building Research, Ottawa.

Griffith, B.T., F. Beck, D. Arasteh, and D. Türler. 1995. Issues associated with the use of infrared thermography for experimental testing of insulated systems. Proceedings of the Thermal Performance of the Exterior Envelopes of Buildings VI, pp.515-524.

Griffith, B.T., D. Türler, and D. Arasteh. 1996. Surface temperature of insulated glazing units: infrared thermography laboratory measurements. ASHRAE Transactions, 102(2), pp.479-488.

Griffith, B., D. Curcija, D. Türler, and D.K. Arasteh. 1998a. Improving computer simulations of heat transfer for projecting fenestration products: using radiation view-factor models. ASHRAE Transactions, Vol. 104 (1B), pp. 845-855.

Griffith, B.T., D. Türler, H. Goudey and D.K. Arasteh. 1998b. Experimental techniques for measuring temperature and velocity fields to improve the use and validation of building heat transfer models. Proceedings of the Thermal Performance of the Exterior Envelopes of Buildings VII Conference. Florida: American Society of Heating, Refrigerating and Air-conditioning Engineers, Inc. pp.337-347.

Griffith, B.T., Finlayson, E.U., Yazdanian M. and Arasteh D. 1998c. The significance of bolts in the thermal performance of curtain-wall frames for glazed façades. ASHRAE Transactions 104 (1): 1063-1069.

Hagentoft. 2001. Introduction to building physics. Carl-Eric Hagentoft and Studentlitteratur.

Han, H., Khusinsky, B.M., and Crooks B. 1992. Numerical prediction of moisture condensation on curtain walls using the finite-element method and its experimental validation. ASHRAE Transactions, pp. 574-583.

Hawken, P., Lovins, A., and Lovins, H.L, 1999. Natural capitalism: creating the next industrial revolution.

Hawthorne, W.A., and S. Reilly, 2000. The impact of glazing selection on residential duct design and comfort. ASHRAE Transactions, pp.553-561.

Heiselberg, P. 1994. Draught risk from cold vertical surfaces. Journal of Building & Environment, 29: 297-301.

Heiselberg, P., H. Overby, and E. Bjorn, 1995. Energy-efficient measures to avoid downdraft from large glazed facades. ASHRAE Transactions, 101(2) pp. 1127-1135.

Henry, R. and A. Patenaude. 1998. Measurements of window air leakage at cold temperatures and impact on annual energy performance of a house. ASHRAE Transactions, Vol. 104 (1), 1254-1260.

Hottel H.C., and A.F. Sarofim. 1967. Radiative Transfer. McGraw-Hill Book Company. pp. 51.

Hutcheon, N.B., 1963. Requirements for exterior walls, Canadian Building Digest. CBD-48. National Research Council of Canada, Division of Building Research, Ottawa.

Ito, N., and K. Kimura. 1972. A field experiment study on the convective heat transfer coefficient on the exterior surface of a building. ASHRAE Transactions 78(2):184.

Killip, I.R. and Cheetham, D.W. 1984. The prevention of rain penetration through external walls and ioints by means of pressure equalization. Journal of Building and Environment, vol. 19, No. 2, pp. 88-91.

Klems, J.H. 1989. U-values, solar heat gain, and thermal performance: Recent studies using the MoWitt. ASHRAE Transactions 95(1), pp.609-617.

Lawrence Berkeley National Laboratory. 1998. THERM 2.0: a program for analyzing two-dimensional heat transfer through building products. Berkeley CA, USA.

Le Fevre, E.J. 1956. Proc. 9th Itern. Congr. Appl. Mech., Brussels 4, p.168.

Ledbetter, S.R. 1991. A comparative study of the façade industry in the UK, Europe, Japan and the USA. Center for Window & Cladding Technology, University of Bath, Claverton Down, Bath.

Lee, Y., and Korpela, S.A. 1983. Multicellular natural convection in a vertical slot. Journal of Fluid Mechanics, Vol. 126, pp. 91-121.

Liley, P.E. 1968. The thermal conductivity of 46 gases at atmospheric pressure. Proceedings of the Fourth Symposium on Thermophysical Properties. Colledge Park, Md.: American Society of Mechanical Engineers.

Lokmanhekim, J. 1975. Procedure for determining heating and cooling loads for computerized energy calculations: Algorithms for building heat transfer subroutines. ASHRAE, New York.

Lyons, P., D. Arasteh, and C. Huizenga. 2000. Window performance for human thermal comfort. ASHRAE Transactions Vol.106(1), pp. 594-602.

McAdams, W.H. 1954. Heat transmission. McGraw-Hill.

McGowan, A.G. 1995. Numerical prediction of window condensation potential. ASHRAE Transactions, Vol. 101(1): pp.832-837.

McGowan, A.G., and J.L. Wright. 1998. Computer simulation of window condensation potential. Thermal performance of the exterior envelope of buildings VII, pp. 229-235.

MNBEC. 1997. Modeling national building energy of Canada. National Research Council of Canada, Ottawa.

National Building Code for Canada. 1995. Institute for Construction, National Research Council of Canada, Ottawa.

Ostrach, S. 1952. An analysis of laminar free-convection flow and heat transfer about a flat plate parallel to the direction of the generating body force. NACA TN2635.

Power, J.P., D.Curcija, and W.P. Goss. 1998. Two-dimensional turbulent flow and heat transfer in tall glazing cavities. Thermal performance of the exterior envelope of buildings VII, Atlanta: American Society of Heating, Refrigerating and Air-conditioning Engineers, Inc., pp. 385-395.

Quirouette, R.L. 1982. Building envelope design using metal and glass curtain Wall systems. Building Practice Note, No.37. Division of Building Research, National Research Council Canada.

Quirouette, R.L. 1985. The difference between a vapor barrier and an air barrier". Building Practice Note No. 54. Division of Building Research, National Research Council Canada.

Raithby, G.D., and K.G.T. Hollands. 1975. A general method of obtaining approximate solutions of laminar and turbulent free convection problems. Advances in Heat Transfer, 11:265-315. Academic Press.

Reardon, J.T., A.K., Kim, and C.Y. Shaw. 1987. Balanced fan depressurization method for measuring component and overall air leakage in single and multifamily dwellings. ASHRAE, Transaction, Vol. 93(2): pp. 137-151.

Reilly, S. 1994. Spacer effects on edge-of-glass and frame heat transfer. ASHRAE Transactions, Vol. 100(1), NO-94-31-3. pp. 1718-1723.

Roodman, D.M. and N. Lenssen. 1995. A building revolution: how ecology and health concerns are transforming construction.

Sakhnovsky, Alexander A. 1991. Full-scale performance testing of curtain walls. ASTM STP 1034, Exterior wall systems: glass and concrete technology, design and construction. pp.47-57.

Schrey, Arne-Chris, R.A. Fraser, and P.F. de Abreu. 1998. Local heat transfer coefficients for a flush-mounted glazing unit. ASHRAE Transactions, Vol.104 (1B), pp.1207-1221.

Shaw, C.Y. 1980. Method for conducting small-scale pressurization tests and air leakage data of multi-storey apartment buildings. ASHRAE Transactions, Vol. 86, part 1, pp. 241-250.

Shaw, C. Y., R. J. Magee, and, G. F. Poirier. 2000. Measured airtightness of an installed skylight", ASHRAE Transactions, 00-9-1 Vol. 106 (1) pp.713-718.

Sullivan, H.F., J.L. Wright, and R. Fraser. 1996. Overview of a project to determine the surface temperatures of insulated glazing units: Thermographic measurement and 2-D simulation. ASHRAE Transactions, Vol.102(2): pp.516-522.

Türler, D., B. T. Griffith, and D. K. Arasteh. 1997. Laboratory procedures for using infrared thermography to validate heat transfer models. ASTM STP 1320: Insulation materials: testing and applications. pp.23-45.

Wright, J.L., and H.F. Sullivan, 1989. Natural convection in sealed glazing units: A Review". ASHRAE Transactions, Vol. 95(1), pp. 592-602.

Wright, J.L., Abreu P.F., Fraser, R.A. and Sullivan, H.F., 1994. Heat transfer in glazing system edge-seals: calculations regarding various design options. ASHRAE Transactions, Vol. 100(1), pp. 1705-1717.

Wright, J.L. 1996. A correlation to quantify convective heat transfer between vertical window glazings. ASHRAE Transactions, Vol.102(1): pp.940-946.

Wright, J.L., 1998. A simplified numerical method for assessing the condensation resistance of windows. ASHRAE Transactions, Vol. 104 (1B), pp.1222-1229.

Yazhanian, M., and J.H. Klems, 1994. Measurement of the exterior convective film coefficient for windows in low-rise buildings. ASHRAE Transactions, Vol.100(1), pp.1087-1096.

Yeoh, G.H., G. de Vahl Davis, and E. Leonardi. 1989. Heat transfer across a double-glazed window with convective boundary conditions. Numerical Methods in Thermal Problems VI(1): 355-365.

Zhao, Y., D. Curcija, and W.P. Goss, 1996. Condensation resistance validation project-detailed computer simulations using finite-element methods. ASHRAE Transactions, Vol. 102(2), pp. 508-515.

Zhao, Y., D. Curcija and W.P.Goss, 1999. Convective heat transfer correlations for fenestration glazing cavities: a review. ASHRAE Transactions, Vol.105(2), pp.900-908.

Zhao, Y., D. Curcija, J.P. Power, and W.P.Goss, 1998. Improved heat transfer correlations for quantifying laminar natural convection across fenestration glazing cavities. Thermal performance of the exterior envelope of buildings VII, pp. 397-403.

Appendix A

Table A.1 Standards to evaluate curtain wall performance

Test	Standards	Remarks
Thermal Performance	C236-89—Standard test method for steady-state thermal performance of building assemblies by means of guarded hot box (1993)	U-factor for wall assembly Discontinued 2001, replaced by C1363-97
	C976-90—Standard test method for thermal performance of building assemblies by means of a calibrated hot box (1996)	U-factor for wall assembly Discontinued 2002, replaced by C1363-97
	C1199-00—Standard test method for measuring the steady-state thermal transmittance of fenestration systems using hot box methods	U-factor for fenestration products
	E1423-99—Standard Practice for determining the steady state thermal transmittance of fenestration systems	
	C1363-97—Standard test method for the thermal performance of building assemblies by means of a hot box apparatus	Replacement of C236 and C976
	CSA-A440.2-1998—Energy performance of windows and other fenestration systems	Windows, doors, curtain walls, U-factor, SHGC, energy rating
	AAMA-1503-98—Voluntary test method for thermal transmittance and condensation resistance of windows, doors and glazed wall sections	Windows and curtain walls, U-factor and condensation resistance factor
Air Leakage	E283-91—Standard test method for determining rate of air leakage through exterior windows, curtain walls, and doors under specified pressure difference across the specimen (1999)	Constant temperature differential with pressure differential-laboratory test
	E1424-91—Standard test method for determining the rate of air leakage through exterior windows, curtain walls and doors under specified pressure and temperature differences across the specimen (2000)	Certain temperature difference and pressure difference-laboratory test
	E779-99—Standard test method for determining air leakage rate by fan pressurization	Blower door test
	E783-93—Standard test method for field measurement of air leakage through installed exterior windows and doors	Field test, discontinued 2000, no replacement

Water Leakage	E331-00—Standard test method for water penetration of exterior windows, skylights, doors and curtain walls by uniform static air pressure difference	Static pressure difference—constant amount of sprayed water
	E547-00—Standard test method for water penetration of exterior windows, skylights, doors and curtain walls by cyclic static air pressure differential	Cyclic static pressure difference—constant amount of sprayed water
	E1105-00—Standard test method for field determination of water penetration of installed exterior windows, skylight, doors and curtain walls by uniform or cyclic static air pressure difference	Static or cyclic pressure difference-field test
	AAMA-501.1-94—"Standard test method for metal curtain wall for water penetration using dynamic pressure	Dynamic pressure difference—constant amount of sprayed water
Structural performance	E330-97—Standard test method for structural performance of exterior windows, curtain walls and doors by uniform static air pressure difference	Static pressure difference—Estimate load and deflection sensors
	E1233-00—Standard test method for structural performance of exterior windows, curtain walls, and doors by cyclic static air pressure differential	Cyclic pressure difference—estimate load and deflection sensors

Appendix B

B.1 External reference emitter

The reference emitter is made of a solid block of copper with a dimension of 3.5" by 3" by ¾" thick as shown in Figure B.1. A continuous fluid channel made of two concentric rectangular spirals with opposing directions was machined out of the copper block and a ½-inch-thick solid portion directly underneath the reference surface was kept. This design can minimize the temperature gradients across the surface since the supply and return continuously exchange heat inside the block. The back of the fluid channel in the block was sealed with an additional copper plate. The entire device except for the front reference surface is insulated. A platinum resistance temperature detector (RTD) was installed at the center of the solid copper portion to monitor the surface temperature. A piece of sample from the test specimen can be glued to the reference emitter with heat sink compound. The temperature-controlled liquid was supplied by a temperature bath with a built-in temperature controller. This bath can maintain temperature in glycol liquid within $0.05°C$ and with an accuracy of $± 0.1°C$ between $-36°C$ and $50°C$. The liquid supply and return pipes were insulated.
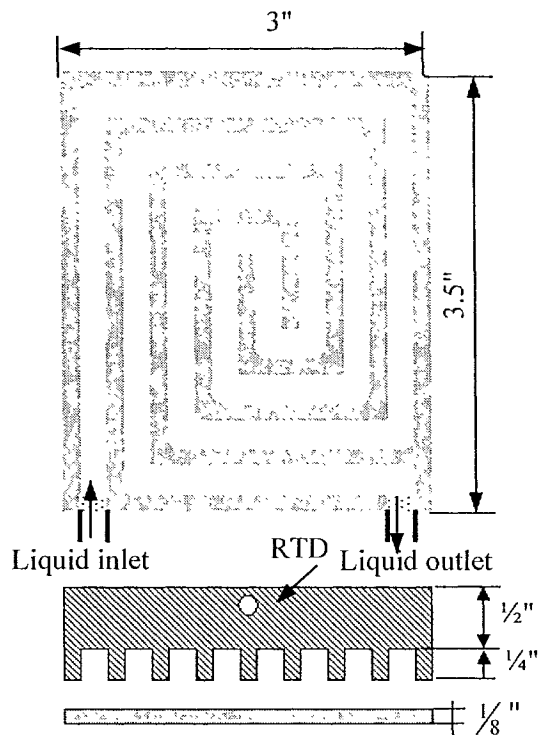
Figure B.1 Configuration of the reference emitter

B.2 Procedure to determine surface emittance

To measure surface emittance (Türler, et al., 1997), a sample with known emissivity and the unknown sample shall be placed side by side on an isothermal, temperature-controlled plate. Good thermal contact need to be maintained between the samples and the plate to bring the samples to the same surface temperature. The temperature should be set at approximately $10^{\circ}C$ to $20^{\circ}C$ above or below the background temperature to ensure high contrast between radiations from specimens and from the background. The surface temperatures can be measured using an IR scanning device or the IR camera with emittance set to 1.0. The temperature obtained $T_{\varepsilon=1}$ is the equivalent blackbody temperature. The emittance of the unknown material can be calculated using equation B.1.

$$\varepsilon_{smpl} = \frac{(T_{\varepsilon=1,smpl}^4 - T_{background}^4)}{(T_{\varepsilon=1,ref}^4 - T_{background}^4)} \varepsilon_{ref}$$

(B.1)

where,

ε_{smpl} = emittance of the sample material, dimensionless;

ε_{ref} = emittance of the reference material, dimensionless;

$T_{e=1, smpl}$ = equivalent blackbody temperature of the unknown sample material, K;

$T_{e=1, ref}$ = equivalent blackbody temperature of the reference material, K; and

$T_{background}$ = background radiation equivalent blackbody temperature, K.

Appendix C

C.1 Procedure to calculate view factors

The view factor between the glazing panel and the hot box floor is calculated first. Then, all of the view factors can be obtained by applying the reciprocity relation, $A_i \cdot F_{ij} = A_j \cdot F_{ji}$, and the unity relation, $\sum_{j=1}^{n} F_{ij} = 1$. The view factor between any two perpendicular rectangle surfaces with a common edge illustrated in Figure C.1 can be calculated using the following equation (Hottel, and Sarofim, 1967):

$$F_{12} = \frac{1}{A_1 \pi} \left\{ \begin{array}{l} \dfrac{1}{4} \ln \left[\dfrac{(X^2 + Y^2 + Z^2)^{Y^2 + Z^2 - X^2} (Y^2)^{Y^2} (Z^2)^{Z^2}}{(X^2 + Y^2)^{Y^2 - X^2} (X^2 + Z^2)^{Z^2 - X^2} (Y^2 + Z^2)^{Y^2 + Z^2} (X^2)^{X^2}} \right] \\ + XY \tan^{-1} \dfrac{X}{Y} + XZ \tan^{-1} \dfrac{X}{Z} - X(Y^2 + Z^2)^{1/2} \tan^{-1} \dfrac{X}{(Y^2 + Z^2)^{1/2}} \end{array} \right\} \quad \text{(C.1)}$$
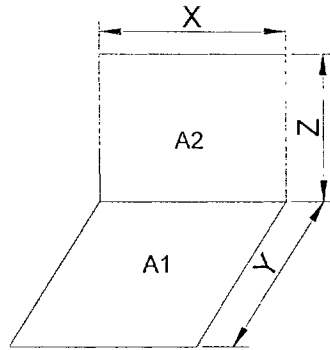

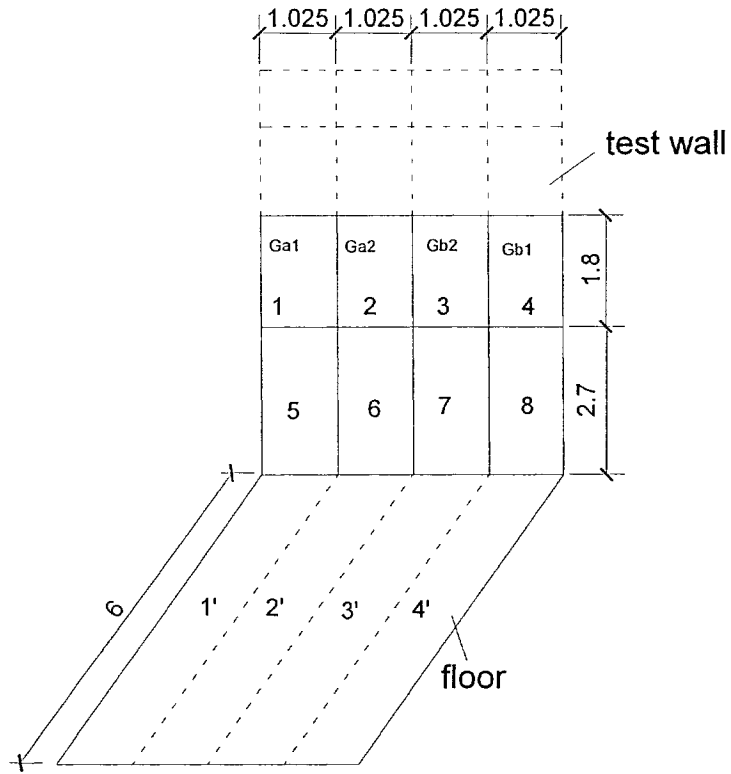Figure C.1 Two perpendicular rectangles with a common edge

Figure C.2 Rectangle arrangement for view factor calculation

The view factors, $F_{1-1'2'3'4'}$, $F_{2-1'2'3'4'}$, $F_{3-1'2'3'4'}$, and $F_{4-1'2'3'4'}$, for glazing panels shown in Figure C.2 can be determined by applying the unity relation and symmetrical rules and can be expressed as

$$F_{1-1'2'3'4'} = F_{4-1'2'3'4'} = \frac{1}{2}(F_{1234-1'2'3'4'} - F_{123-1'2'3'} + F_{1-1'}) \qquad (C.2)$$

$$F_{2-1'2'3'4'} = F_{3-1'2'3'4'} = \frac{1}{2}(F_{123-1'2'3'} - F_{1-1'}) \qquad (C.3)$$

C.2 Properties of gases filled in glazing cavity

Table C.1 Thermal properties of gases in glazing cavity

Thermal Properties	Correlation	Air		Argon	
		a	b	a	b
Thermal Conductivity k (W/m·K)	$k=a+bT_m$	2.3012×10^{-3}	7.9870×10^{-5}	2.4773×10^{-3}	5.0713×10^{-5}
Viscosity (g/m·s)	$\mu=a+bT_m$	3.5165×10^{-3}	4.98×10^{-5}	3.618×10^{-3}	6.44×10^{-5}
Specific heat at constant pressure C_p (J/gmole·K)	$C_P=a+bT_m$	29.021	0.42493×10^{-3}	21.000	-0.54964×10^{-3}

Note: T_m in K,

Appendix D

Table D.1 Thermal conductivity of materials used in the simulations

Materials	Thermal Conductivity, k in W/ m·K
Aluminum	160
Stainless steel	14.3
Steel	48
Glass	1.0
Rigid fiberglass insulation	0.036
Extruded Polystyrene	0.029
Flexible vinyl	0.12
Neoprene gasket	0.19
Fiberglass reinforced nylon	0.23
Polyisobutylene	0.24
Butyl Rubber	0.24